DSPACE

https://dspace.org/

Modification of the cast structure of stainless steel AISI310s and its influence on mechanical properties

Ozbayraktar, Serdar

1992
https://hdl.handle.net/10539/27915

Downloaded from a DSpace repository. https://dspace.org/

MODIFICATION OF THE CAST STRUCTURE OF STAINLESS STEEL AISI310S AND ITS INFLUENCE ON MECHANICAL PROPERTIES

Serdar Ozbayraktar

A thesis submitted to the Faculty of Engineering, University of the Witwatersrand, Johannesburg, in fulfilment of the requirements for the degree of Doctor of Philosophy

Johannesburg, 1992

DECLARATION

I declare that this thesis is my own, unaided work. It is being submitted for the Degree of Doctor of Philosophy in the University of the Witwatersrand, Johannesburg. It has not been submitted before for any degree or examination in any other University.

S Ozbay-akter

(Signature of candidate)

11th day of September 1992

ACHIEVEMENTS

This study established that under certain cooling conditions steel AISI310S solidifies as δ-ferrite and goes through a peritectic reaction before transforming to austenite.

It also established mathematical relationships between percentage equiaxed zone and superheat, grain width and superheat, primary arm spacing and superheat, grain width and primary dendrite arm spacing as well as mechanical properties and grain size. An original explanation is proposed for the relationship between macrostructure and microstructure. The concept of a "grain width ratio" was developed to investigate the nucleation and growth kinetics under different conditions and thus study the effects of the addition of nucleants.

ABSTRACT

A close relationship exists between the macrostructure of as-cast alloys and their mechanical properties and extensive research has gone into the modification of as-cast structures in attempts to improve mechanical properties.

Chemical grain refining methods have been widely used to modify the cast structures of Al- and Mg-base alloys as well as cast iron and so improve their mechanical properties and formabilities. For these materials very substantial improvements have been obtained through very small additions of what may be called inoculants. More recently the modification of cast steel, including ferritic and austenitic grades, has been receiving considerable attention.

Several effective grain refining agents, notably TiN, have been used successfully with ferritic stainless steels. Although rare earths and FeSiZr have been reported to modify the steels which solidify as austenite, the mechanisms whereby these agents influence the nucleation of austenite are not well understood.

The major emphasis of this work has been to develop a description of the effects of casting temperature and additions of Misch Metal and FeSiZr on the macrostructure and microstructure of as-cast AISI310S stainless steel.

For this purpose, columnar grain widths as well as primary and secondary arm spacings were measured in ingots cast from different temperatures with or without additions. The term "grain width ratio" has been introduced to describe the relationship between the shape and the nucleation and growth kinetics of the columnar grains.

A quasi empirical solidification model was developed to describe the evolution of macrostructure and microstructure in AISI310S on solidification. The experimental results of this work showed that the macrostructure and the microstructure of the cast material responded differently to variations in casting temperature and additions. The proposed model, based on these findings, suggested that if the structure modification mechanism relied on constitutional supercooling then a coarser primary dendrite arm spacing would inevitably be obtained as the columnar grain width decreased. The relatively coarser microstructure of ingots containing additions of Misch Metal suggested that these additions modified the structure through their influence on constitutional supercooling. The macrostructures of ingots containing Misch Metal were refined by up to 50%. It was also possible to treat the development of the equiaxed zone in the base (reference) ingots by using a similar model which was based on the constitutional supercooling hypothesis.

The tensile properties of the ingots were correlated with the shape and size of the grains in the material. Thus the improved tensile properties obtained with coarser columnar grains and differences in properties depending on specimen orientation were explained by taking into account the three-dimensional anisotropy of the cast structure.

Selected ingots were tested after hot and cold rolling to investigate the influence of cast structure modification on the mechanical properties of rolled material. Improved tensile properties were obtained in the as-hot rolled condition due to the grain refining effect of the Misch Metal and FeSiZr additions on the steel.

Cold rolled AISI310S steel with smaller grain sizes showed very smooth edge surface characteristics whereas the pieces with larger grains had rough surface features.

To Mom and Dad

ACKNOWLEDGEMENTS

I wish to express my sincere thanks to my supervisor Dr A. Koursaris for his patient guidance, constant encouragement, and valuable suggestions throughout the course of this work.

I am grateful to Middelburg Steel and Alloys and CSIR/FRD for the financial assistance they provided.

The support of my friends and collegues: Ercan, Yunus, Guven, Orhan has been a constant source of encouragement. Special thanks are extended to Bondonno family and Angela for their unforgettable friendship and italian dishes which enriched my life during the course of this work.

I am thankful to J. Morfitt, J. Ndengeza, Shadrack Moqabolane for their technical assistance.

I am also grateful to Dr P. Anagnostaras for his valuable time and effort he spared for proof reading the text of this work.

Finally I am very much indebted to Magda, for her patience, support and encouragement during the last two years.

CONTENTS

Page

DECLARATION.....i
ACHIEVEMENTS.....ii
ABSTRACT.....iii
DEDICATION.....vi
ACKNOWLEDGEMENTS.....vii
CONTENTS.....viii
LIST OF FIGURES.....xii
LIST OF TABLES.....ixx
LIST OF SYMBOLS.....xxii

1. INTRODUCTION.....1

2. NUCLEATION AND GROWTH MECHANISMS IN THE LIQUID-SOLID TRANSFORMATION OF ALLOYS.....8

2.1 Nucleation.....8
2.1.1 Nucleation Mechanisms in Stainless Steels.....12
2.2 Growth.....18
2.2.1 Solute Redistribution by Diffusion.....19
2.2.2 Constitutional Undercooling.....24
2.2.3 Growth Morphologies.....25

3. STRUCTURE OF CASTINGS.....36

4. MECHANISMS OF CHEMICAL GRAIN REFINEMENT.....37

4.1 The Effects of Solute Redistribution on Cast Structures.....37
4.2 The Effect of Alloy Variables on Cast Structures.....46
4.3 The Role of Solute Activities in Chemical Grain Refinement of Stainless Steels.....50
4.4 The Role of Nucleation Entropy in Chemical Grain Refinement of Stainless Steels.....53

4.5 The Problems that may be Encountered during the Grain Refinement Process.....55

4.6 Summary of the Mechanisms of Chemical Grain Refinement in Stainless Steels.....56

5. EXPERIMENTAL PROCEDURES.....58

5.1 Introduction.....58

5.2 Materials and Melting Practice.....58

5.3 Macrostructural Examination of the As-Cast Structures.....64

5.4 Microstructural Examination of the As-Cast Structures.....68

5.5 Chemical Analyses.....73

5.6 Hot Rolling.....74

5.7 Cold Rolling.....74

5.8 Heat Treatment of Cold Rolled Material.....75

5.9 Microscopic Examination of As Rolled Structures.....75

5.10 Mechanical Tests.....75

5.10.1 Hardness Tests.....77

5.10.2 Tensile Tests.....77

5.10.3 Charpy Impact Tests.....79

6. EXPERIMENTAL RESULTS..... 80

6.1 Chemical Composition of the Castings.....80

6.1.1 Recovery of Rare Earths in the Cast Metal....88

6.1.2 Recovery of Zr in the Cast Metal.....92

6.2 Ingot Macrostructure.....94

6.2.1 Base Castings with no Additions.....94

6.2.2 Castings with Misch Metal Additions.....108

6.2.3 Castings with Additions of FeSiZr.....121

6.2.3.1 Grain Width Ratio Analyses for Ingots with Zirconium Additions.....129

6.3 Results of the Microstructural Evaluation of the As-Cast Ingots.....132

6.3.1 Microstructural Evaluation of Base Metal Ingots.....132

6.3.1.1 Solidification Pattern of Base Ingots.....132

6.3.1.2 Primary and Secondary Dendrite Arm Spacings.....135

6.3.2 Microstructural Evaluation of Ingots with Additions of Misch Metal.....154

6.3.2.1 Results of Primary and Secondary Dendrite Arm Spacing Measurements of Castings Containing Misch Metal.....154

6.3.3 Microstructural Evaluation of Ingots with FeSiZr Additions.....165

6.3.3.1 Primary and Secondary Dendrite Arm Spacings in Castings Containing FeSiZr.....165

6.4 Mechanical Properties of the As-Cast AISI310S with and without Additions.....173

6.4.1 Tensile and Impact Test Properties.....173

6.4.1.1 Tensile Properties in the As Cast Condition..183

6.4.1.2 Impact Test Results.....187

6.4.3 Hardness Test Results.....187

6.4.4 Summary of Mechanical Test Results for Material in the As-Cast Condition....192

6.5 Properties of Stainless Steel AISI310S in the As-Rolled Condition.....196

6.5.1 The Relationship Between As-Cast and As-Rolled Grain Sizes.....196

6.5.2 Tensile Properties.....196

6.5.2.1 Yield Strength.....196

6.5.2.2 Tensile Strength.....199

6.5.2.3 Elongation.....202

6.5.2.4 Reduction in Area.....205

6.5.3 Charpy Impact Tests.....205

6.5.4 Hardness Tests.....206

6.6 Properties of Stainless Steel AISI310S in the As-Cold Rolled Condition.....210

7. **DISCUSSION AND THE PROPOSED QUASI-EMPRICAL SOLIDIFICATION MODEL FOR AISI310S STAINLESS STEEL**.....219

7.1 **Effect of Superheat on the Solidification Mode of AISI310S**.....221

7.2 **Effect of Superheat on the As-Cast Macrostructure of AISI310S Stainless Steel Without Additions**.....239

7.2.1 Effect of Superheat on the Formation of Equiaxed Zone.....243

7.3 **Effect of Superheat on the As-Cast Microstructure**.....252

7.3.1 Proposed Primary Arm Spacing Model.....259

7.4 **The Relationship Between Microstructure and Macrostructure**.....268

7.5 **The Influence of Additions on the Macro- and Microstructure of AISI310S Stainless Steel**.....280

7.6 **Effect of Macrostructural Changes on the Mechanical Properties of the As-Cast AISI310S Steel**.....284

8. **CONCLUSIONS**.....292

9. **REFERENCES**.....298

LIST OF FIGURES

Figure		Page
2.1	The spherical cap model of heterogeneous nucleation	9
2.2	Pseudo-binary phase diagram for Fe-Cr-Ni alloys	14
2.3	Schematic representation of atomic plane matching	15
2.4	Phase diagram with a continuous range of solid solutions	21
2.5	The solute profile ahead of the solid/liquid interface	22
2.6	Constitutional supercooling in alloy solidification	22
2.7	Influence of undercooling on morphology and growth	26
2.8	Cellular substructure formed by undercooling	26
2.9	Dendritic growth pattern	28
3.1	Three basic zones of as-cast ingot structure	30
3.2	The development of the constitutionally supercooled region	33
4.1	Influence of temperature gradient and freezing rate on solidification morphology	45
4.2	Variation of the grain size of nickel alloy castings as a function of the parameter P	48
4.3	Variation of the grain size of aluminium alloy castings as a function of the parameter P	49
4.4	Relation between activity of an element B and its solubility in the system AB	51

4.5 Reduced solubility of B due to an increase in a_B 52

5.1 Flowsheet summarizing the experimental and analytical procedures followed in this study 59

5.2 Vacuum induction furnace used for the melting and casting of AISI310S steel 62

5.3 Plots of temperature against time for metal held in the melting furnace with the power off 65

5.4 Positions of the slices cut from as-cast ingots for measurements 66

5.5 "Concentric" squares used to measure the grain widths 67

5.6 Position and orientation of the samples cut from the ingots for mechanical tests 76

5.7 Shape and dimensions of the tensile test pieces 78

5.8 Dimensions of the Charpy impact test pieces 79

6.1 Change in the O_2 concentration in AISI310S with changes in the amount of misch metal added 87

6.2 Changes in the recovery of Ce and La with changes in the amounts of misch metal added 90

6.3 Change in the percentage loss of REM with holding time 91

6.4 Effect of casting temperature on the recovery of Zr 93

6.5 Macrostructures of ingots with no additions 95

6.6 Change in grain width measured at 6mm for ingots without additions 100

6.7 Change in grain width measured at 14mm for ingots without additions 100

6.8 Plots of grain width at 6 and 14mm against superheat 102

6.9 Development of the equiaxed zone with casting temperature 103

6.10 Influence of degree of superheat on the proportion of equiaxed zone 105

6.11 Change in grain width ratio with casting temperature 107

6.12 Change in grain width ratio with grain width at 14mm 107

6.13 Macrostructures of ingots with additions of misch metal 109

6.14 Change in grain width for the ingots with misch metal additions and cast between 1608 and 1637°C 115

6.15 Change in grain width for the ingots with misch metal additions and cast between 1523 and 1551°C 116

6.16 Change in grain width for the ingots with misch metal additions and cast from 1490-1510°C 118

6.17 Measured grain width ratios for ingots containing misch metal as a function of casting temperature 118

6.18 Change in grain width ratio with recovered Ce and La 119

6.19 Change in grain width ratio as a function of grain width for ingots with misch metal addition 120

6.20 Macrostructures of ingots with FeSiZr additions 122

6.21 Change in grain width with casting temperature for ingots with FeSiZr additions 127

6.22 Change in grain width with Zr additions 128

6.23 Change in grain width ratio with casting temperature for ingots containing FeSiZr additions 130

6.24 Change of grain width ratio with grain width for ingots with FeSiZr additions 131

6.25 Microstructure showing δ-grain boundaries preserved in ingots cast in the temperature range 1476 to 1564°C 133

6.26 EDS analyses of th elements in γ grains, in δ grain boundar and in γ dendrite boundary 134

6.27 Changes in cooling rate of base ingots with distance from the chill zone 139

6.28 Variation in primary dendrite arm spacing with casting temperature 141

6.29 Variation in secondary dendrite arm spacings with ca ting temperature 142

6.30 Microstructure of base metal ingots ca from different temperatures 143

6.31 Change in primary dendrite arm spacing of ingots with changes in grain width 147

6.32 Change in secondary dendrite arm spacing of ingots with changes in grain width 149

6.33 Change of secondary arm spacing with changing primary arm spacing 150

6.34 Logarithmic regression lines for the change in secondary arm spacing with changing primary arm spacing 151

6.35 Comparison between regression lines of secondary and pri ry arm spacing obtained in this st with similar regression lines found in the literature 151

6.36 Change in the slope of plots of secondary arm spacing against primary arm spacing with columnar grain width 152

6.37 Change in the slope of plots of secondary arm spacing against primary arm spacing with grain width ratio 153

6.38 Micrographs of the as-cast structures of AISI310S ingots cast with misch metal additions 155

6.39 Regression curves of primary arm spacing against distance for ingots B5 and MM14 161

6.40 Regression curves of primary arm spacing against distance for B4 and MM16 161

6.41 Change of secondary arm spacing with primary arm spacing for the ingots with misch metal additions 163

6.42 Δsecondary arm spacing/Δ100μm primary arm spacing with grain width for the ingots with misch metal additions 164

6.43 Δsecondary arm spacing/Δ100μm primary arm spacing with grain width ratio for the ingots containing misch metal 164

6.44 Micrographs of as-cast AISI310S ingots with FeSiZr additions 166

6.45 Regression curves of primary arm spacing against distance for B4 and ZR9 169

6.46 Regression curves of primary arm spacing against distance for B6 and ZR10 169

6.47 Change of primary and secondary arm spacings with changing amount of Zr addition 170

6.48 Change of primary and secondary arm spacings against grain widths for the ingots with FeSiZr additions 171

6.49 Δ secondary arm spacing/Δ100μm primary arm spacing as a function of Zr addition 172

6.50 Tensile strength as a function of grain width for the ingots with additions and for the base ingots 175

6.51 Yield strength as a function of grain width for the ingots with additions and for the base ingots 177

6.52 % Elongation as a function of grain width for the ingots with additions and for the base ingots 179

6.53 % Reduction in area as a function of grain width for the ingots with additions and for the base ingots 181

6.54 Differences in percentage reduction in diameter along two perpendicular axes of the fracture surfaces 182

6.55 Fracture surfaces of selected tensile test pieces 184

6.56 Change in yield strength due to heat treatment 185

6.57 Change in tensile strength due to heat treatment 185

6.58 Change in % elongation due to heat treatment 186

6.59 Change in % RA due to heat treatment 186

6.60 Change in notch impact energy with columnar width 188

6.61 Changes in hardness with primary arm spacing 191

6.62 As-rolled grain size against as-cast grain width 198

6.63 As-rolled grain size against secondary arm spacing 198

6.64 Change in yield strength with as-rolled grain size 200

6.65 Change in tensile strength with as-rolled grain size 200

6.66 Change in % elongation with as-rolled grain size 202

6.67 Change in % reduction in area with as-rolled grain size 207

6.68 Change in notch impact energy with as-rolled grain size 207

6.69 Change of hardness with as-rolled grain size 209

6.70 Surface characteristics of cold rolled billets 211

6.71 Change in hardness with annealing times of the cold rolled billets 216

6.72 Micrographs of cold rolled billets 217

7.1 Section from the Fe-Cr-Ni equilibrium phase diagram 222

7.2 Fe-Cr-Ni pseudo-binary phase diagram at 25 wt% Cr 223

7.3 The transition of primary δ-ferrite to austenite as a function of nitrogen content and cooling rate 226

7.4 Schematic description of solidification modes of AISI310S steel in separate casting temperature ranges 229

7.5 The schematic description of how the prior δ-ferrite grain boundaries are preserved in γ-grains 234

7.6 Illustrations showing the relationship between grain ratio and nucleation and growth rate 240

7.7 Changes in the amount of constitutional supercooling and the width of the supercooled region with change in the slope of the thermal gradient 244

7.8 The change of the proportion of equiaxed zone with superheat 247

7.9 Illustrations showing the influence of superheat on primary arm spacing 257

7.10 Primary arm spacings calculated by the proposed model and measured by Suzuki et al 261

7.11 The plot of grain width/primary dendrite arm spacing against 1/superheat 279

7.12 The plot of the equation y = 1/(e*lnx) 279

7.13 Schematic representations of the sections of a columnar grain 286

7.14 Schematic representations of the alignment of columnar grains in tensile test pieces 287

7.15 Schematic representations of the deformation modes for tensile test pieces A and B and the corresponding fracture surfaces 289

7.16 Schematic representations of the deformation mode for tensile test pieces cut from cast ingots with equiaxed structure 291

LIST OF TABLES

Table		Page
1.1	Some grain refining nucleants and possible mechanisms	4
2.1	Crystallographic data of effective nucleating agents for δ-iron	14
2.2	Summary of effective inoculating and microalloying agents for steels classified according to initial nucleating phase	16
4.1	Summary of effective inoculating and microalloying agents for iron and its alloys	38
5.1	Chemical composition of the AISI310S stainless steel	60
5.2	Chemical analyses of the misch metal and FeSiZr	60
5.3	Average primary arm spacings measured at various distances with their 95% confidence limits	70
5.4	Average secondary arm spacings measured at various distances with their 95% confidence limits	71
6.1	Chemical analysis of as-received and as-cast AISI310S stainless steel	81
6.2	Chemical analysis of ingots containing misch metal	82
6.3	Chemical analysis of ingots containing FeSiZr	84
6.4	Concentrations of C, S, Cr, Ni and O_2 in three different groups of ingots	86
6.5	Concentrations and % recoveries of rare-earth elements after different holding times	89

6.6 The statistical relationship between the amounts of Ce and La added to the steel as misch metal and th amounts recovered in the alloy 91

6.7 Recovery of Zr in the cast AISI310S ingots for different casting temperatures, holding times and additions of FeSiZr 93

6.8 Change in macrostructure with casting temperature for ingots with no addition 99

6.9 Macrostructure measurements on ingots with misch metal additions 113

6.10 Macrostructure measurements on ingots containing FeSiZr 124

6.11 Primary and secondary dendrite arm spacings for base metal castings 136

6.12 Primary and secondary arm spacing measurements of AISI310S steel castings with additions of misch metal 158

6.13 Primary and secondary arm spacings for ingots containing FeSiZr 167

6.14 Mechanical properties of the as-cast AISI310S ingots with and without additions 174

6.15 Vickers hardness values for as-cast base metal ingots 189

6.16 Vickers hardness values for selected as-cast ingots with additions 190

6.17 Tensile and impact test results for the hot rolled AISI310S ingots with and without additions 197

6.18 Regression equations for tensile strength as a function of grain size in hot rolled and annealed conditions 201

6.19 Micro- and macro-hardness values for the hot-rolled AISI310S ingots with or without additions 208

6.20 Hardness measurement results obtained on the cold rolled and the cold rolled/annealed materials 215

7.1 Secondary arm spacing values measured for various types of continuous cast steels 227

7.2 Comparison of the λ_1 values calculated using the quasi-empirical equation with Suzuki et al's experimental data for AISI310S 264

7.3 Comparison of the λ_1 values calculated using the quasi-empirical equation with Suzuki et al's experimental data for Cr-Mo steel 265

LIST OF SYMBOLS

a	activity
at	atomic
α	constant for the proportion of equiaxed zone
$\alpha_{1,2}$	constants for primary dendrite arm spacing
$\beta_{1,2}$	constants for columnar grain width
C	solute concentration
C_s	solute concentration in the solid
C_L	solute concentration in the liquid
C_o	initial solute concentration
d	grain size (hot rolled)
D	diffusion coefficient
λ_1	primary dendrite arm spacing
λ_2	secondary dendrite arm spacing
λ_s	primary dendrite arm spacings measured by Suzuki et al
λ_c	primary dendrite arm spacings calculated by the model
ε	constant related to the growth pattern of the secondary dendrite arm
e	interaction coefficient or number e (= 2.71828...)
f	activity coefficient
G	thermal gradient
ΔG^*	critical free energy barrier for nucleation
ΔG_v	volume free energy change
gw	columnar grain width
gw_6	columnar grain width measured at 6mm from the chill zone
gw_{14}	columnar grain width measured at 14mm from the chill zone
gwr	grain width ratio
ΔH	enthalpy change
I	nucleation rate
k_o	partition coefficient
k	Boltzmann's constant
K	constant for nucleation rate
$K^{\delta/L}$	distribution coefficient
$K^{\gamma/L}$	distribution coefficient

L	liquid
ln	natural logarithm
m	slope of liquidus
P	constitutional supercooling parameter
pct	percent
R	growth rate
ΔS_v	volume entropy change
t	time
t_f	local solidification time
Δt	increment of time
T_a	ambient temperature
T_o	outer mould wall temperature
ΔT	undercooling, supercooling
ΔT_s	solidification range
T_i	interface temperature or inner mould wall temperature
T_L	liquidus temperature or temperature of the liquid metal
T_M	melting temperature
wt	weight
X	distance ahead of solid-liquid interface
γ_{lc}	surface energy of the liquid-crystal interface
Θ	contact angle between the crystal and the substrate

1. INTRODUCTION

Most ferrous and non-ferrous alloys are cast into ingots or slabs which undergo subsequent shaping and heat treatment. The remainder are directly cast into their final shapes and may require further heat treatment to relieve residual stresses, bring about microstructural changes and improve their mechanical properties.

The properties of cast and wrought alloys are influenced by the structure that forms upon solidification. An inferior structure in the as cast condition is difficult to process by rolling or forging[1-4]. In the case of shaped castings an inferior macrostructure gives inferior properties after heat treatment due to the inability of the treatment to homogenize the material completely[5,6].

The major macrostructural features contributing to these properties are the grain size and grain shape of the as cast metal[7,8]. A fine grain size is normally required and there have been many attempts to reduce the grain size of cast metals. Various methods of cast structure modification have been investigated and applied on the laboratory and industrial scales, especially in the production of aluminium alloys and cast irons. Recently increasing attention has been focused on grain size control in steels and other alloys.

One of the primary objectives of research into the grain size control of steels has been to suppress the coarse columnar zone that forms upon solidification. This can be achieved by inducing conditions that promote the formation and widening of the equiaxed zone at the expense of the columnar zone.

There are two basic preconditions which have to be realized in order to enhance the formation of this zone:

(i) there has to be a fine and homogeneous dispersion of nucleation sites in the melt for the solidifying phase to nucleate on, and

(ii) sufficient undercooling in the vicinity of the nucleation sites is necessary to provide the thermal driving force for nucleation.

The nucleation sites may be found in the molten metal endogenously as an impurity[9], or as a product of high temperature reactions, or as initially solidified crystals which drift into the liquid by convection[10-16]. They may also be found as exogenously added inoculants which possess the chemical and physical properties that enhance their nucleation effectiveness[17-20].

Three different types of grain refining techniques may be recognized as follows.

(i) Dynamic methods which may include magnetic[21-25], sonic and ultrasonic stirring[26-28], vibration and shaking[29-31] of the melt in the mould during solidification.

(ii) Thermal methods such as microchilling[32-40], low superheat pouring, heating up the mould and similar techniques.

(iii) Chemical methods including inoculating and microalloying.

All the above techniques are believed to provide the two preconditions for grain refining, i.e. ready sites for nucleating and undercooling as the thermal driving force. Each method however has its own practical limitations and its effectiveness varies with different processes. For example dynamic methods are difficult to apply with castings made in nonmetallic moulds and add another step to the casting process. In microchilling a homogeneous distribution of the solid particles must be obtained in the melt and a low superheat is required which is not practical for complicated and large castings.

Of these three techniques, chemical grain refining appears to be the most promising owing to its practical nature and its potential applicability. It is basically the addition of a certain element or mixture of elements to the melt before pouring.

The possibilities of chemical grain refinement have been extensively investigated in aluminium alloys[41-82] and cast iron[83-86]. In these two types of alloys very substantial improvements in properties have been brought about by simple inoculation techniques. Various master alloys for use as additives to molten metal just before pouring have been developed and have proved to be successful in modifying the structure. For example, Al-Ti-B master alloys for pure aluminium[87-97], Sr-containing alloys for Al-Si alloys[98-109] and Si-containing aluminium or alkaline earth metals for grey cast iron[110-111] are now established and widely used inoculants in foundry applications of these alloys. A summary of grain refiners and the related mechanisms for these alloys as well as others like Mg, Cu, Au and Pb is given in Table 1.1.

TABLE 1.1 Some Grain Refining Nucleants and Possible Mechanisms

Metal or alloy	Grain Refiner	Mechanisms	References
Aluminium and its alloys	Nb;Zr;Sc;B;Ta	Al_3Nb; Al_3Zr; Al_3Sc; AlB_2 act as nucleation sites for Al.	53,48,64, 42,63
Aluminium and its alloys	Ti+B;Ti+S;Ti+Si	Al_3Ti acts as nucleation sites for Al	87-97
Al-Si Eutectic	Na; Sr; REM	Na and Sr poison the growth steps of Si rich phase	80,98-102,104-109
Al-Si Hyper-eutectic	P + Na	Al phosphide and Na phosphide act as nuclei	79
Al-Si-Mg	Sb	Sb modifies eutectic structure	78
Bronzes	Pb, transition nitrides borides or FeB		246
Cu-9% Al	Ti; Zr Bi		247
Cu-7% Al	Mo; Nb; W; V		247
Cu-Al_2Cu Eutectic	Ti	Ti nucleates primary Al	249
Cu	Te;Bi;Ti;B;Ce	They promote constitutional supercooling	250,248, 252
Cu-Zn-Al and Cu-Al-Ni	Ti; B	Ti-rich particle or Al-rich borides act as nuclei	253
Brass (70/30)	Fe		255-254
Gold	Ba;Zr;Nb Ta		256
Dental Gold	Ir;Ru;Rh;Co	They promote constitutional supercooling and form stable precipitates	257-258

TABLE 1.1 Some Grain Refining Nucleants and Possible Mechanisms (Cont'd)

Metal or alloy	Grain Refiner	Mechanisms	References
Mg and Mg-Zr alloys	Zr	Zr or Zr enriched Mg peritectic nuclei	245
Mg-Al	C	[illegible] or $AlNaAl_4C$ nuclei	259-260
Mg-Al	Superheating	In presence of C, Al_4C_3 and/or Al- [illegible] nuclei	261
Mg-Al-Mn	$FeCl_3$	Fe-Al-Mn or Al_4C_3 nuclei	245
Mg-Zn	$FeCl_3$ or Zn-Fe	Fe compound nuclei	245
Tin Alloys	Ge; In		262
Lead Alloys	S;Se;S+Te;Te	PbS; PbSe; PbTe act as nuclei	263
Grey Cast Iron	C; Si alloys containing aluminium, alkaline earths and/or rare earths	Refines eutectic, may nucleate through precipitation of carbides or graphite	84
Nodular Cast Iron	Mg+Ca;Mg+Ca+S	(Mg, Ca) and (Mg, Ca, Sr) S act as nuclei for graphite	83
Low Alloy Steels	Al+Ti+B; Fe-Si-Ca; Fe-Zr; Ca; Mg;Co borates; Rare Earth Metals	Some form stable nuclei to nucleate δ-ferrite and others promote constitutional cooling	244
High Alloy W-Cr-Mo steel	Disulphides of Mo, W, V	They act as nuclei	177

An analysis of this table will reveal that other than a few exceptions like the role of Na and Sr in Al-Si eutectic alloy modification, most of the grain refiners form stable compounds in the melt and act as nuclei for the solidifying alloy. Solute elements which have low solid solubilities in the parent alloy promote constitutional supercooling. It seems that the additions which provide the nucleation centres and thermal driving force prevail over the ones which trigger other mechanisms to refine the structure.

Unlike aluminium alloys and cast irons the modification of the cast structure of steels had not received any considerable attention until recently. This appears to be due to the fact that steels are generally supplied in the wrought form in which the microstructure is mainly determined by the hot work and the cold work/anneal cycles received by the alloy. There is, however, a growing realization that a finer isotropic as-cast macrostructure can result in better properties in as-cast and heat treated components, improved formability during hot working[112-117] and improved physical and mechanical properties in later use[118-126]. An improved as-cast macrostructure is particularly important in alloys that do not undergo allotropic transformations and therefore cannot be grain refined by thermal cycles alone. The problems associated with the detection of internal flaws by ultrasonic means in coarse grained austenitic steels are well known[127]. In addition, recent developments[128] in strip casting enhance the significance of a fine homogeneous as cast structure since the amount of deformation possible is reduced greatly. Properties such as corrosion resistance[129-132], weldability[120,133-141] and others[142-154] are also sensitive to grain size.

During the last decade, various steel grades including ferritic and austenitic stainless steels have received a lot of attention[155-244]. This is due to their widening fields of application and growing demands for better mechanical properties.

For cast steels, modification of the structure involves the widening of the equiaxed zone and its grain refinement as well as the reduction of the dendrite arm spacing.

The next section highlights the basic theories of chemical grain refinement and summarizes the theoretical and experimental insight gained to date, with particular reference to stainless steels.

2. NUCLEATION AND GROWTH MECHANISMS IN THE LIQUID-SOLID TRANSFORMATION OF ALLOYS

2.1 Nucleation.

Like most metals and alloys, the liquid-solid transformation in steels takes place by heterogeneous nucleation. The new solid phase may start by nucleation on the surface of a mould or it may appear on solid surfaces which are already present in the melt.

These solid surfaces in the melt may originate from different sources[266,265]. Some minor solid phases may form at higher temperatures and then act as nucleants for the major solidifying phase. Fragments of dendrites or their branches may drift into the liquid phase by convection and grow as equiaxed grains at the centre of the solidifying ingot. This convection may be enhanced by dynamic methods like stirring, vibrating, and shaking of the mould. In chemical grain refinement formation of the nucleating phase is believed to occur by reactions in the melt.

The atoms of the major solidifying phase should be able to form a nucleus on the surface of the nucleant. In order to achieve this they should have the required driving force to create two new surfaces: one between the nucleus and nucleant and the other between the nucleus and the liquid phase. The critical free energy barrier to be surmounted before forming a solid spherical cap on a planar substrate (Figure 2.1) in the melt is given by[266,267]:

$$\Delta G^* = \frac{4\pi\gamma_{LC}^3 T_M^2}{3\Delta H^2 \Delta T^2} (2-3\cos\Theta+\cos^3\Theta) \quad \ldots\ldots\ldots\ldots\ldots\ldots 2.1$$

where γ_{lc} is the surface energy of the liquid-crystal interface, T_M is the melting temperature in K, ΔH is the enthalpy change due to the liquid-solid transformation, ΔT is the undercooling and θ is the contact angle between the crystal and the substrate.

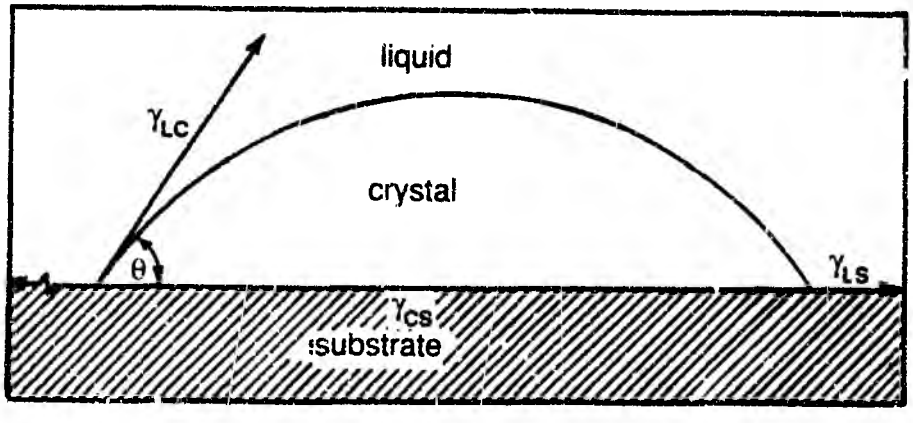

Figure 2.1. The spherical cap model of heterogeneous nucleation.

Equation 2.1 shows that $\Delta G^* = 0$ when $\Theta = 0$. This means that there will be no nucleation barrier for the formation of the new phase on the substrate, if the value of Θ is equal to zero. And the value of Θ tends to zero as the value of γ_{cs}, which is the interfacial energy between the nucleating crystal and the substrate, approaches zero[268]. If Θ is equal to 180°, ΔG^* heterogeneous will be equal to ΔG^* homogeneous, i.e. the substrate will be ineffective as a nucleant. Thus, heterogeneous nucleation is favourable for values of Θ between 0 an 180°. This relationship between the critical nucleation energy and the interfacial energy between the nucleating crystal and the substrate is one of the most important aspects of solidification[269,270]. However, a simple description of the interfacial energy is not possible, since it is composed of several contributing factors. Some of these factors are the chemical nature of the substrate[271], the topographic features of the substrate surface[272], the electrostatic potential between the substrate and the nucleated solid[273], and the lattice strain or disregistry between the two components of the interface[274].

The relevance of the degree of lattice misfit between the nucleant and the substrate to the degree of effectiveness of a certain nucleant has been tested for many combinations of materials[267,272,274-284]. Although there are exceptions[271,276], lattice misfit seems to be the parameter that determines the effectiveness of a substrate. The other factors are difficult to quantify or calculate.

The lattice misfit between respective planes of the nucleant and the crystal can be described in terms of angular difference between the crystallographic directions of the nucleated solid and the substrate as follows[285]:

$$\delta^{(hkl)_s}_{(hkl)_n} = \sum_{i=1}^{3} = \frac{\dfrac{(d[uvw]^i_s \cos\Theta) - d[uvw]^i_n}{d[uvw]^i_n}}{3} \times 100 \quad \ldots\ldots 2.2$$

where,

$(hkl)_s$ is a low-index plane of the substance

$[uvw]_s$ is a low-index direction in $(hkl)_s$

$d[uvw]_s$ is the interatomic spacing along $[uvw]_s$

$(hkl)_n$ is a low-index plane in the nucleated solid

$[uvw]_n$ is a low-index direction in $(hkl)_n$

$d[uvw]_n$ is the interatomic spacing along $[uvw]_n$

Θ is the angle between $[uvw]_n$ and $[uvw]_s$

2.1.1. Nucleating Mechanisms in Stainless Steels.

Cast steels may be classified under two main categories if their solidification history is taken into consideration:

(i) the ones in which δ-ferrite is the initial solidifying phase,

(ii) the ones in which austenite is the initial solidifying phase.

This classification is of utmost importance in view of the fact that their crystal structures and lattice parameters are different. Hence they need different nucleating agents which have at least one atomic plane symmetrical with that of the respective solidifying phase.

The size, distribution and shape of the initial nucleating phase will determine the final cast structure via transformations like

1. δ-Fe + Liq -> γ-Fe

2. δ-Fe + Liq -> δ-Fe

3. Liq + γ-Fe -> γ-Fe

In the first case, the austenite phase starts to form at the grain boundaries of δ-Fe which is rich in carbon and other austenite forming elements due to the inability of the solution to even out the solute pile up under normal diffusion controlled conditions. Thus, as the number of δ-Fe grains per unit volume increases, the number of nucleation sites for the austenite phase and in turn the

number of austenite grains increases resulting in a finer as cast structure. The other two are cases in which the initially solidifying phases, δ-Fe or γ-Fe are retained as the final phases and there is a one to one correspondence between the initial number of nuclei and the final number of grains.

The initial nucleating phases and the subsequent transformation that takes place during solidification depend on whether the ferrite forming elements or the austenite forming elements dominate the constitution of the melt.

It is possible to predict the initial nucleating phase by making use of the appropriate ternary of pseudo binary phase diagrams and to choose a suitable nucleating agent accordingly. This is illustrated in Figure 2.2 which shows a pseudo binary diagram of the Fe-Ni-Cr system. Depending on the composition of the alloy chosen, the initial nucleating phase may be δ-Fe or γ-Fe.

These nucleating agents should have a habit plane similar or symmetrical to one of the atomic planes of the solidifying phase although the lattice structures may not be the same. A hexagonal close packed nucleant may nucleate a bcc phase if certain coherency exists between their two respective atomic planes which are mostly close packed low index planes of the two structures. Figure 2.3 shows how this matching takes place between the respective atomic planes of several known effective nucleating agents and δ-ferrite. The lattice disregistries between some carbides and nitrides and δ-ferrite are given in Table 2.1. Additions, effective concentration ranges and probable mechanisms of the grain refinement process are classified according to initial solidifying phases in steels and given in Table 2.2.

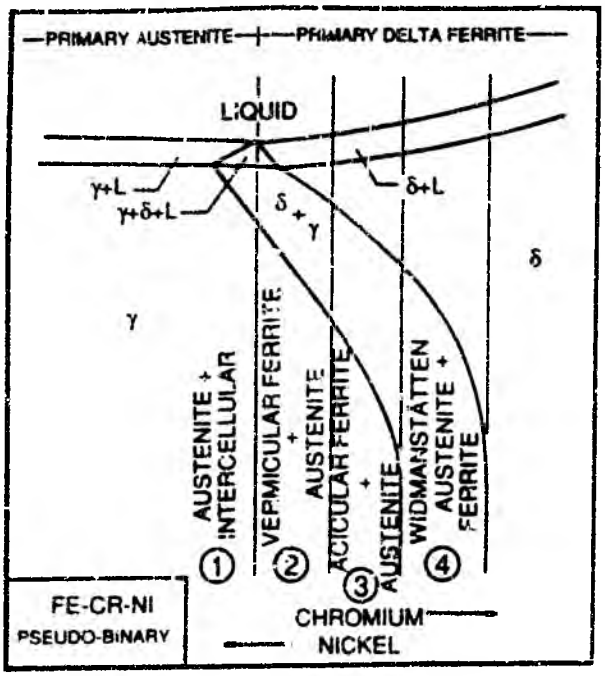

Figure 2.2 Pseudo-binary phese diegram for iron-chromium-nickel elloys.

Table 2.1 Crystallographic data of the affective nucleating agents for δ-iron

Compound	Crystal System	Lattice Parameter at 25°C	Lattice Parameter at 1500°C	Disregistry %
TiN	Cubic NaCl	4.246	4.308	3.9
TiC	Cubic NaCl	4.327	4.390	5.9
SiC	Cubic ZnS	4.359	4.3954	6.0
ZrN	Cubic NaCl	4.560	4.610	11.2
ZrC	Cubic NaCl	4.696	4.744	14.4
δ-Fe	Cubic Body-Cent	-	2.93151	-

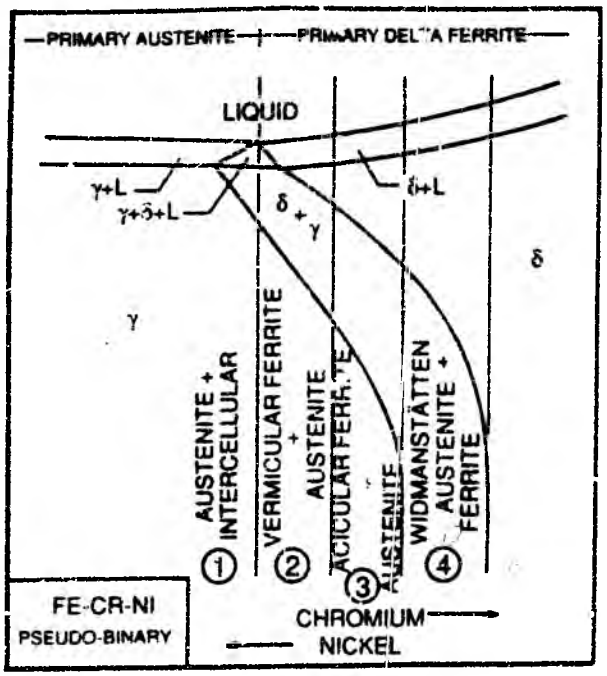

Figure 2.2 Pseudo-binary phase diagram for iron-chromium-nickel alloys.

Table 2.1 Crystallographic data of the effective nucleating agents for δ-iron

Compound	Crystal System	Lattice Parameter at 25°C	Lattice Parameter at 1500°C	Disregistry %
TiN	Cubic NaCl	4.246	4.308	3.9
TiC	Cubic NaCl	4.327	4.390	5.9
SiC	Cubic ZnS	4.359	4.3954	6.0
ZrN	Cubic NaCl	4.560	4.610	11.2
ZrC	Cubic NaCl	4.696	4.744	14.4
δ-Fe	Cubic Body-Cent	-	2.93151	-

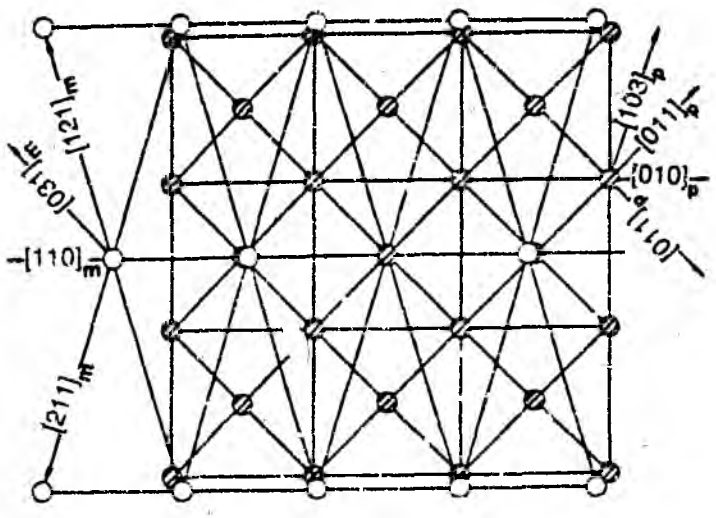

m = δ-ferrite, p = TiN

(a)

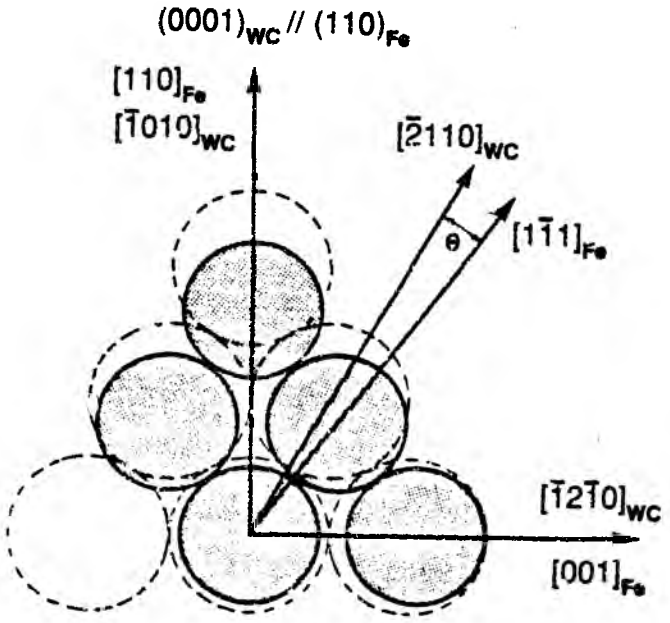

(b)

Figure 2.3. Schematic representation of atomic plane matching between (a) iron and TiN, (b) iron and WC.

Table 2.2 Summary of effective inoculating and microalloying agents for steels classified according to initial nucleating phase.

Initial Nucleating Phase	The Most Effective Additions	Concentration Range in which Refining may be expected	Probable Mechanisms
δ-ferrite or α-ferrite	Ti Fe-Ti Ti + Al_2O_3 Al_2O_3 + N_2 gas Ti + Al_2O_3 + B REM Ta	Ti 0,1 - 1.0% Al 0,005 - 0,2% N 0,0001 - 0,1% B 0,003 - 0,05% REM 0,01 - 1.0%	Al_2O_3 may act as substrate for TiN nucleation probably due to its high surface energy in the melt. In turn, TiN will nucleate δ-ferrite or α-ferrite due to low lattice disregistry between TiN and nucleating phase. B, REM, N, Ti are known to promote constitutional supercooling. REM oxides or sulfides also act as substrates.
γ-austenite	Ca (CN) Fe-Cr REM FeSiZr Ti and/or B	No concentration ranges are specified in literature	The mechanisms are not clear but REM are known to have low solid solubilities in iron and are potential constitutional supercooling promoters. High melting oxides or nitrides may also act as substrates since they have a high surface energy in the melt. Fe-Cr and Ca(CN) additions should be made just before or during pouring of the melt and at a low superheat due to fading effect. B, N, Ti may have a beneficial effect since they are known to be constitutional supercooling promoters.

As can be seen from these tables several effective nucleating agents, the best being TiN, ha · been used for the nucleation of δ-ferrite. However for the austenite phase, there is no reported nucleating agent which has low lattice disregistries on close packed planes and directions with respect to those of austenite The use of a few modifiers such as rare earths[234] and FeSiZr[242] for steels which solidify initially as austenite, has bee· reported. However, the mechanisms whereby these materials influence the nucleatio· of austenite are not well understood.

It appears that rare earths promote constitutional supercooling due to their low solubilities in austenite and the steep liquidus lines of the respectiv· binary systems[234]. The nucleating agents used for δ-ferri·e ha·e disregistries of more than 10% with respect to austenite and are therefore unsuitable as nucleants of this phase.

Nucleating agents when added to the melt may remain solid throughout the proces· or they may dissolve in the molten metal. Soluble additions can only be eff· ·ive if they form an intermetallic stable compound before the liquid reaches its liquidus temperature. Particles of the intermetallic compound may then act as ready surfaces for the nucleation of the major solidifying phase. ·reover, these endogenous particles which form in the ·elt also need ready nucleation sites themselves. For example it is believed that Al_2O_3 particles in molten steel act as substrates for TiN which in turn nucleates δ-ferrite[197].

The formation of inert and stable compounds, in the melt, having high liquid - solid interface energies may promote the nucleation of the γ phase by decreasing the overall free energy of the system.

As can be seen from these tables several effective nucleating agents, the best being TiN, have been used for the nucleation of δ-ferrite. However for the austenite phase, there is no reported nucleating agent which has low lattice disregistries on close packed planes and directions with respect to those of austenite. The use of a few modifiers such as rare earths[234] and FeSiZr[242] for steels which solidify initially as austenite, has been reported. However, the mechanisms whereby these materials influence the nucleation of austenite are not well understood.

It appears that rare earths promote constitutional supercooling due to their low solubilities in austenite and the steep liquidus lines of the respective binary systems[234]. The nucleating agents used for δ-ferrite have disregistries of more than 10% with respect to austenite and are therefore unsuitable as nucleants of this phase.

Nucleating agents when added to the melt may remain solid throughout the process or they may dissolve in the molten metal. Soluble additions can only be effective if they form an intermetallic stable compound before the liquid reaches its liquidus temperature. Particles of the intermetallic compound may then act as ready surfaces for the nucleation of the major solidifying phase. Moreover, these endogenous particles which form in the melt also need ready nucleation sites themselves. For example it is believed that Al_2O_3 particles in molten steel act as substrates for TiN which in turn nucleates δ-ferrite[197].

The formation of inert and stable compounds, in the melt, having high liquid - solid interface energies may promote the nucleation of the γ phase by decreasing the overall free energy of the system.

2.2 Growth

The growth mechanisms of alloys and impure metals are quite complex due to the redistribution of solute during solidification.

This can cause the growth morphology to change from one type to another and solute segregation to occur on both a microscale and a macroscale. Before reviewing the solute redistribution effects, it would be helpful to become familiar with the terminology used frequently in this field.

(a) The growth rate, R, is a measure of the rate of advance of the interface between the liquid and the solid.

(b) The temperature gradient, G, is usually taken to refer to the gradient in the liquid away from the interface in the direction of growth.

(c) The diffusivity, D, determines the rate at which atoms can move in the liquid. For all metallic liquids D is of the order of $5 \times 10^{-5} cm^2 sec^{-1}$. In solids it is $10^{-8} cm^2 sec^{-1}$ for common metals just below their melting points.

(d) The equilibrium distribution coefficient, k_o, is defined by the phase diagram, assuming the liquidus and solidus lines to be straight:

$$[k_o = \frac{\text{solute concentration in the solid at temperature } T}{\text{solute concentration in the liquid at the same temperature}} = \frac{C_s}{C_l}] \quad ..2.3$$

(e) The slope of the liquidus line is given the symbol m.

2.2.1 Solute Redistribution by Diffusion.

Considering an alloy with an initial composition of C_o and $k_o < 1$, on cooling down to temperature T, the first solid to form will have a composition of $C_o k_o$ (Figure 2.4). Due to the rejection of solute into the immediate vicinity of the solid-liquid boundary, a local solute enrichment of the liquid will occur. Solute diffusion will take place down the concentration gradient into the liquid whose solute concentration away from the interface is C_o (Figure 2.5). Since this solute pile up cannot be evened out by normal diffusion rates which fall behind the rates of growth under normal conditions, the next element of solid deposited will have a composition $(C_o + \partial C_o)k_o$, where ∂C_o represents the local enrichment, and so on. When the temperature at the interface decreased to T_1, the concentration of the liquid just ahead of the solid-liquid interface will be C_o/k_o. At this moment, the liquid is able to freeze solid of composition C_o. When this occurs, the steady state has been attained and the solid, which is formed from the liquid layer enriched in solute B atoms, is the same as the liquid drawn into this layer.

The solute distribution in the liquid ahead of the solid-liquid interface at steady state is given by the equation[264]:

$$C = C_o\left[1 + \frac{1 - k_o}{k_o} \exp\left(-\frac{Rx}{D}\right)\right] \quad \ldots\ldots\ldots\ldots\ldots\ldots 2.4$$

where x is the distance ahead of the solid-liquid interface and the boundary conditions are;

(a) $x = o, \quad C = C_o/k_o$

(b) $x = \infty, \quad C = C_o$

A short, steep pile-up is produced at high growth rates and for low solute diffusivities. nsiderable amounts of solute may accumulate at the interface for systems in which k_o is very small.

For solute concentrations higher than about 0,5%, the solute pile up effects are very marked and the morphology of the interface changes to non-planar[264]. Under these conditions equation 2.4 is no longer valid, although it can be used to give an approximate indication of the solute distribution near the interface.

If the slope of the liquidus line, m, in the A rich portion of the phase diagram shown in Figure **2.6 (a)**, is assumed to be constant, the equilibrium liquidus temperature, T_L, is given by

$$T_L = T_m - mC \quad \ldots\ldots\ldots\ldots\ldots\ldots\ldots\ldots\ldots\ldots 2.5$$

where T_m is the melting temperature of the pure metal and C is the composition of the liquid. Under steady-state conditions, the interface temperature, T_i, of an alloy of initial composition, C_o, is,

$$T_i = T_m - \frac{mC_o}{k_o} \quad \ldots\ldots\ldots\ldots\ldots\ldots\ldots\ldots 2.6$$

For a solute distribution given by equation **2.4**, the equilibrium liquidus temperature corresponding to different points ahead of the interface will be

$$T_L = T_i + \frac{mC_o - k_o}{k_o}\left[1 - \exp\left(-\frac{Rx}{D}\right)\right] \quad \ldots\ldots\ldots\ldots\ldots\ldots 2.7$$

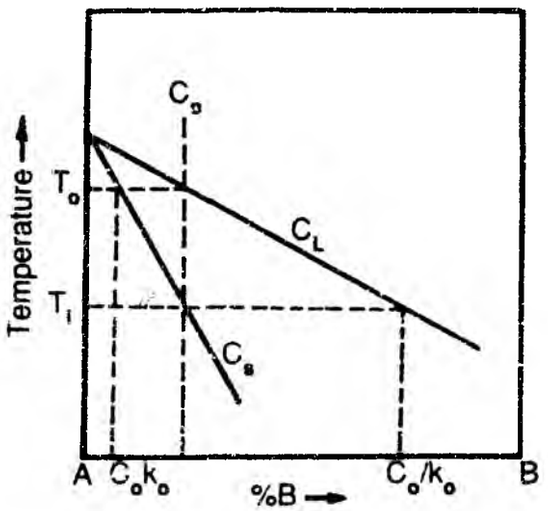

Figure 2.4 **Thermal equilibrium diagram for two metals forming a continuous range of solid solutions**

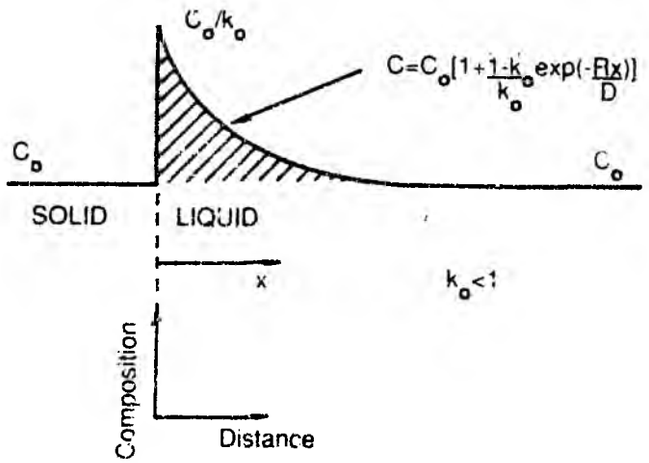

Figure 2.5 **The solute profile ahead of the interface during steady-state solidification with solute distribution by diffusion only**

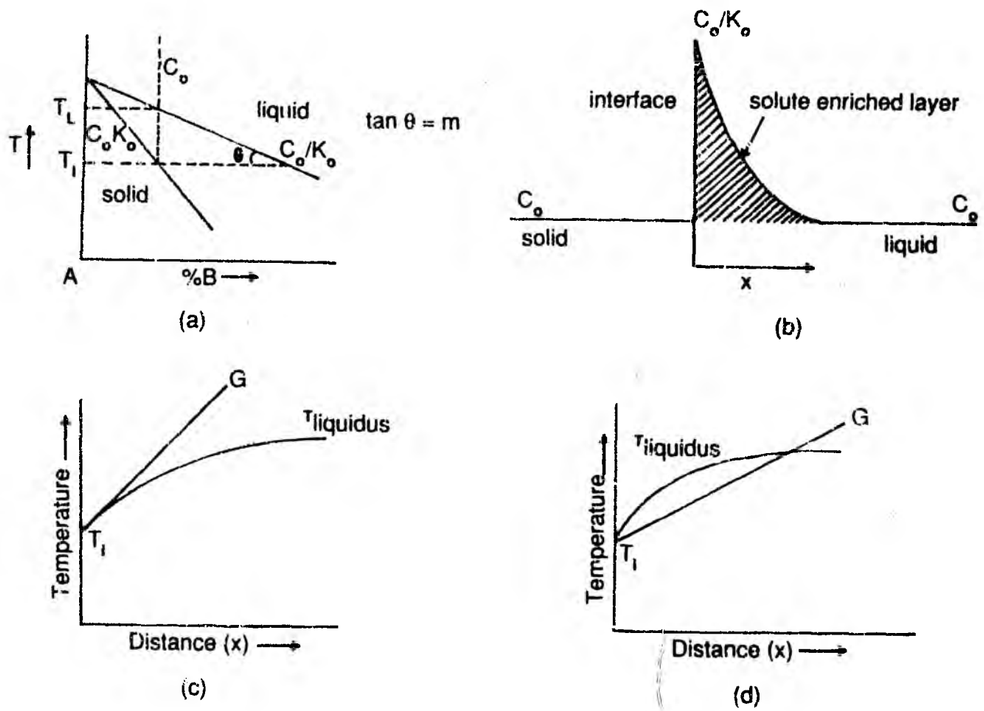

Figure 2.6 Constitutional supercooling in alloy solidification (a) Phase diagram (b) solute enriched layer in front of liquid-solid interface (c) stable interface (d) unstable interface.

The temperature in the liquid at a distance x from the interface is given by

$$T = T_i + Gx \quad \ldots\ldots\ldots\ldots\ldots\ldots\ldots\ldots \quad 2.8$$

where G is the temperature gradient in the liquid ahead of the interface.

During solidification, within a certain region ahead of the interface, the liquid may be at a temperature lower than its liquidus temperature as the thermal gradient, G, varies together with the position of the solidification front; this phenomenon is known as constitutional supercooling (Figure **2.6 (c)** and **(d)**).

To promote constitutional supercooling ahead of the interface, the criterion is:

$$G < \left(\frac{\partial T_L}{\partial x}\right)_{x=0} \quad \ldots\ldots\ldots\ldots\ldots\ldots\ldots\ldots\ldots\ldots 2.9$$

Using equation 2.7 this criterion can be made much more explicit:

$$G/R < \frac{mC_o}{D}\,\frac{(1-k_o)}{k_o} \quad \ldots\ldots\ldots\ldots\ldots\ldots\ldots\ldots 2.10$$

Here, the terms are grouped with growth parameters on the left hand side and material and system parameters on the right hand side. Using this equation, the conditions which will promote constitutional supercooling can be stated as:

(i) shallower temperature gradients in the liquid
(ii) high growth rates
(iii) steep liquidus lines
(iv) high alloy contents
(v) low diffusivity in the liquid
(vi) very low k_o for $k_o < 1$.

2.2.2 Constitutional Undercooling

In the presence of constitutional supercooling, the undercooling is:

$$\Delta T = T_L - T \quad \ldots\ldots 2.11$$

Using the equations for T_L and T (equations 2.7 and 2.11), undercooling can be expressed as:

$$\Delta T = \frac{mC_o(1 - k_o)}{k_o}\left[1 - \exp\left(-\frac{Rx}{D}\right)\right] - Gx \quad \ldots\ldots 2.12$$

and the maximum undercooling can be found by differentiating the above equation with respect to x and substituting the value of x which satisfies the condition:

$$\left[\frac{\partial \Delta T}{\partial x}\right] = 0 \quad \ldots\ldots 2.13$$

in equation 2.12 which gives:

$$\Delta T_{max} = \frac{mC_o(1 - k_o)}{k_o} - \frac{GD}{R}\left[1 + ln\frac{mC_o(1 - k_o)\,R)}{GDk_o}\right] \ldots 2.14$$

This maximum undercooling occurs at a point given by

$$x = \frac{D}{R}\, ln\left[\frac{mC_o(1 - k_o)R}{GDk_o}\right] \quad \ldots\ldots 2.15$$

This treatment is valid when solute mixing in the liquid is the result of diffusion only. However, it can be modified to allow for partial or complete mixing in the liquid[286].

2.2.3 Growth Morphologies

Growth morphologies in a cast structure depend on the composition of the alloy and on the thermal conditions. They can be classified as:

(i) Planar interface
(ii) Cellular interface
(iii) Dendritic interface
(iv) Independent nucleation.

These forms of interfaces are shown diagrammatically in Figure **2.7**, which also shows the influence of undercooling on the transition from one mode of growth to another.

(i) Planar Interface

If the temperature of the solid liquid interface is just below the solidification temperature - that is slightly undercooled - as is the case in pure metals, an irregularity on the surface of the solid front will find itself in a melt of temperature higher than its melting point and melt away to preserve the isothermal interface. Thus the growth pattern takes the form of a smooth planar interface. Freezing can occur in this manner when the latent heat of solidification is insufficient to reverse the direction of heat flow in the liquid adjacent to the interface. This condition is promoted by steep thermal gradients and slow growth rates.

(ii) Cellular Interface

The cellular structure is a transition interface morphology which is typical of a less marked undercooling than that promoting a dendritic growth pattern. It

always precedes the dendritic form and is produced as a cluster of hexagonal rods which grow into the liquid (Figure 2.8).

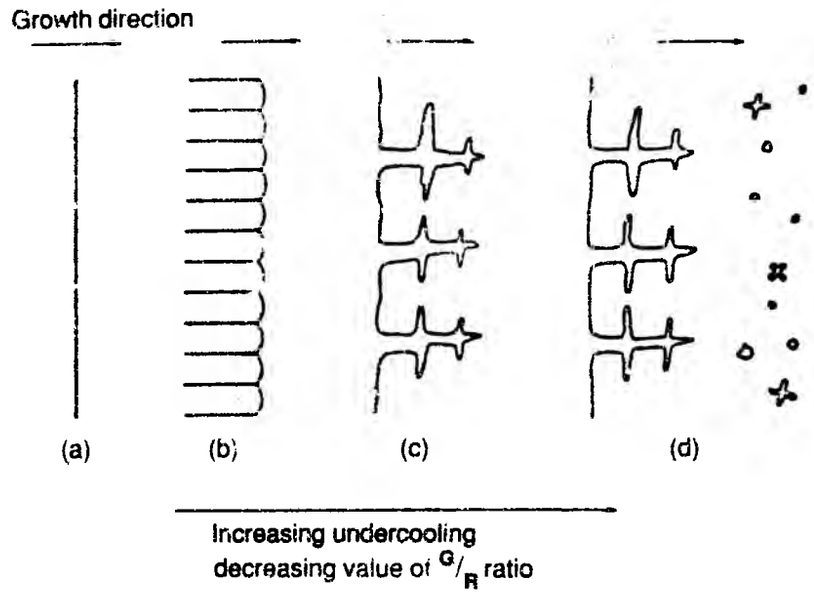

Figure 2.7 Influence of undercooling on interface morphology and mode of growth (a) Planar interface, (b) cellular interface, (c) dendritic growth, (d) independant nucleation

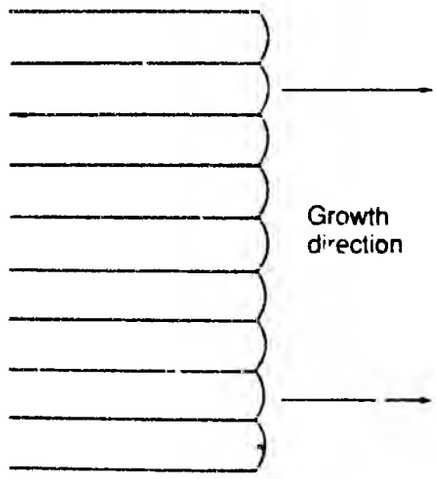

Figure 2.8 Cellular substructure formed by undercooling.

When a certain level of undercooling is reached, the dendritic mode of growth starts to appear on this cellular substructure by the preferential development of a limited number of cells.

(iii) Dendritic Interface

In most cases, the growth rate of the interface is so high as to cause heat flow into the melt. This results in a reverse thermal gradient ahead of the interface. Thus the minimum temperature in the liquid is no longer adjacent to the interface. This phenomenon allows any protuberance on the solid front to become stable and act as a centre for preferential growth. These local growth centres can probe further into the undercooled liquid and grow dendritically (Figure 2.9). This is the type of growth most commonly encountered in the freezing of commercial castings of solid solution alloys. The primary axis of the dendrite is the result of preferred growth at an edge or corner of an existing crystallite. This projection develops into a needle and subsequently a plate in a particular crystallographic direction which is for example the <100> direction for cubic metals. Growth of this primary axis is then inhibited by the latent heat of solidification as in the case of the plane front growth pattern. But secondary and tertiary branches can develop by a similar mechanism to that which led to the growth of the primary stem.

(iv) Independent Nucleation

If solidification takes place under a shallow temperature gradient or at a very high rate, the undercooling may be sufficient to promote fresh nucleation at points distant from the main interface. Under these conditions, further solidification produces equiaxed grains such as are frequently present in the central zone of castings and ingots. The degree of undercooling at which this will occur will depend upon the potency of the nuclei present and will be affected by other conditions which will be discussed in detail at a later stage.

This purely thermal explanation of the equiaxed structure has so far assumed that all such grains originate from heterogeneous nucleation in situ[10]. Other mechanisms contributing to the formation of this are examined in detail in the following sections.

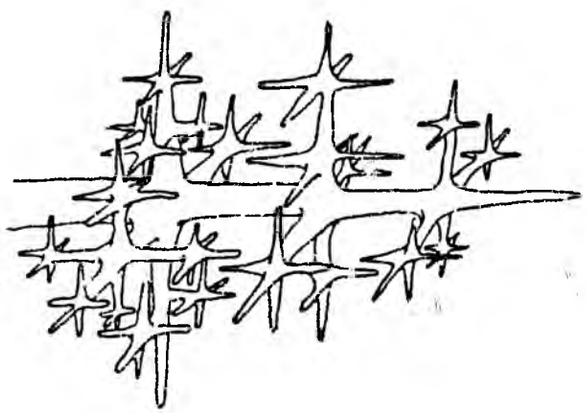

Figure 2.3 Dendritic growth pattern

with a direction of growth parallel to the direction of heat flow (normal to the mould walls)[247,289]. As discussed earlier, the growth morphology of columnar grains can vary from planar to free dendritic.

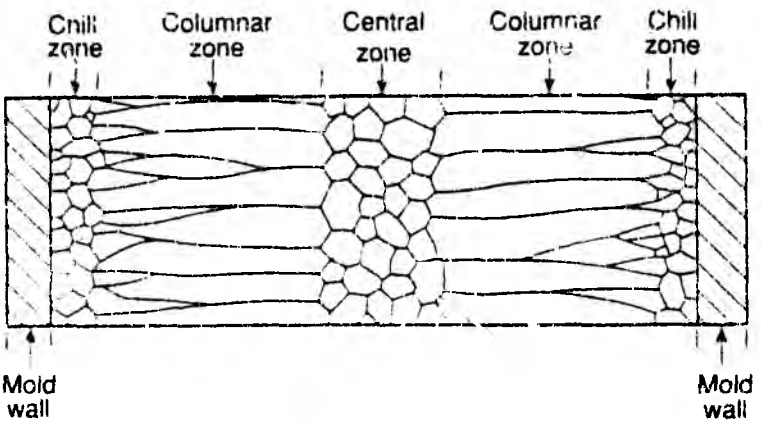

Figure 3.1 **A section through a large ingot, and the three basic zones of freezing that may be found in a casting.**

3. THE STRUCTURE OF CASTINGS

Three distinct zones form in almost every casting[264,286]. The presence and extent of these zones depend on the thermal conditions and alloy variables as indicated earlier and the inherent nucleation and growth conditions in the liquid.

The three zones, shown schematically in Figure **3.1** can be described as:

1. The chill zone which forms in a narrow band next to the mould wall, and consists of small equiaxed grains. These usually have a random orientation and are nucleated by either impurities or irregularities (like cavities) on the mould wall[286]. After nucleation their further growth is retarded by the considerable degree of supercooling due to the chilling effect of the mould walls which are usually at room temperature.

   Also, since the nucleation rate is relatively rapid due to this undercooling, many grains will nucleate within a small period of time limiting each other's growth. Thus the average grain size in this zone will be very small.

   The chill zone is only a few grain diameters thick and has little effect on ingot behaviour during deformation. However it may be a desirable feature of ingots as it provides an improved surface finish after rolling.

2. The columnar zone consists of large and elongated crystals extending inwards from the chill zone. These grains have a very strong preferred orientation

Columnar grains may show segregation[6]. Interdendritic segregation will lead to low-melting material or second phases between dendrite arms which can lead to hot shortness or poor ductility during rolling. Because the columnar crystals are extremely large, the overall grain boundary area is small and even small amounts of interdendritic segregation will have a significant influence on hot ductility. During hot working, cracks are likely to initiate in the columnar zone due to its inferior deformation characteristics.

Since the columnar crystals will persist provided that the conditions are not favourable for the formation of equiaxed crystals, control over the columnar growth is normally exerted by inducing the formation of equiaxed crystals. It is this control which is foremost in the control of the overall cast structure.

3. The equiaxed zone lies at the centre of the ingot and represents the last metal to freeze. In this region, the crystals usually have a grain size larger than that of the chill zone and have a random orientation.

Various theories have been proposed to explain the origin of the equiaxed zone in castings.

Essentially, there have been four theories on the mechanisms of formation of the equiaxed zone which can be summarized as follows:

i) It was initially proposed by Winegard and Chalmers[239] that it is the constitutional supercooling ahead of the columnar growth front which provides the thermal driving force for

independent nucleation to occur at the later stages of solidification. As the solid-liquid interfaces that start from opposite sides of a mould approach each other at the centre of a large ingot, their respective zones of constitutional supercooling eventually overlap. This is shown schematically in Figure 3.2. The figure on the left hand side represents an early stage in the freezing process, while the figure on the right hand side represents a later stage when the zones come together.

At this point, a very large amount of supercooling can occur in the liquid near the centre of the ingot for two reasons. First, the concentration of solute in the liquid just ahead of the interface tends to increase with increasing growth of the columnar zone, thus requiring lower and lower temperatures at the interface for continued solidification. Second, the temperature at the centre of the ingot tends to approach that of the interfaces as the latter get closer together. This suppresses the slope of the thermal gradient in the liquid considerably, and promotes constitutional supercooling which in turn enhances the independent nucleation in the liquid at the centre of the casting.

However, the existence of constitutional undercooling, alone, cannot explain fully the formation of the equiaxed zone. The origin of the nuclei from which the equiaxed grains grow needs to be explained. Various theories have been proposed in this regard.

iv) to act as promoters of constitutional supercooling in the liquid ahead of the solid liquid interface, so providing the required thermal driving force for the solidifying phase to nucleate on substrates present within the supercooled region,

v) the additive or its stable compounds may nucleate the nucleating agents which in turn will be nucleating the major solidifying phase.

These major mechanisms still need further clarification. In the case of steels the problem is much more obscure, since modification of these alloys was achieved recently, and only to a limited extent and for certain grades. A summary of selected works on the chemical grain refinement of steel alloys is given in Table **4.1**. Thus further experimental work is required to develop practical methods for foundry applications and to collect sufficient and reliable data for the theoretical explanation of the phenomenon.

It will be helpful to describe the properties of potential agents which could take part in one or more of the above mechanisms. The surface characteristics of such agents as well as their physicochemical properties are of fundamental importance.

4.1 The Effects of Solute Redistribution on Cast Structures

Solidification usually takes place under non-equilibrium conditions and therefore the rate and form of solute redistribution vary throughout the solidification process. The solute concentration gradient at the solid-liquid interface is believed to cause the different modes of growth patterns all of which may be observed in a

ii) The "Big bang" theory[10] proposes that the nuclei for both the columnar and the equiaxed zones form during nucleation of the chill zone. These nuclei then either grow as columnar crystals or drift into the central zone to become equiaxed crystals. The formation of equiaxed crystals blocks the further growth of the columnar front, and thus gives out the typical ingot centreline structure.

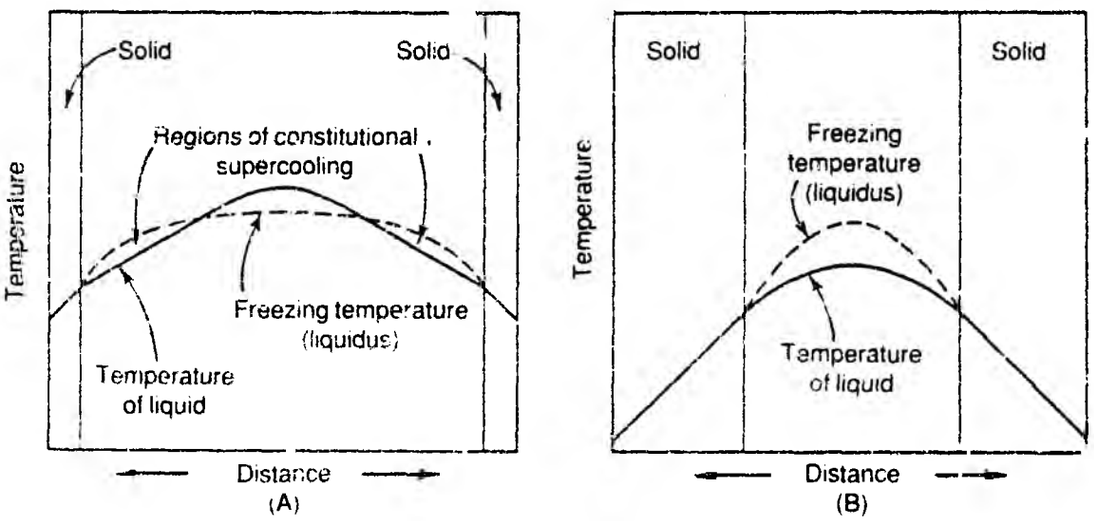

Figure 3.2 The development of the constitutionally supercooled region at the centre of an alloy ingot that produces the central equiaxed zone

iii) The nuclei of the equiaxed grains may also originate from the remelting of dendrite branches[11]. During dendritic growth a solute rich layer builds up in the vicinity of the dendrite tip. Any side branches must grow through this layer and this leads to the formation of a neck of lower melting point material which in turn has a great tendency to remelt in the presence of thermal fluctuations. These thermal fluctuations are attributed to natural convection of melt filling up the voids which are formed due to shrinkage during solidification. The downward flow of liquid is also a contributing factor[12]. The presence of large temperature fluctuations during growth, and the close correlation between convection and the development of the equiaxed zone has been shown by direct observations[13].

iv) Another distinctive theory[14,15] is that independent nucleation takes place at the free surface of the ingot. The solid particles shower down into the liquid ahead of the columnar zone, growing as they descend. The nuclei may simply be considered as free surface dendrites which sink due to gravitational effects, or alternatively, dendrite remelting may contribute to the phenomenon.

There is no clear evidence yet as to which one of these major theories or of other minor ones[13,16] generates the equiaxed zone, but it is highly probable that two or more mechanisms may be contributing, together with the constitutional supercooling which is the prime requirement to provide the thermal driving force for nucleation.

As the grains in this zone are smaller and randomly oriented, unlike columnar grains, the equiaxed zone is a desirable feature in ingots. The benefits, such as improvement in impact properties, hot workability, greater resistance to solidification cracking and grain boundary corrosion that may arise from a larger equiaxed zone and naturally a smaller columnar zone, justify the concerted efforts that have been made to enlarge the former at the expense of the latter in castings of different alloys.

4. MECHANISMS of CHEMICAL GRAIN REFINEMENT

The addition of some agents to molten metal just before pouring or during pouring to enhance grain refinement through "quasi"-liquid state reactions can be considered to be a process chemical in nature.

Even though great improvements have been attained in Al and Mg[41] alloys as well as cast iron, the mechanisms or reactions taking place in chemical grain refinement are not clearly understood. The functions of additions in different alloys may differ due to the unique solidification process of each alloy. In addition there may be more than one mechanism involved in a solidification process.

The probable functions of additions in a specific alloy may be one or more of the following:

i) to form stable compounds in the melt to act as ready sites for the nucleation of the solidifying phase,

ii) to wet the surface of the substrates already present in the melt thus lowering the interfacial energy between the substrate and the nucleating phase or they may increase the interfacial energy between the melt and the substrate making nucleation easier,

iii) to poison the nucleation of growth steps of the solidifying phase thus suppressing the occurrence of both phenomena down to lower temperatures. This results in the multiplication of nucleation centres and slower growth rates which in turn yield a refined cast structure,

Table 4.1 Summary of effective inoculating and microalloying agents for iron and its alloys

Grade of Base Metal	The Most Effective Additions	Wt% of Addition in Cast Metal	Probable Mechanisms of Grain Refinement	Reported Mechanical Properties
Pure Iron[68]	TiN, TiC, SiC, ZrC	-	Additions act as substrates which have low planar disregistries with the δ-ferrite as given below: TiN 3,9 TiC 5,9 ZrN 11,2 ZrC 14,4	
17% Chromium Stainless Steel[220,276]	Ti, Al_2O_3, B	Ti 1,0 B 0,005	Ti reacts with N and forms TiN particles which seem to nucleate on oxide particles presumably Al_2O_3 or Ti_2O_3 or SiO_2. The TiN particles act as substrates for δ-ferrite and have a planar disregistry with δ-ferrite as given below: $(113)_\delta // (001)_{TiN} \approx 3,4\%$ The nucleation of TiN on Al_2O_3 may be due to one of the following: 1. The higher surface energy of Al_2O_3 in liquid steel due to its high melting point. 2. The destruction of bonds between aluminium and oxygen followed by formation of a monolayer of Ti-atoms resulting in low wetting angle, and a decrease in the work of nucleation of TiN.	
18/10/3 (AISI316) Stainless Steel[283,284]	FeCr, Ti, V, N	Ti 0,10 V 0,70	Nitrogen, Ti, V are suitable elements for promoting constitutional supercooling. FeCr when added at 30°C superheat and with 0,2% Nitrogen content gives an equiaxed structure probably due to microchilling behaviour.	Inoculation with different materials had no marked effect upon the mechanical properties but inoculation with mixtures of oxides had a deleterious effect on impact properties and ductility. A significant improvement in the tensile strength and proof stress values accompanied by a slight improvement in impact properties is expected.

Table 4.1 Summary of effective inoculating and microalloying agents for iron and its alloys (Continued)

Grade of Base Metal	The most Effective Additions	Wt % of Addition in Cast Metal	Probable Mechanisms of Grain Refinement	Reported Mechanical Properties
18/8 Stainless Steel[223,224]	Increase Ni content or Ti, Nb, V, Zr	Ni 12 Ti 0,1 Nb 0,5 V 0,6 Zr 0,5	Higher nickel content and low superheat make it possible to obtain a refined structure, probably through the occurrence of constitutional super-cooling due to these additions.	
13% Mn Steel[223,224]	Ca(CN) and nitrided Fe-Cr	N 0,03-0,04		
Low Interstitial 18% Cr, 2% Mo[229]	Ti, Nb Ti + Nb	Ti 0,45 Ti 0.27 + Nb 0,12 Nb 0,40 N 0,006-0,009	TiN acts as the nucleating agent, and is itself nucleated probably by Al_2O_3 and surrounded by titanium sulphide. TiN starts to precipitate at 1520°C. Structure is coarser with a slower cooling rate.	
25% Cr - 4% Ni - 4% Mo[229]	Ti, Al	Ti 0,60 Al 0,076 N 0,012	Above mechanism for 18% Cr, 2% Mo steel is also valid for this alloy.	
26% Cr - 6,5% Ni - Stainless Steel Weld[205]	Filler Material used was of similar composition to base metal	Ti 0,26 Al 0,17 N 0,265 Al (Weld) 0,01-0,2 N (Weld) 0,002-0,06	Fine carbides of the grain boundary and titanium carbonitrides act as growth inhibitors. Centre of the grains is aluminium-rich. Aluminium nitrides or other nitrides and carbides of appropriate size can exist as stable nuclei in liquid metal; these may act as sites for the formation of small, individual dendrites during cooling of weld metal. Very narrow solidification range would promote rapid freezing and limit grain growth in the weld deposit. A peritectic reaction may be involved and provide an additional source of grain refinement.	Aluminium containing weld showed an elongation of 173% as compared to the 61% exhibited by a coarse grained alloy. The maximum superplastic elongation was obtained at an aluminium to nitrogen ratio of about 1,8 to 1. The finest grain size was found to correspond to the highest elongation value.

Table 4.1 Summary of effective inoculating and microalloying agents for iron and its alloys (Continued)

Grade of Base Metal	The Most Effective Additions	Wt % of Addition in Cast Metal	Probable Mechanisms of Grain Refinement	Reported Mechanical Properties
High Strength Steels[211]	Ti and B	Ti 0,014-0,060 B 0,003-0,04 N 90ppm	A moderate reduction in the prior austenite grain size was noted with the addition of titanium and boron. The finest grain size was observed in the weld with the Fe-Ti additions only. Boron acts as a promoter of constitutional undercooling on solidification since its P factor (P=m(1-ko)/ko is considerably higher.	Transverse weld tensile tests give results from 842 to 923 MPa. Another test piece gave 1050 MPa and 14% elongation. The addition of boron and titanium has also indicated an increase in the weld metal hardness, most likely by solid solution hardening and also resulted in a drop of the average brittle-ductile transition temperature.
0,1% C 1,7% Mn[244]	Fe-Ti, Ti Ti +Al_2C_3 (Fe-Ti had 1,4 w/o Al as impurity)	Ti 0,51-0,95 Al 0,020-0,18 N 63ppm- 181ppm	Since the initial phase is δ-ferrite the above mechanisms are also valid for these grades of steel. The high nucleation rate of δ-ferrite results in a refined, equiaxed austenite microstructure in C-Mn steels because of the peritectic reaction. Only a fraction of the TiN particles are effective as nucleation sites because of the additional requirement for sufficient undercooling at the particle/melt interface. Complete refinement of the solidification structure is achieved only when both a critical number of TiN nuclei in the melt is exceeded (controlled by Al and to a smaller extent Ti) and when a minimum level of undercooling is present in their vicinity (controlled by Ti). Addition of Fe-Ti plus boron produced even finer grains at lower Ti concentration.	
18% Cr, 10% Ni austenitic stainless steel (δ-ferrite nucleating)[244]	Fe-Ti Fe-Ti + B	Ti 0,51-0.85 Ti 0,45 B 0,028		
17% Cr Ferritic stainless steel[244]	Fe-Ti	Ti 0,40		
18% Cr, 20% Ni (γ-nucleating)[244]	Fe-Ti	Ti 0,49	Grain refinement does not occur since there is no epitaxial relationship between TiN and γ-phase	

Table 4.1 Summary of effective inoculating and microalloying agents for iron and its alloys (Continued)

Grade of Base Metal	The Most Effective Additions	Wt % of Addition in Cast Metal	Probable Mechanisms of Grain Refinement	Reported Mechanical Properties
0,10-0,15 C, 5,0 Ni, Mo Tool Steel[238]	Sr, Zr, Y Nb	Sr 0,02 Zr 0,0012 Y 0,47 Nb 0,01		Modified steel shows a high level of mechanical properties with extreme toughness at both normal and subzero temperatures, probably because of Y.
AISI 4330 Steel[239]			Vacuum melting of steel gives a grain refined structure due to low gas pressure which reduces the solubility of carbon in iron and enhances constitutional supercooling.	
AISI 304 and 316[240]	Fe-Ti+ Fe-B Al+ Calsibar Al+ REM	Al 0,13 Calsibar 0,10 REM 0,16 Ti 0,60 B 0,10	Boron promotes constitutional super-cooling, Ti forms carbonitrides which are believed to serve as potent substrates. REM have a very low solubility in steel and may provide sufficient constitutional super-cooling.	
AISI C1018 Steel[241]	FeCb, FeTi, FeV, FeB, TiC Ti + TiC Ti + ZrC	All Fe alloys are added at about 0,5 wt% Ti 0,3-0,5 TiC 0,3-0,5 ZrC 0,3	Cb, Ti act as grain growth restrictors enhancing constitutional supercooling. TiC, V, B provide a source of foreign nuclei	Grain refinement increases the tensile strength and hardness but also imparts an embrittling effect on the metal. This is believed to be the result of an intergranular precipitate caused by these additions.

Table 4.1 Summary of effective inoculating and microalloying agents for iron and its alloys (Continued)

Grade of Base Metal	The Most Effective Additions	Wt % of Addition in Cast Metal	Probable Mechanisms of Grain Refinement	Reported Mechanical Properties
Plain Carbon Steel[166]	Ce	0,025	Ce increases the rate and stability of crystallization	Ce increases the microstructural density, inhibits segregation phenomenon and modifies the morphology of the sulphide phase, which results in high physicomechanical properties of the inoculated material.
Low Alloy Steel[180]	Al	0,5 kg per ton of steel is added		Increases dispersion hardening effect.
AISI 430 Steel[176]	Ti, Co-borates other borates		Ti forms TiN, this acts as nuclei for ferrite. Co-borates and others promote constitutional supercooling.	
High Speed Steel[178] (0,75% C, 4% Cr, 18% W)	Mo, V, S	Mo 1,0 V 0,75-2,10	Disulphides of Mo, W and V act as substrates.	Improved wear resistance
40Cr4 Steel[217]	FeAlTi, FeAlTiB	Added at a rate of 1,5 kg per ton of steel.		FeAlTiB addition gives good hardenability.
Fe-3,3 Si Fe-0,55 Si[222]	TiC + ZrB_2 Si_3N_4	TiC 0,5 ZrB_2 0,5	TiC is effective as a grain refiner, and ZrB_2 is considered to be an active nucleant. Si_3N_4 reacts with carbon forming SiC which is shown to be an effective nucleant for ferrite.	

Table 4.1 Summary of effective inoculating and microalloying agents for iron and its alloys (Continued)

Grade of Base Metal	The Most Effective Additions	Wt% of Addition in Cast Metal	Probable Mechanisms of Grain Refinement	Reported Mechanical Properties
High Strength Low Alloy Steels[28]	Ti, Al_2O_3 B	Ti 0,005-0,230 B 7ppm -41ppm Al 0,005-0,012 O 303-662ppm	Since no epitaxial relationships were observed it appears that inclusions nucleate ferrite by acting on inert substrates. An inclusion will be a favourable nucleation site if a high energy interface exists. The inclusion and the prior austenite thus lower the energy barrier for nucleation. TiO_2, $Al_2O_3.MnO$, SiO_2, MnS and Al_2O_3 would be expected to have high surface energies. Compound MP°C Al_2O_3 2050 $3Al_2O_3.SiO_2$ 1850 TiO_2 ~1800 SiO_2 1723 $Al_2O_3.MnO$ 1650 MnS 1620 Mn_2O_3 1560	

single cast structure. The slope and the shape of the solute concentration profile itself are thought to be determined by the solidification parameters which are believed to affect the extent of the constitutionally supercooled region[266,271].

The solidification parameters which determine the nature of the cast structure may be classified under two categories as indicated in equation **2.10**.

These are:

(1) the ratio of temperature gradient (G) to growth rate (R) which has been shown to be a significant parameter with respect both to the mode of growth and the final grain structure produced in solid solution alloys[264,290,291,292,293].

(2) the alloy variables grouped on the right hand side of equation **2.10** include the liquidus slope m, solute distribution coefficient k_o, and initial solute concentration (C_o). To facilitate comparisons of the effect of different alloying elements, it is convenient to equate the right hand side of equation **2.10** to a parameter P as follows:

$$P = \frac{m(1 - k_o) C_o}{k_o} \qquad \text{.....4.1}$$

The progressive change in the G/R ratio will result in changes in the growth pattern on solidification. As the value of the ratio decreases, the effect of undercooling becomes more pronounced. The changes in growth morphology and the associated thermal conditions are illustrated in Figure **4.1**.

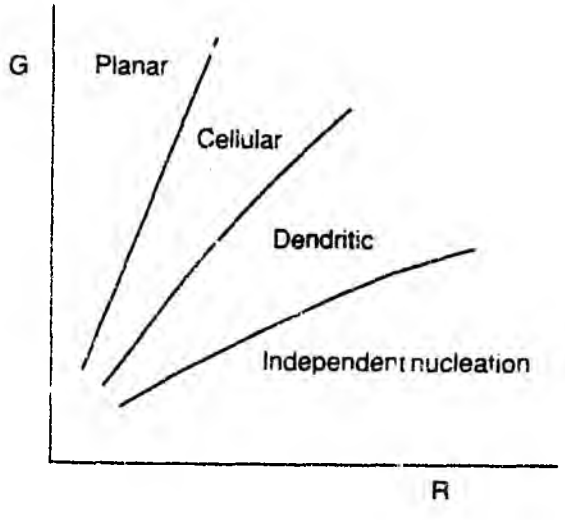

Figure 4.1 Influence of temperature gradient G and freezing rate R on solidification morphology of a given alloy

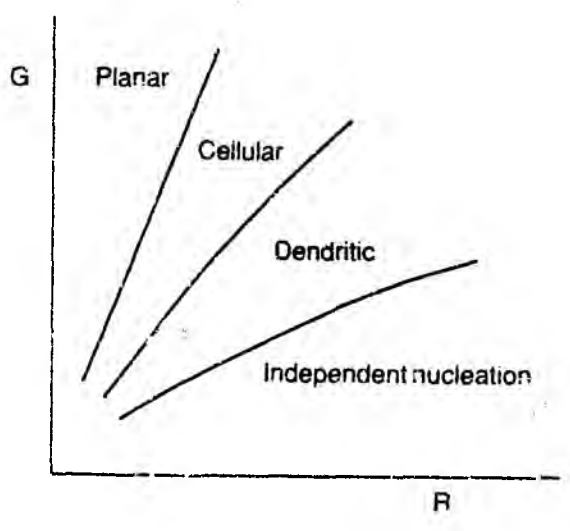

Figure 4.1 Influence of temperature gradient G and freezing rate R on solidification morphology of a given alloy

With a very high G/R ratio, cellular or cellular-dendritic growth is observed. At relatively low values of G/R, columnar growth takes place with a dendritic morphology. The dendrites find themselves in a constitutionally supercooled zone just ahead of the interface and thus are thermally activated to grow and to branch. At much lower G/R values, supercooling is considerable and nucleation takes place ahead of the interface. The grains that form may grow either in a dendritic pattern or with a spherical morphology as evidenced by some researchers[6].

For example, in continuous casting the temperature gradients are quite high throughout the solidification process. So, the cast structure usually shows a fully columnar morphology. In ingot casting, temperature gradients become shallower as the solidification front approaches the centre of the ingot, and this promotes the formation of equiaxed grains in this zone.

4.2 The Effect of Alloy Variables on Cast Structures

As seen in the preceding section, thermal conditions influence the morphology and extent of the different zones in the as-cast structure. However for constant thermal conditions the structure will be determined by the nature of the alloy[254]. The variables which make the right hand side of the constitutional supercooling criterion can be grouped and named as shown in equation 4.1.

A marked change in the as cast structure is observed as a function of the parameter P. Low values of P result in predominantly oriented, columnar structures. Large values of P result in fine equiaxed structures. Intermediate values give a mixture of columnar and

equiaxed grains.

The dependence of microstructure on parameter P has been demonstrated with Ni and Al[294], to which various alloying additions were made. Figures 4.2 and 4.3 illustrate the dependence of microstructure on the value of P. It can be seen that large values of P give a fine-grained (equiaxed) structure whereas small values of P correspond to relatively large (columnar) grains. An exception to this general result is the Ni - 1 at.pct W alloy which falls below the general trend. This discrepancy may be due to the fact that tungsten is the only element studied, other than cobalt, which increases the melting temperature of nickel ($K_o > 1$). Also changing the concentration of the alloying additions to 5 at.pct (which makes the value of P five times as great as in the case of 1 at.pct addition) reduced the average grain size as predicted by the value of the parameter P.

It was concluded[294] that for systems with P values less than approximately 10, the cast structure is essentially columnar, and the grain size decreases markedly with slight increase in P. For alloys with P>10 the grains are predominantly equiaxed and the grain size decreases with increasing P but the variation is much less dependent on P.

It has been shown[295] that additions of Ti, Nb, Zr, B and Y to a 17% Cr stainless steel tend to produce finer grain sizes in the as-cast alloy. This effect is believed to be due to the high P values of these elements in the alloy.

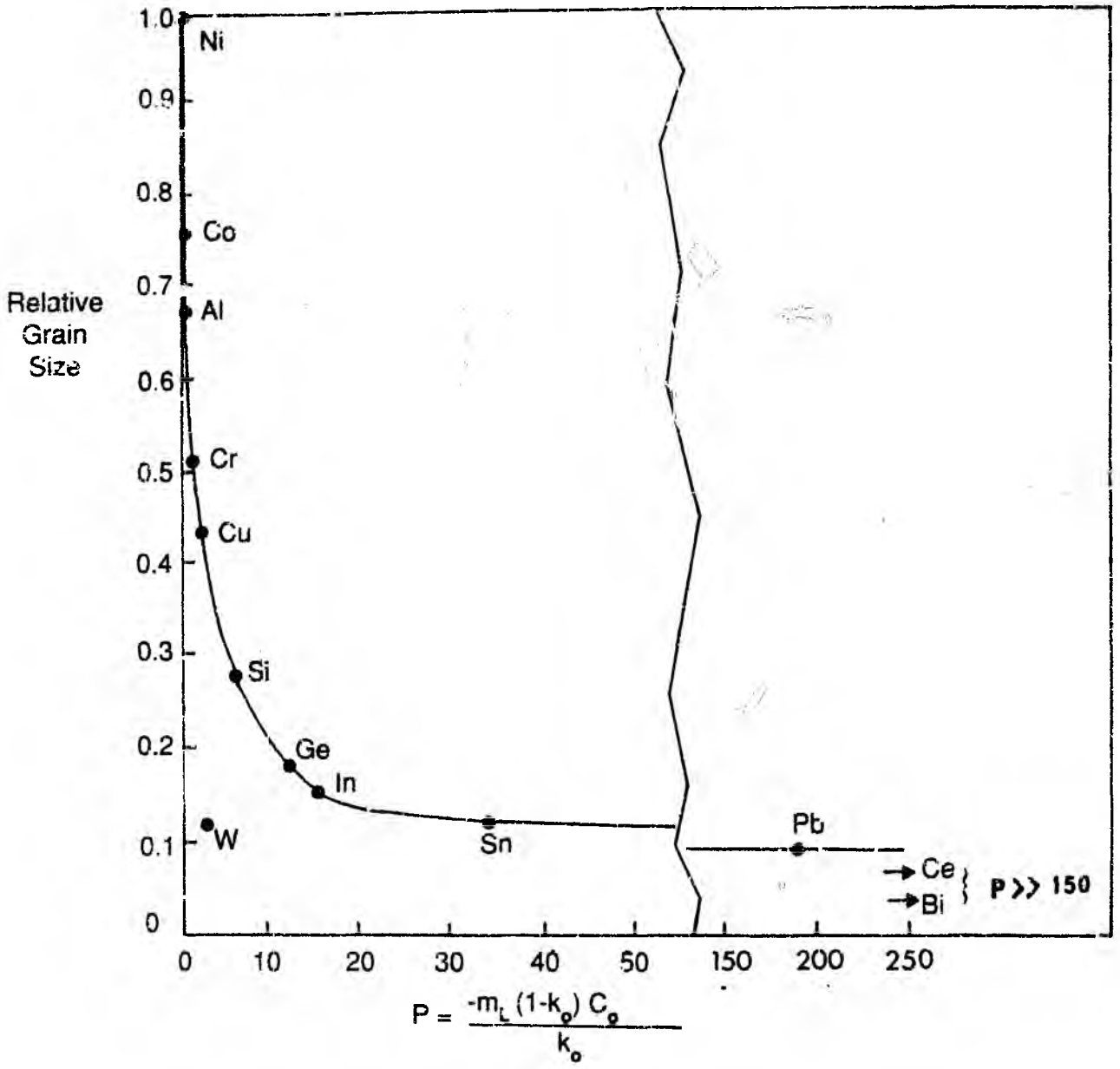

Figure 4.2 Variation of the linear-averaged grain size of nickel alloy castings as a function of the paramater P at 1 at.pct of solute concentration[294]

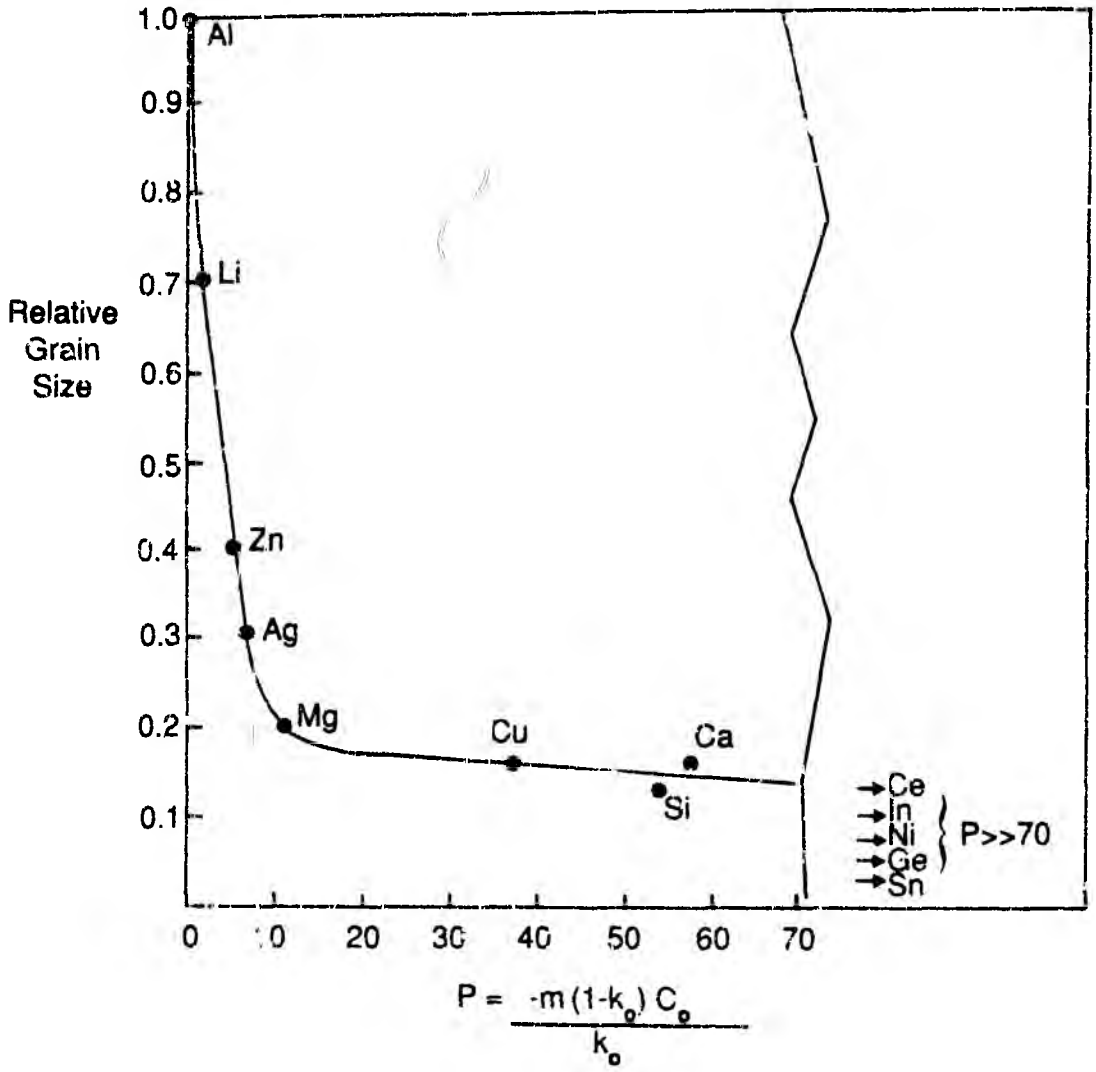

Figure 4.3 Variation of the linear-averaged grain size of aluminium alloy castings as a function of the parameter P at 1 at.pct of solute concentration[284].

4.3 The Role of Solute Activities in Chemical Grain Refining of Stainless Steels.

The elimination or addition of certain elements is known to influence the activity of other elements present in a solution. This in turn changes the solubility limits of these solute elements. The relationship between the activity of a certain element and the concentration of solute elements present in the solution can be expressed as follows, assuming that the solutes obey Henry's law of solutions :

$$a_1 = f_1^1 f_1^2 f_1^3 f_1^4 wt\%1 \quad \ldots\ldots 4.2$$

$$\log a_1 = \log f_1^1 + \log f_1^2 + \log f_1^3 + \log f_1^4 + \log wt\%1 \quad \ldots\ldots 4.3$$

$$\log a_1 = \log f_1^1 + e_1^2 + e_1^3 + e_1^4 + \log wt\%1 \quad \ldots\ldots 4.4$$

where a is the activity of solute 1 in the solution, $f_1^i (i = 1,\ldots,4)$ is the contribution of other solute elements to the activity coefficient of solute 1, e_1^i is the interaction coefficient of solute i on solute 1.

Therefore, as the elements which have positive interaction coefficients on solute 1 are added to the solution, the activity of solute 1 will be increased, lowering its solubility in the solvent as demonstrated i Figure **4.4**. The same effect would be expected if the elements which have negative interaction coefficients on solute 1 are removed from the solution. The hypothetical binary system in Figure **4.5** shows how the increased activity of the solute in liquid and solid will produce a decrease in solubility assuming ideal solution

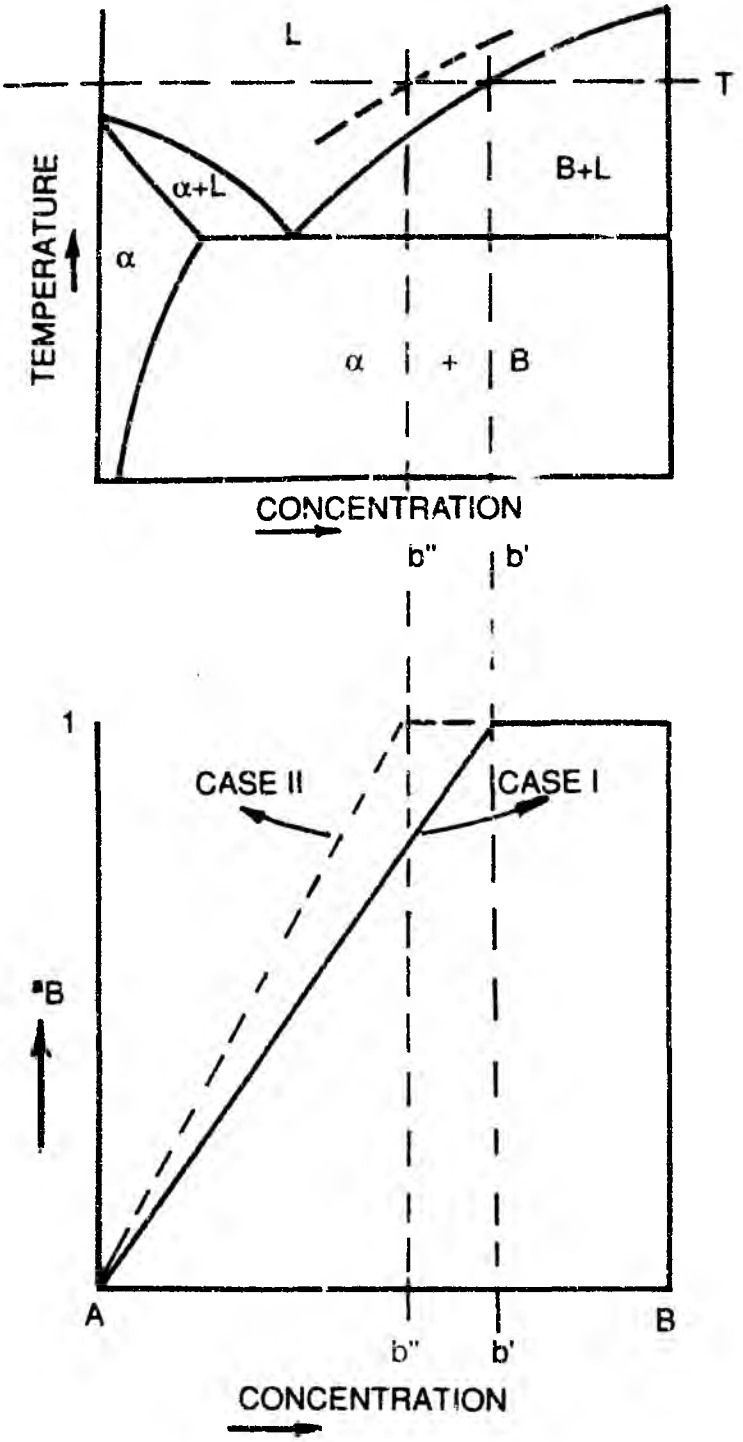

Figure 4.4. Relation between activity of an element B and its solubility in the system AB. Case I: activity of B at temperature T in a binary system AB. Case II: activity of B at temperature T in a system AB containing a third element C, where e_B^C has a positive value[236]

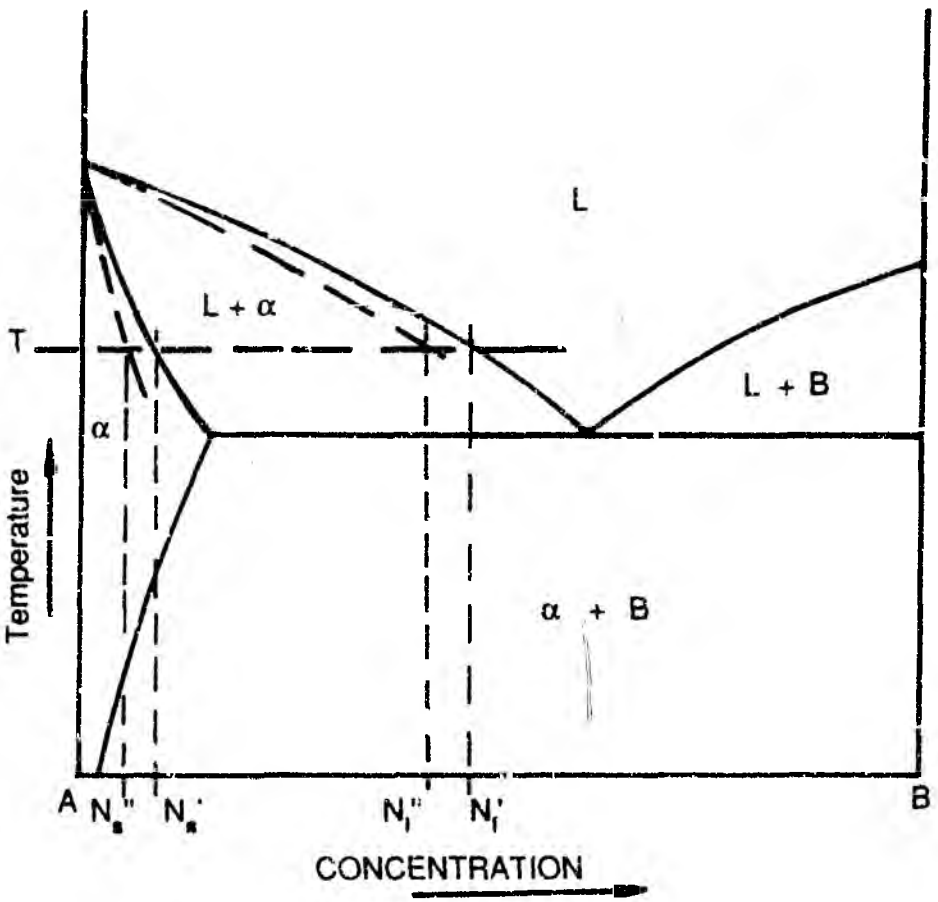

$$k_o = N_s/N_l$$

$$k''_o < k'_o$$

Figure 4.5 Reduced solubility of B in the liquid and solid due to an increase in activity of B (a_s) and resultant decrease of the distribution coefficient k_o[236]

behaviour. This phenomenon has been observed[436] in vacuum melting of AISI4330 steel where a refined structure was obtained when oxygen was partially removed and thus the activities of several elements such as aluminium, carbon, chromium, sulphur, silicon, titanium, and vanadium were increased. Oxygen has a negative interaction coefficient on all these elements. Also in 17% Cr ferritic stainless steels, the addition of elements like Ti, Zr and alkali metals which have positive interaction coefficients on chromium were observed[274] to refine the structure.

4.4 The Role of Nucleation Entropy in Chemical Grain Refinement of Stainless Steel

As the free energy barrier to be surmounted before nucleation starts is reduced, the number of independent crystal nuclei in a specific volume increases. This is demonstrated by the statistical relationship:

$$I = K\exp\left(-\frac{\Delta G^*}{kT}\right) \qquad \ldots\ldots 4.5$$

where I is the nucleation rate, K is a system parameter whose value is determined by nucleus geometry, contact angle, etc., k is Boltzmann's constant, and

$$\Delta G^* = \frac{16\pi\gamma^3}{3\Delta G_v^2} \qquad \ldots\ldots 4.6$$

where γ denotes the solid/liquid interfacial energy.

Equation **4.5** can be written as

$$I = K\exp\left(-\frac{16\pi\gamma^3}{3\Delta S_v^2 \Delta T^2 kT}\right) \qquad \ldots\ldots 4.7$$

where ΔS_v is the volume entropy of nucleation and ΔT is the supercooling, to show that the nucleation rate increases exponentially with the square of the volume entropy change on solidification. Therefore alloy systems having high nucleation entropies should correspondingly exhibit fine solidification structures assuming all other factors are constant[277].

It has been shown[277] that the nucleation entropy for a phase increases with the composition difference between the solid phase and the liquid phase from which the solid phase precipitates. Also it increases with the number of components which are in dilute concentrations in the liquid phase but found in remarkably higher concentrations in the precipitating solid phase. The role of nucleation entropy in the solidification kinetics of several alloy systems was studied[279-283] and grain refinement was found to be in good agreement with the increased nucleation entropy and corresponding nucleation rates of the precipitating phases or compounds on cooling.

For stainless steels it is possible to study the behaviour of precipitating components which have high nucleation entropies. These might give homogeneously and finely dispersed second phase particles which might provide suitable nucleation sites for the major solidifying phase.

4.5 The Problems that may be encountered during the Grain Refinement Process.

In alloys containing titanium, eutectic type inclusions have been found, consisting mainly of titanium and sulphur[228,275]. This type of inclusion is undesirable, because it affects the mechanical properties and reduces corrosion resistance.

Increased nitrogen content in the alloy would counteract precipitation of eutectic through nucleation of titanium nitrides, thus keeping sulphur in solid solution.

Also decomposition of nucleants (carbides and borides) may introduce a larger amount of carbon in the melt with subsequent segregation along grain boundaries and reduction of toughness and ductility[228]. Furthermore, the existence of high carbon concentrations will reduce the corrosion resistance of stainless steels. Excess titanium and boron additions may increase the probability of embrittlement and thus cracking of the finished material[227].

Another major problem is the fading phenomenon which is the loss of effectiveness of an inoculant above a certain degree of superheat and over a certain holding time. This is especially true for Ca(CN) and Fe-Cr additions for austenitic stainless steels[223,224]. To overcome this problem, further research is required to find suitable microalloying additions to act as nucleating agents or grain growth inhibitors or constitutional supercooling promoters. These additions should have a reproducible effect in repeated melting and casting processes.

4.6 Summary of the Mechanisms of Chemical Grain Refinement in Stainless Steels.

It can be stated that for the formation of a fine equiaxed cast structure in stainless steels, one should develop methods to provide:

(i) constitutional supercooling ahead of the solid-liquid interface

(ii) nucleation sites to take advantage of this supercooling and allow nucleation to occur ahead of the solid-liquid interface breaking down the columnar growth front.

In order to provide the above conditions, a modifying element should have one or more of the following properties:

(a) it should have steep liquidus lines and very low distribution coefficients. It should also have a low solid solubility in iron or decrease the solid solubility of one of the components of the alloys in ferrite or austenite. These properties promote solute enriched liquid-solid interface for constitutional supercooling.

(b) itself or its compounds should be stable at the melting temperature of steel, i.e. it should have a high melting temperature and low diffusion rates during pouring to prevent coalescence of particles.

(c) it should have a similar lattice parameter or an epitaxial relationship in which there is at least one plane with symmetry and similar to one of the planes of the nucleating phase.

(d) it should retard the further growth of the nucleating phase by poisoning its growth steps or by suppressing the liquidus temperature, preventing its nucleation at higher temperatures, that is by lowering the surface tension of its melt.

(e) it should have a solid-liquid interfacial energy much higher than that of the nucleating phase. Complex structured and high melting point compounds have high solid-liquid interface energies.

(f) its density should be comparable with that of liquid steel for homogeneous distribution throughout the casting.

(g) there should be a strong electronegativity attraction between the atoms in the inoculant and the atoms in the nucleating phase.

5. EXPERIMENTAL PROCEDURES

5.1 Introduction

The principal experimental procedure used to study the modification of type AISI 310 stainless steel by making small additions of a grain refining agent or a mixture of agents to the alloy. These agents were in the form of alloys or compounds and were selected for their potential as grain refining additions.

The procedure aimed to achieve the following:

(a) to gain understanding of the solidification process of AISI310 stainless steel,
(b) to find a suitable grain refiner for the modification of the cast structure of AISI310,
(c) to find the optimum amount and combination of grain refining agents necessary to modify the alloy,
(d) to contribute to the understanding of the chemical grain refining mechanisms of stainless steels,
(e) to compare the mechanical properties of modified and conventional ingots of AISI310 stainless steel.

A flowsheet showing the various steps of the experimental procedure and the various stages of the analysis and modelling of the results is given in Figure **5.1**.

5.2 Materials and Melting Practice

Strips of stainless steel AISI310S, whose chemical composition is given in Table **5.1**, were provided by Middelburg Steel and Alloys (Pty) Ltd. These strips were cut into smaller sizes to fit in the melting crucible and cleaned by sand blasting to remove the oxide layer, dirt and other contaminants from the surface.

EXPERIMENTAL FLOWSHEET	ANALYSES AND MODELLING OF RESULTS
Chemical Analyses of as received AISI310S steel	
Melting under protective atmosphere	
Additions FeSiZr, Misch Metal	
Casting (1436-1630°C)	
Chemical analyses of the ingots	Regression analyses of recoveries of additions
Metallographic analyses grain width, primary and secondary arm spacing measurements	Error analyses of measurements Analyses of refinement effect of additions AISI310S solidification modelling (macro and microstructure against superheat and constitution)
Homogenizing of the ingots 1200°C 2h wq	
Mechanical properties of the ingots Tensila, Impact, Hardness	Regression analyses of the properties against grain widths Explanation brought to anisotropic mechanical properties
Hot Rolling of selected ingots (85%, 1200°C 2h wq)	
Grain size measurement of the hot rolled ingots	
Mechanical properties of the hot rolled ingots Tensile, Impact, Hardness	Regression analyses of the properties against grain sizes
Cold Rolling of selected hot rolled ingots (25, 50, 75%, 975°C 10, 15, 20 and 60min, wq)	
Visual inspection and metallographic analyses Hardness measurements	Analyses of the hardness values against annealing times and reduction rates

Figure 5.1 Flowsheet summarizing the experimental and analytical procedures followed in this study

The chemical compositions of the misch metal and FeSiZr additions which were supplied by Metallurg S A Ltd., are listed in Table **5.2**.

Table 5.1 Chemical composition of the AISI310S stainless steel

Heat No. : 126999								
C%	S%	P%	Mn%	Si%	Cu%	Co%	Ti%	Mo%
0.047	0.005	0.026	1.67	0.46	0.070	0.040	0.008	0.010
	V%	Nb%	Al%	B%	Cr%	Ni%	N_2ppm	O_2ppm
	0.12	0.001	0.013	0.002	24.48	19.24	177	64

Table 5.2 Chemical analyses of the misch metal and FeSiZr used for grain refining

Misch Metal

Elements	Ce	La	Nd	Pr	Y	Fe	Sm	Eu	Ba	Ca+C+Mo
Concent.Wt%	48.87	23.73	17.23	5.88	1.66	1.95	0.48	0.006	0.009	<0.2

FeSiZr

Elements	Zr	Si	Fe
Concent. Wt%	35-40	47-52	Balance

Aluminium foil was used to facilitate the process of adding the other materials to the molten steel.

A vacuum induction melting furnace fitted with a generator capable of delivering 100 kw at 3000 Hz, and a built-in sintered magnesia crucible with a magnesite pouring spout, was used to melt the material. The molten metal was poured into flake graphite cast iron moulds of 6kg capacity placed on a water cooled mould table (Figure 5.2).

The melting and casting were done under an argon atmosphere which was held at 500 mbars for all castings. The temperature of the molten metal was measured with a Pt-6% Rhodium / Pt-30% Rhodium thermocouple which was inserted into the furnace through a built-in air tight pipe.

The steels were charged into the crucible and preheated under vacuum for 30 minutes at a power input of 20 kW. Argon was then allowed into the chamber via the gas inlet to 500 mbar pressure. This was followed by an increase in the power input to 40 kW. Once the metal had melted, in the case of castings without additions, the thermocouple was dipped into the melt to record the temperature of the metal. Heating was continued to a predetermined degree of superheat at which the power was switched off and the melt allowed to cool down to the casting temperature for that specific ingot. The alloy was then poured, into ingots of 65mm x 65mm x 250mm size and allowed to cool in the furnace.

Initially additions were made just after the metal had melted and before dipping the thermocouple into the melt. But the analyses of these castings indicated that some of the additions made to the melt were lost,

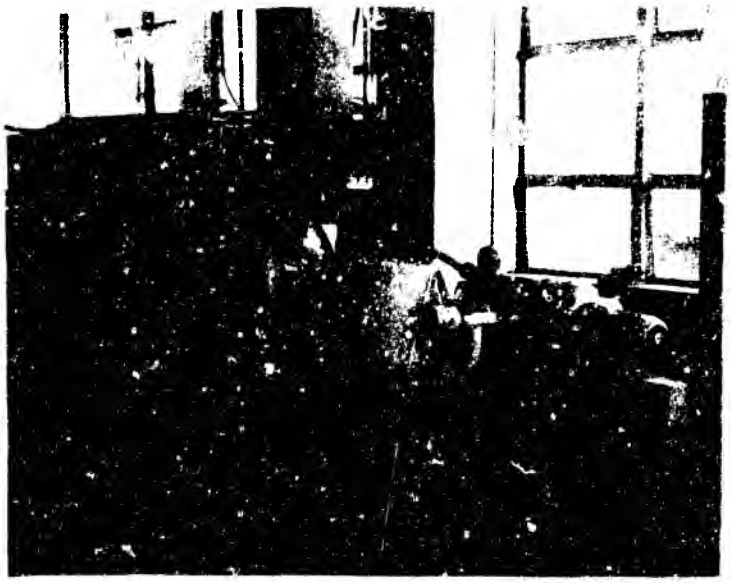



Figure 5.2 Vacuum induction furnace used for the melting and casting of AISI310S steel

probably to the furnace atmosphere due to volatilization. It was therefore decided to change the melting and casting procedures so as to minimise melting losses. The new procedure involved the melting of the alloy and holding of the melt temperature at a predetermined level. The thermocouple which was dipped into the alloy as soon as the latter was in the liquid state was then withdrawn from the melt and the additions made . The alloy was poured immediately after the addition was made.

The procedures described above are summarized below for comparison.

Initial procedure for ingots with additions

1. Melt the base metal
2. Make addition
3. Preheat alumina thermocouple sheath to avoid thermal shock.
4. Measure the temperature
5. Continue heating to the predetermined temperature.
6. Switch off the furnace at that temperature
7. Pour the metal immediately

(Total time taken from stages 2 to 7 was about 15 to 20 min)

New procedure for ingots with additions

1. Melt the base metal
2. Measure and stabilize the temperature of the melt 10-15 degrees above the casting temperature
3. Make addition
4. Switch off the furnace
5. Pour immediately.

(Total time taken from stages 3 to 5 was about 2 min)

Procedure for ingots without additions

1. Melt the base metal
2. Measure the temperature
3. Continue heating to the predetermined temperature
4. Switch off the furnace at that temperature
5. Allow the alloy to cool down to the casting temperature for that ingot
6. Pour immediately

(The predetermined temperature at stage 2 was 1650°C for ingots cast from 1610 to 1583°C, 1600°C for ingots cast from 1564 to 1526°C, 1550°C for ingots cast from 1512 to 1476°C and 1500°C for lower temperature castings.

In order to determine the degree of cooling of the molten metal in the crucible during the time lapsed from switching off the furnace to pouring the metal, a few trial cooling experiments were conducted. Cooling curves were produced for castings superheated to different temperatures before the furnace was switched off (Figure **5.3**). These were used to determine the true pouring temperature of castings by keeping a record of the time taken between switching off the furnace and the start and end of pouring. Holding time, which is the time duration between making the addition and end of pouring was also recorded.

Sixteen ingots were cast without addition to determine the influence of temperature on macro- and micro-structure, and on the solidification mode of AISI310S. This information, besides serving as a basis for comparison between ingots with and without additions, would contribute to the understanding of the solidification process of the steel. Although this steel is normally assumed to solidify by the nucleation and growth of austenite this is not always the case as discussed in section **7.1**. Castings without additions will be referred to as base metal castings or base metal.

5.3 Macrostructural Examination of the As-Cast Structures

Three transverse slices whose position are shown in Figure **5.4**, were cut from each ingot and were used for

chemical analysis and for microstructural and macrostructural examinations as indicated. Hot mixed acid solution (38ml HCl, 12ml H_2SO_4, and 50ml H_2O) was used to reveal the macrostructure. After etching the surfaces were examined visually to determine the effect of additions on the macrostructure. The width of the columnar grains was determined by the linear intercept method in which the number of grains intersected by the perimeters of "concentric" squares was determined (Figure 5.5). The outer square of 53mm side was chosen so as to exclude the chill zone from measurements. The inner square was of 51mm side. Thus the grain width measurements were taken at 6 and 14mm from the edges of the transverse slices.

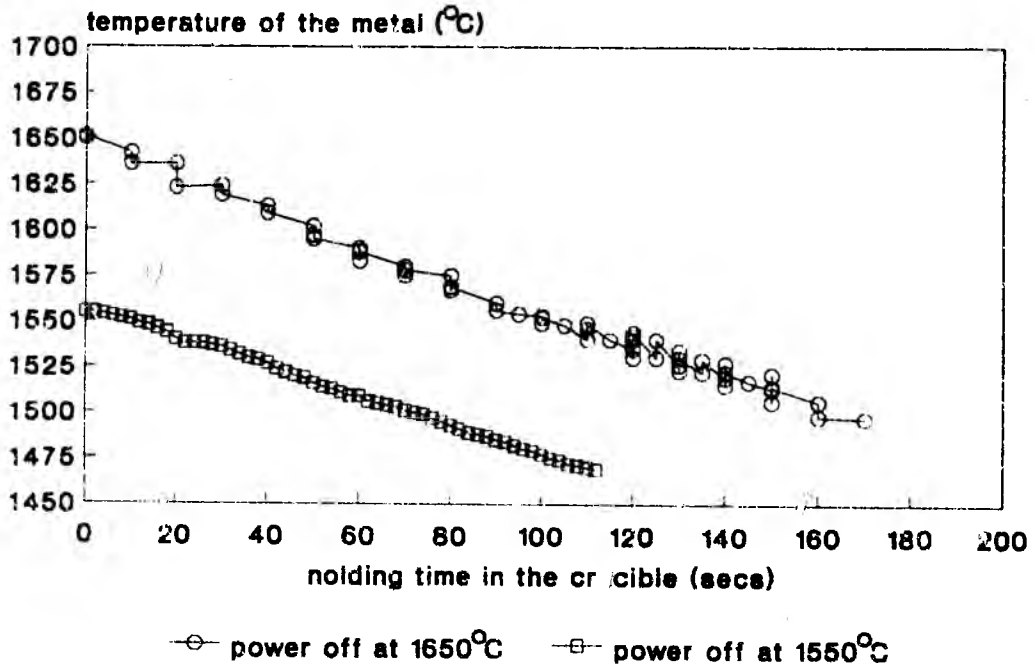

Figure 5.3 Plots of temperature against time for metal held in the melting furnace with the power off

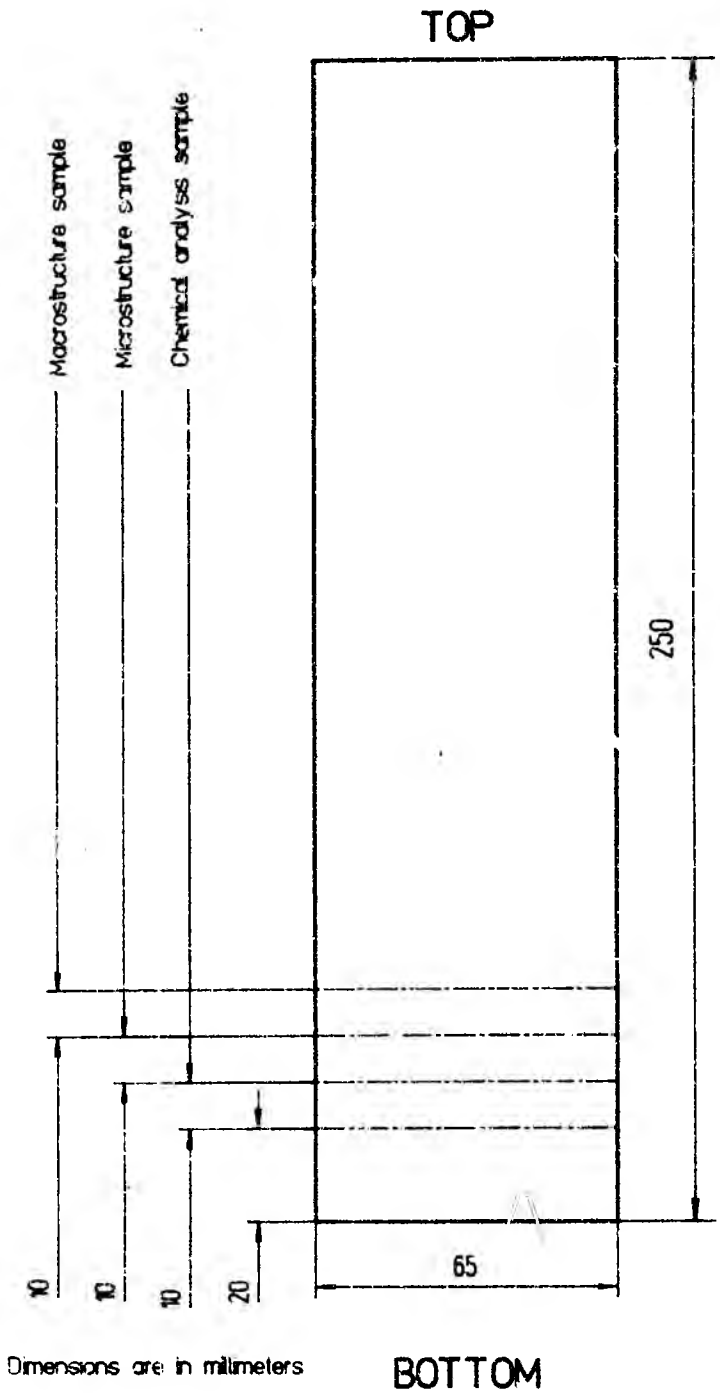

Figure 5.4 **Positions of the slices cut from as-cast ingots for measurements**

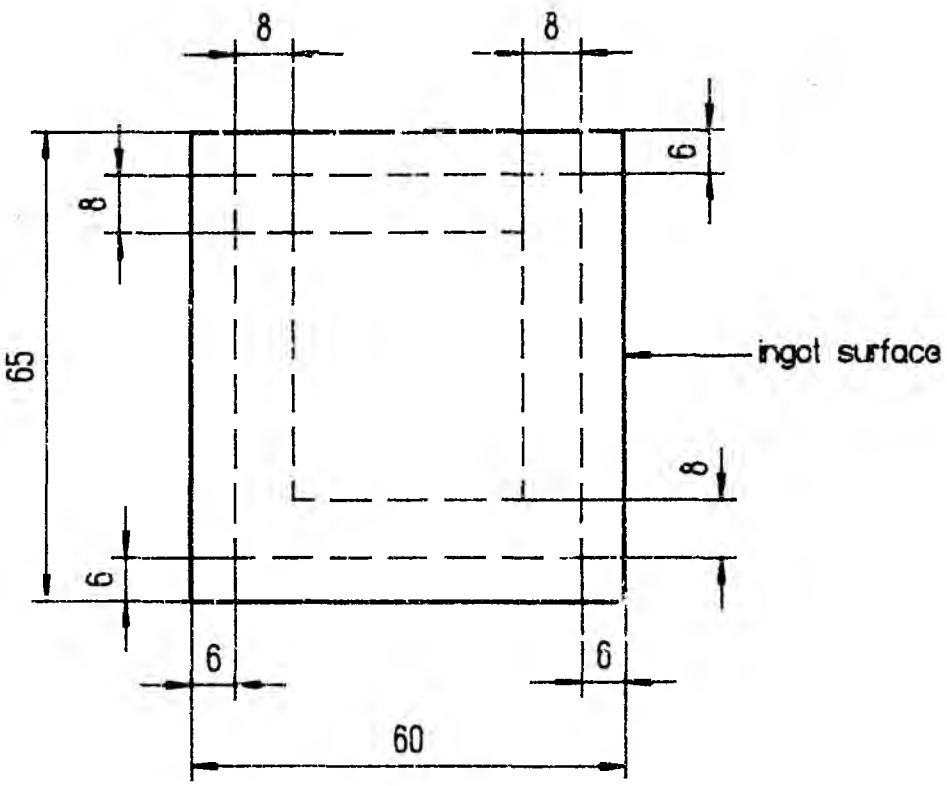

Figure 5.5 "Concentric" squares used to measure the grain widths

The grains were counted at least five times for each ingot and a statistical analysis was performed to ensure that at the 95% confidence limit, the variance of the counts did not exceed 10%. To minimize errors, the grain widths measured at 6 and 14mm from the edges are given separately.

Regression analysis was carried out for the change which took place in grain widths of the base metal castings with respect to casting temperature. The grain widths obtained in ingots with additions were compared to the estimated grain widths of the base metal castings corresponding to that casting temperature. The % change in grain widths were calculated and reported to show the degree of grain refinement which took place with the additions.

5.4 Microstructural Examination of the As-Cast Structures

One slice from each ingot was ground on successively finer grades of carbide paper up to 1200 grit. Final polishing was done by use of 3µm and 1µm diamond lapping compounds.

An electrolytic etch in oxalic acid was used to reveal the microstructure. The samples were etched for 15 seconds at a voltage of 8V.

These slices were examined with the optical microscope and the scanning electron microscope. The matrix and inclusions were analyzed by use of an EDS system coupled to a scanning electron microscope.

Primary and secondary dendrite arm spacings were measured as a function of distance from opposite edges of all the base metal ingots and of selected modified ingots. Selection of such ingots was based on the apparent degree of grain refinement. Measurements were taken at two magnifications namely 40 and 100x with the aid of a filar eyepiece. For each sample, spacings were measured at varying distances from two opposite edges of the slice. For each distance selected, 10 to 18 counts of dendrite arm spacings were obtained and averaged to calculate the mean arm spacing at that distance. For each sample 12 to 18 average arm spacings were obtained for a corresponding number of distances from the edges. Thus the total individual counts could be as high as 500 for each sample.

A statistical analysis was performed to calculate the error and the significance of the measurements. The average primary and secondary arm spacings with their 95% confidence limits at varying distances from the edges for two samples are given in Tables **5.3** and **5.4**. For the primary arm spacings, the 95% confidence limits are within 15% of the average values. The confidence limits for primary arm spacings increase with increasing distance from the edge indicating a greater degree of scatter in the measurements. This was due to the fact that dendritic growth is competitive and the dendrites coarsened with increasing distance from the edge. Thus measurements were taken from fewer dendrites. The control measurements in Tables **5.3** and **5.4** were made a few months later to examine whether the new mean values obtained would fall within the confidence limits. Examination of Table **5.3** will show that the control values of primary arm spacing are indeed within the confidence limits. This indicates that the original measurements were reliable.

Table 5.3 Avarege primary arm spacings measured at various distances with their 95% confidence limits and control measurements taken at the same distances at a later stage.

Specimen . ZR 20

Distance from the edge (mm)	Mean Primary Arm Spacings (μm) and Confidence Limits				Control Measurements (μm)	
	Side A		Side B		Side A	Side B
2	93.4	± 15.0	69.5	± 10.7		
4	111.6	± 13.2	81.9	± 11.4	113.3	94.1
6	125.7	± 15.0	111.0	± 7.4	133.0	102.6
8	158.3	± 21.6	136.2	± 20.6	147.2	166.0
10	223.8	± 33.7	178.6	± 27.7	202.6	179.6
12	200.8	± 23.3			182.0	
16			184.5	± 27.7		185.0
18	210.6	± 41.3			225.0	

Specimen : ZR 10

Distance from the edge (mm)	Mean Primary Arm Spacings (μm) and Confidence Limits				Control Measurements (μm)	
	Side A		Side B		Side A	Side B
2	39.9	± 6.9	63.7	± 10.1		
4	59.8	± 9.7	88.7	± 14.2	52.5	84.5
6	107.7	± 14.7	118.6	± 15.1		
8			126.3	± 12.1		109.6
10	148.5	± 23.4	167.5	± 26.6	137.9	
12	140.6	± 18.2	167.5	± 23.3	141.6	
14	149.8	± 19.9	162.7	± 20.4		
16	166.7	± 19.2	220.6	± 27.7		207.5
18	189.2	± 42.0	250.0	± 41.3		208.5
20	209.7	± 37.7			231.0	

Table 5.4 Average secondary arm spacings measured at various distances with thair 95% confidence limits and control measurements taken at tha same distances at a later stage.

Specimen : ZR 20

Distance from the edge (mm)	Mean Secondary Arm Spacings (μm) and Confidence Limits		Control Measurements (μm)	
	Side A	Side B	Side A	Side B
2	22.4 ± 0.8		21.4	18.9
8	30.1 ± 2.0	27.0 ± 1.5		28.0
10	30.8 ± 2.5	30.6 ± 3.4	33.5	
11		31.8 ± 2.9	32.4	
12	33.6 ± 3.5			
16		29.3 ± 3.7		26.1
18	31.0 ± 4.2			

Specimen : ZR 10

Distance from the edge (mm)	Mean Secondary Arm Spacing (μm) and Confidence Limits		Control Measurements (μm)	
	Side A	Side B	Side A	Side B
2	14.3 ± 0.8	18.8 ± 1.3		
4	19.9 ± 0.9	24.6 ± 1.7	20.5	
6	26.2 ± 5.5	26.0 ± 2.1		28.2
8	36.3 ± 1.9			
10	37.8 ± 4.3	35.2 ± 1.9	36.1	
12	37.6 ± 2.8	31.1 ± 3.8		
14	44.0 ± 4.1	33.0 ± 2.2		
16	36.6 ± 4.6	34.7 ± 2.1		
18	47.2 ± 5.7	32.2 ± 1.6	52.4	
20		34.8 ± 2.5		34.2

The scatter about the mean secondary arm spacings was about 7%. The higher precision in the measurement of secondary arm spacings is most probably due to a larger number of counts at any given distance from the edge, sometimes up to 20 times more. Control measurements were carried out in a way similar to that described for primary arm spacings and for the same reasons. The results obtained mostly fell within the confidence limits of the original measurements confirming the significance of the 95% confidence limits.

These procedures showed that the errors were well within acceptable limits. Some other factors which may have limited the precision of the measurements are as follows

1. There is an element of judgement, and consequently a source of experimental error, in the selection of the point where the primary arms are more or less parallel to each other, which makes it easier to measure the spacings.

2. It is often observed that besides fully developed secondary arms which usually occur at fairly regular intervals, there are also, depending on the size of the primary arm, 2 to 10 underdeveloped arms between these arms. It was again a matter of judgement whether to include or exclude certain partially developed arms.

3. The different magnifications used might be another source of error. At 40x magnification, the field of view is wider and measurements may be taken over a wider range of distances from the predetermined distance. It was calculated that with a magnification of 40x measurements might be off the predetermined line by up to 1mm. With a

magnification of 100x measurements were within 0.4mm of the predetermined line.

4. Due to variations in etching intensity it became difficult to differentiate between individual arms or to decide if an arm was missing due to dissolution by the etchant. In these cases, counts were made by considering the rhythm of the spacing.

5. In the equiaxed zone, since the plane of the section is considerably more random with respect to the growth direction of the individual dendrites, which would make the measurements less accurate, counts of the arms were not included in the results.

5.5 Chemical Analyses

All the ingots produced were analysed chemically to determine their composition and the % recovery of added modifying agents.

Twenty three slices taken from ingots containing misch metal and sixteen slices from ingots containing Zr were analyzed for their residual concentrations of Ce, La and Zr.

Middelburg Steel and Alloys (Pty) Ltd analysed samples on an A.R.L. 72000S XRF spectrometer. Al and B were determined with an A.R.L. emission analyser 3460. Carbon analyses were carried out with a LECO carbon and sulphur determinator (CS044).

5.6 Hot Rolling

Five of the ingots with no addition and 13 of the ingots with misch metal or FeSiZr additions were annealed at 1200°C for two hours.

They were then hot rolled to slabs of 15mm thickness (76% reduction) in a two-high reversing mill with a capacity of 50 tonnes. All rolling was done using flat rolls of 200mm diameter and a roll speed of 25 rpm (equivalent to a linear speed of $0.26ms^{-1}$).

Details of the rolling procedure are given below:

Rolling temperature	1200°C
Soaking time	2 h
Rolling temperature range	1200-800°C
Number of intermediate reheats	3
Reheating time between reductions	15 minutes

After rolling, the ingots were solution treated for two hours at 1200°C and water quenched. Their surfaces were examined visually for cracks and other defects.

5.7 Cold Rolling

One of the hot rolled slabs with no addition and five of the hot rolled slabs with misch metal or FeSiZr additions were cold rolled by means of the same rolling mill by use of appropriate rolls of 160mm diameter. The roll speed was 50rpm and the slabs were reduced by about 0.20mm in thickness per pass to reductions of 25, 50 and 75%.

5.8 Heat Treatment of Cold Rolled Material

Small pieces were cut from the cold rolled material and heat treated at 975±5°C in a horizontal tube furnace for periods of 10, 15, 20 and 60 minutes. After heat treatment the bars were quenched in water. These treatments were applied to material cold reduced by 25, 50 and 75% in order to determine the influence of additions on the recrystallization characteristics of the alloy. After heat treatment the bars were quenched in water.

5.9 Microscopic Examination of As Rolled Structures

Specimens were prepared metallographically and examined by light and scanning electron microscopy. The specimens were mounted separately in plastic and prepared by grinding to 1200 grit finish on silicon carbide paper and polishing to a 1µm finish with diamond. Specimens were etched electrolytically in saturated oxalic acid. The etching time varied from 40s to 2 minutes and the voltage from 2 to 10 V. The grain sizes of the as hot-rolled material were determined according to ASTM specification E112-84.

5.10 Mechanical Tests

Specimens for Charpy and tensile tests were prepared from the selected as-cast, as-hot-rolled and as-cold-rolled materials. Hardness tests were done on the samples that were taken for metallographic examination. The positions in the ingots and slabs, from where these samples were taken are shown in Figure **5.6**.

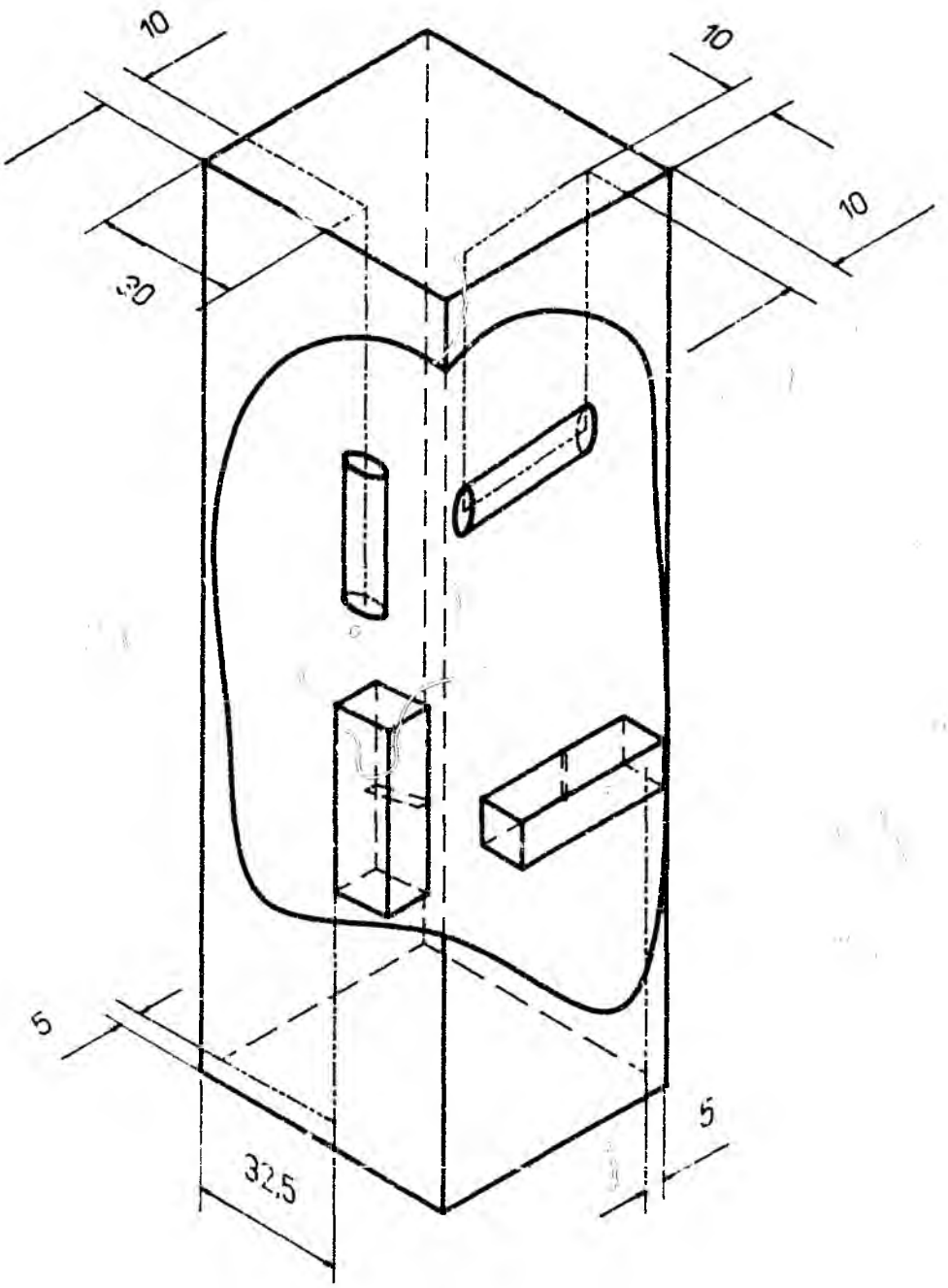

Figure 5.6 Position and orientation of the samples cut from the ingots for mechanical tests.

5.10.1 Hardness Tests

The hardnesses of the as-cast and as-rolled ingots were measured using Vickers hardness tests with loads of 300g and 5 kg according to standard ASTM E 92-82. The specimen surfaces were prepared by grinding and polishing to a finish of one micron. Five tests were carried out on each specimen and the average value for the sample determined.

5.10.2 Tensile Tests

Tensile specimens were prepared from longitudinal and transverse sections taken from selected ingots before hot rolling. From the ingots that were tested in the cast condition 16 were selected and re-tested after hot rolling, reheating and water quenching. The design of the tensile test specimens is shown in Figure **5.7.**

Tests were also carried out on samples prepared from longitudinal sections taken from material cold rolled as described in section **5.7.** The tests were carried out at ambient temperature according to the ASTM standard A370-77.

The yield strength, tensile strength, percentage reduction in area and percentage elongation of the as-cast and as-hot rolled specimens were measured whereas for cold rolled samples only tensile strength was recorded. The results quoted are the means of at least 2 tests.

The fracture surfaces were examined by scanning electron microscopy.

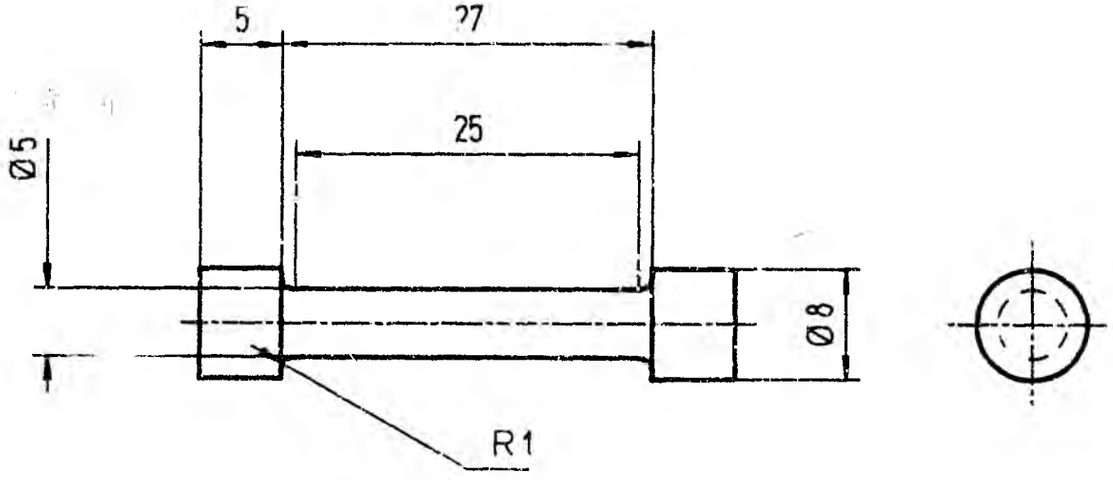

Figure 1.7 Shape and dimensions of the tensile test pieces

5.10.3 Charpy Impact Tests

Longitudinal and transverse sections were taken from selected as-cast and from all hot-rolled ingots for the preparation of Charpy V-notch impact specimens.

The specimens were machined and tested in accordance with the requirements of standards ASTM A 370-77 and ASTM E 23-82. The dimensions of Charpy impact specimens are shown in Figure 5.8.

The tests were performed at ambient temperature on a Tinius Olsen machine capable of registering absorbed impact energies of up to 358J. The energy values were recorded to the nearest 0.5 Joule and each value quoted is the average of two tests.

With some of the ingots, this maximum recording capacity of the machine was attained without fracture of the specimens which had a cross-section of 100mm^2. It was therefore decided, for these ingots, to prepare subsize specimens of 50mm^2 cross section in order to be able to measure the energy absorbed. Fracture surfaces of specimens were examined by scanning electron microscopy.

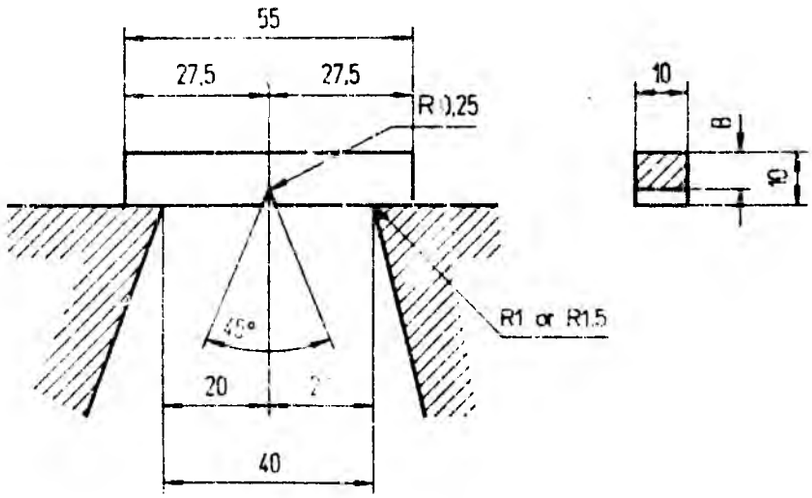

Figure 5.8 Dimensions of the Charpy impact test pieces

6. EXPERIMENTAL RESULTS

6.1 Chemical Composition of the Castings

The chemical compositions of the castings with and without additions are given in Tables **6.1, 6.2** and **6.3,** together with the chemical analysis of the material in the as-received condition. The nominal composition of AISI310S is also given in these tables. It can be seen that the material used in this study contained an appreciable amount of vanadium (about 0.12%) although the ASTM composition does not specify vanadium in this steel. A comparison was made of C, S, Cr, Ni and O_2 concentrations in base metal ingots and ingots containing additions to examine the influence of remelting and of additions on the concentrations of these elements in the alloy (Table **6.4**).

The base metal castings (denoted by B1, B2 etc.) did not show any significant deviation from the composition of the as-received material other than a marginal reduction in the amount of Ni and a small increase in O_2 most probably due to leaks into the furnace atmosphere from the environment. These changes in composition increased when the molten metal was kept for a longer time in the crucible to effect a temperature drop to the specific pouring temperature as in the case of castings B3 to B10. Castings poured with a minimal holding time showed lower O_2 levels irrespective of casting temperature.

The castings with misch-metal additions appeared to show a marginal increase in %C of about 0.003% to 0.004% on average. The Ni loss was lower than that experienced with the base metal.

Table 6.1 Chemical analysis of as-received and as-cast AISI 310S stainless steel

Chemical Analyses wt%																	
Sample no	C	S	P	Mn	Si	Cu	Co	Ti	Mo	V	Nb	Al	B	Cr	Ni	N_2	O_2
as-received	0.047	0.005	0.026	1.67	0.48	0.07[illegible]	0.040	0.008	0.01	na	0.001	0.[illegible]3	0.0020	24.48	19.24	177	64
B1	0.040	0.006	0.020	1.53	0.40	0.098	0.028	0.001	0.15	0.13	0.0[illegible]	na	na	25.00	18.14	187	204
B2	0.041	0.009	0.027	1.42	0.44	0.100	0.050	nil	0.04	0.12	0.004	na	na	24.58	19.03	124	245
B3	0.046	0.007	0.028	1.67	0.45	0.150	0.030	0.001	0.04	0.13	0.001	0.003	0.0028	24.38	18.55	170	290
B4	0.049	0.006	0.026	1.68	0.47	0.100	0.030	0.001	0.04	0.12	0.001	0.007	0.0027	24.39	19.04	170	440
B5	0.043	0.007	0.026	1.68	0.45	0.100	0.030	0.001	0.03	0.13	0.001	0.006	0.0028	25.14	19.01	170	310
B7	0.046	0.007	0.023	1.64	0.44	0.100	0.030	0.001	0.03	0.12	0.001	0.008	0.0028	24.47	18.87	170	380
B9	0.039	0.007	0.025	1.67	0.44	0.100	0.040	0.001	0.03	0.12	0.001	0.009	0.0028	24.77	18.95	330	120
B10	0.057	0.004	0.030	1.67	0.41	0.100	0 040	nil	0 03	0.13	0.003	0.009	0.0028	24.44	18.94	200	240
B12	0.043	0.004	0.030	1.67	0.41	0.100	0.040	nil	0.03	0.13	0.003	0.008	0.0028	24.42	18.98	200	230
B14	0.051	0.006	0.029	1.67	0.44	0.100	0.040	nil	0.03	0.13	0.004	0.013	0.0027	24.43	18.97	190	120

Table 6.2 Chemical analysis of ingots containing misch metal

Chemical Analyses wt%																	
Sample No	C	S	P	Mn	Si	Cu	Co	Ti	Mo	V	Nb	Al	B	Cr	Ni	N_2 ppm	O_2 ppm
as-received	0.047	0.005	0.026	1.67	0.46	0.070	0.040	0.008	0.010	na	0.001	0.013	0.002	24.48	19.24	177	64
MM1	0.048	0.007	0.027	1.63	0.50	0.085	0.031	0.001	0.027	0.12	0.001	na	na	24.44	19.01	166	318
MM2	0.053	0.009	0.026	1.68	0.66	0.080	0.031	0.001	0.024	0.12	0.001	na	na	24.31	19.01	191	100
MM3	0.052	0.002	0.027	1.66	0.42	0.100	0.040	nil	0.040	0.11	0.004	na	na	24.24	18.78	160	34
MM4	0.052	0.002	0.033	1.58	0.41	0.100	0.040	nil	0.040	0.11	0.004	na	na	24.00	18.81	292	132
MM5	0.047	0.002	0.031	1.57	0.42	0.100	0.040	nil	0.040	0.11	0.004	na	na	23.78	18.83	132	192
MM6	0.047	0.002	0.031	1.62	0.45	0.100	0.040	0.29	0.050	0.14	0.004	0.450	0.0029	24.26	18.93	270	120
MM7	0.066	0.003	0.028	1.69	0.37	0.100	0.030	nil	0.040	0.13	0.005	0.009	0.0029	24.43	19.07	160	165
MM8	0.047	0.002	0.027	1.59	0.41	0.100	0.030	nil	0.030	0.13	0.004	0.011	0.0030	24.38	19.03	160	165
MM9	0.049	0.002	0.031	1.66	0.41	0.100	0.030	nil	0.040	0.14	0.004	0.021	0.0030	24.19	19.07	140	140
MM10	0.047	0.002	0.030	1.70	0.40	0.100	0.030	nil	0.040	0.13	0.005	0.010	0.0029	24.38	19.07	160	150
MM11	0.050	0.003	0.032	1.67	0.44	0.100	0.030	nil	0.040	0.13	0.004	0.013	0.0029	24.39	19.18	150	170
MM12	0.046	0.002	0.029	1.72	0.44	0.100	0.030	nil	0.040	0.14	0.004	0.028	0.0030	24.64	19.27	150	210

Table 6.2 Continued

Chemical Analyses wt%																	
Sample No	C	S	P	Mn	Si	Cu	Co	Ti	Mo	V	Nb	Al	B	Cr	Ni	N_2 ppm	O_2 ppm
as-received	0.047	0.005	0.026	1.67	0.46	0.070	0.040	0.008	0.010	na	0.001	0.013	0.0020	24.48	19.24	177	64
MM13	0.048	0.005	0.034	1.67	0.43	0.100	0.040	nil	0.040	0.13	0.005	0.354	0.0030	24.13	19.85	130	220
MM14	0.051	0.004	0.027	1.64	0.38	0.080	0.030	0.006	0.040	0.13	0.002	0.006	na	24.66	19.98	169	na
MM15	0.049	0.003	0.027	1.59	0.36	0.090	0.040	0.010	0.040	0.12	0.003	0.008	0.0029	24.50	19.98	194	42
MM16	0.056	0.003	0.028	1.64	0.35	0.100	0.030	0.007	0.050	0.12	0.004	0.005	0.0029	24.37	19.98	127	41
MM17	0.041	0.003	0.027	1.68	0.36	0.090	0.030	0.006	0.030	0.12	0.002	0.004	0.0029	24.92	19.20	164	57
MM18	0.051	0.002	0.029	1.64	0.40	0.090	0.040	0.005	0.040	0.12	0.003	0.006	0.0029	24.49	19.13	148	31
MM19	0.060	0.006	0.027	1.60	0.42	0.093	0.028	0.004	0.048	0.11	0.001	0.011	0.0032	24.92	19.17	160	240
MM20	0.061	0.004	0.029	1.65	0.51	0.080	0.030	0.002	0.040	0.12	0.002	0.011	na	24.53	18.87	180	na
MM21	0.043	0.010	0.036	1.65	0.42	0.120	0.020	0.003	0.010	0.13	0.003	0.070	na	24.16	18.73	230	na
MM22	0.048	0.004	0.029	1.65	0.49	0.090	0.030	0.001	0.040	0.13	0.002	0.008	na	24.62	18.90	150	na
MM23	0.054	0.003	0.030	1.71	0.40	0.090	0.020	0.003	0.050	0.13	0....	0.090	na	24.87	18.99	170	na

Table 6.3 Chemical analyses of ingots containing FeSiZr

Chemical Analyses wt%																	
Sample No	C	S	P	Mn	Si	Cu	Co	Ti	Mo	V	Nb	Al	B	Cr	Ni	N_2 ppm	O_2 ppm
as-received	0.047	0.005	0.026	1.67	0.46	0.070	0.040	0.008	0.01	na	0.001	0.013	0.0020	24.48	19.24	177	64
ZR1	0.052	0.004	0.028	1.65	0.48	0.078	0.030	0.001	0.023	0.12	0.001	na	na	24.25	19.02	204	386
ZR2	0.049	0.006	0.025	1.66	0.53	0.062	0.031	0.001	0.031	0.12	0.002	na	na	24.39	19.07	177	262
ZR3	0.050	0.003	0.026	1.55	0.78	0.100	0.050	nil	0.040	0.11	0.004	na	na	24.38	18.81	147	220
ZR4	0.047	0.004	0.026	1.65	0.94	0.100	0.040	nil	0.050	0.11	0.004	na	na	24.35	18.83	150	137
ZR5	0.051	0.004	0.026	1.50	0.66	0.100	0.040	0.060	0.050	0.13	0.004	0.140	0.0029	24.48	18.96	240	136
ZR6	0.050	0.005	0.029	1.65	0.96	0.100	0.040	0.310	0.040	0.14	0.005	0.430	0.0029	24.41	18.85	110	100
ZR7	0.070	0.002	0.031	1.62	0.45	0.100	0.040	0.290	0 050	0.14	0.004	0.120	0.0029	24.26	18.83	270	126
ZR8	0.048	0.006	0.026	1.67	1.04	0.100	0.030	0.007	0.040	0.12	0.002	0.208	0.0028	24.33	19.04	160	120
ZR9	0.061	0.006	0.026	1.71	1.09	0.100	0.030	0.005	0.040	0.13	0.001	0.310	0.0030	23.98	18.53	120	180
ZR10	0.051	0.006	0.026	1.66	1.04	0.11	0.030	0.006	0.030	0.12	0.002	0.286	0.0029	24.63	18.80	180	120
ZR11	0.054	0.006	0.026	1.70	1.06	0.100	0.030	0.005	0.040	0.12	0.001	0.180	0.0029	24.51	18.78	150	70
ZR12	0.052	0.006	0.025	1.69	1.05	0.100	0.030	0.004	0.040	0.12	0.001	0.130	0.0028	24.44	18.76	170	280
ZR13	0.059	0.004	0.028	1.71	1.05	0.100	0.040	0.002	0.030	0.13	0.003	0.049	0.0028	24.29	18.84	220	170

Table 6.3 Continued

Chemical Analyses wt%																	
Sample No	C	S	P	Mn	Si	Cu	Co	Ti	Mo	V	Nb	Al	B	Cr	Ni	N_2 ppm	O_2 ppm
as-received	0.047	0.005	0.026	1.67	0.46	0.070	0.040	0.008	0.01	na	0.001	0.013	0.0020	24.48	19.24	177	84
ZR14	0.035	0.004	0.026	1.71	0.96	0.10	0.040	0.002	0.040	0.13	0.004	0.045	0.0028	24.20	19.61	170	230
ZR15	0.053	0.006	0.028	1.70	0.99	0.090	0.040	0.002	0.040	0.13	0.003	0.041	0.0028	24.16	18.82	210	120
ZR16	0.053	0.003	0.028	1.57	0.95	0.100	0.030	nil	0.050	0.13	0.005	0.020	0.0030	24.35	19.06	?	150
ZR17	0.057	0.004	0.027	1.65	0.98	0.100	0.030	nil	0.040	0.13	0.005	0.020	0.0030	24.37	19.05	160	120
ZR18	0.048	0.004	0.029	1.62	0.97	0.100	0.030	nil	0.050	0.13	0.005	0.025	0.0028	24.34	19.11	130	130
ZR19	0.046	0.005	0.029	1.72	0.44	0.100	0.030	nil	0.040	0.14	0.004	0.028	0.0029	24.37	18.97	220	280
ZR20	0.061	0.005	0.027	1.65	1.26	0.080	0.030	0.010	0.040	0.13	0.002	0.012	na	24.33	18.96	440	na
ZR21	0.039	0.010	0.032	1.63	0.29	0.123	0.027	0.004	0.094	0.11	0.001	0.075	0.0033	24.82	18.29	240	530
ZR22	0.047	0.006	0.035	1.73	0.40	0.110	0.020	0.004	0.100	0.13	0.004	0.080	na	24.49	18.97	180	na
ZR30	0.057	0.005	0.030	1.68	0.95	0.100	0.040	nil	0.060	0.13	0.005	0.317	0.0030	24.17	18.90	170	340
ZR31	0.050	0.006	0.027	1.60	0.99	0.100	0.040	0.002	0.050	0.13	0.005	0.278	0.0030	24.34	18.93	140	180

25×IC

Table 6.4 Concentrations of C, S, Cr, Ni and O_2 in three different groups of ingots

(a) Ingots without additions

Elements	Average Concentration wt%	Concentration range within which lie 95% of the results
C	0.0459	0.0421 - 0.0497
S	0.0063	0.0052 - 0.0074
Cr	24.60	24.40 - 24.80
Ni	18.85	18.64 - 19.05
O_2	287.9ppm	215.4 - 360.4 ppm

(b) Ingots with misch metal additions

C	0.0504	0.0475 - 0.0533
S	0.003	0.0023 - 0.0044
Cr	24.36	24.24 - 24.48
Ni	19.04	18.97 - 19.11
O_2	140.4ppm	100.5 - 180.3 ppm

(c) Ingots with FeSiZr additions

C	0.0514	0.0481 - 0.0548
S	0.0046	0.0038 - 0.0053
Cr	24.32	24.25 - 24.39
Ni	18.87	18.79 - 18.95
O_2	181.8ppm	141.0 - 222.6 ppm

Table 6.5 Concentrations and % recoveries of rare-earth elements in AISI310S ingots cast from different temperatures and after different holding times.

Ingot no	Casting Temp.°C	Holding Time (min)	Addition ppm	Analyses ppm	Recovery %
MM1	1617	15	Ce 2052 La 888	7.1 0.6	0.4 0.1
MM2	1627	15	Ce 4007 La 1946	646 142	16.0 7.3
MM3	1630	15	Ce 6109 La 2966	1172 176	19.2 5.9
MM4	1605	15	Ce 6986 La 3393	5290 1656	75.3 48.5
MM5	1624	30	Ce 7873 La 3727	6935 2127	90.4 57.1
MM6	1637	15	Ce 4496 La 2183	1737 394	38.8 18.0
MM7	1535	25	Ce 2541 La 1234	32.7 6.5	1.3 0.7
MM8	1530	7	Ce 1515 La 736	17.25 2.25	1.1 0.3
MM9	1549	15	Ce 4887 La 2373	3406 679	70.0 28.8
MM10	1523	12	Ce 2053 La 997	1349 241	65.7 24.2
MM11	1550	20secs	Ce 2450 La 1200	1800 703	73.5 58.5
MM12	1535	15	Ce 2969 La 1464	858 144	20.3 8.8
MM13	1545	38secs	Ce 4067 La 1992	3100 1215	76.2 61.0
MM14	1550	25secs	Ce 314 La 154	222 101	71.2 65.6
MM15	1550	25secs	Ce 939 La 264	280 92	52.8 34.8
MM16	1551	38secs	Ce 823 La 403	478 143	58.1 35.5
MM17	1547	30secs	Ce 1058 La 515	524 175	59.0 33.8
MM18	1545	33secs	Ce 1299 La 636	790 281	60.8 44.2
MM19	1544	5	Ce 49 La 24	45 6.9	91.8 28.7
MM20	1543	5	Ce 147 La 72	5 5	3.6 6.9
MM21	1539	30secs	Ce 982 La 199	5 5	1.4 2.8
MM22	1509	38secs	Ce 982 La 324	854 137	83.9 42.3
MM23	1504	5	Ce 368 La 192	248 80	62.5 26.1

Table 6.6 **The statistical relationship between the amounts of Ce and La added to the steel as misch metal and the amounts recovered in tha alloy**

Casting Temperature Range	Element	Regression Equation	Correlation Coefficient
1608-1637°C	Ce	y = 3382.1+1.151x	0.86
	La	y = 1106.3+0.733x	0.83
1539-1551°C	Ce	y = -150.6+0.794x	0.99
	La	y = - 91.3+0.648x	0.99

x = amount added
y = amount recovered in the alloy

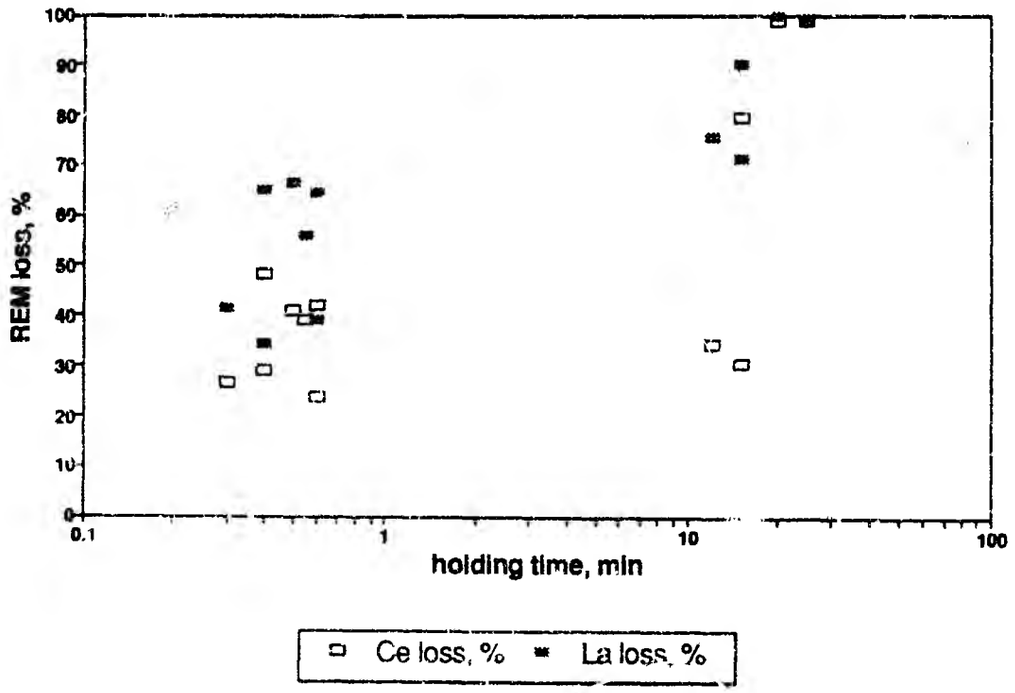

Figure 6.3. Change in the percentage loss of REM with holding time

Table 6.7 Recovery of Zr in the cast AISI310S ingots for different casting temperatures, holding times and additions of FeSiZr

Ingot no	Casting Temp.°C	Holding Time (min)	Addition wt%	Analyses wt%	Recovery %
ZR1	1625	10	Zr 0.16	0.04	24.5
ZR3	10	15	Zr 26	0.04	15.5
ZR4	161[illegible]	30	Zr 0.38	0.17	44.3
ZR8	1613	15	Zr 0.37	0.07	18.8
ZR9	1560	15	Zr 0.36	0.11	30.2
ZR10	1545	15	Zr 0 38	0.09	23.7
ZR13	1504	12	Zr 0.38	0.18	47.4
ZR15	1460	10	Zr 0.38	0.09	23.7
ZR18	1545	70secs	Zr 0.39	0 125	31.9
ZR19	1546	30secs	Zr 0.38	0.13	33.9
ZR20	1542	5	Zr 0.51	0 15	29.2
ZR21	1544	37secs	Zr 0.25	0.13	51.8
ZR22	1510	40secs	Zr 0.39	0.17	43.6
ZR30	154[illegible]	30secs	Zr 0.39	0.13	33.3
ZR31	1530	5	Zr 0.40	0.14	35.0

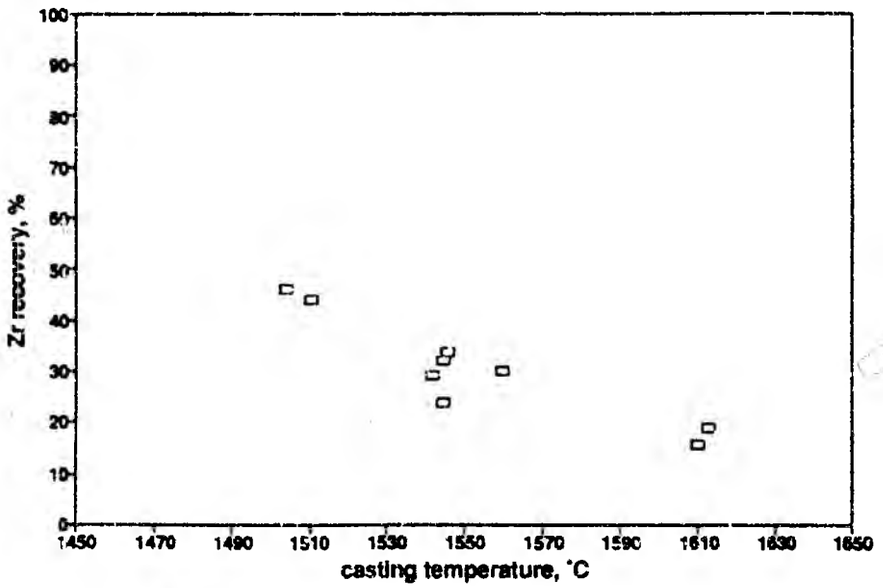

Figure 6.4 Effect of casting temperature on the recovery of Zr in the cast steel

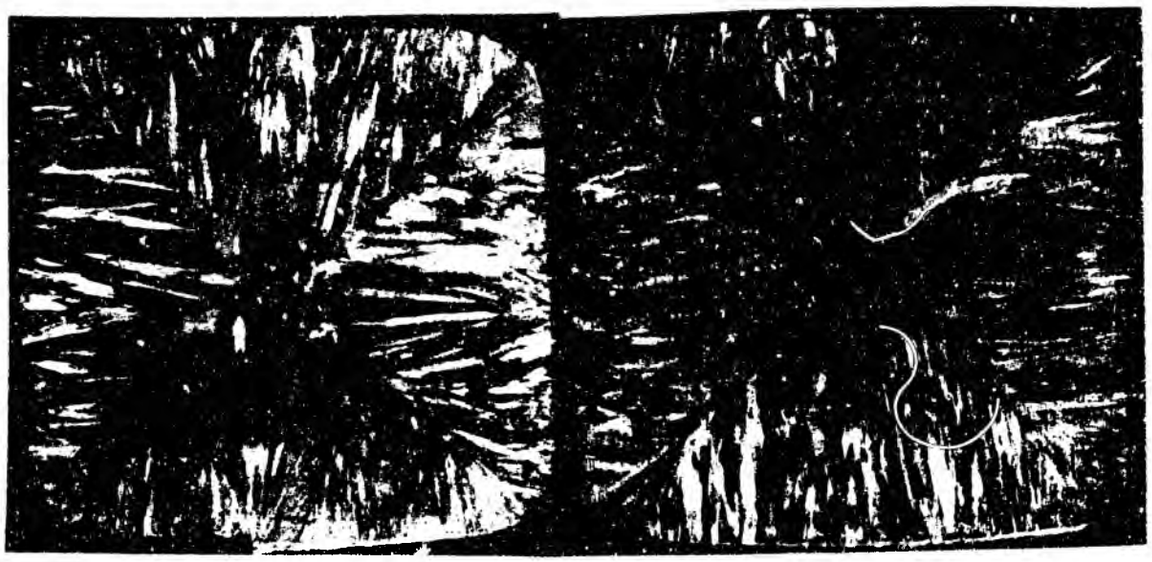

1545°C 1537°C



1526°C 1520°C

Figure 6.5. continued



1476°C 1455°C

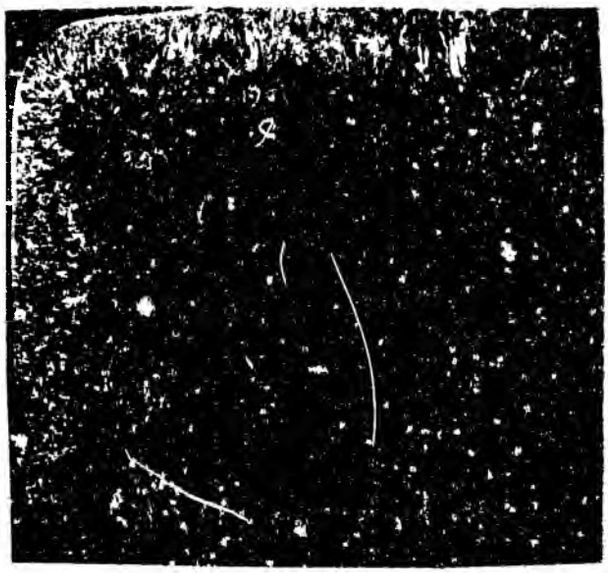

1436°C

Figure 6.5. continued

The most significant effect of misch metal addition was seen in the S and O_2 levels in the as-cast ingots. The sulphur concentration in the metal was, in most cases, less than half of that in the base metal. On average the sulphur concentration was down from 0.0063% to 0.0021%. Also, O_2 levels, on average, decreased by about 50% relative to the concentration in the base metal castings. There seems to be a relationship between the amount of O_2 picked up from the furnace atmosphere and the amount of misch metal added to the alloy. As can be seen from Figure 6.1, the effect of misch metal addition is especially significant at concentrations in the range 0.01 to 0.1 wt%. Above and below this range O_2 levels are higher but still low compared to those found in base metal castings.

Castings with FeSiZr additions also showed an average increase of 0.006% in C. Ni and Cr concentrations were found to be the same as those in the base metal castings. However there was a drop in S and O_2 levels compared to the base metal. The concentration of sulphur decreased from 0.0065% to 0.0040% whereas the oxygen concentration decreased from 288ppm to 182ppm.

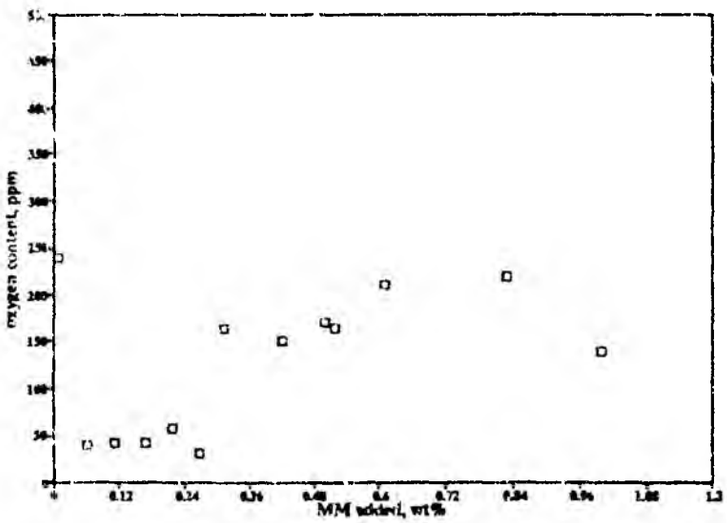

Figure 6.1 Change in O_2 concentration in AISI310S stainless steel with changes in the amount of misch metal addad

The most significant effect of misch metal addition was seen in the S and O_2 levels in the as-cast ingots. The sulphur concentration in the metal was, in most cases, less than half of that in the base metal. On average the sulphur concentration was down from 0.0063% to 0.0021%. Also, O_2 levels, on average, decreased by about 50% relative to the concentration in the base metal castings. There seems to be a relationship between the amount of O_2 picked up from the furnace atmosphere and the amount of misch metal added to the alloy. As can be seen from Figure 6.1, the effect of misch metal addition is especially significant at concentrations in the range 0.01 to 0.1 wt%. Above and below this range O_2 levels are higher but still low compared to those found in base metal castings.

Castings with FeSiZr additions also showed an average increase of 0.006% in C. Ni and Cr concentrations were found to be the same as those in the base metal castings. However there was a drop in S and O_2 levels compared to the base metal. The concentration of sulphur decreased from 0.0065% to 0.0040% whereas the oxygen concentration decreased from 288ppm to 182ppm.

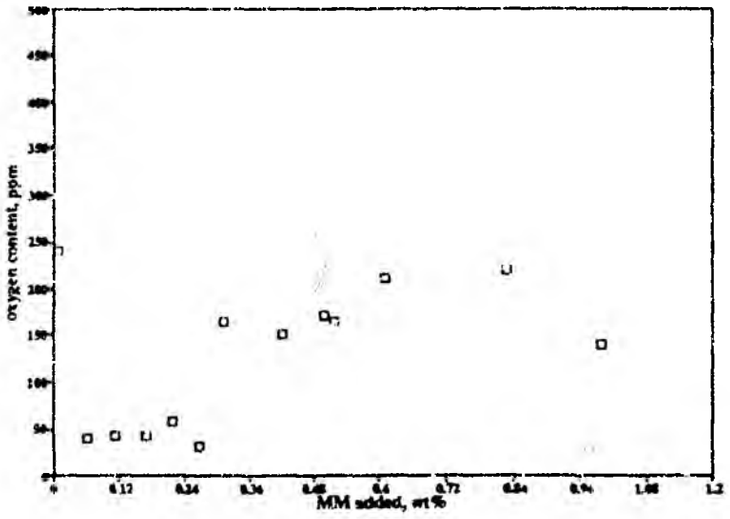

Figure 6.1 Change in the O_2 concentration in AISI310S stainless steel with changes in the amount of misch metal added

6.1.1 Recovery of Rare Earths in the Cast Metal

Table **6.5** shows the casting temperatures, holding times, the amounts of Ce and La added to castings as misch metal, the amounts recovered in castings and the calculated recovery of these two elements.

The results were grouped into three groups depending on holding time and casting temperature in order to minimize the effect of these two variables within groups. The concentrations of Ce and La recovered in the alloy were plotted against the amount added to the steel. The amount added was calculated from the composition of the misch metal used (Table **5.2**) and the amount of misch metal added to the alloy. Plot (**a**) in Figure **6.2** shows the change in recovered Ce and La with changes in the amounts of these elements added to the alloy for casting temperatures in the range of 1608 to 1637°C and a holding time of 15 mins. Plot (**b**) shows the same relationship for castings poured between 1539 and 1557°C after being held at temperature for 20 to 36s. Plot (**c**) is similar to (**a**) and (**b**) for castings poured between 1523 and 1549°C and holding times between 3 and 15 mins.

From Figure **6.2** it appears that the recovery of La is lower than that of Ce. The casting temperature differences of 30 to 40°C, within any one of the three groups mentioned above, do not appear to make a significant difference to the recovery of these elements. Within each group there was a strong correlation (Table **6.6**) between the amounts of added and recovered La and Ce.

The effect of holding time on the loss of rare earths is shown in Figure **6.3**. It is evident that there is a scatter in the data but it appears that the loss of Ce and La increased with increasing holding time.

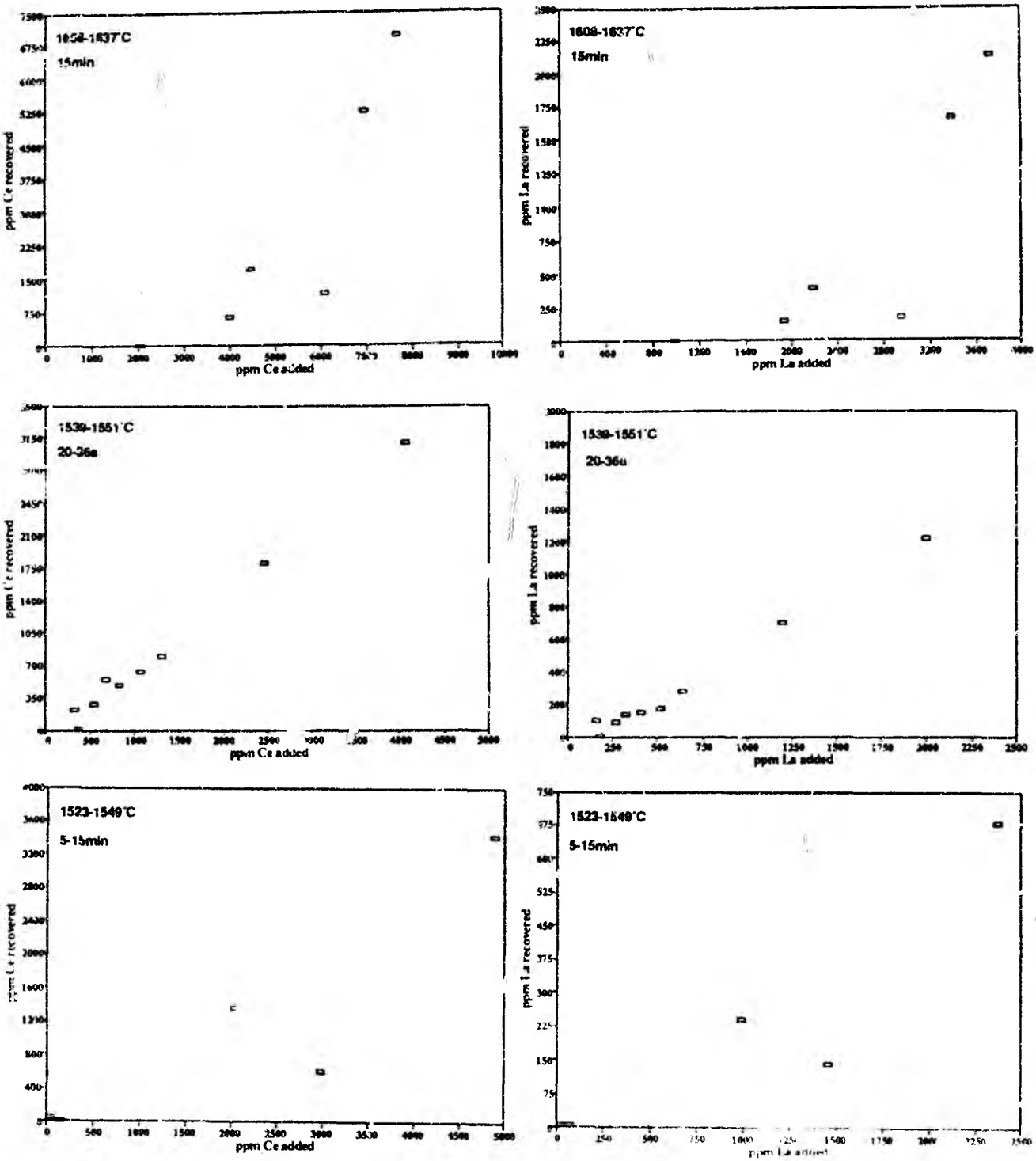

Figure 6.2 Changes in the recovery of Ce and La with changes in the amounts of misch metal added to the alloy for castings poured from three different temperature ranges

6.1.2 Recovery of Zr in the As-Cast Metal

The amount of Zr recovered in castings poured from different temperatures after different holding times and for different initial additions of FeSiZr is shown in Table 6.7. An analysis of this data indicated that there is no clearcut relationship between holding time and recovery of Zr in the metal. The amount of FeSiZr added to the metal also had no effect on the recovery of Zr. However as can be seen from Figure 6.4 casting temperature had a strong effect on the recovery of Zr in the cast metal. The recovery of Zr decreased with increasing casting temperature. The relationship between recovery and casting temperature was linear with the line of best fit giving a correlation coefficient of 0.92.

6.2 Ingot Macrostructure

6.2.1 Base Castings with no Additions

The transverse sections of conventional ingots cast from temperatures between 1436 to 161[illegible] are shown in Figure **6.5**. Changes in macrostructure with casting temperature for those ingots are given in Table **6.8** and in Figures **6.6** and **6.7**.

The columnar grain widths shown in these figures were measured at distances of 6mm and 14mm from the edges of the ingots and plotted against casting temperature separately. Regression analyses were carried out on each set of data and the following relationships were obtained.

$$\text{Grain width (at 6mm)} = 50.46 - 69.71*10^{-3}T + 24.28*10^{-6}T^2 \quad \ldots\ldots 6.1$$

correlation coefficient = 0.94

$$\text{Grain width (at 14mm)} = 53.67 - 73.20*10^{-3}T + 25.27*10^{-6}T^2 \quad \ldots\ldots 6.2$$

correlation coefficient = 0.91

T is the casting temperature in °C, and grain width is in mm.

The data points are plotted with their upper and lower 95% confidence limits to show the degree of scatter in different measurements in the same sample.

The re ationship between the columnar grain widths and the degree of superheat was analyzed and could be expressed by the equations:

$$\ln(\text{grain width at 6mm}) = 5.66 + 6.36*10^{-3}\Delta T \quad \ldots\ldots 6.3$$

correlation coefficient = 0.91 and,

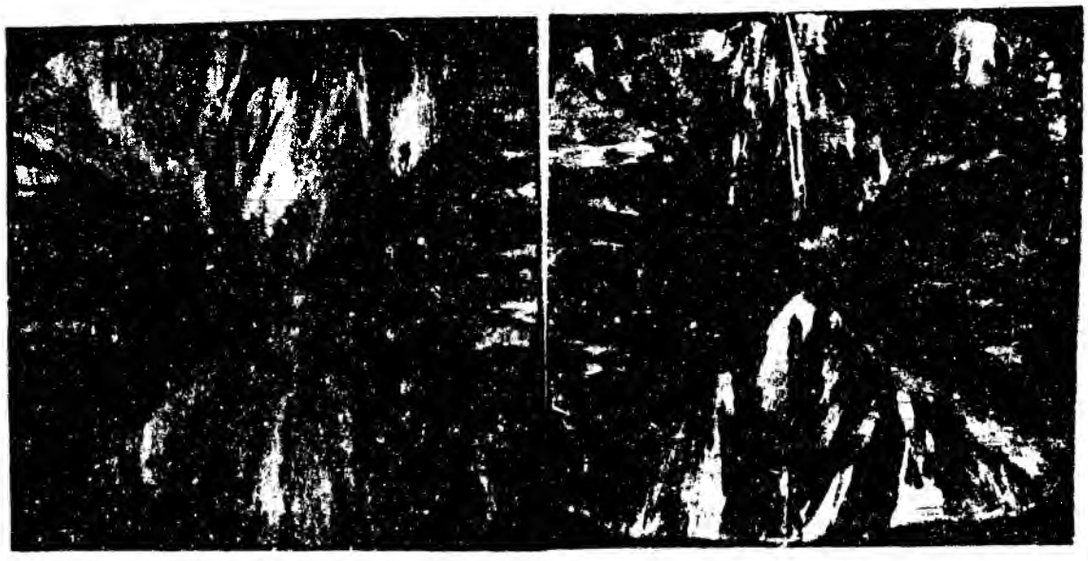

1610°C 1600°C



1585°C 1564°C

Figure 6.5 Macrostructures of ingots with no addition cast from different temperatures



1510°C 1502°C



1496°C 1493°C

Figure 6.5. continued

Table 6.8 Change in macrostructure with casting temperature for ingots with no addition.

Ingot no	Casting Temp. °C	Columnar grain width (mm) with 95% confidence limits measured at 6 and 14mm from the edge		Grain width ratio gw at 14mm/ gw at 6mm	Equiaxed zone %
		6mm	14mm		
B1	1610	1.140±0.119	1.330±0.05	1.17	0
B2	1600	1.055±0.145	1.134±0.178	1.07	3
B3	1585	1.047±0.092	1.204±0.069	1.22	0
B4	1564	0.844±0.062	1.030±0.030	1.15	4
B5	1545	0.666±0.082	0.920±0.060	1.38	3
B6	1537	0.711±0.107	0.975±0.129	1.37	4
B7	1526	0.551±0.059	0.704±0.054	1.28	7
B8	1520	0.517±0.062	0.710±0.096	1.37	10
B9	1510	0.496±0.059	0.672±0.072	1.35	13
B10	1502	0.456±0.046	0.647±0.013	1.42	8
B11	1496	0.511±0.049	0.669±0.092	1.31	7
B12	1493	0.749±0.091	0.920±0.012	1.23	13
B13	1476	0.434±0.042	0.666±0.066	1.53	23
B14	1455	0.482±0.049	-	-	50
B15	1436	0.365±0.051	-	-	77

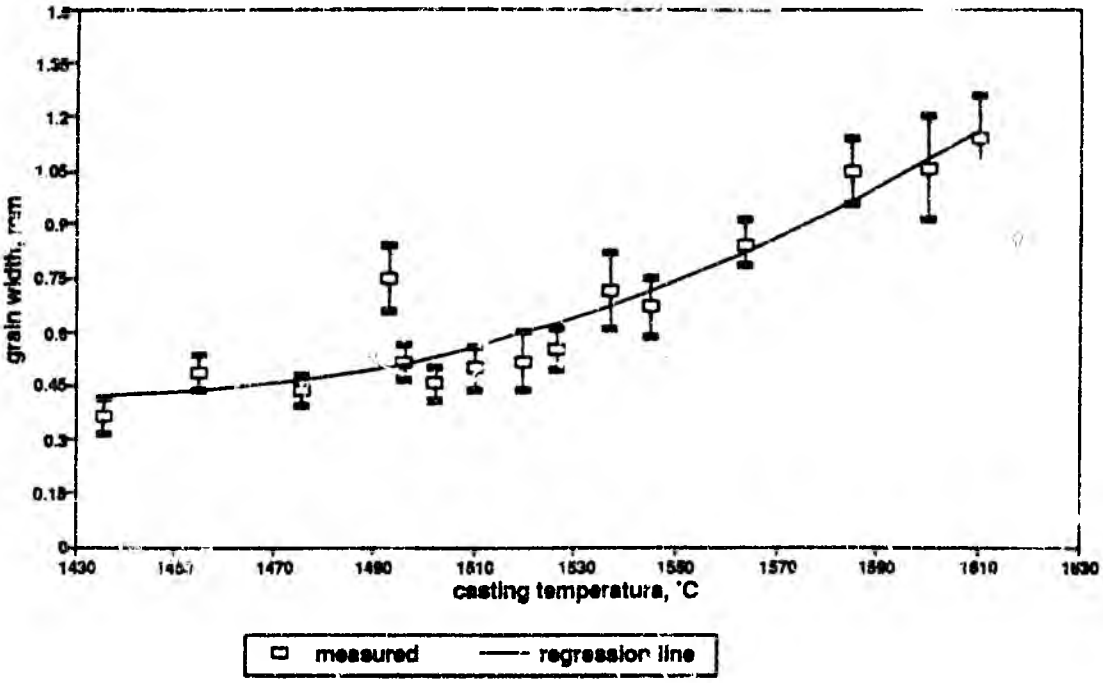

Figure 6.6 Change in grain width measured at 6mm from the edge for ingots without additions

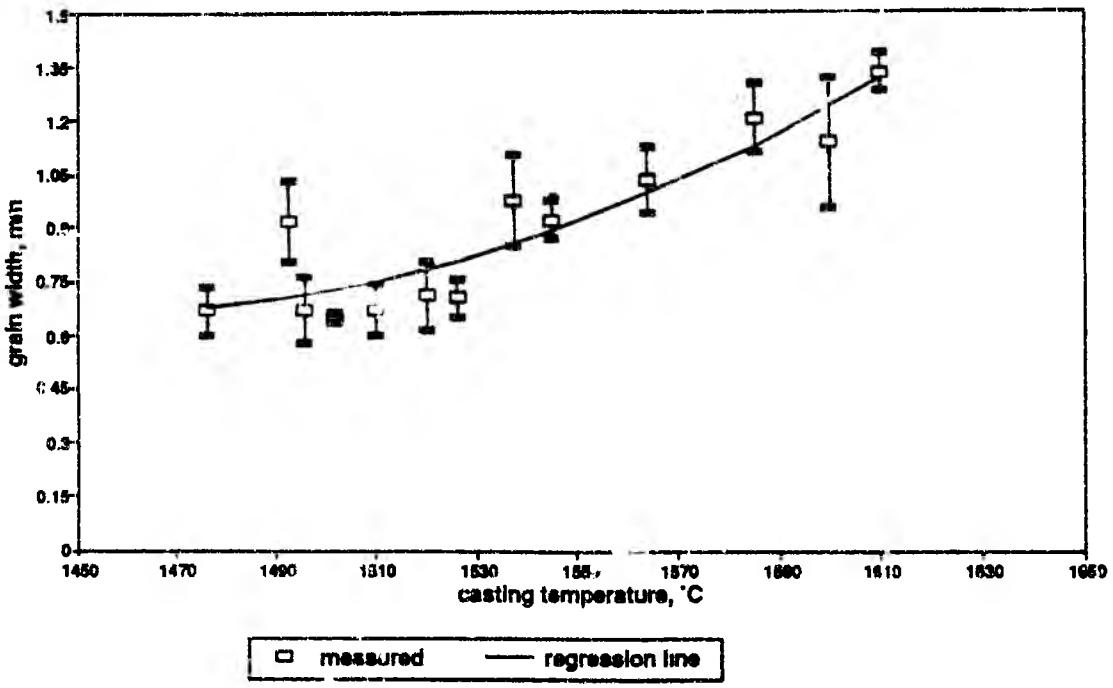

Figure 6.7 Change in grain width measured at 14mm from the edge for ingots without additions

$$\ln(\text{grain width at 14mm}) = 6.05 + 5.25*10^{-3}\Delta T \quad \ldots\ldots\ldots \quad 6.4$$

correlation coefficient = 0.88.

grain width is in μm, and ΔT is superheat in °C.

The change in grain width at 6mm and 14mm with changing degree of superheat and the regression curves are shown in Figure **6.8**. This figure demonstrates that the slope of the plot of grain width against superheat is a function of the distance from the edge of the ingot. As can be seen, the two lines approach each other as the superheat increases.

It was evident that as the casting temperature decreased the grain size of the columnar zone decreased and the volume of the equiaxed zone increased considerably. At casting temperatures below about 1450°C corresponding to a superheat of about 50°C the equiaxed zone started to dominate the macrostructure as can be seen from Figure **6.5**.

The development of the equiaxed zone with changing casting temperature of AISI310S base metal ingots is shown in Figure **6.9**. This graph clearly shows that at pouring temperatures below 1500°C (<100°C superheat), the proportion of equiaxed zone increased rapidly with decreasing casting temperature dominating the structure at pouring temperatures of about 1450°C. The proportion of the equiaxed zone reached 77% at a casting temperature of 1436°C. Regression analysis gave a fourth degree polynomial expressing the change in the proportion of the % equiaxed zone with changing casting temperature. The polynomial was as follows.

$$1-\frac{\%EquiaxedZone}{100} = 320.4-4622.7\left(\frac{10^3}{T}\right)^2+9572.0\left(\frac{10^3}{T}\right)^3-5574.6\left(\frac{10^3}{T}\right)^4 \quad \ldots 6.5$$

correlation coefficient = 0.991

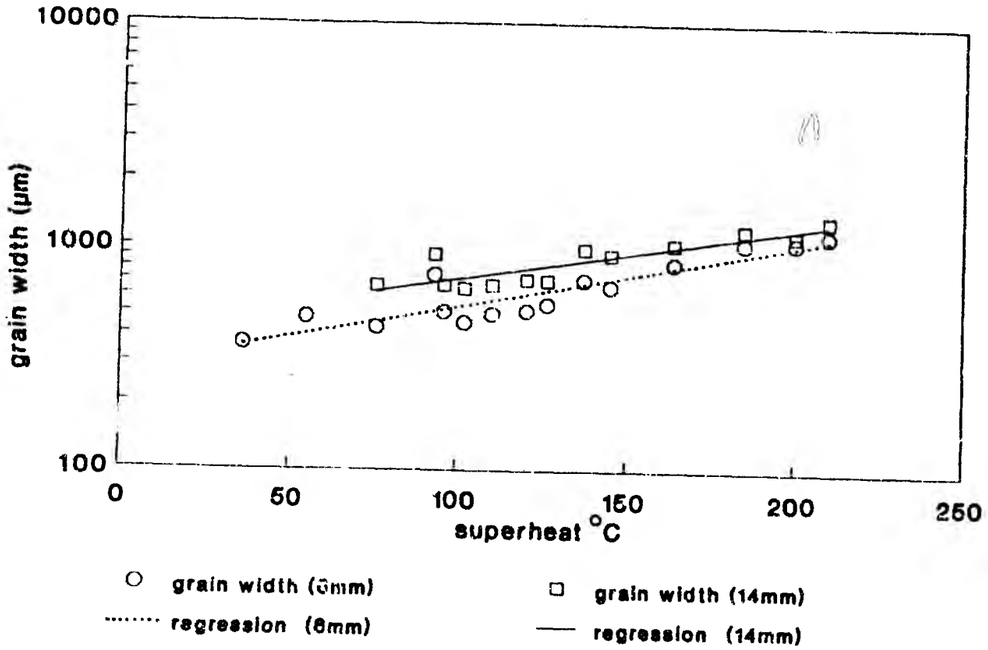

Figure 6.8 Plots of grain width at 6 and 14 mm from the edge of ingots against superheat

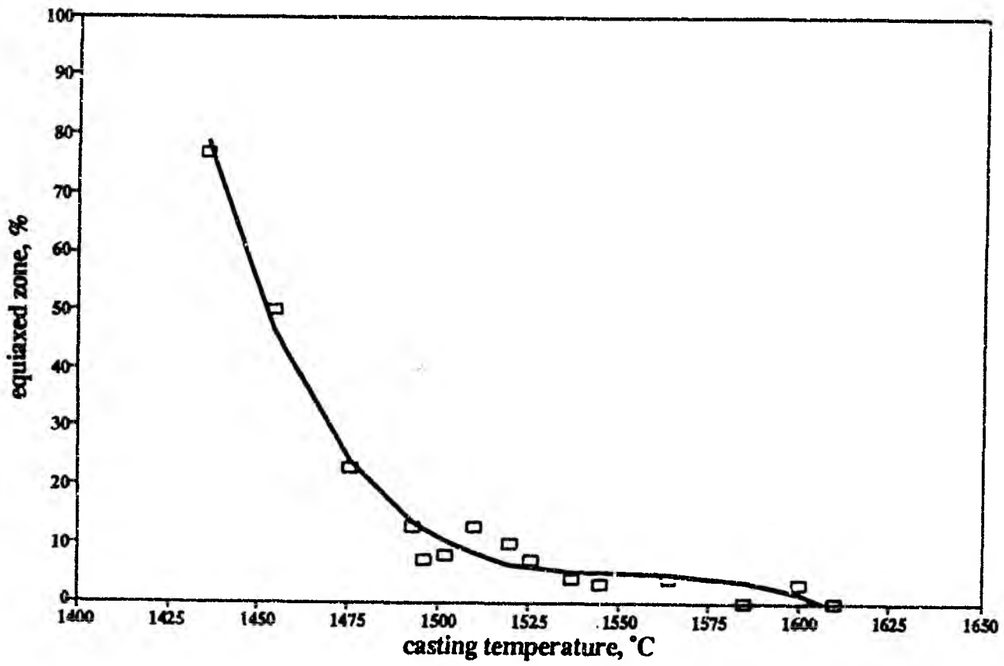

Figure 6.9 Development of the equiaxed zone with changing casting temperature for AISI310S steel

The left hand side of the equation gives the proportion of the columnar zone, T is the casting temperature in °C.

Second and third degree polynomials were also found to fit this data but had correlation coefficients of 0.964 and 0.966 respectively which are lower than that of the fourth degree polynomial given above. They also failed to describe the results obtained at high temperatures adequately, both showing a positive slope in the temperature range 1550 - 1610°C. Within the temperature range of 1436°C to 1610°C the above equation described the development of the equiaxed zone with casting temperature better than the second and third degree polynomials.

A relationship was also established between the proportion of equiaxed zone and the degree of superheat as follows.

$$\%EquiaxedZone = 170.7 - 328.2 * \left(\frac{T}{100}\right) + 212.4 * \left(\frac{T}{100}\right)^2 - 45.2 * \left(\frac{T}{10}\right)^3 \quad (6.6)$$

correlation coefficient = 0.99. T is the temperature in °C.

This regression equation and the experimental data are plotted in Figure **6.10.** It can be seen from this graph that the proportion of equiaxed zone decreased rapidly as the degree of superheat increased from 36°C to about 100°C. A small equiaxed zone, however, persisted with further increase in superheat. The proportion of the equiaxed zone was about 5% for superheat values of about 160 to 170°C.

From equation **6.6** it was possible to calculate the degree of superheat required to obtain 100% equiaxed structure. This was 25°C above the liquidus temperature.

Equations **6.5** and **6.6** made it possible to calculate the degree of grain refinement in ingots with REM, and Zr additions cast from any temperature.

The degree of grain refinement or percentage change in columnar grain width was calculated on the basis of what the grain size would have been had the ingots been cast from the same temperature without additions. The calculation was performed by using the following relationship.

$$\%\text{Change in grain width} = \left[\frac{(g.w.\text{with ad.}) - (g.w.\text{with no ad.})}{g.w.\text{with no ad.}}\right]_{T_i} \times 100 \quad ..6.7$$

where **g.w.** is grain width, **ad.** is addition, and T_i is the temperature at which pouring was carried out for that specific ingot with addition.

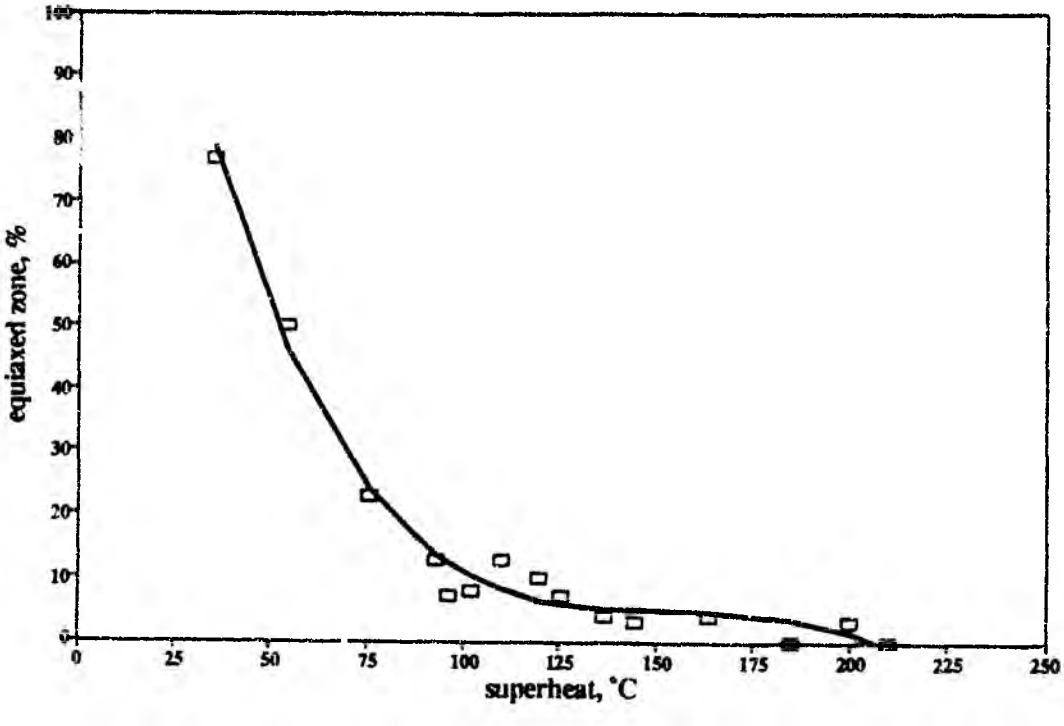

Figure 6.10 **Influence of degree of superheat on the proportion of equiaxed zone**

The grain size of an ingot without addition poured at temperature T_i is calculated using Equations **6.1** and **6.2** and subtracted from the measured grain size with addition. The value obtained is divided by the calculated grain size with no addition and multiplied by 100 to find the percent change in grain size.

The grain width measured at a distance of 14mm from the edge was divided by the grain width measured at 6mm from the edge for each ingot and these data are given in Table **6.8**. When the grain width ratios for base castings are plotted against their corresponding casting temperatures as given in Figure **6.11**, it is seen that as the pouring temperature increased, the grain width ratio decreased. This means that, in ingots cast with low superheat the width of columnar grains increased as they grew towards the centre of the ingot. The width of grains in ingots cast with high superheat did not change significantly as these grew towards the centre of the ingot. Expressed simply, these observations mean that the nucleation and growth behaviour of columnar grains depended on the degree of superheat.The significance of this will be discussed in the next chapter.

When the grain width ratio was plotted against the grain widths measured at 14mm, it could be seen that as the grain widths decreased, the grain width ratio increased (Figure **6.12**).

The grain width ratio obtained with additions and their comparison with those of base metal castings will be given in sections **6.2.2** and **6.2.3**.

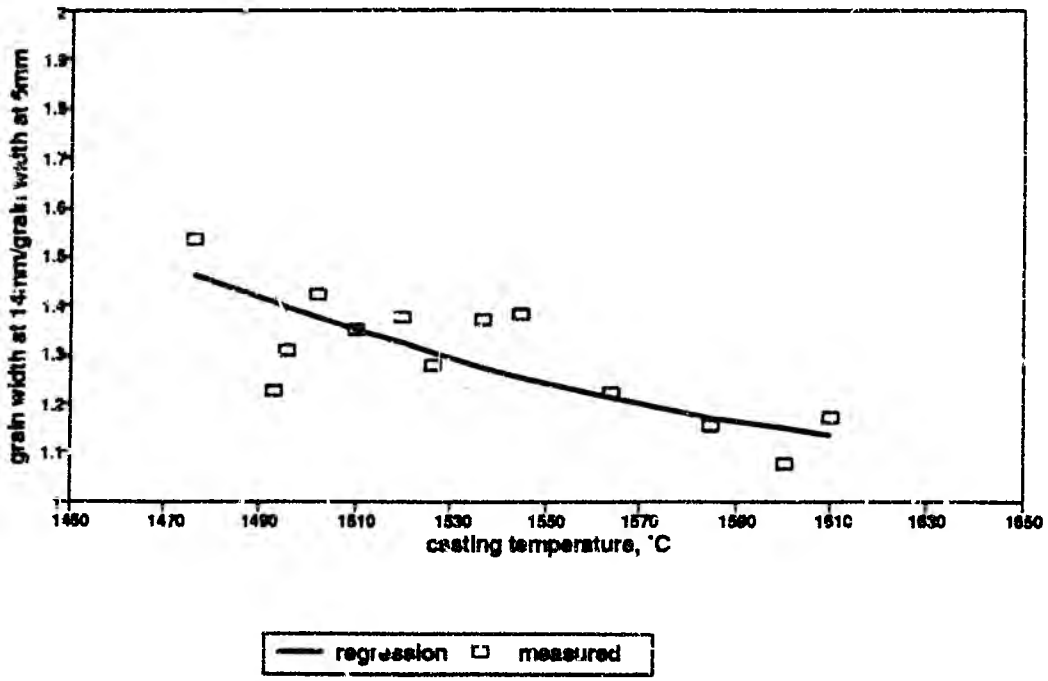

Figure 6.11 Change in grain width ratio (gw_{14}/gw_6) with casting temperature

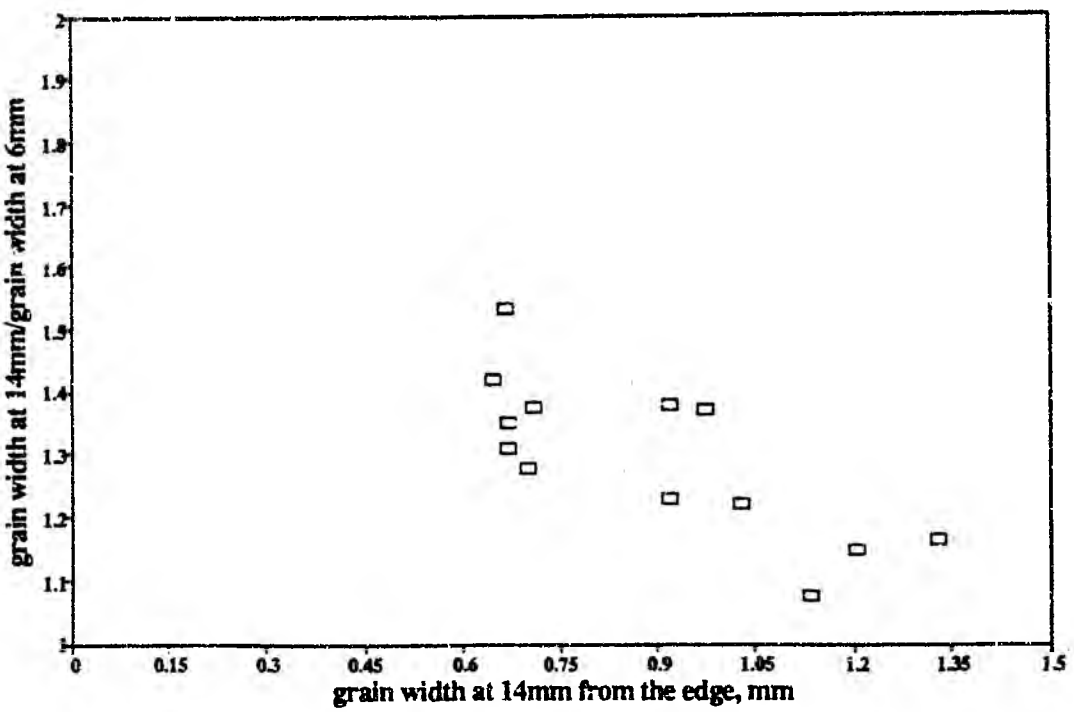

Figure 6.12 Change in grain width ratio with grain width at 14mm

6.2.2 Castings with Misch Metal Additions

Transverse sections of selected ingots containing misch metal are shown in Figure **6.13**. The results of the macrostructural evaluation of these ingots are shown in Table **6.9** from which it can be seen that grain widths were reduced by up to 56% with small additions of misch metal.

The data in Table **6.9** were classified into three groups with respect to casting temperature in order to facilitate analysis of the influence of misch metal on the macrostructure of ingots. A high casting temperature range of 1608 to 1637°C, a medium temperature range of 1523 to 1551°C and a low temperature range of 1490 to 1510°C were identified. Changes in grain widths measured at 6 and 14mm from the edge are plotted in Figures **6.14** to **6.19** against the amount of added misch metal and the amounts of residual Ce and La in the alloy.

The trend in Figure **6.14(a)** suggests that a continuous increase in grain refinement would occur with increasing amount of added misch metal for casting temperatures between 1608 and 1637°C. Figure **6.14(b)** and **(c)** shows that grain refinement increased with increasing residual concentrations of Ce and La up to certain limits. Beyond 0.2% of residual Ce and 0.05% of residual La no significant refining of the grain size was obtained.

For casting temperatures between 1523 and 1551°C very small additions of misch metal and very low concentrations of residual Ce and La had a strong grain refining effect on the alloy(Figure **6.15(a)** and **(b)**). Further increases in the amount of misch metal added and in the residual concentrations of Ce and La appeared, in general, not to have a significant effect on grain width.

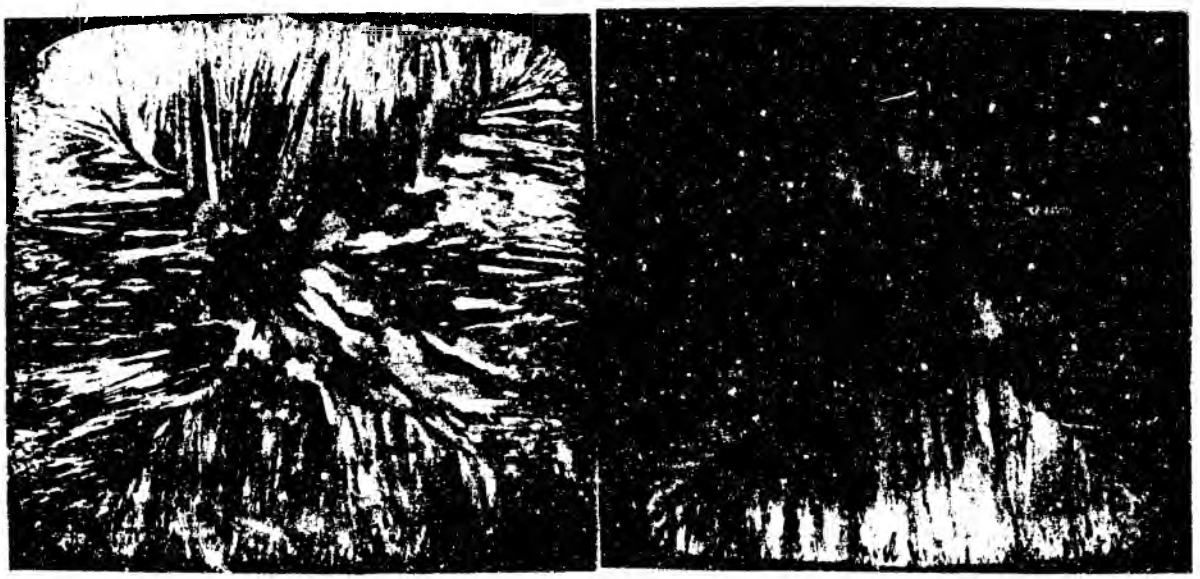

MM7 (0.52wt%) 1535°C

MM8 (0.31wt%) 1539°C



MM9 (1.0wt%) 1549°C

MM10 (0.42wt%) 1523°C

Figure 6.13 Macrostructures of ingots cast from different temperatures with additions of misch metal



MM12 (0.61wt%) 1525°C

MM13 (0.83wt%) 1545°C

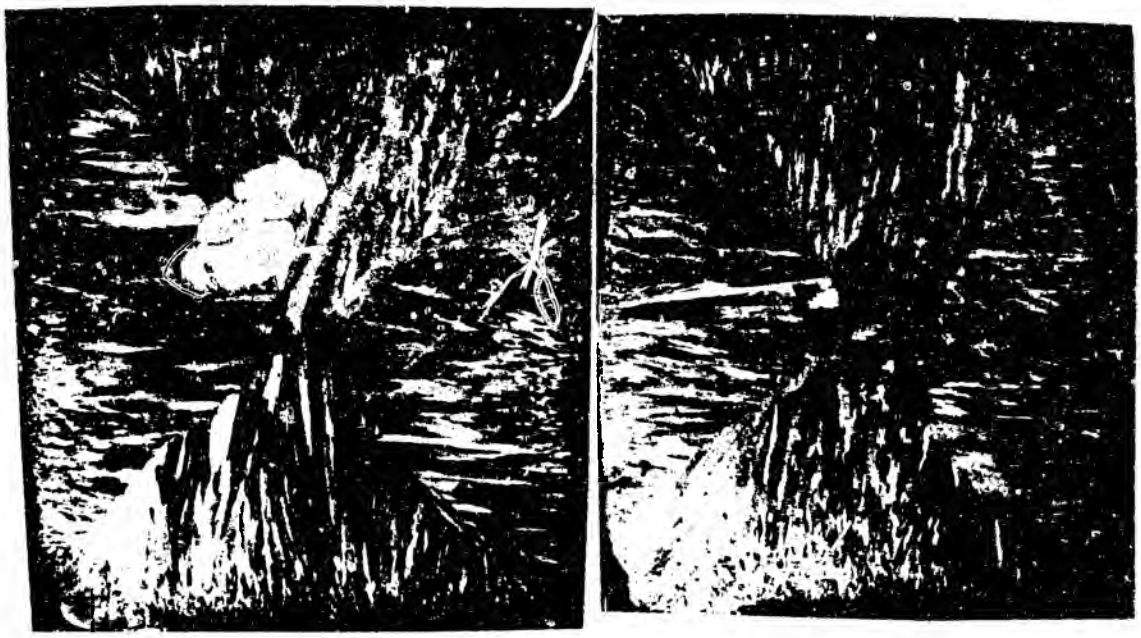

MM14 (0.064wt%) 1550°C

MM15 (0.11wt%) 1550°C

Figure 6.13 continued

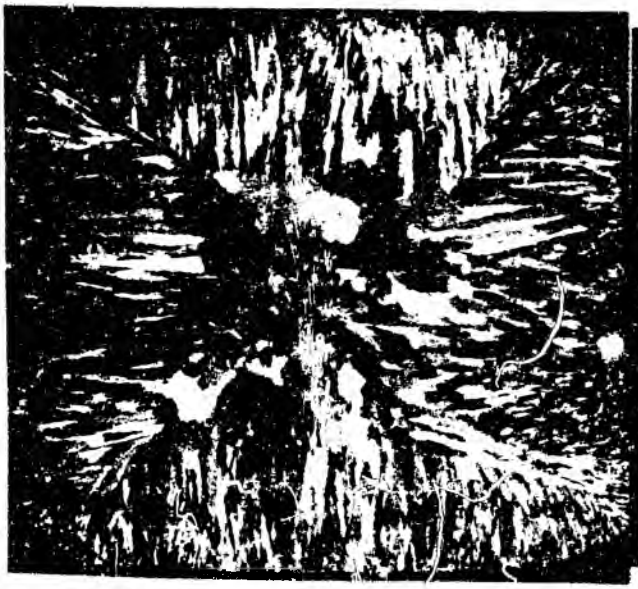

MM16 (0.168wt%) 1551°C



MM17 (0.216wt%) 1547°C



MM18 (0.265wt%) 1545°C



MM19 (0.010wt%) 1544°C

Figure 6.13 continued

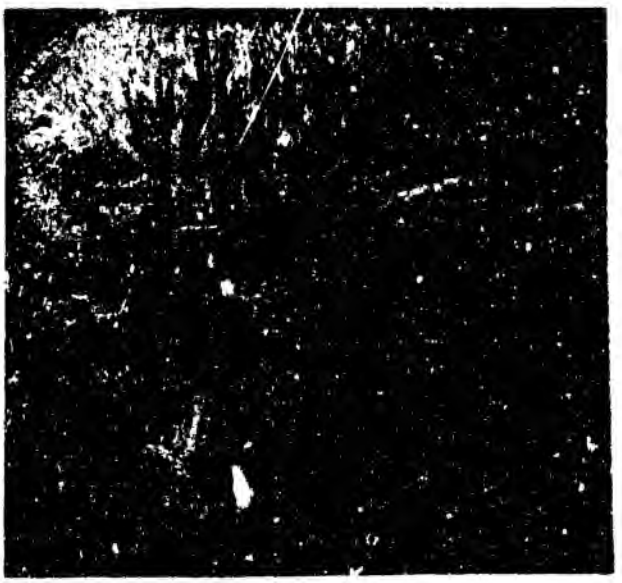

MM20 (0.030wt%) 1543°C



MM21 (0.075wt%) 1539°C

Figure 6.13 continued

Table 6.9 Macrostructure measurements on ingots with misch metal additions

Ingot no	Addition wt%	Casting temp.°C	Residual concentrations of rare earths in ingots (ppm)		Columnar grain width (mm) with 95% confidence limits measured at 6 and 14mm from the edge		Change in columnar grain width %		Grain width ratio gw 14mm/ gw 6mm	Equiaxed zone %
			Ce	La	6mm	14mm	6mm	14mm		
MM1	MM 0.42	1617	7.1	0.6	0.962 ±0.148	1.168 ±0.151	21.1	14.9	1.21	3
MM2	MM 0.82	1627	645	142	0.941 ±0.067	1.088 ±0.110	28.2	25.8	1.16	6
MM3	MM 1.25	1630	1172	176	0.835 ±0.094	0.943 ±0.086	37.8	36.8	1 13	15
MM4	MM 1.43	1608	5260	1856	0.606 ±0.050	0.721 ±0.096	46.9	44.5	1.19	0
MM6	MM 1.57	1624	6935	2127	0.568 ±0.053	0.701 ±0.109	35.7	51.1	1.23	9
MM6	MM 0.92	1637	1737	394	0.816 ±0.096	0.787 ±0.118	56.2	49.3	1.28	5
MM7	MM 0.52	1535	32.7	6.8	0.377 ±0.016	0.617 ±0.086	43.0	27.0	1.64	10
MM8	MM 0.31	1539	17.25	2.25	0.530 ±0.063	0.695 ±0.061	22.1	19.4	1.31	10
MM9	MM 1.00	1549	3406	679	0.350 ±0.026	0.476 ±0.072	52.3	47.6	1.36	8
MM10	MM 0.42	1523	1349	241	0.345 ±0.043	0.516 ±0.078	43.1	34.9	1.50	12
MM11	MM 0.50	1550	1800	703	0.336 ±0.051	0.493 ±0.074	54.5	46.2	1.47	4
MM12	MM 0.61	1525	608	144	0.364 ±0.049	0.568 ±0.043	40.8	29.3	1.56	4
MM13	MM 0.83	1545	3100	1215	0.311 ±0.049	0.456 ±0.064	56.3	48.8	1.47	0
MM14	MM 0.061	1550	223	101	0.391 ±0.048	0.685 ±0.088	47.1	25.2	1.75	0
MM15	MM 0.11	1550	280	92	0.345 ±0.019	0.487 ±0.069	53.3	47.4	1.39	4
MM16	MM 0.168	1551	478	143	0.370 ±0.033	0.530 ±0.032	50.3	42.5	1.43	23
MM17	MM 0.218	1547	624	175	0.353 ±0.055	0.505 ±0.045	51.1	44.0	1.43	10
MM18	MM 0.265	1545	790	281	0.323 ±0.027	0.441 ±0.063	54.6	50.5	1.36	8

Table 6.3 continued

Ingot no	Addition wt%	Casting temp.°C	Residual concentrations of rare earths in ingots (ppm)		Columnar grain width (mm) with 95% confidence limits measured at 6 and 14mm from the edge		Change in columnar grain width %		Grain width ratio gw 14mm/ gw 6mm	Equiaxed zone %
			Ce	La	6mm	14mm	6mm	14mm		
MM19	MM 0.010	1544	45	8.9	0.351 ±0.042	0.493 ±0.042	50.3	44.4	1.40	12
MM20	MM 0.030		5	8	0.355 ±0.041	0.485 ±0.050	49.4	45.0	1.37	10
MM21	MM 0.075	1539	5	5	0.464 ±0.049	0.553 ±0.054	31.8	36.9	1.19	6
MM22	MM 0.135	1509	554	137	0.440 ±0.03[illegible]	0.572 ±0.043	20.3	23.8	1.30	8
MM23	MM 0.080	1504	245	50	0.429 ±0.037	0.549 ±0.024	19.8	36.3	1.28	10
MM24	MM 0.032	1491			0.380 ±0.044	0.525 ±0.070	23.4	25.2	1.38	10
MM25	MM 0.045	1484			0.417 ±0.018	0.597 ±0.062	12.8	13.2	1.43	13
MM26	MM 0.090	1496			0.407 ±0.017	0.600 ±0.082	15.8	13.2	1.47	8
MM27	MM 0.060	1490			0.481 ±0.031	0.571 ±0.047	2.5	18.4	1.19	3
MM28	MM 0.052	1489			0.400 ±0.053	0.531 ±0.048	16.8	23.9	1.33	10

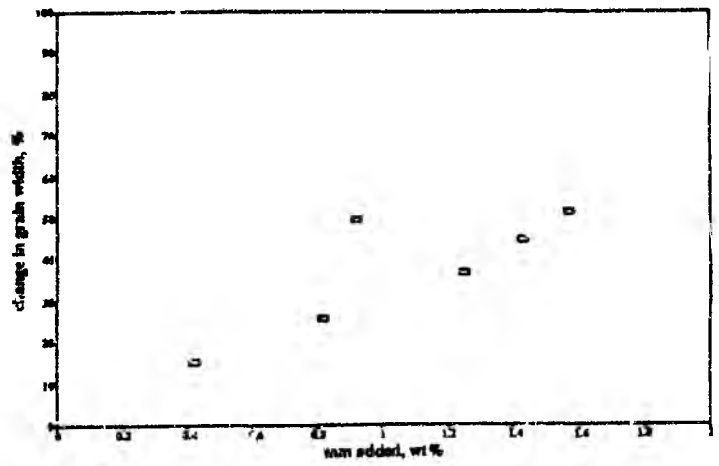

(a)

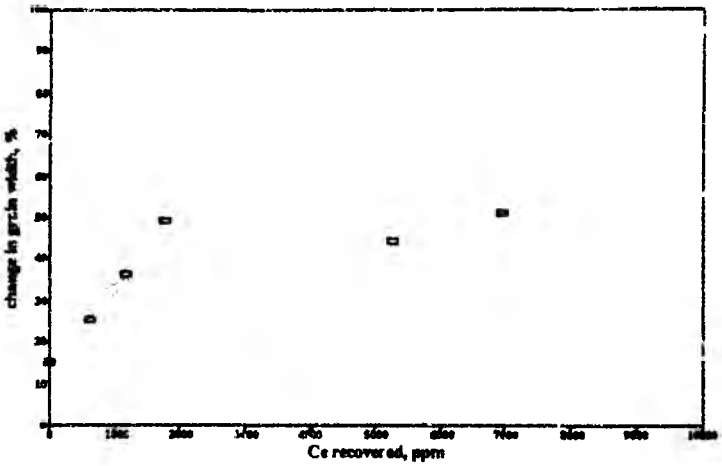

(b)

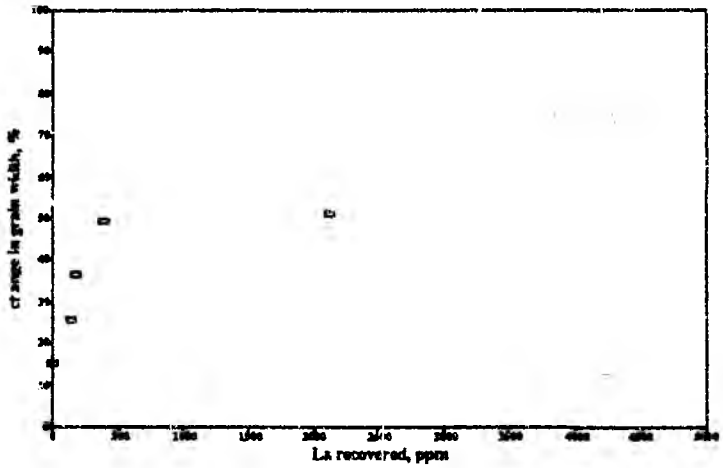

(c)

Figure 6.14 Change in grain width measured at 14 mm with (a) misch metal addition, (b) ppm recovered Ce and (c) ppm recovered La for ingots cast between 1608 and 1637°C

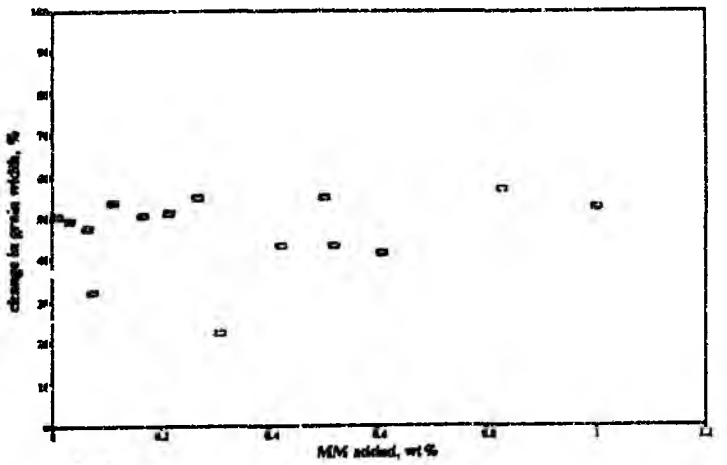

(a)

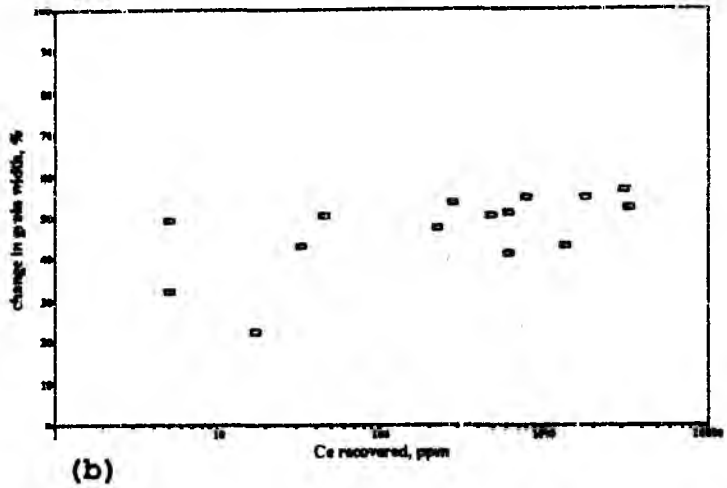

(b)

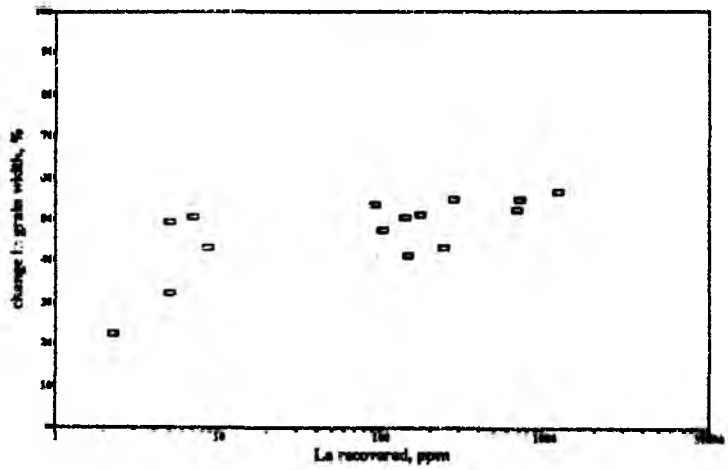

(c)

Figure 6.15 Change in grain width measured at 6 mm with (a) mischmetal addition, (b) ppm of recovered Ce and (c) ppm of recovered La for ingots cast between 1523 and 1551°C

In the casting temperature range of 1490 to 1510°C the addition of misch metal had little effect on grain width (Figure **6.16**). A maximum grain refinement of 25% was obtained with an addition of 0.03% misch metal.

When the grain width ratios calculated for ingots containing misch metal were plotted against casting temperature (Figure **6.17**) it could be seen that the data points for these ingots deviated significantly from the regression line calculated for the base metal castings, especially for ingots cast between 1525 and 1550°C.

These data were analyzed against various other parameters obtained from ingots cast in the three temperature ranges mentioned earlier. It was found that the positive deviation was strongest in the concentration ranges of 30 to 300 ppm for cerium and 10 to 200 ppm for lanthanum in the casting temperature range of 1535 to 1551°C. (Figures **6.18(a)** and **(b)**). When these points were plotted against columnar grain widths measured at 6 and 14mm (Figure **6.19**), it could be seen that as the grain width increased, the grain width ratios tended to increase as well. This trend is the opposite of that found with base metal castings.

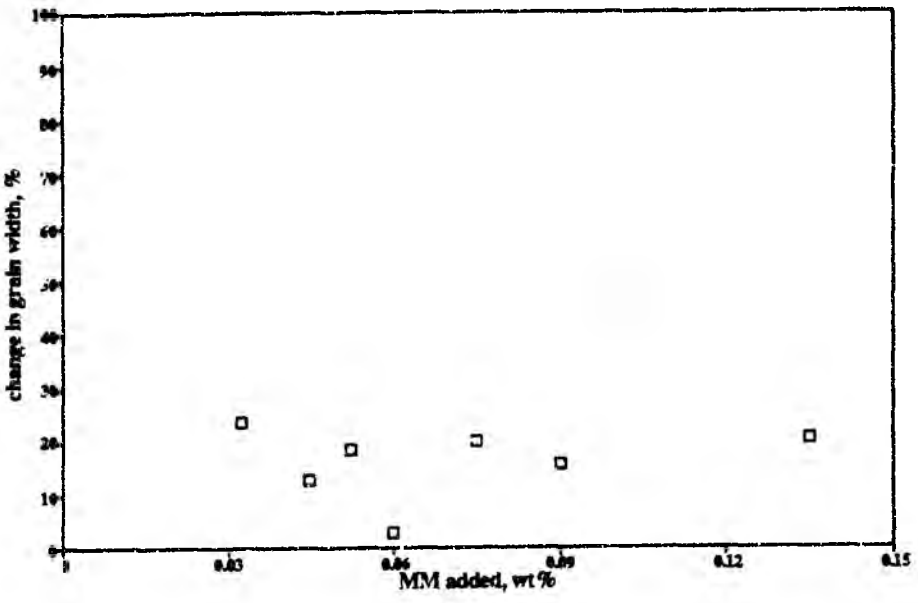

Figure 6.16 Change in grain width measured at 6mm from the edge for ingots with misch metal addition cast from 1490-1510°C

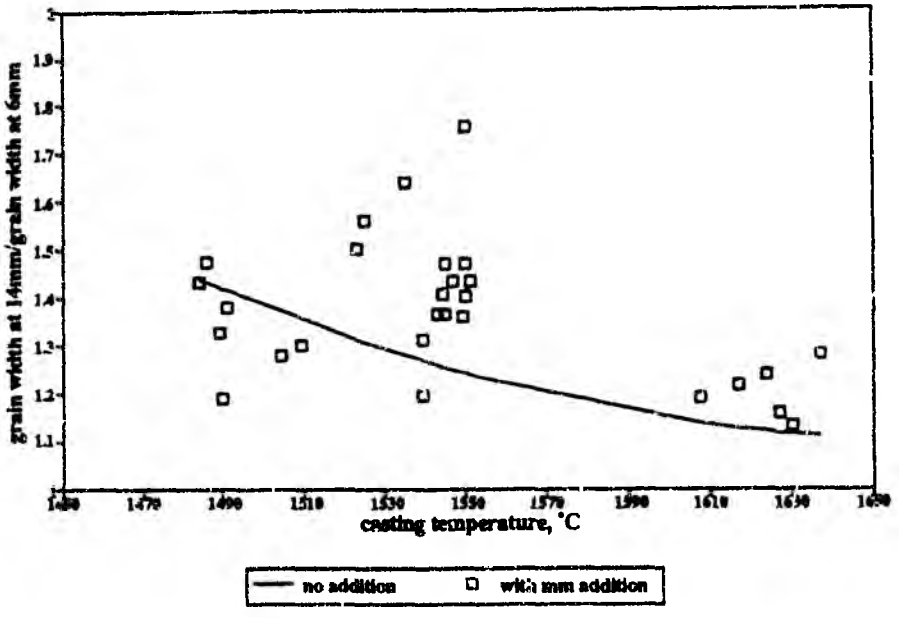

Figure 6.17 Measured grain width ratios for ingots containing misch metal and calculated regression points for base metal castings poured between 1480 and 1636°C

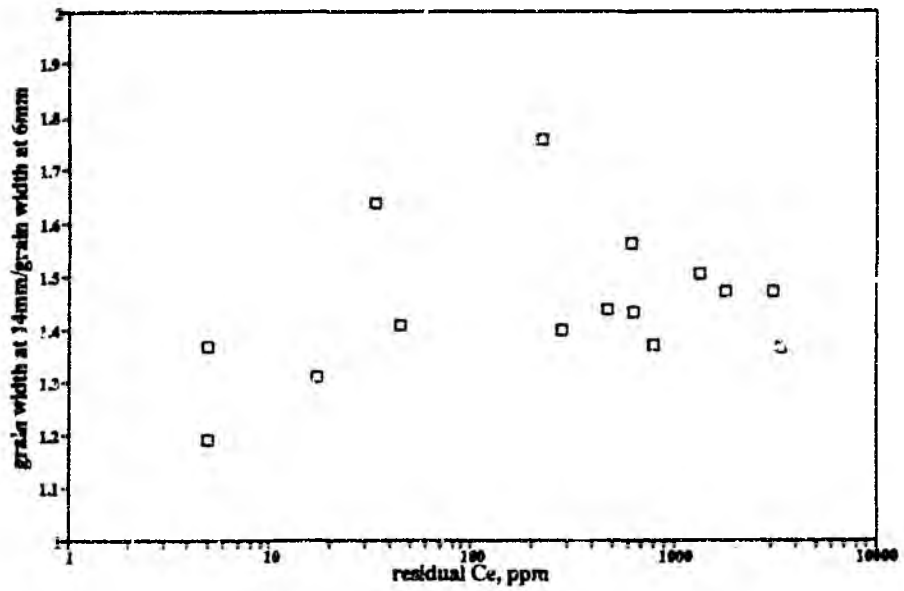

(a)

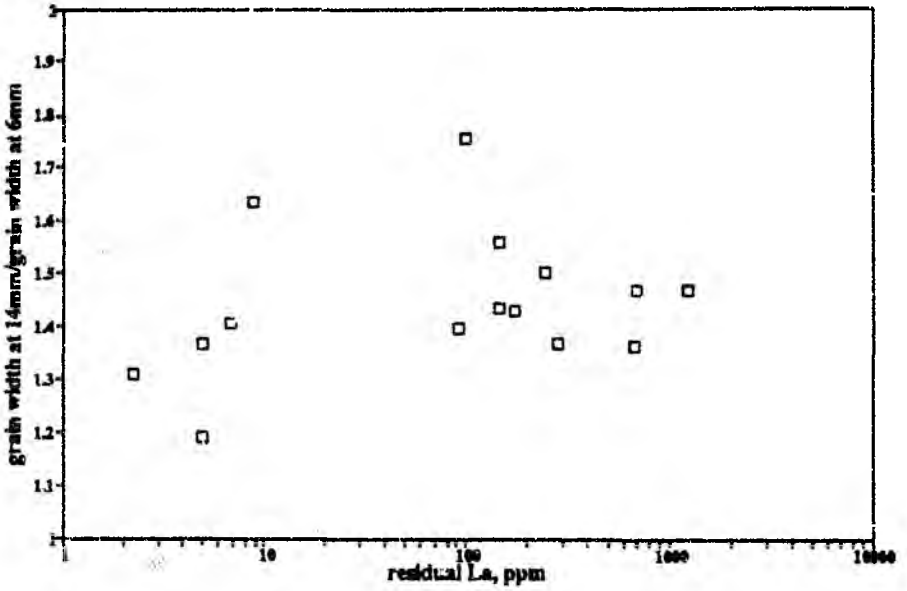

(b)

Figure 6.18 Change in grain width ratio with (a) recovered Ce and (b) recovered La for ingots cast between 1535 and 1551°C

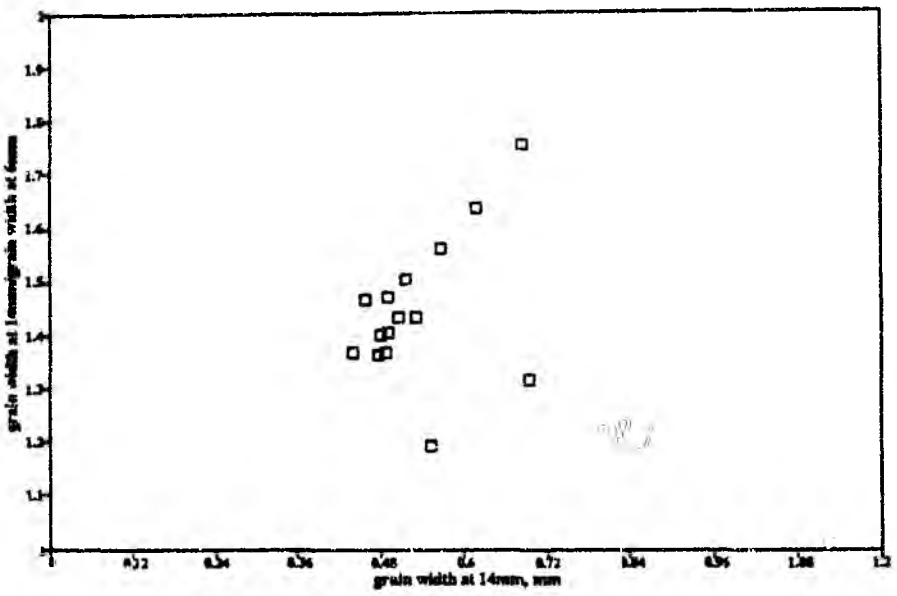

Figure 6.19 Change in grain width ratio as a function of grain width at 14mm from the edge for ingots containing misch metal and cast between 1535 and 1551°C

6.2.3 Castings with Additions of FeSiZr

Transverse sections of selected ingots cast with additions of FeSiZr are shown in Figure **6.20**. The results of a macrostructural evaluation of these ingots are given in Table **6.10**. As can be seen, aluminium and/or misch metal were added to some of the selected ingots to examine their combined effect on the macrostructure. For this purpose special emphasis was given to aluminium which was added in varying amounts at different casting temperatures.

Figure **6.21** shows the change in grain width with casting temperature. It can be seen that Zr is especially effective in the casting temperature range of 1540 - 1560°C. It seems unlikely that grain refinement can be obtained for casting temperatures below 1510°C. It should be noted that in Figure **6.21** no distinction is made between ingots with aluminium additions and ingots which contained only zirconium. Only the amount of Zr addition was kept constant. At casting temperatures above 1600°C, there appears to be some further potential for grain refining with zirconium but it is not as high as that obtained for casting temperatures of 1540 to 1560°C. It can be seen from Table **6.10** that aluminium and misch metal did not restore the grain refining effect of zirconium at lower casting temperatures, (see castings ZR22, ZR27, ZR28 and ZR29). Aluminium does not appear to contribute to the grain refining potential of zirconium (see ZR10, ZR11, ZR18, ZR19, ZR20, ZR21).

When the grain refinement values for these ingots were plotted against Zr addition in the temperature ranges 1481-1513°C and 1532 - 1625°C (Figures **6.22(a)** and **(b)**), it became apparent that grain refinement was a function of the amount of Zr added as well as of the casting temperature.



ZR8 (Zr: 0.372wt%) 1613°C ZR9 (Zr: 0.365wt%) 1560°C



ZR10 (Zr: 0.380wt%) 1545°C ZR11 (Zr: 0.391wt%) 1532°C

Figure 6.20 Macrostructures of ingots cast from different temperatures with FeSiZr additions



ZR23 (Zr: 0.100wt%) 1481°C ZR13 (Zr: 0.391wt%) 1504°C

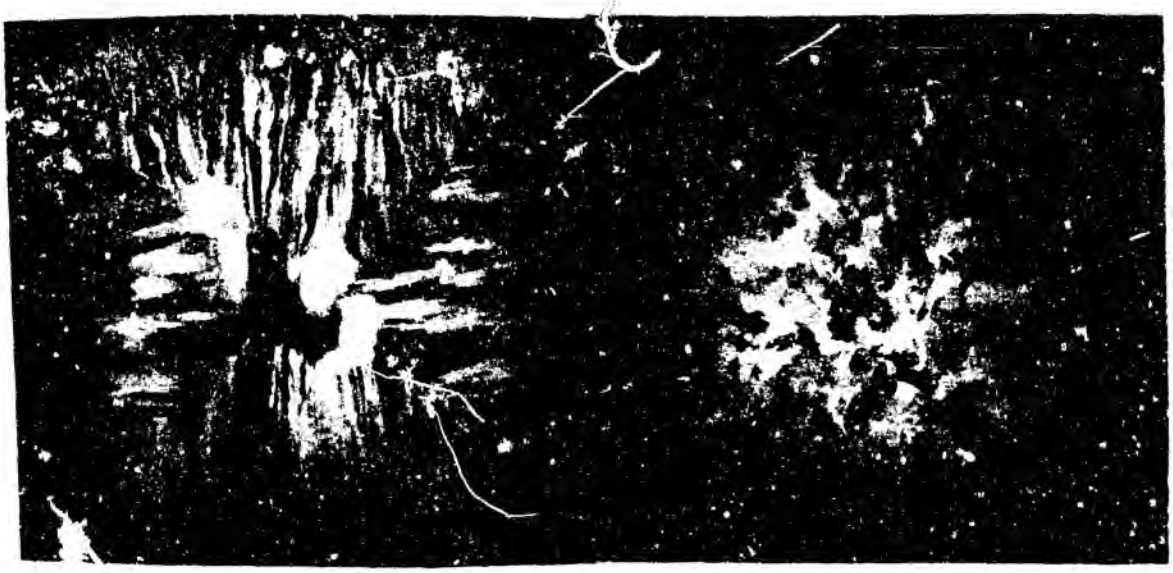

ZR14 (Zr: 0.391wt%) 1487°C ZR15 (Zr:0.380wt%) 1460°C

Figure 6.20 continued

Table 6.10 Change in macrostructure for ingots containing FeSiZr

Ingot no	Addition wt%	Casting temp.°C	Residual concentrations of Zr and Al in ingots (wt%)		Columnar grain width (mm) with 95% confidence limits measured at 6 and 14mm from the edge		Change in columnar grain width %		Grain width ratio gw 14mm/ gw 6mm	Equiaxed zone %
			Zr	Al	6mm	14mm	6mm	14mm		
ZR1	Zr 0.163	1625	0.04	-	1.051 ±0.132	1.204 ±0.129	18.81	12.39	1.30	5
ZR2	Zr 0.084	1625	-	-	1.495 ±0.227	1.269 ±0.152	-15.77	10.66	0.86	0
ZR3	Zr 0.238	1610	0.040	-	0.671 ±0.093	0.89[illegible] ±0.131	42.11	32.00	1.33	3
ZR4	Zr 0.381	1615	0.170	-	0.736 ±0.116	0.897 ±0.093	38.76	33.66	1.22	3
ZR5	Zr 0.328 Al 0.090	1615	-	0.140	0.943 ±0.091	1.010 ±0.156	21.54	25.53	1.07	5
ZR6	Zr 0.357 Al 0.090	1608	-	0.430	0.768 ±0.072	0.982 ±0.127	32.76	24.38	1.28	4
ZR7	Zr 0.167 Al 0.040	1604	-	0.120	0.807 ±0.042	1.098 ±0.065	27.24	13.32	1.36	0
ZR8	Zr 0.372 Al 0.100	1613	0.070	0.208	0.503 ±0.069	0.813 ±0.068	57.54	39.30	1.62	3
ZR9	Zr 0.365 Al 0.103	1580	0.110	0.310	0.413 ±0.054	0.507 ±0.015	48.16	47.73	1.23	4

Table 6.10 continu

Ingot no	Addition wt%	Casting temp.°C	Residual concentrations of Zr and Al in ingots (wt%)		Columnar grain width (mm) with 95% confidence limits measured at 6 and 14mm from the edge		Change in columnar grain width %		Grain width ratio gw 14mm/ gw 6mm	Equiaxed zone %
			Zr	Al	6mm	14mm	6mm	14mm		
ZR10	Zr 0.380 Al 0.100	1545	0.090	0.286	0.445 ±0.051	0.640 ±0.090	37.47	28.18	1.44	10
ZR11	Zr 0.391 Al 0.050	1532	-	0.180	0.450 ±0.052	0.592 ±0.039	30.43	28.85	1.32	3
ZR12	Zr 0.380	1512	-	0.130	0.453 ±0.027	0.595 ±0.058	19.55	21.48	1.31	8
ZR13	Zr 0.391 Al 0.030	1504	0.180	0.049	0.408 ±0.040	0.557 ±0.064	23.74	24.08	1.37	5
ZR14	Zr 0.391	1487	-	0.045	0.479 ±0.068	0.658 ±0.054	1.38	5.10	1.37	5
ZR15	Zr 0.380	1480	0.090	0.041	0.412 ±0.050	0.514 ±0.061	5.55	22.04	1.25	40
ZR16	Zr 0.380	1513	-	0.028	0.409 ±0.041	0.567 ±0.037	27.84	28.12	1.34	0
ZR17	Zr 0.395	1481	-	0.020	0.373 ±0.052	0.482 ±0.038	20.92	29.39	1.29	3
ZR18	Zr 0.391	1545	0.125	0.025	0.354 ±0.039	0.493 ±0.062	50.26	44.68	1.39	0
ZR19	Zr 0.384	1548	0.130	0.028	0.373 ±0.044	0.471 ±0.044	47.98	47.44	1.26	3

Table 6.10 continued

Ingot no	Addition wt%	Casting temp.°C	Residual concentrations of Zr and Al in ingots (wt%)		Columnar grain width (mm) with 95% confidence limits measured at 6 and 14mm from the edge		Change in columnar grain width %		Grain width ratio gw 14mm/ gw 6mm	Equiaxed zone %
			Zr	Al	6mm	14mm	6mm	14mm		
ZR20	Zr 0.513	1542	0.150	-	0.373 ±0.027	0.479 ±0.019	48.41	45.37	1.28	3
ZR21	Zr 0.251 Al 0.030	1544	0.130	0.075	0.448 ±0.031	0.578 ±0.063	36.60	34.80	1.29	3
ZR22	Zr 0.386 Al 0.100	1510	0.170	-	0.507 ±0.043	0.674 ±0.030	8.78	10.31	1.33	8
ZR23	Zr 0.100	1481	-	-	0.452 ±0.039	0.592 ±0.078	4.17	13.28	1.31	19
ZR24	Zr 0.214	1482	-	-	0.468 ±0.055	0.609 ±0.052	1.24	11.00	1.30	23
ZR25	Zr 0.313	1493	-	-	0.459 ±0.034	0.654 ±0.089	8.48	7.36	1.42	8
ZR26	Zr 0.416	1496	-	-	0.389 ±0.035	0.544 ±0.380	23.74	23.70	1.40	10
ZR27	Zr 0.363 MM 0.06	1490	-	-	0.481 ±0.031	0.571 ±0.047	2.51	18.36	1.19	3
ZR28	Zr 0.271 Al 0.017 MM 0.05	1489	-	-	0.400 ±0.053	0.501 ±0.048	18.50	23.88	1.33	10
ZR29	Zr 0.300 Al 0.023	1488	-	-	0.480 ±0.029	0.675 ±0.069	1.68	2.93	1.41	19

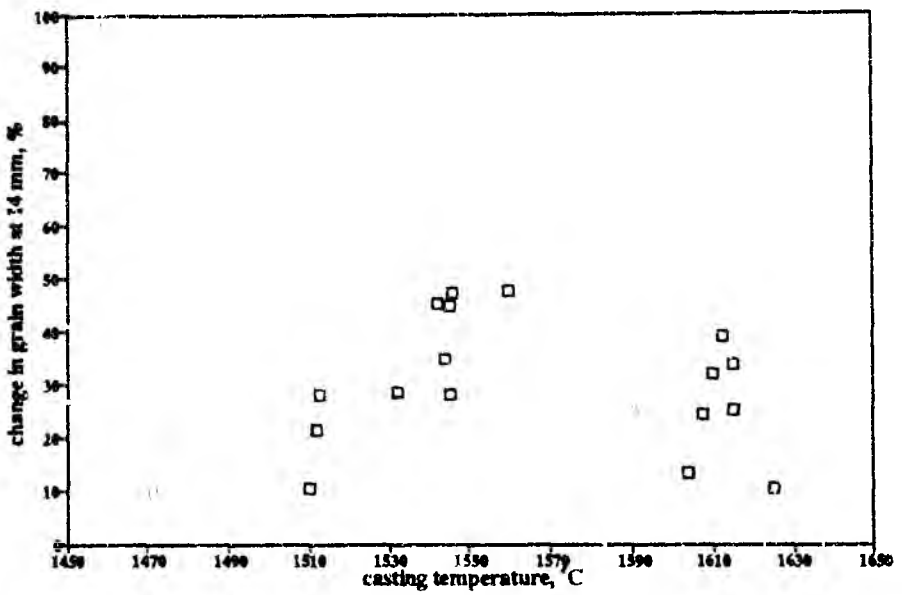

Figure 6.21 Change in grain width measured at 14 mm with casting temperature for ingots with FeSiZr additions

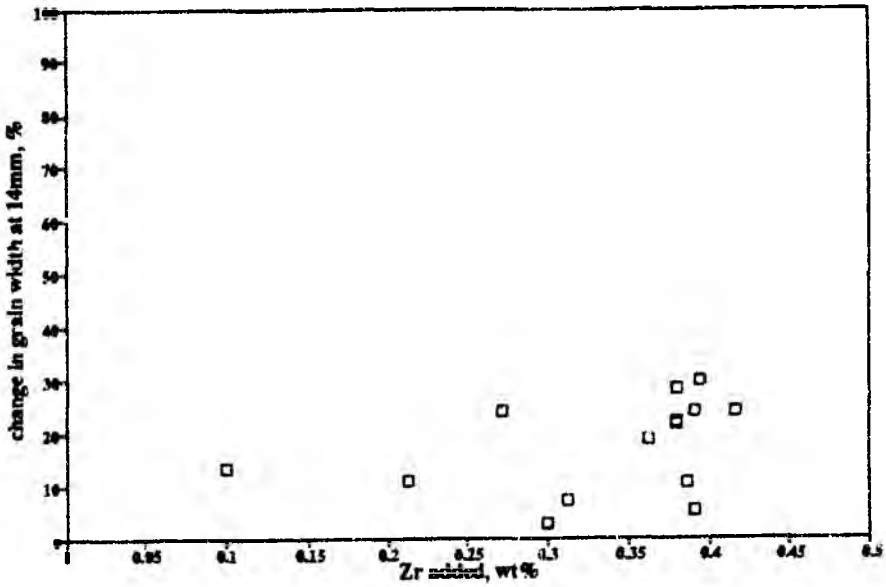

(a)

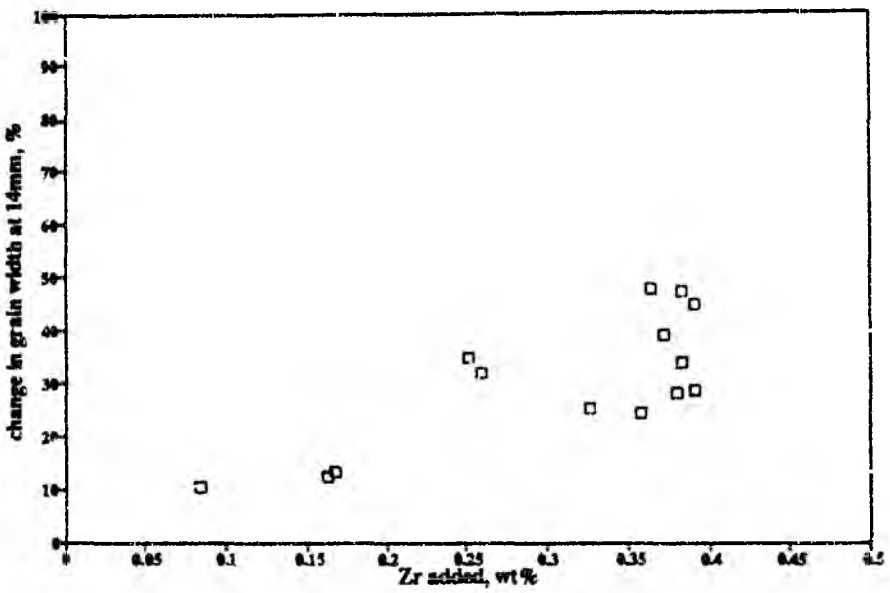

(b)

Figure 6.22 Change in grain width with Zr additions for ingots cast from (a) 1481-1513°C and (b) 1532-1625°C

The data points which deviate significantly from the main trend represent castings poured outside the optimum range of temperatures. From these graphs, it appears that the higher the amount of zirconium the greater the grain refinement, which may go up as high as 60% at about 0.4% Zr.

6.2.3.1 Grain Width Ratio Analyses for Ingots with Zirconium Additions

The graph in Figure **6.23**, shows the effect of casting temperature on grain width ratios for ingots containing Zr as well as the regression curve for base metal ingots cast from similar temperatures. It can be seen that the grain width ratios showed a positive deviation at high casting temperatures, whereas at low temperatures (1460 to 1500°C), there appeared to be a negative deviation from the base metal regression curve. However in the temperature range 1530 to 1560°C where the highest degree of grain refinement was obtained, except for two ingots, the data showed the same trend as those obtained with base metal ingots. The same data were plotted against grain widths for different casting temperatures as shown in Figure **6.24**. It can be seen that the grain width ratios in the high temperature range have a downward slope, whereas in the low temperature range, the slope is positive.

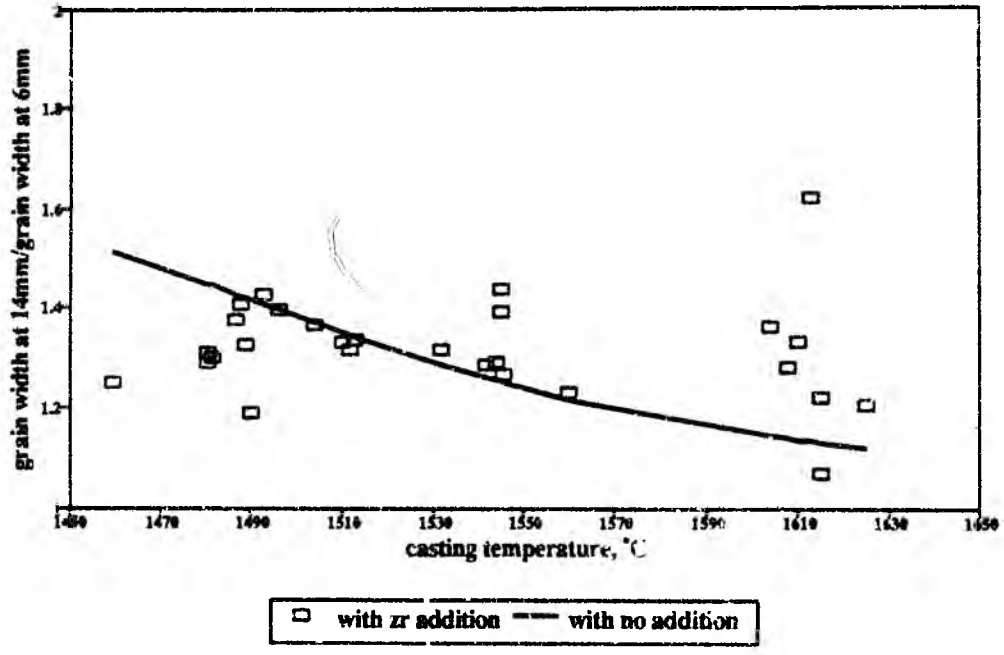

Figure 6.23 Change in grain width ratio with casting temperature for ingots containing FaSiZr additions

(a)

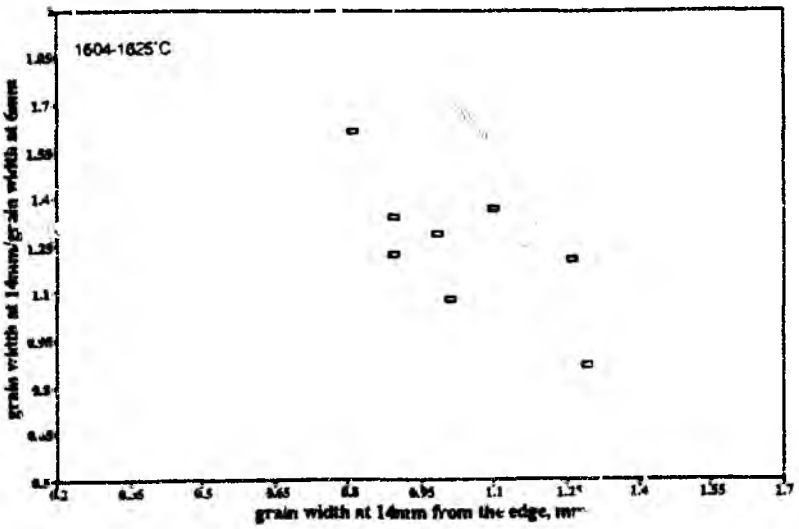

(b)

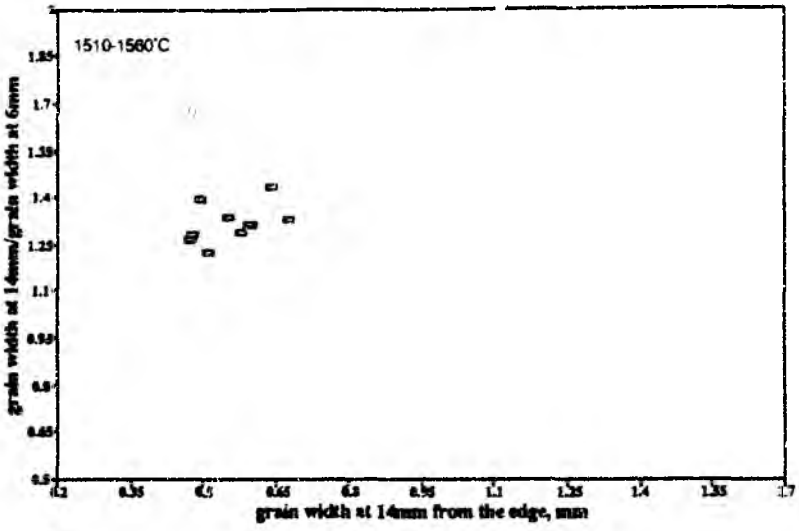

(c)

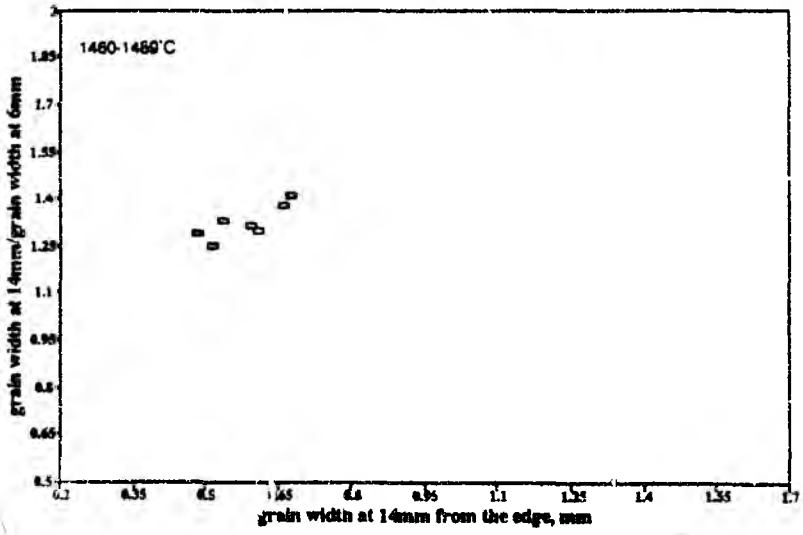

Figure 6.24 Change of grain width ratio with grain width measured at 14 mm for ingots with FeSiZr additions cast from (a) 1604-1625°C, (b) 1510-1560°C and (c) 1460-1489°C

6.3 Results of the Microstructural Evaluation of the As-Cast Ingots

6.3.1. Microstructural Evaluation of Base Metal Ingots

In order to assess the solidification pattern of AISI310, one transverse slice from each of 15 base metal ingots, cast from varying temperatures, was examined by optical microscopy and scanning electron microscopy (SEM). When the microstructures obtained from these ingots were analyzed and compared, two important observations were made:

1. The solidification mode of AISI310S changed from $L \rightarrow \gamma$ to $L \rightarrow \delta + L \rightarrow \delta + L + \gamma \rightarrow \gamma + L \rightarrow \gamma$ below a certain casting temperature, and again to $L \rightarrow \gamma$ at a lower range of casting temperatures under the conditions specific to these sets of experiments.

2. Primary dendrite arm spacings decreased with increasing casting temperature contrary to expectation.

6.3.1.1 Solidification Pattern of Base Ingots

As can be seen from the micrographs taken from areas very close to the edge of ingots (Figure **6.25**), the ingots which were cast in the temperature range 1476 to 1564°C showed "ghost" δ-grain boundaries which are not in one-to-one correspondence with austenite dendrites. EDS analyses showed that these grain boundaries are Cr rich (Figure **6.26**).

The existence of these grain boundaries strongly suggests a peritectic transformation of the type $L \rightarrow L + \delta \rightarrow \gamma$ the details of which will be discussed in the next chapter.



Figure 6.25 Microstructure showing δ-grain boundaries preserved in ingots cast in the temperature range 1476 to 1564°C

(a)

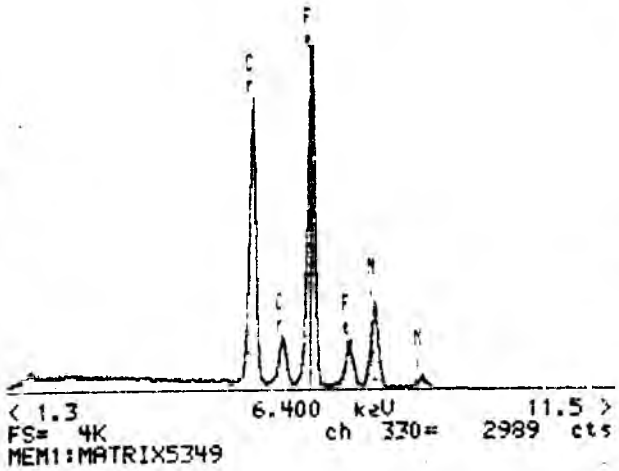

(b)

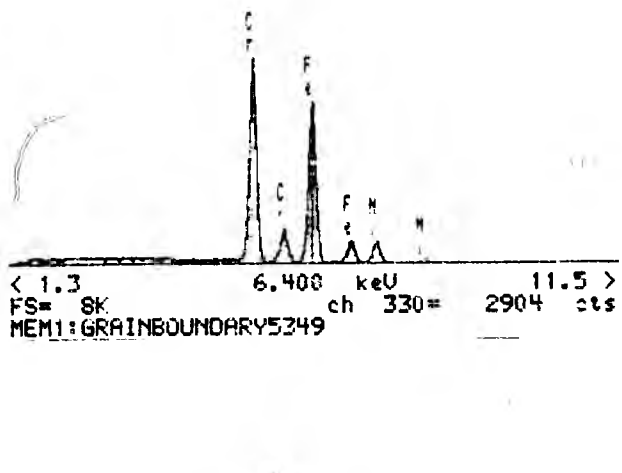

(c)

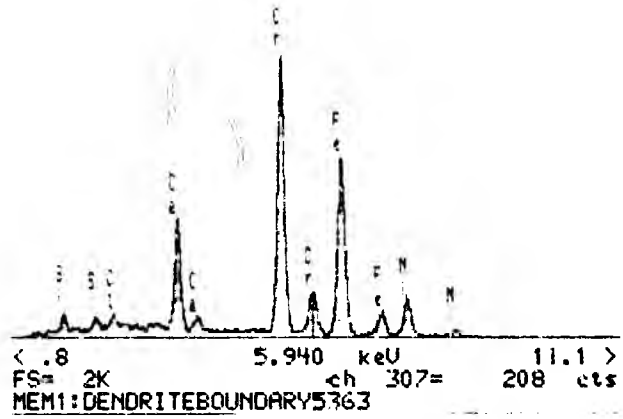

Figure 6.26 EDS analyses of the elements in γ grains (a), in δ grain boundary (b) and in γ dendrite boundaries (c)

6.3.1.2 Primary and Secondary Dendrite Arm Spacings

The results of measurements of dendrite arm spacings (primary and secondary) for the base metal castings are given in Table **6.11**. The measurements were carried out at different distances from two opposite edges of the ingot section. The results obtained from the two sets of measurements are tabulated separately.

As can be seen from the data in Table **6.11**, dendrite arm spacings may differ considerably between the two halves of the ingot, even if the spacings are measured along parallel lines at the same distance from the two edges of the ingot section. The difference may be as high as 30% which is well above the 95% confidence limit of 17% calculated for the primary arm spacing measurements. This discrepancy cannot be attributed to measurement errors, but rather to unequal cooling rates from opposite sides of the ingot. Suzuki and Nakaoka[304] derived the following empirical relationship for secondary arm spacing for AISI310 grade steel:

$$\lambda_2 = 44R^{-0.38} \quad \ldots\ldots\ldots\ldots\ldots\ldots \quad 6.8$$

where λ_2 is secondary dendrite arm spacing in μm and R is the cooling rate in Ks^{-1}. Using this relationship the cooling rates were calculated for the base metal ingots.The results (Figure .27) show that there is a difference in cooling rates between the high temperature castings and low temperature castings up to distances of 4 to 5mm from the edge. This difference decreases drastically as the solidification front proceeds further towards the center.

Table 6.11 Primary and secondary dendrite arm spacings for base metal castings

Ingot no	Edge 1			Edge 2		
	Distance from the edge (mm)	Primary arm spacing (μm)	Secondary arm spacing (μm)	Distance from the edge (mm)	Primary arm spacing (μm)	Secondary arm spacing (μm)
B1	2	34.7	14.4	2	40.4	17.9
	4	50.3	18.1	4	63.3	24.9
	6	62.1	21.2	5	69.0	23.2
	8	90.3	25.0	8	138.6	28.9
	10	103.[illegible]	34.0	10	156.3	30.9
	15	189.2	38.9	13	213.8	36.4
	20	147.2	38.8	18	197.5	43.1
	25	176.7	36.3			
B2	[illegible]	45.2	18.1	2	46.0	17.5
	4	52.4	22.5	4	63.1	21.0
	5	51.8	25.8	5	106.2	29.5
	10	103.0	33.7	10	165.4	48.0
	15	213.8	42.8	15	188.0	55.2
	20	269.7	51.5	20	261.5	39.2
	25	258.8	44.1			
B3	2	38.9	14.6	2	32.3	18.4
	4	53.4	19.3	4	51.7	21.8
	5.2	61.4	23.8	8	117.8	62.5
	10.2	82.5	36.2	14	173.8	48.6
	15.2	168	38.9	19	291.8	41.4
	20.2	297.9	39.8	24	259.9	40.0
	25.2	186.7	40.4			
B4	2	82.5	25.3	2	44.0	17.5
	4	56.3	27.8	4	58.3	23.3
	9	116.5	45	9	184.7	37.5
	14	178.5	55.6	14	269.7	43.4
	19	222.3	49.8	19	283.2	42.4
				24	221	31.7

Table 6.11 continued

Ingot no	Edge 1			Edge 2		
	Distance from the edge (mm)	Primary arm spacing (μm)	Secondary arm spacing (μm)	Distance from the edge (mm)	Primary arm spacing (μm)	Secondary arm spacing (μm)
B5	2	38.1	14.9	2	46.7	17.0
	4	57.7	25.0	4	64.1	24.4
	6	96.5	26.2	8	72.2	26.6
	11	104.0	42.2	11	131.3	40.4
	16	232.6	55.2	16	247.0	43.1
	21	272.5	41.3	21	269.8	40.2
	26	195.7	37.4	26	255.8	32.5
				31	270.3	30.0
B6	2	39.8	17.7	2	53.8	18.0
	4	59.5	25.0	4	127.6	27.8
	6	91.4	29.7	6	172.4	33.4
				7	256.5	37.4
	9	106.9	37.9	12	183.8	42.8
	14	196.8	37.5	17	259.0	37.8
	19	138.9	36.6	22	130.3	29.8
B7	2	45.0	18.2	2	37.8	16.3
	3	48.6	20.0	4	72.7	22.4
	4	67.1	21.1	5	142.5	22.0
	6	92.9	26.1	10	118.2	25.7
	13	175.2	35.6	15	297.9	33.8
	18	292.8	42.3	20	244.3	34.8
	23	394.0	41.7			
B8	2	40.3	12.3	2	57.0	15.0
	4	59.0	16.8	4	68.4	20.8
	6.8	89.2	21.7	5	99.4	23.0
	11.8	141.7	28.7	9	184.9	32.4
	16.8	241.8	40.1	14	342.0	41.5
	21.8	192.4	30.3			
B9	2	50.3	18.0	2	43.8	19.2
	4	61.2	21.3	4	152.2	22.8
	5	96.6	20.7	5	135.9	24.9
	10	178.1	30.0	9	149.7	33.5
	15	284.0	39.5	13	265.0	42.1
	20	197.9	36.6	18	441.9	43.9

Table 6.11 continued

Ingot no	Edge 1			Edge 2		
	Distance from the edge (mm)	Primary arm spacing (μm)	Secondary arm spacing (μm)	Distance from the edge (mm)	Primary arm spacing (μm)	Secondary arm spacing (μm)
B10	2	61.2	17.2	2	111.9	20.5
	4	118.9	23.6	4	106.3	27.2
				6	114.0	30.4
	[illegible]	103.0	26.7	11	310.9	46.7
	11	170.3	32.2	16	222.1	44.7
	16	199.8	34.4	21	272.3	40.6[illegible]
	21	298.2	32.7			
B11	2	52.1	18.7	[illegible]	70.4	18.[illegible]
	3.2	59.4	18.3	4	105.7	27.2
	6	129.6	29.7	[illegible]	146.2	32.4
	8.2	199.5	32.9	9	212.7	36.6
	13	228.0	37.9	14	281.3	41.3
	18.2	227.4	35.6			
	23.2	2[illegible].8	103.6			
B12	2	35 3	15.5	2	98.7	22.5
	4	108.1	22.0	4	179.6	33.2
	6	206.3	31.3	6	267.2	33.3
	8	193.0	34.2	8	291.8	42.5
	12	275.8	36.3	12	293.8	44.7
	15	272.6	34.6	15	333.5	41.7
B13	2	[illegible]3.6	15.0	3	81.8	14.5
	4	61.2	21.6	5	103.3	19.7
	6	158.9	[illegible]4.9	7	137.9	26.9
	9	206.2	36.[illegible]	9	282.2	34.5
	13	238.0	34.7	14	250.0	37.5

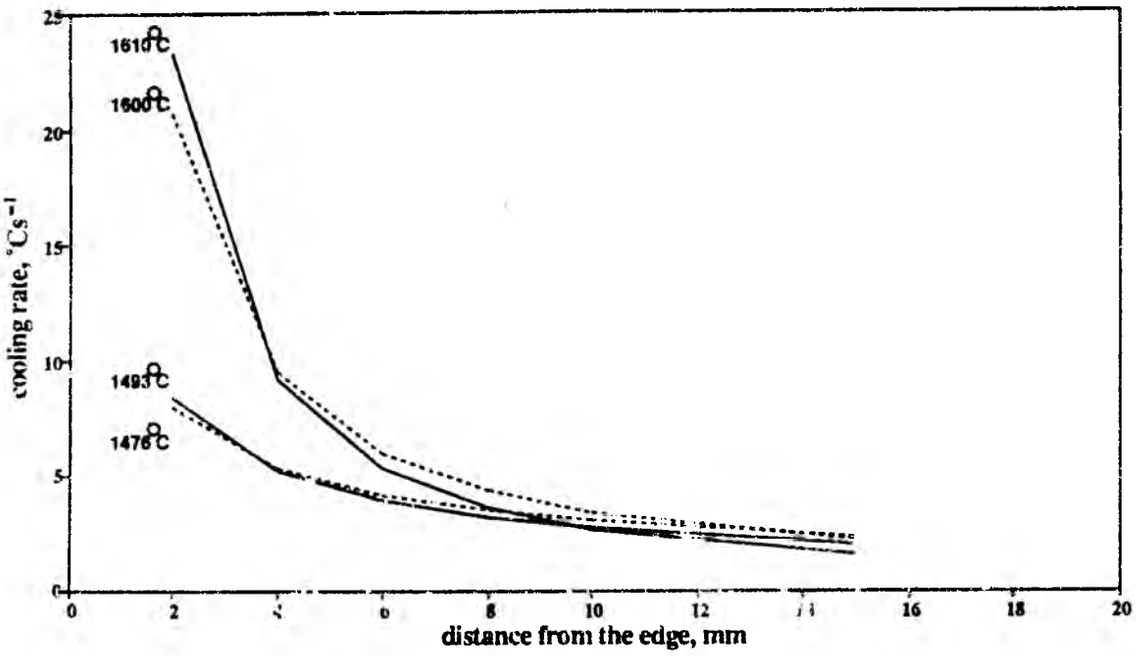

Figure 6.27 Changes in cooling rate of base ingots with distance from the chill zone

The cooling rates from opposite edges of the same casting also showed significant differences for some of the ingots. However, at distances of 4mm or more from the edges the differences in cooling rate were insignificant. Cooling rates at 2mm from the edge varied from $23Ks^{-1}$ ($1380Kmin^{-1}$) for ingots cast from 1610°C to $5Ks^{-1}$ ($300Kmin^{-1}$) for ingots cast from 1493°C. At 15mm from the edge, the variation in cooling rate was within the error limits calculated for secondary dendrite arm spacing measurements.

The tabulated dendrite arm spacing measurements indicate that there is a strong relationship between casting temperature and primary arm spacings (Figure **6.28**), whereas it seems that the secondary arm spacing is insensitive to casting temperature variations at distances of 10mm and 15mm from the edge of the ingots (Figure **6.29**). These figures show that as the casting temperature is increased, the primary dendrite arm spacing gets smaller in other words, the microstructure is finer when pouring takes place at higher temperatures. This is also evidenced by the micrographs taken at various distances from the edges of these ingots (Figure **6.30**). As can be seen from these micrographs, the number of primary arms comprising one macrograin, in castings poured from high temperatures, is a few times larger than that of castings poured from lower temperatures. Compare for instance the microstructures of ingot B4 cast from 1564°C and ingot B11 cast from 1496°C; they had primary dendrite arm spacings of 130µm and 210µm respectively at 10mm from the chill zone. However columnar grain width measurements for the same ingots gave 0.844mm and 0.511mm respectively at 6mm from the chill zone. In castings poured from low temperatures the number of columnar grains was higher but the number of primary dendrite arms in these grains was lower. The result was a coarser primary arm spacing in ingots cast from lower temperatures.

These opposing trends of primary arm spacings and columnar grain widths with casting temperature became obvious when the spacings were plotted against each other. In Figure **6.31**, the primary arm spacing has a negative slope especially in the smaller grain width region from about 0.4mm to 0.8mm widths. Above 0.8mm the dendrite arm spacing seems to remain constant at about 190-200 µm.

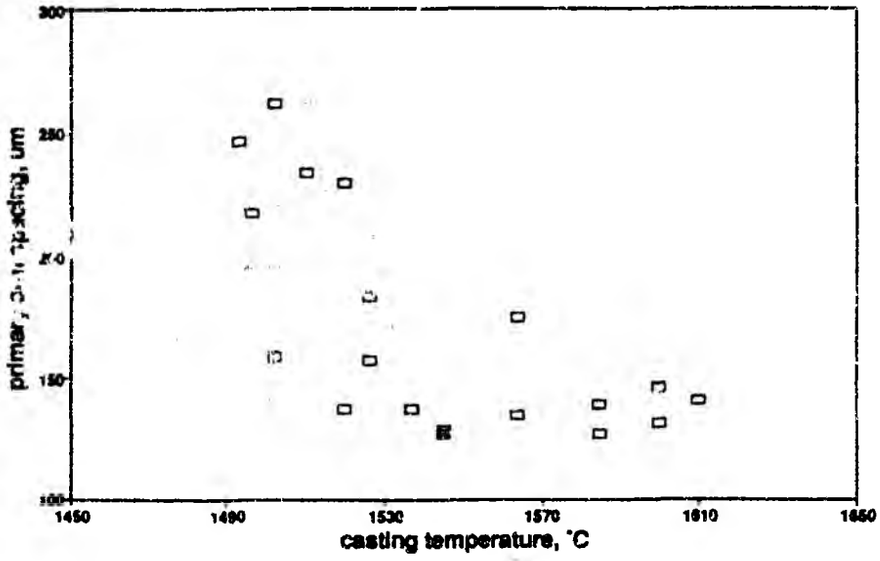

(a)

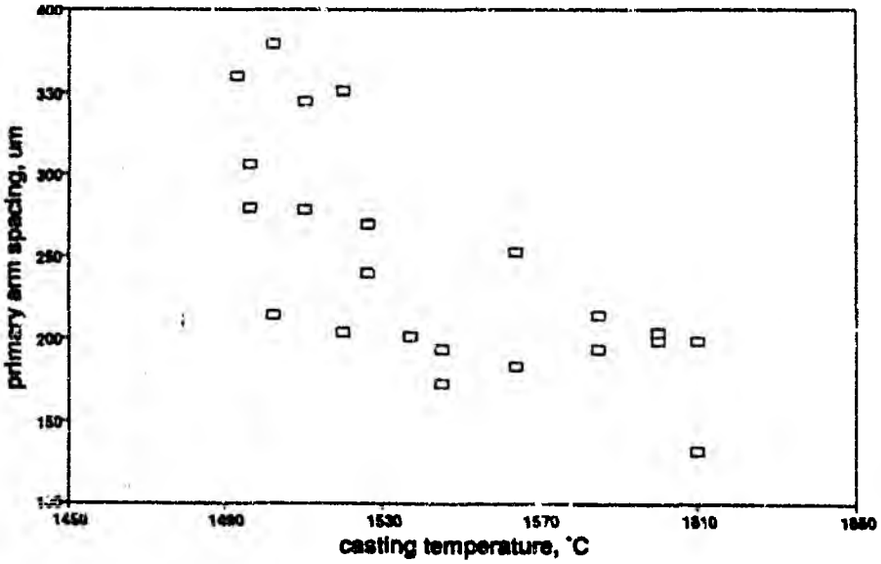

(b)

Figure 6.28 Variation in primary dendrite arm spacing with casting temperature measured at (a) 10 mm and (b) 15 mm from the chill zone

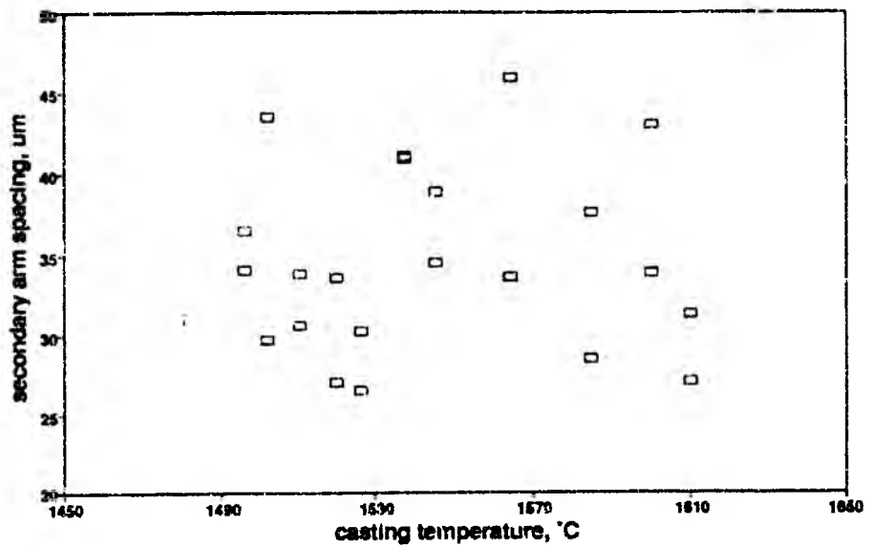

(a)

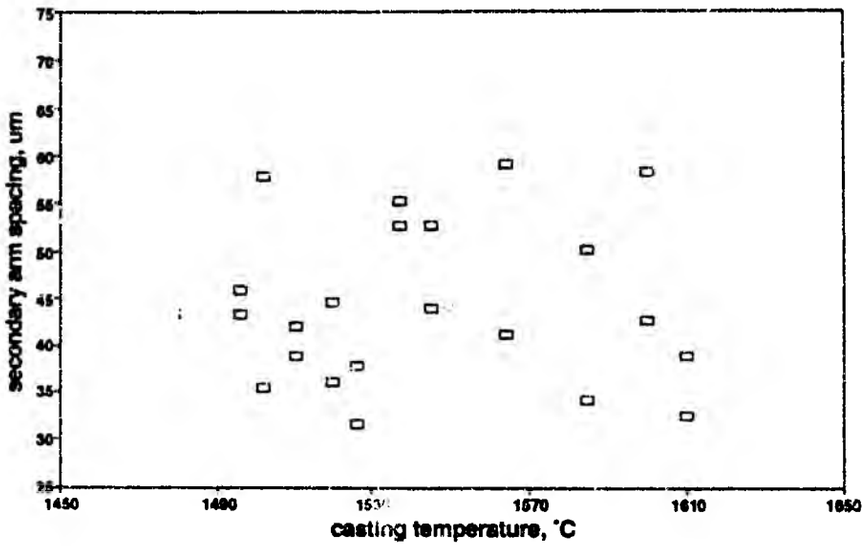

(b)

Figure 6.29 Variation in secondary dendrite arm spacings with casting temperature measured at (a) 10 mm and (b) 15 mm from the chill zone

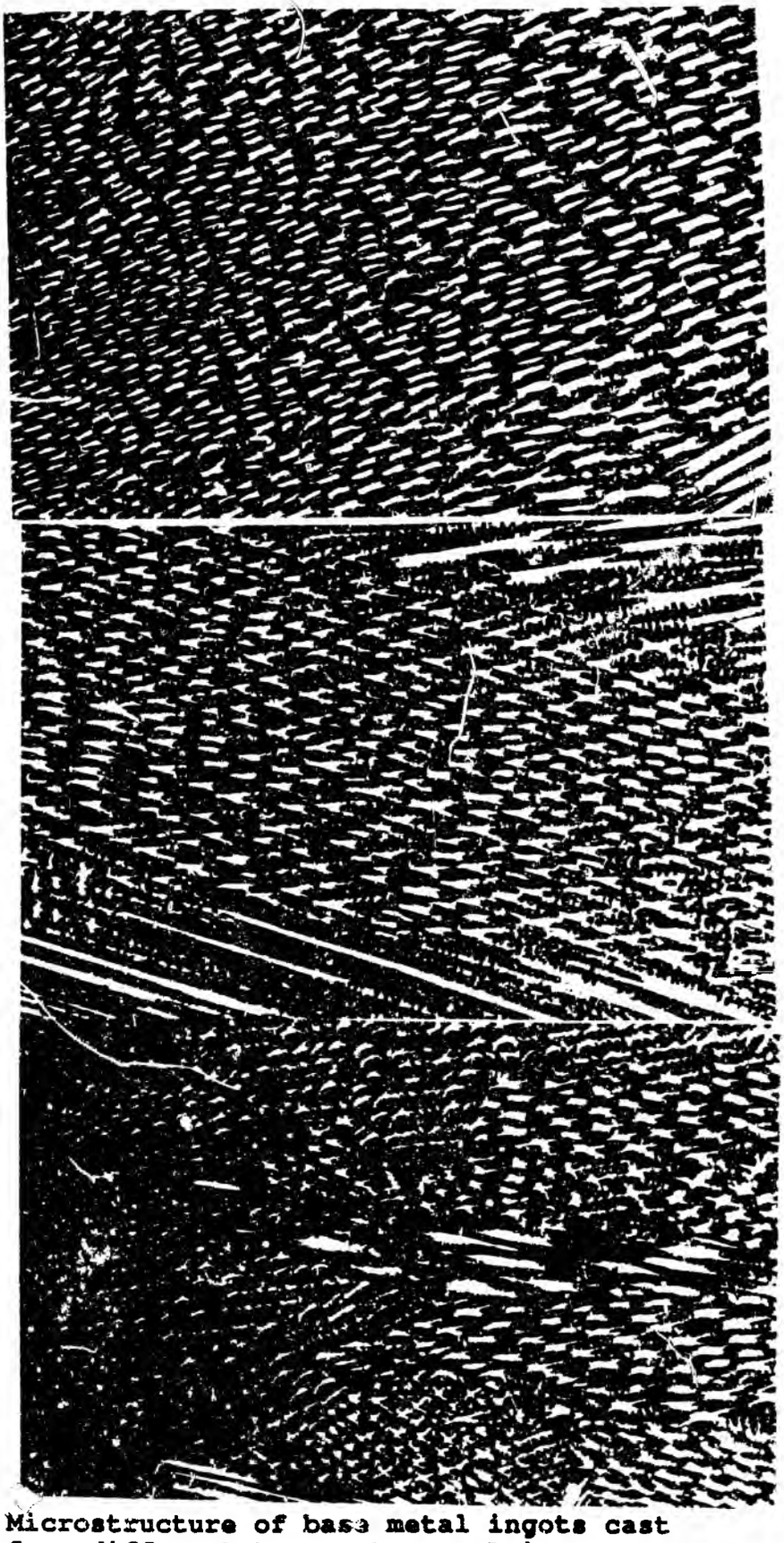

Figure 6.30 Microstructure of base metal ingots cast from different temperatures. Primary dendrite arm spacings given were measured at 10mm from the chill zone.



Figure 6.30 continued



Figure 6.30 continued; primary dendrite arm spacings given were measured at 15mm from the chill zone.

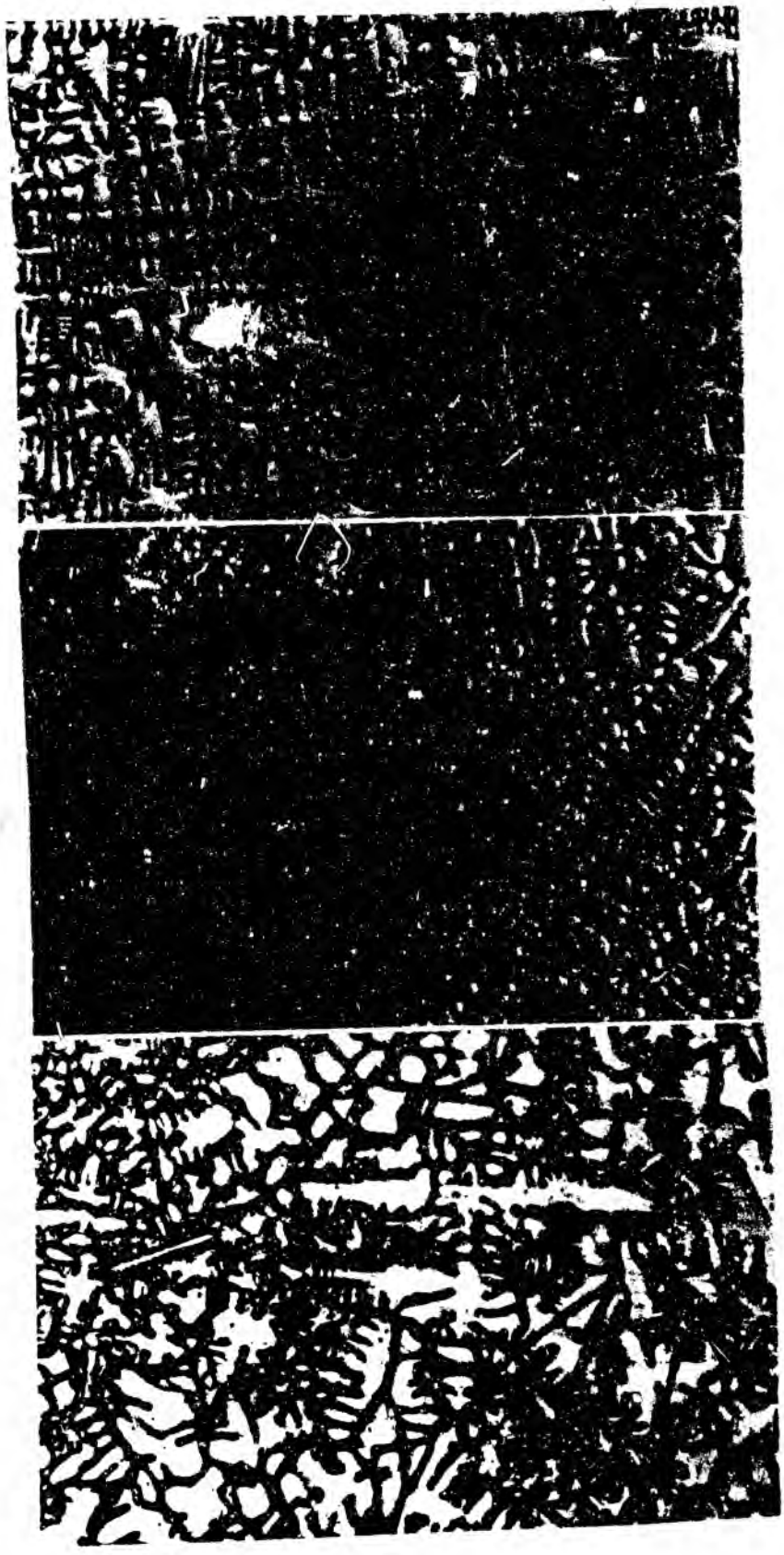

Figure 6.30 continued

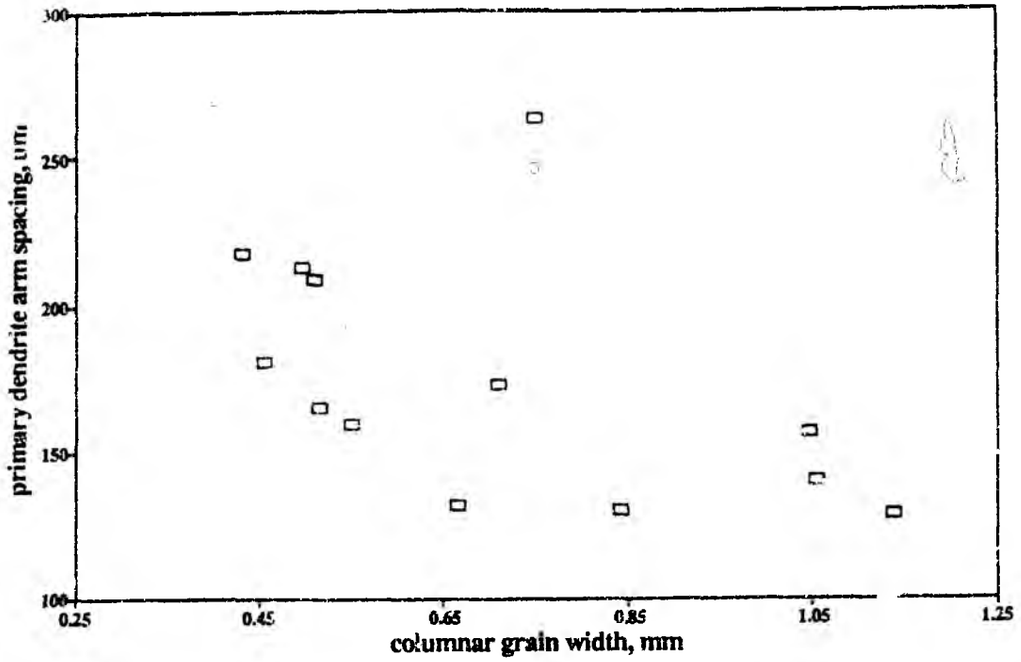

(a)

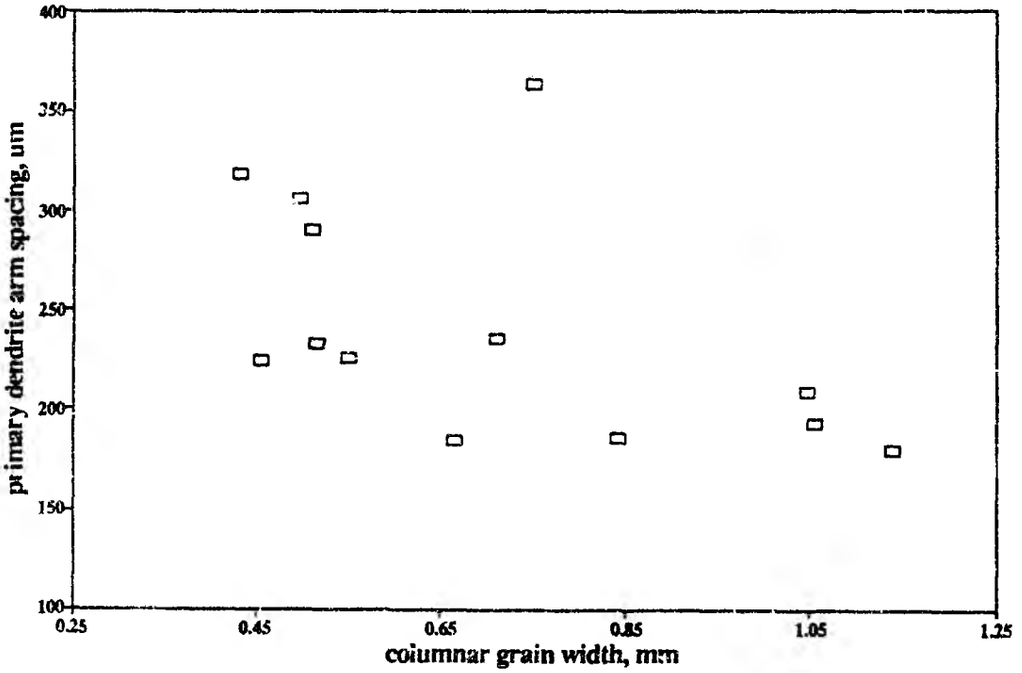

(b)

Figure 6.31 Change in primary dendrite arm spacing of ingots measured at (a) 10mm and (b) 15mm from the chill zone with changes in grain width measured at 6mm from the chill zone

These trends correspond to casting temperature ranges of 1470 to 1545°C and 1545 to 1610°C respectively.

When the secondary dendrite arm spacings were plotted against grain widths (Figure **6.32**) no significant trend was observed. Since deviations from the average were within the range of measurement error, no conclusion could be drawn from these plots.

The changes in secondary arm spacing with changing primary arm spacing were initially analyzed separately for castings in which a temperature effect on this relationship suggested itself. In order to simplify matters, the data were grouped into two temperature ranges in which the cut off temperature between the two was decided after a careful analysis of the slopes obtained by regression analyses of each ingot sample (Figure **6.33** and **6.34**). These two power curves (Figure **6.34**) were plotted together with the curves for other alloys found in the literature (Figure **6.35**). As can be seen, the higher the casting temperature, the larger the secondary dendrite arm spacing per unit primary arm spacing. This confirms the above results which show refinement in the primary arm spacing as the casting temperature is increased. It can also be said that the secondary arm spacing was not very sensitive to thermal gradient effects during solidification. The change in the slope of the plot of secondary arm spacing against primary arm spacing was plotted against the corresponding columnar grain widths measured at 6mm and 14mm and against grain width ratios obtained for the same samples and given in Figures **6.36** and **6.37**. As could be expected from the relationships observed in these figures, the slope of secondary arm spacing against primary arm spacing increased as the grain width increased, but decreased as the grain width ratio increased.

Table 6.12 continued

Ingot no	Edge 1			Edge 2		
	Distance from the edge (mm)	Primary arm spacing (μm)	Secondary arm spacing (μm)	Distance from the edge (mm)	Primary arm spacing (μm)	Secondary arm spacing (μm)
MM19	2	84.8	15.8	2	81.6	18.0
	4	106.3	17.7	4	108.4	25.0
	6	116.6	19.3	6	127.6	26.6
	8	92.6	21.7	8	139.4	28.9
	13	83.8	31.3	10	152.0	32.7
	18	106.9	34.5	11	156.8	31.4
	23	131.5		13	192.4	34.3
MM20	2	57.3	17.2	2	78.0	21.1
	4	95.4	21.9	4	150.0	28.9
	6	120.8	32.0	5	128.2	29.8
	11	168.3	38.9	10	268.0	36.2
	16	191.7	33.7	15	221.7	33.1
	21	156.3	34.2			
MM21	2	37.2	13.9	2	40.3	13.7
	4	41.5	17.0	3.5	45.6	19.7
	6	60.9	21.9	6	53.6	22.3
	9	62.0	25.9	8.5	84.0	26.9
	10	127.8	31.1	10	123.2	28.2
	12	120.8	32.0	12	169.0	32.5
	14	138.8	36.5	13.5	175.9	32.9
	19	99.4	34.5	18.5	120.6	33.3
MM22	2	48.8	20.6	2	67.0	23.6
	3	82.9	23.3	4	122.0	28.0
	4	72.4	27.1	6	159.5	31.2
	6	100.7	30.0	9	222.0	36.1
	8	101.9	30.5	14	253.7	47.9
	13	182.7	35.1	19	222.0	37.9
	18	199.0	37.2			
	23	176.3	37.8			
MM23	2	34.9	16.9	2	57.8	13.2
	4	123.2	26.4	3	83.5	23.9
	6	90.8	28.0	6	121.7	32.0
	9	240.8	32.7	8	212.7	34.8
	14	268.4	37.5	13	239.5	31.1
	19	292.0	31.2	18	167.3	39.9

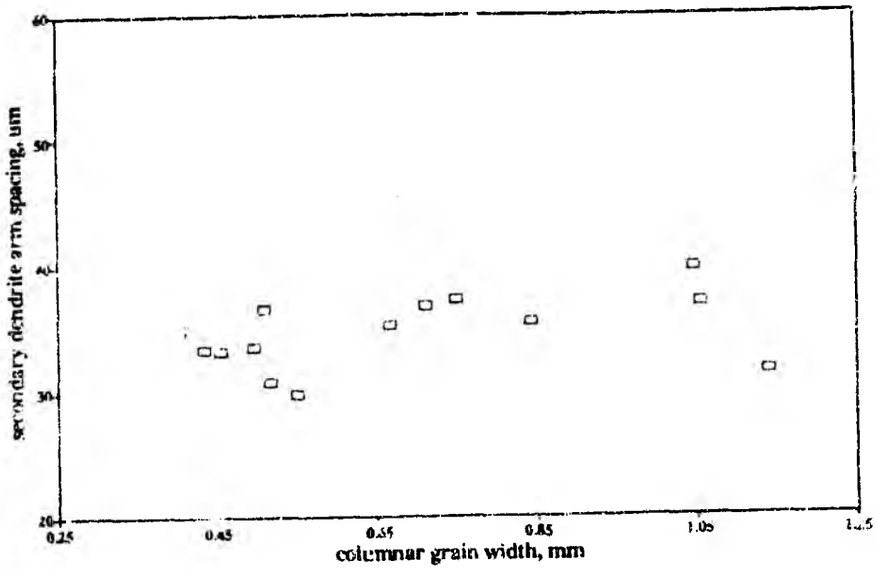

(a)

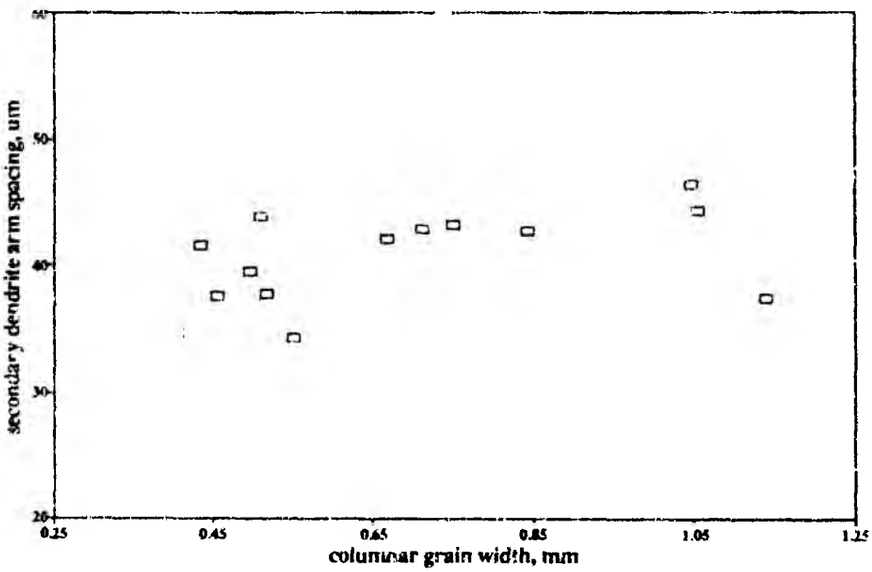

(b)

Figure 6.32 Change in secondary dendrite arm spacing of ingots measured at (a) 10mm and (b) 15mm from the chill zone with changes in grain width measured at 6mm from the chill zone

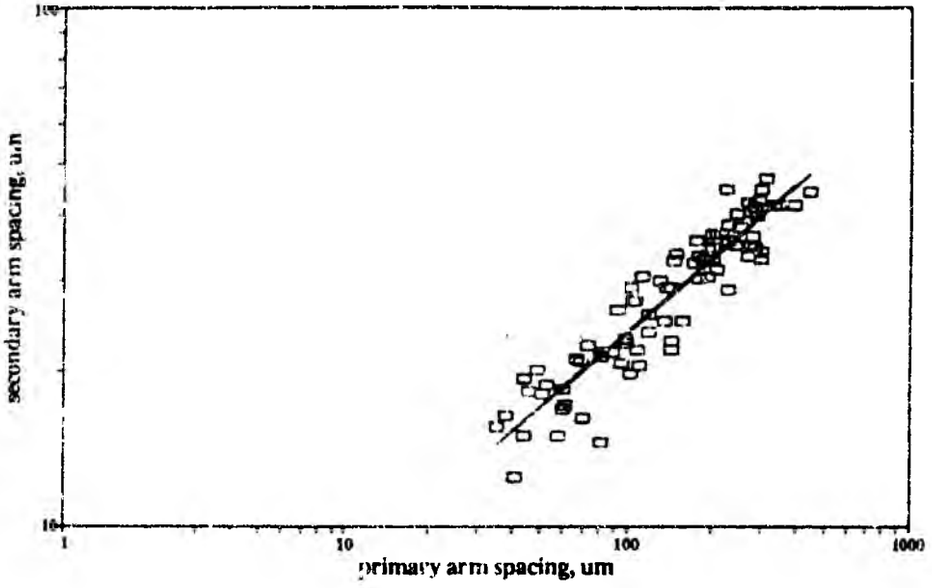

(a)

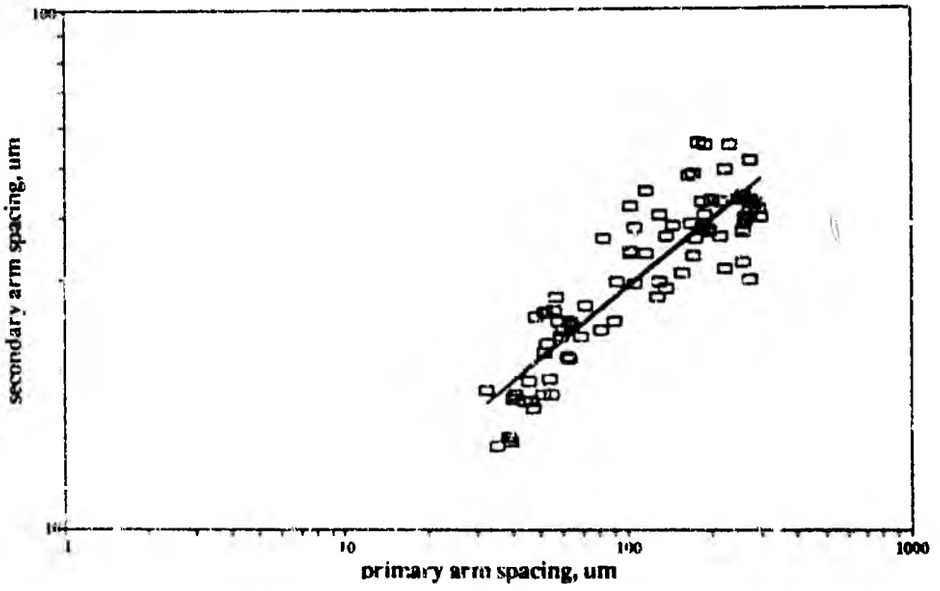

(b)

Figure 6.33 Change of secondary dendrite arm spacing with changing primary arm spacing for ingots poured in the temperature ranges (a) 1476-1526°C and (b) 1537-1610°C

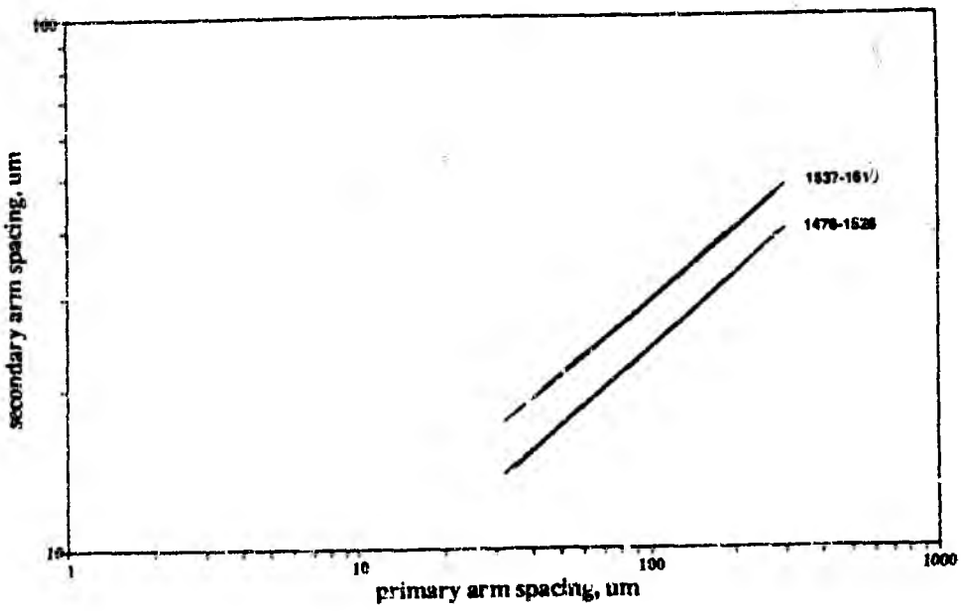

Figure 6.34 Logarithmic regression lines for the change in secondary arm spacing with changing primary arm spacing for two different casting temperature ranges

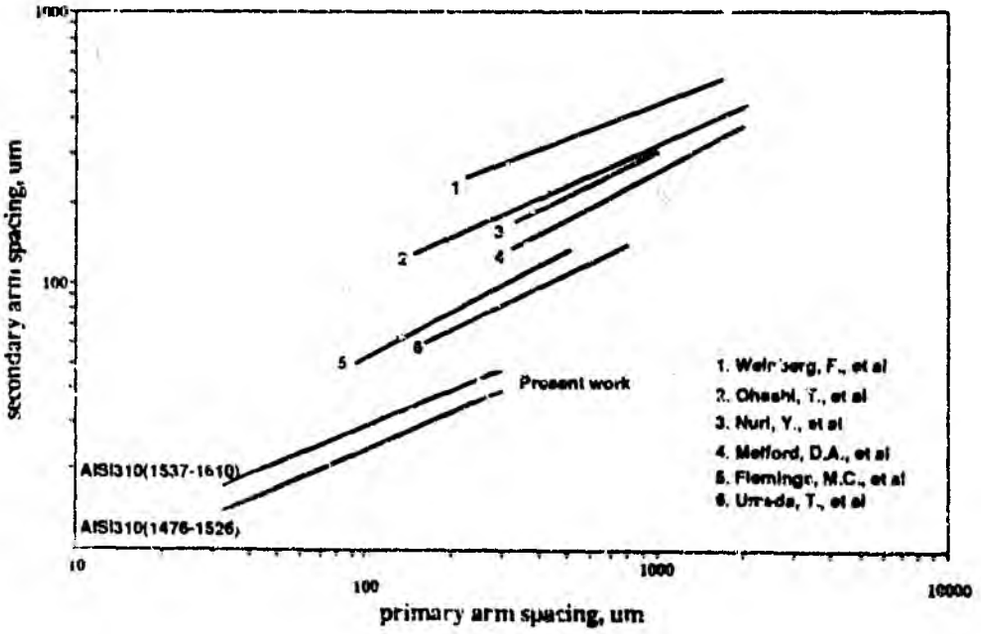

Figure 6.35 Comparison between regression lines of secondary and primary arm spacing obtained in this study with similar regression lines found in the literature[239]

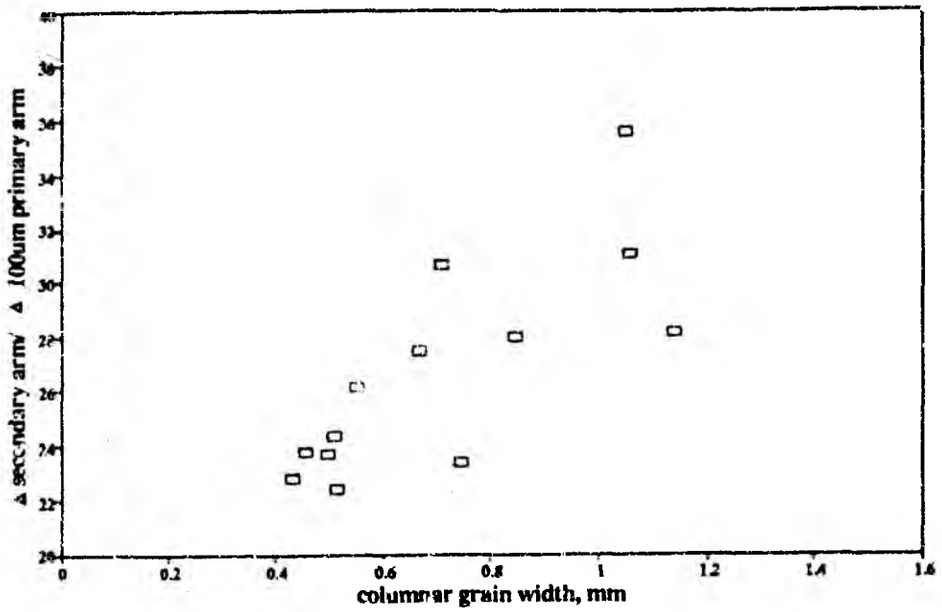

(a)

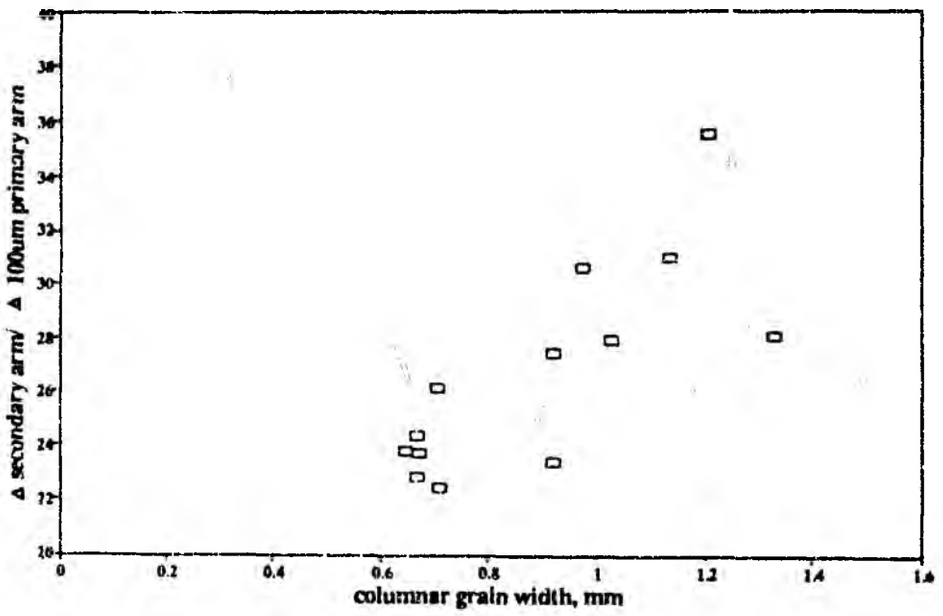

(b)

Figure 6.36 Change in the slope of plots of secondary arm spacing against primary arm spacing for columnar grain widths measured at (a) 6mm and (b) 14mm from the chill zone.

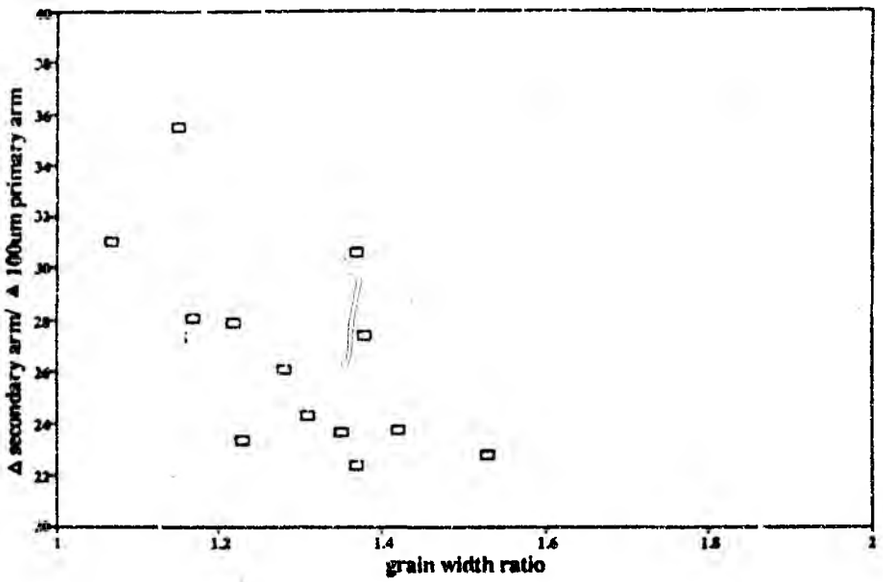

Figure 6.37 Change in the slope of plots of secondary arm spacing against primary arm spacing with grain width ratio for AISI310S ingots cast from a temperature range of 1476-1610°C

However it should be noted that these trends are not similar to the relationship between primary arm spacing and casting temperature (Figure 6 28). This may suggest that secondary dendrite arm spacings are not very sensitive to changes in primary arm spacings.

6.3.2 Microstructural Evaluation of Ingots with Additions of Misch Metal

In order to investigate the microstructural changes in AISI310S with additions of misch metal micrographs were taken at various distances from the edge of the samples. As can be seen from the micrographs in Figure **6.38**, in which micrographs from selected base metal ingots are also given for comparison purposes, dendrite arm spacings were not refined. On the contrary, the columnar dendritic structure seems to be coarser compared to that in base metal castings poured from the same temperature range. The primary arm spacing in ingots cast with misch metal varied but it was generally coarser than that in base metal ingots cast under otherwise equivalent conditions. Increase in the randomness of the dendritic structure was observed to correspond to shorter and thinner columnar grains and a larger equiaxed grain zone in the macrostructure.

6.3.2.1 Results of Primary and Secondary Dendrite Arm Spacing Measurements of Castings Containing Misch Metal

The results of the dendrite arm spacing measurements (primary and secondary) for the castings with misch metal additions are given in Table **6.12**. These results when compared with the results obtained for base metal castings poured from the same temperature range, show that the microstructure coarsened by up to 35 to 40% [illegible] towards the center of the ingots. This becomes evident when the data for ingots B4 to B7 are compared with those for ingots MM7 and MM14 to MM17. These effects can also be followed from Figures **6.39** and **6.40** which show plots of the data in Tables **6.11** and **6.12**.

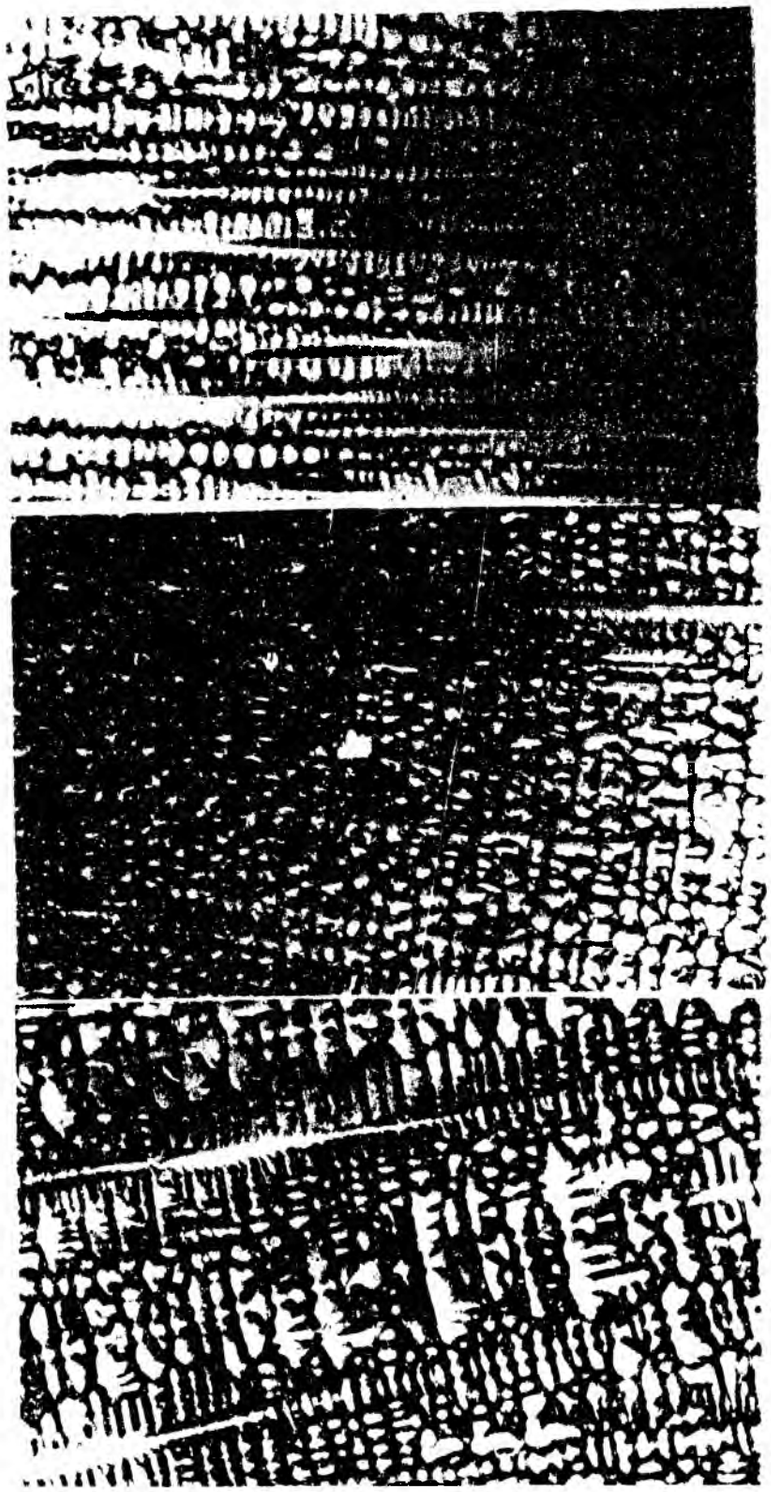

Figure 6.38 Micrographs of the as-cast structures of AISI310S ingots cast with misch metal additions

MM14
1550°C
λ_1=175μm
Macro-grain
refinement:
27%

MM17
1547°C
λ_1=185μm
Macro-grain
refinement:
44%

MM20
1543°C
λ_1=185μm
Macro-grain
refinement:
45%

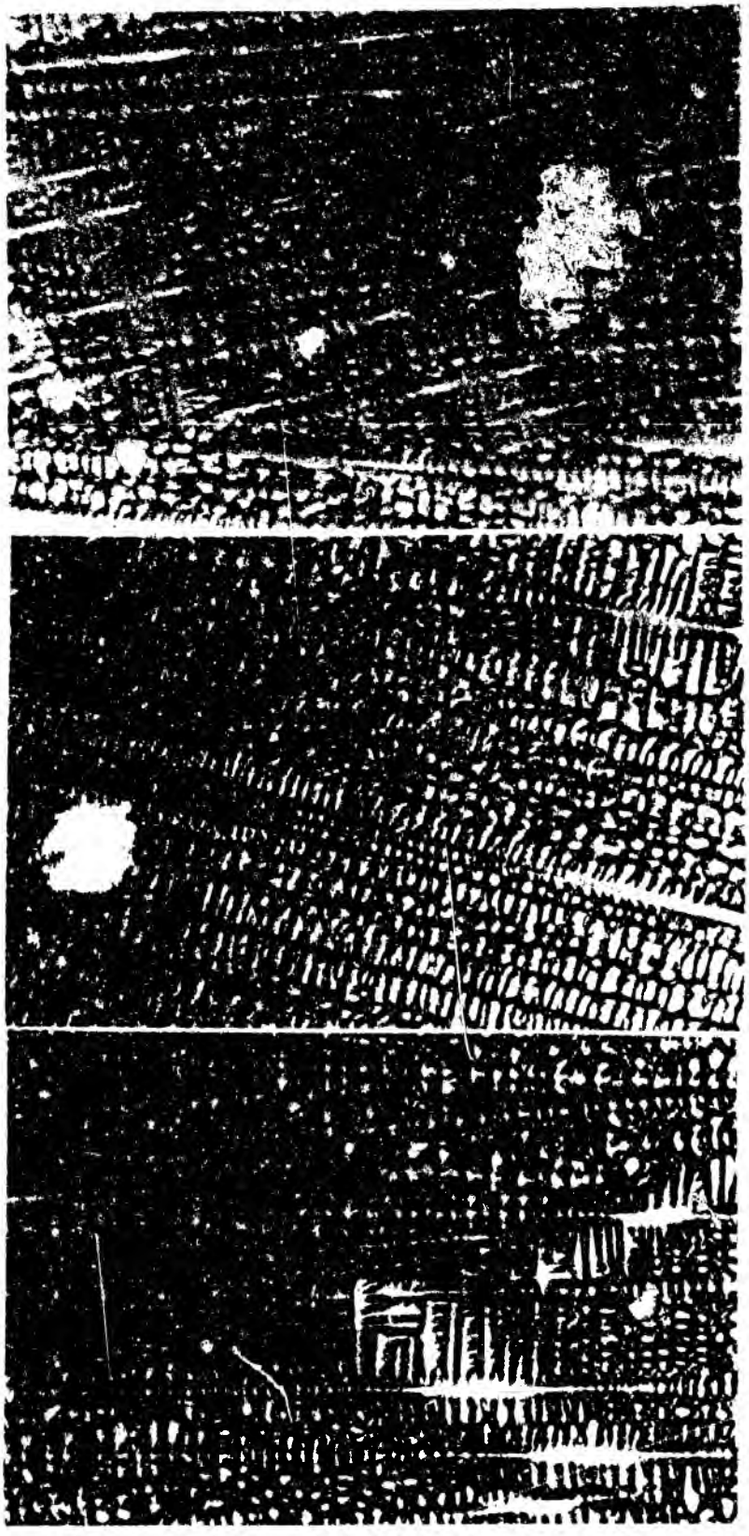

Figure 6.[illegible]

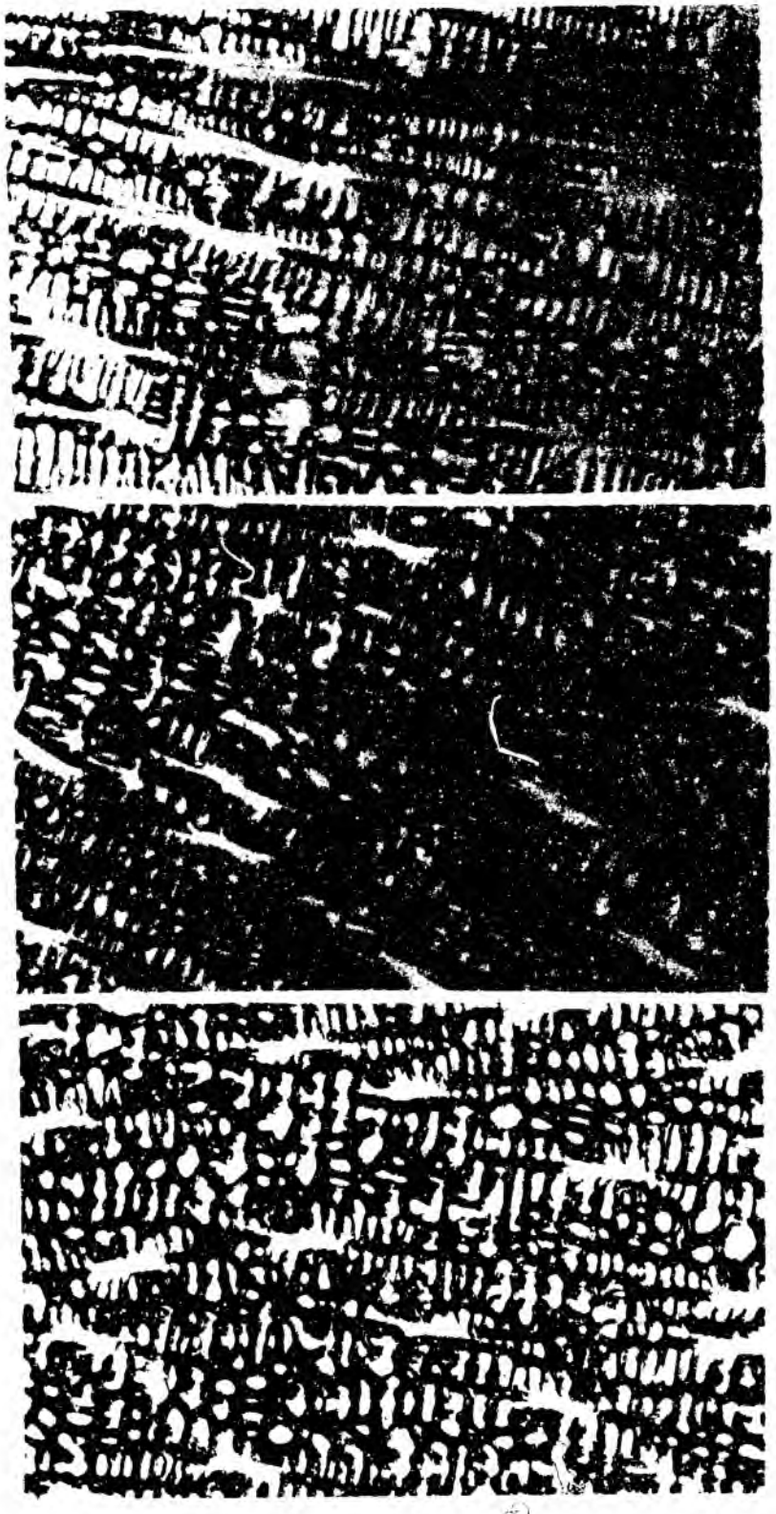

B9
1510°C
λ_1=175μm

MM22
1509°C
λ_1=200μm
Macro-grain
refinement:
20%

MM23
1504°C
λ_1=180μm
Macro-grain
refinement:
27%

Figure 6.38 continued

Table 6.12 Primary and secondary arm spacing measurements of AISI310S steal castings with additions of misch metal

Ingot no	Edge 1			Edge 2		
	Distance from the edge (mm)	Primary arm spacing (μm)	Secondary arm spacing (μm)	Distance from the edge (m.m)	Primary arm spacing (μm)	Secondary arm spacing (μm)
MM7	3	108.6	35.0	2	70.1	19.4
	5	203.3	36.6	4	80.9	26.6
	7	155.3	38.3	6	114.6	26.6
	9	224.6	40.4	8	137.9	39.6
	11	213.4	38.7	10	177.4	34.8
	13	230.2	43.1	14	434.0	58.3
	16	187.7	38.7	16	308.6	55.8
	17	210.3	37.1	20	270.3	46.1
	19	194.8	35.6			
	21	201.8	37.6			
MM8	2	46.7	20.7	2	84.3	23.9
	4	69.0	21.7	4	114.3	34.8
	6	85.4	26.9	6	119.8	32.3
	8	157.0	33.4	8	121.7	41.6
	10	205.1	43.1	10	153.9	44.5
	12	228.6	43.0	12	236.6	43.7
	14	253.8	46.0	14	229.5	42.2
	16	254.0	48.6	16	271.1	41.1
	20	261.5	47.8	20	354.5	40.3
	24	253.0	47.4			
MM9	2	54.8	21.4	2	54.0	18.9
	4	88.1	25.8	4	68.8	21.6
	6	83.5	27.5	6	69.0	25.2
	8	123.3	31.0	8	117.0	32.6
	10	137.6	31.9	10	133.7	34.0
	12	141.6	33.9	12	191.9	36.6
	14	220.0	37.8	14	251.3	41.8
	16	213.7	42.0	16	364.6	43.6
	18	199.1	41.6	18	300.8	44.9
	20	235.8	37.5	20	326.8	40.8

Table 6.12 continued

Ingot no	Edge 1			Edge 2		
	Distance from the edge (mm)	Primary arm spacing (μm)	Secondary arm spacing (μm)	Distance from the edge (mm)	Primary arm spacing (μm)	Secondary arm spacing (μm)
MM14	2	54.5	24.0	4.5	85.9	24.1
	7	147.2	30.5	9.5	206.8	35.6
	12	166.7	37.2	14.5	375.0	42.8
	17	189.2	43.0	19.5	367.0	42.8
	22	256.8	41.3	24.5	239.2	37.4
	27	219.2	32.1			
MM15	2	44.7	18.2	2	85.8	16.8
	4	63.3	22.4	4	64.3	22.4
	6	104.8	26.4	6	80.2	28.2
	8	115.0	25.5	8	98.9	28.7
	10	163.8	36.9	13	227.0	48.3
	15	267.0	45.3	18	362.8	43.9
	20	228.6	41.4	23	391.0	32.1
	25	202.1	32.9			
MM16	2	84.7	21.5	2	129.2	21.8
	4	118.3	26.1	4	114.3	27.3
	6	114.6	28.8	6	148.4	32.9
	9	211.3	43.1	7	250.7	45.0
	14	282.2	49.1	12	303.2	43.6
	19	207.0	40.9	17	175.8	37.4
MM17	2	35.0	15.7	2	41.4	20.5
	4	60.9	23.1	3	70.0	23.8
	5	57.7	25.1	4	72.2	26.2
	6	91.1	29.5	6	122.1	31.4
	10	193.5	36.5	7	189.0	37.2
	15	221.4	40.4	12	221.4	33.3
	20	216.0	33.5	17	200.2	34.4
MM18	2	69.5	27.9	3	46.4	21.1
	4	98.9	28.9	4	53.7	26.3
	6	129.5	29.6	6	125.0	33.8
	7	122.0	33.9	8	189.2	42.1
	10	126.1	30.7	10	207.5	36.7
	12	138.0	30.2	13	184.0	39.2
	17	106.9	31.6	18	157.7	39.8
	22	100.7	32.7	23	119.3	38.2
	27	150.0	38.9	28	159.8	33.1

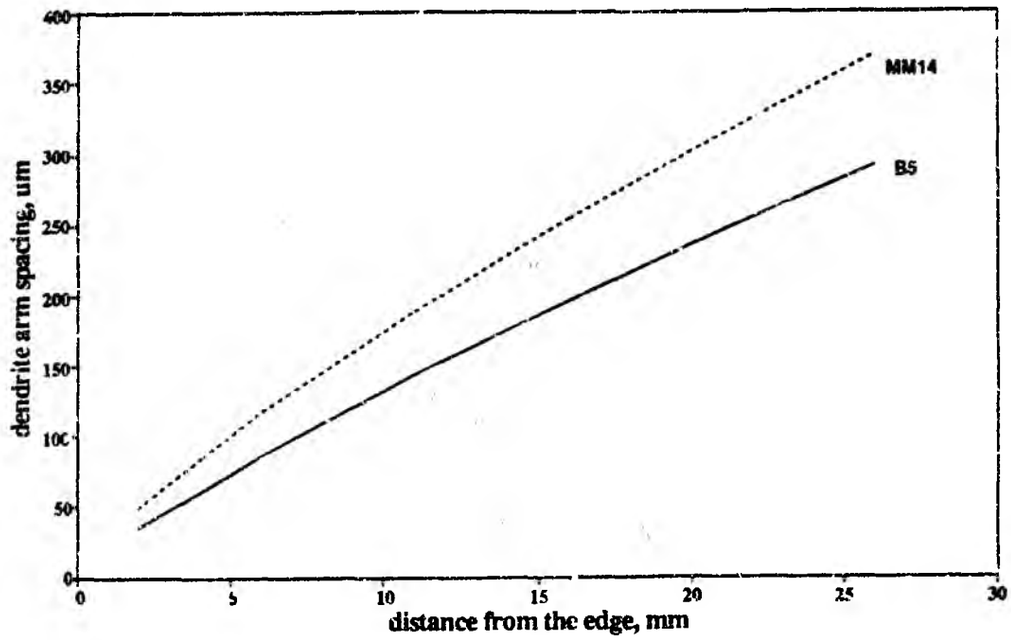

Figure 6.39 Regression curves showing arm spacing against distance from the chill zone for a base metal ingot cast from 1545°C and for an ingot containing misch metal (MM14) cast from 1550°C

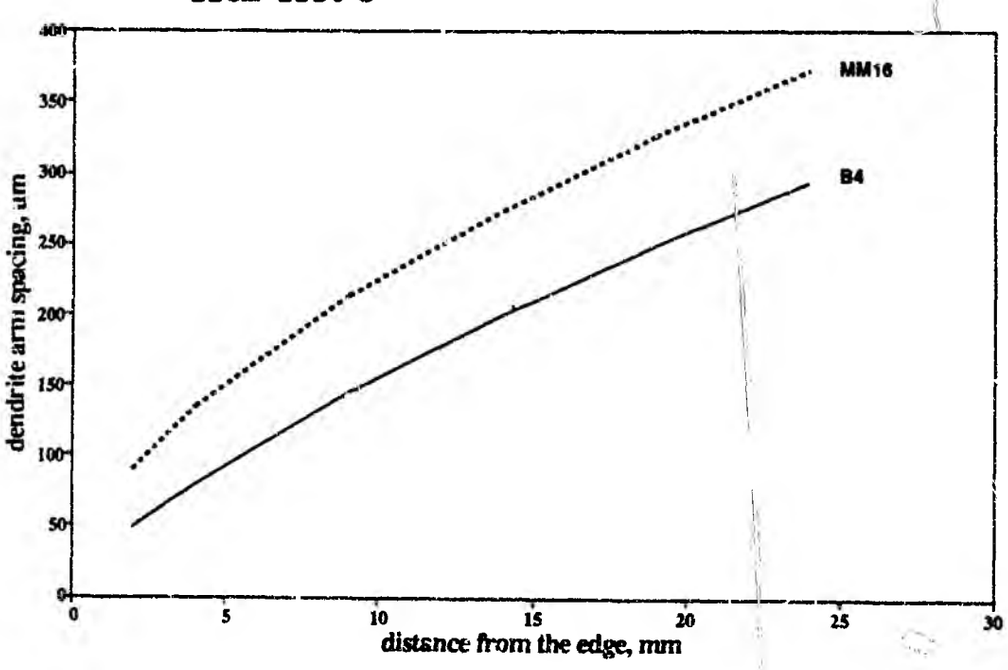

Figure 6.40 Regression curves of primary dendrite arm spacing against distance from the chill zone for a base metal ingot cast from 1564°C and for an ingot containing misch metal (MM16) cast from 1551°C

Figure **6.39** shows regression lines obtained from the measured primary arm spacings in ingot B5, (base metal ingot cast from 1545°C) and for ingot MM14 whose macrostructure was about 40% finer than that of ingot B5. It can be seen that the microstructure of ingot MM14 is about 40% coarser than that of the base metal ingot B5. The same effect can be seen in Figure **6.40**, which compares ingots MM16 and B4. The macrostructure of ingot MM16 was about 50% finer than that of B4. However its microstructure is coarser by an average value of more than 50%. The regions closer to the edges were more than 100% coarser.

The change in secondary arm spacing with primary arm spacing was analysed, separately for each sample. All the data were then combined to get an overall view and compare the results with those obtained from base metal ingots (Figure **6.41**). The logarithmic regression line obtained with ingots containing misch metal almost coincided with that of base metal ingots cast from a low temperature (Figure **6.32(a)**). However it should be noted here that the average casting temperature range for ingots containing misch metal was about 40°C higher than the temperature range in Figure **6.32(a)**. The macrostructure of ingots containing misch metal corresponded to that of base metal ingots cast from 1476 to 1526°C.

Thus for the same range of grain width the relationships between primary and secondary arm spacings for ingots with and without misch metal were similar. This could be evidenced further by plotting the change in secondary arm spacings per 100 µm change in primary arm spacing against columnar grain width and grain width ratio (Figures **6.42** and **6.43**).

As can be seen from Figure 6.42, the change in secondary arm spacing per 100 µm primary arm spacing decreased 11µm with about 210µm increase in macro grain width.

A similar trend was observed when the same data was plotted against grain width ratios obtained for these samples (Figure 6.43). As the grain width ratio increased from about 1.3 to 1.7, the change in secondary arm spacing per 100 µm primary arm spacing decreased 11µm. When percent increase in grain width ratio and percent decrease in secondary arm spacing change was calculated from Figure 6.43 they were both found to be 20%. This means that as the grain width ratio increased, the ratio of secondary to primary arm spacing decreased in the ratio of 1 to 1.

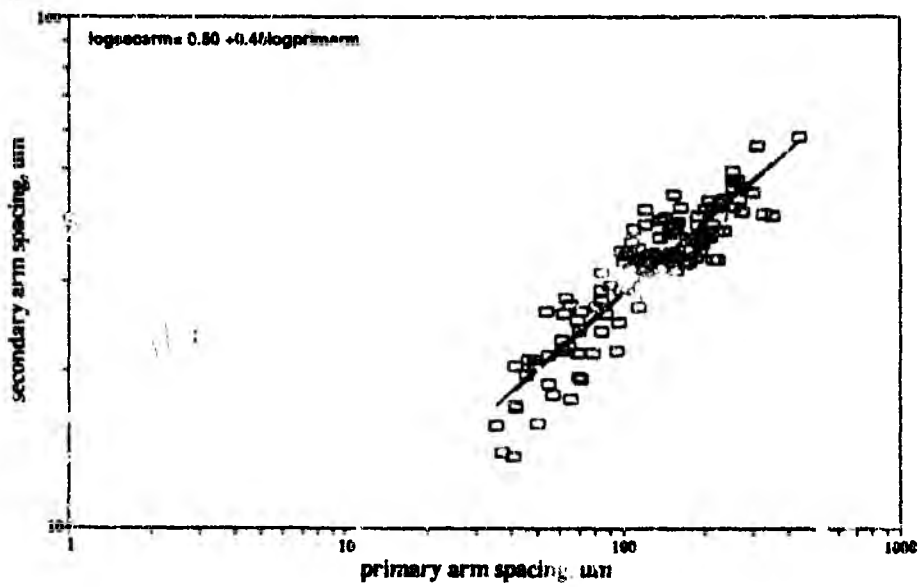

Figure 6.41 Change of secondary arm spacing with changing primary arm spacing for the AIST310S ingots with misch metal additions

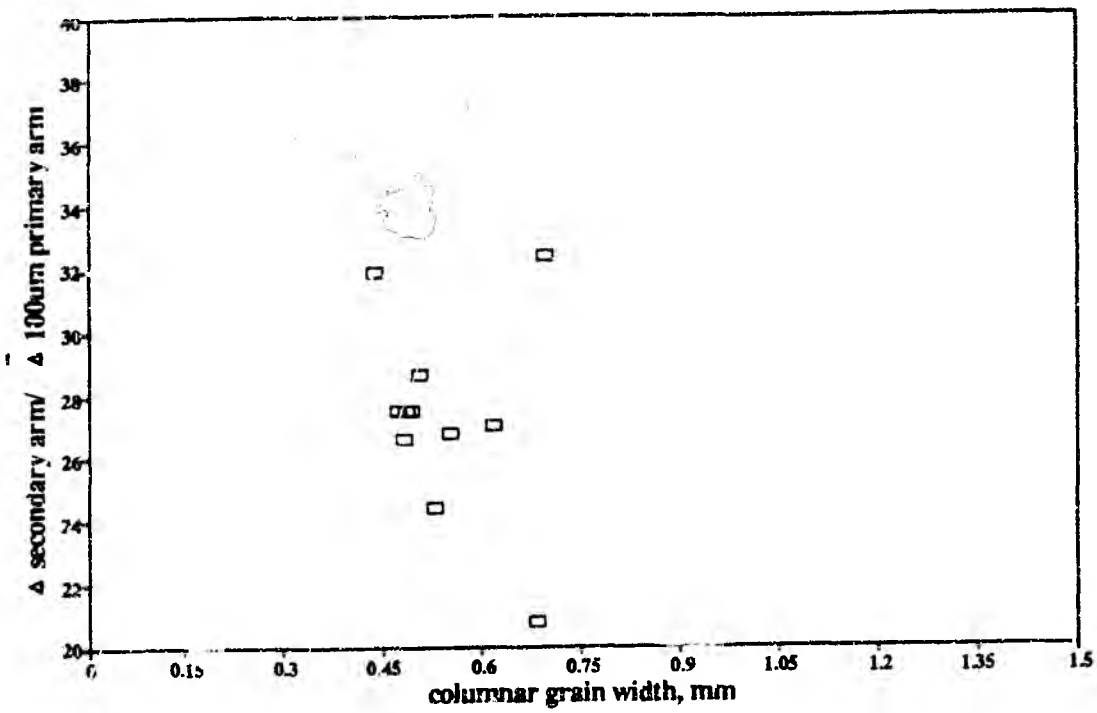

Figure 6.42 Change of Δ secondary arm spacing/Δ100μm primary arm spacing with columnar grain width for AISI310S steel with misch metal additions

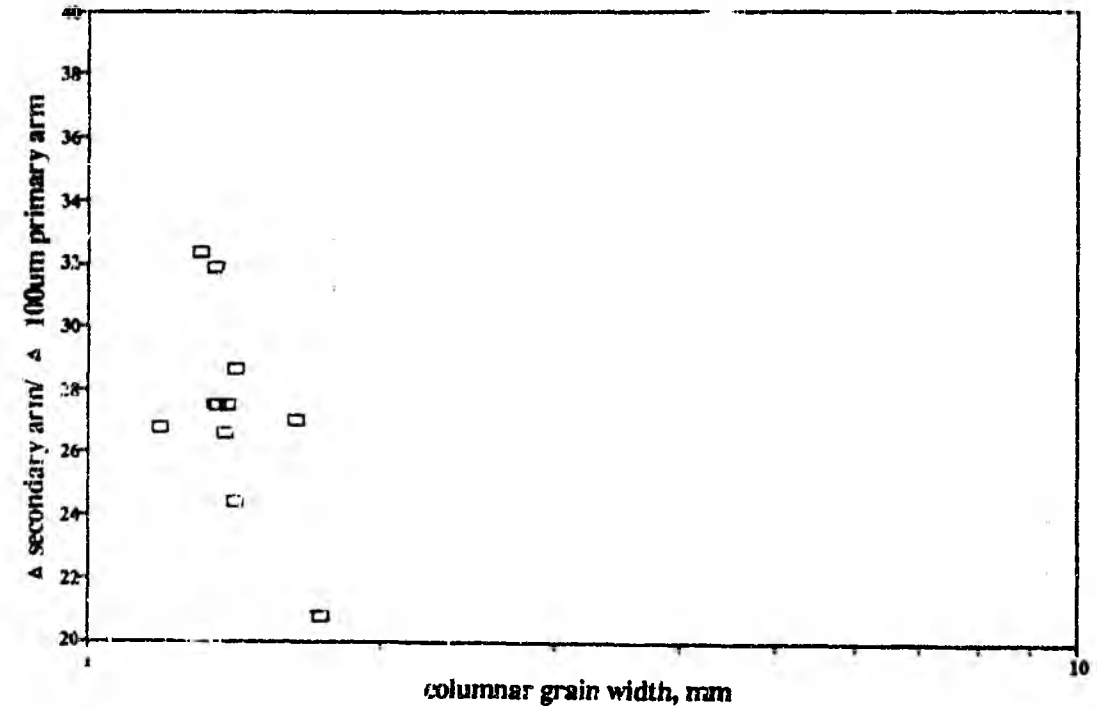

Figure 6.43 Change of Δ secondary arm spacing/Δ100μm primary arm spacing with grain width ratio for AISI310S steel with misch metal additions

6.3.3 Microstructural Evaluation of Ingots with FeSiZr Additions

This section deals with the analyses of ingots cast with additions of FeSiZr together with Al and/or misch metal.

As can be seen from the micrographs in Figure **6.44**, in which the micrograph of a base metal ingot is also given for comparison, although there was a strong orientation effect in the microstructure with FeSiZr additions, the primary and secondary arm spacings appeared to be finer than those observed with base castings.

6.3.3.1 Primary and Secondary Dendrite Arm Spacings in Castings Containing FeSiZr

The results of measurements of dendrite arm spacings (primary and secondary) for the selected castings with FeSiZr additions are given in Table **6.13**. These results when compared with the results obtained for base metal B4, B5, and B6 cast from the same temperature range, show that the refinement of the primary arm spacings could be as high as 50-60%. The secondary arm spacings seem to be smaller by about 20%. These results are evident from Figures **6.45** and **6.46**. In the low casting temperature region the refinement of the dendritic arm spacing was more significant. Secondary arm spacing also showed considerable refinement. However when primary and secondary arm spacings were plotted against added Zr (Figure **6.47**) they displayed opposite trends; i.e. as the amount of Zr addition increased, the secondary dendrite arm spacing tended to get smaller, whereas the primary arm spacing increased. When the same data was plotted against columnar grain width (Figure **6.48**), the primary dendrite arm spacing decreased as the grain width increased.



Figure 6.44 Micrographs of as-cast AISI310S ingots with FeSiZr additions

Table 6.13 Primary and secondary arm spacings for ingots containing FeSiZr

Ingot no	Edge 1			Edge 2		
	Distance from the edge (mm)	Primary arm spacing (μm)	Secondary arm spacing (μm)	Distance from the edge (mm)	Primary arm spacing (μm)	Secondary arm spacing (μm)
ZR9	2	30.9	14.5	2	42.8	21.6
	4.2	87.0	23.9	3.8	82.3	20.4
	6	87.1	22.5	6	87.3	22.1
	8	93.7	26.0	8.8	116.4	27.7
	9.2	105.7	32.4	10	113.8	28.8
	10	109.2	29.5	13.8	154.5	34.2
	12	161.1	31.3	15	166.9	33.3
	14	158.1	30.6	18	180.5	33.0
	14.2	193.0	34.7	18	284.3	32.5
	16	237.2	36.8	18.8	316.7	35.2
	19.2	229.8	37.0	23.8	268.4	29.2
ZR10	2	36.8	14.3	2	57.0	18.8
	4	56.8	19.8	3	82.5	18.2
	4.5	84.5	21.8	4	88.7	24.4
	6	104.2	23.6	6	111.2	25.7
	8	125.7	36.1	8	145.0	28.2
	9.5	106.6	36.1	10	148.8	38.2
	10	167.5	37.2	12	146.1	36.4
	12	166.3	37.6	14	32.7	32.8
	14	176.7	43.1	16	171.8	34.5
	16	221.5	45.3	18	183.7	32.0
	18	250.0	45.9	20	207.1	34.4
	24.5	247.8	42.5	23	231.0	34.7
				26	237.5	35.8
ZR20	2	81.1	16.9	2	72.7	21.4
	4	77.7	26.1	4	106.8	23.6
	6	107.3	28.0	6	125.8	27.1
	8	155.4	26.7	8	157.8	29.7
	10	164.7	29.3	10	211.0	30.1
	11	179.6	31.2	12	211.1	32.5
	16	185.0	28.7	18	204.0	30.4
				26	135.9	23.1

Table 6.13 continued

Ingot no	Edge 1			Edge 2		
	Distance from the edge (mm)	Primary arm spacing (μm)	Secondary arm spacing (μm)	Distance from the edge (mm)	Primary arm spacing (μm)	Secondary arm spacing (μm)
ZR21	5	63.4	17.7	2	52.0	19.6
	7	81.6	22.5	4	71.3	20.0
	10	116.6	33.4	6	101.5	22.8
	12	96.9	35.4	8	100.9	26.5
	15	133.6	38.9	9	123.8	31.4
	20	143.6		10	121.0	32.1
				12	117.6	32.7
				14	105.3	36.2
				16	124.0	34.0
				19	133.6	48.6
ZR22	2	56.9	18.2	3	70.8	18.1
	4	88.6	19.8	5	87.0	23.1
	8	96.1	24.9	10	103.6	29.3
	11	132.7	28.7	15	141.6	34.2
	18	145.4	32.6	20	144.2	36.2

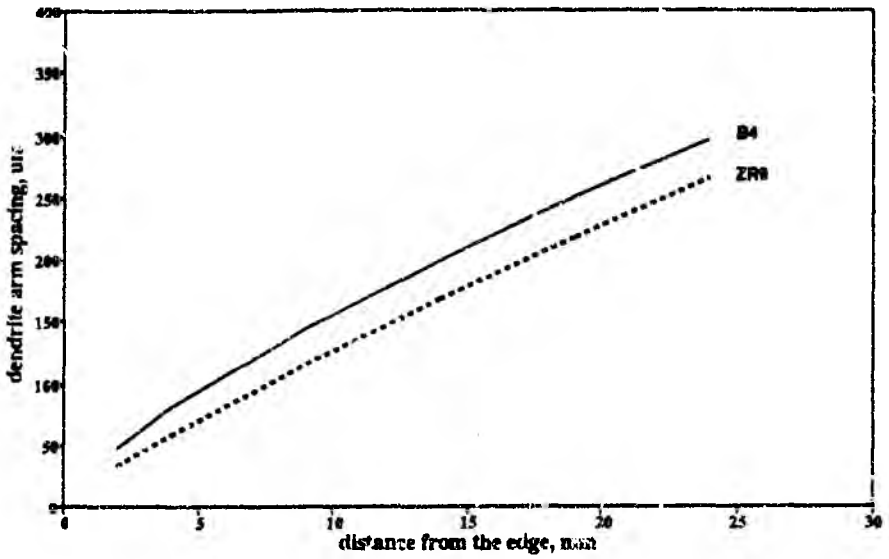

Figure 6.45 Primary dendrite arm spacings against distance from the chill zone: (a) regression curve for base metal ingot (B4) cast from 1564°C and (b) similar curve for FeSiZr containing ingot (ZR9) cast from 1560°C

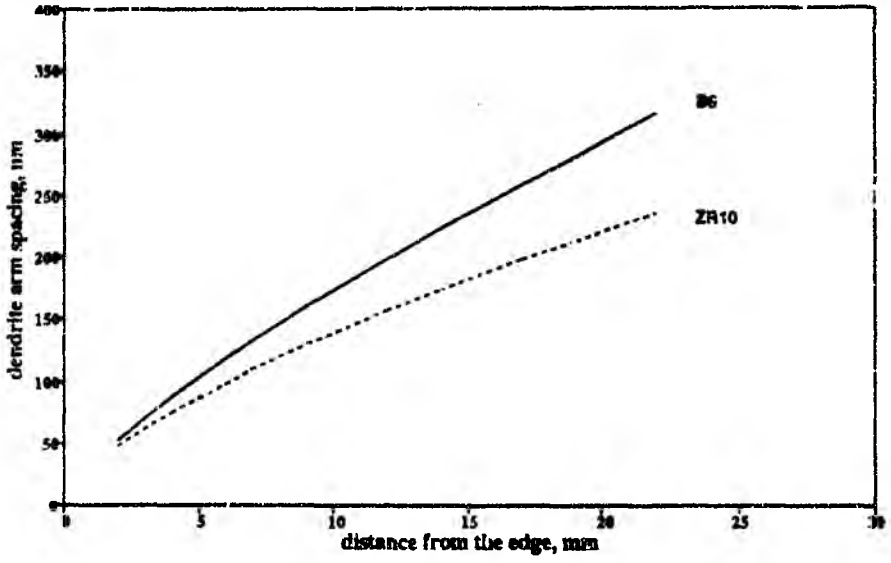

Figure 6.46 Primary dendrite arm spacings against distance from the chill zone: (a) regression curve for base metal ingot B6 cast from 1537°C and (b) similar curve for FeSiZr containing ingot ZR10 cast from 1545°C

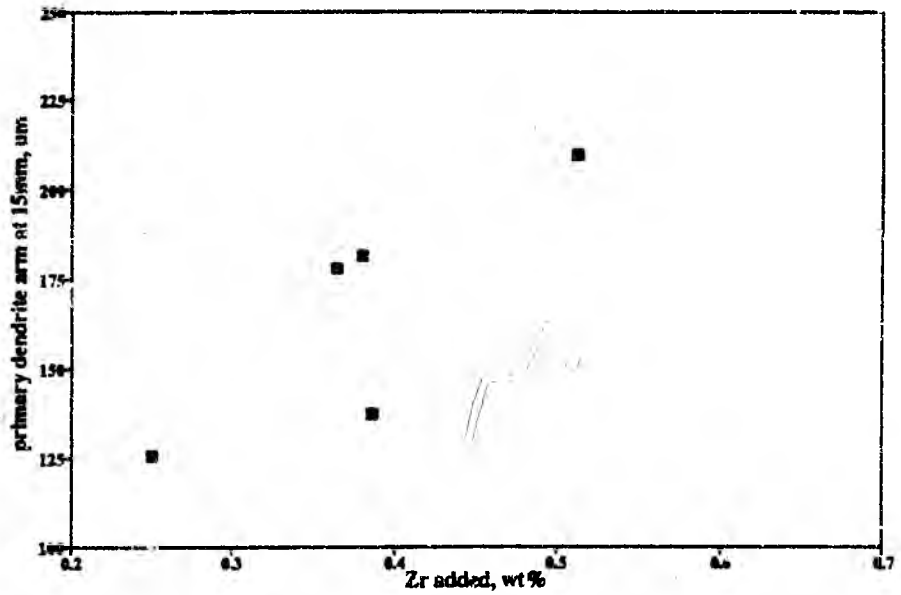

(a)

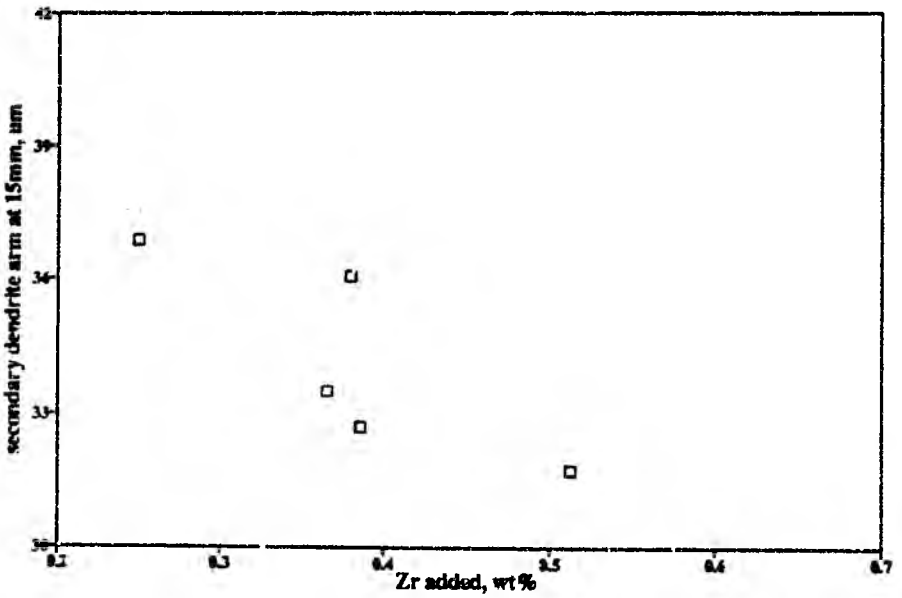

(b)

Figure 6.47 Change of (a) primary and (b) secondary arm spacings measured at 15mm from the chill zone of ingots with changing amount of Zr addition

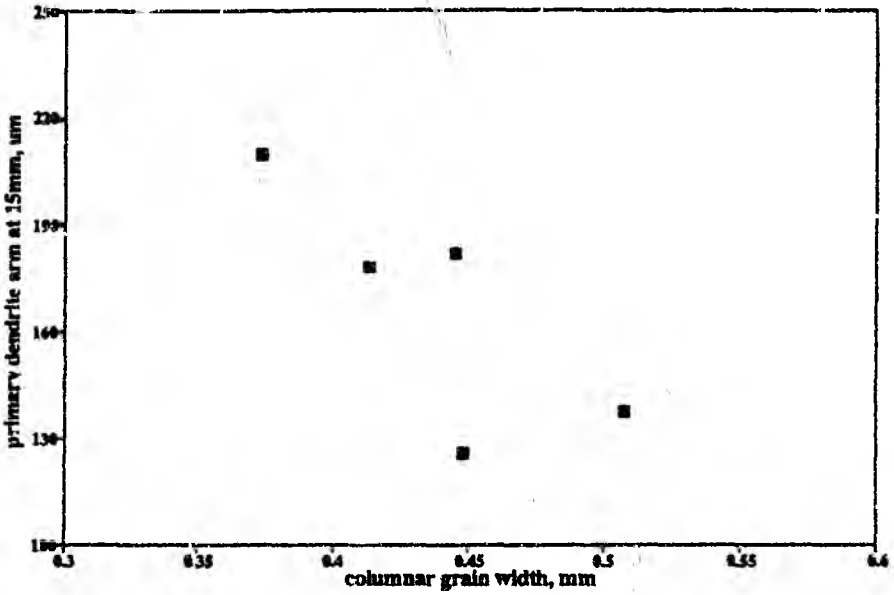

(a)

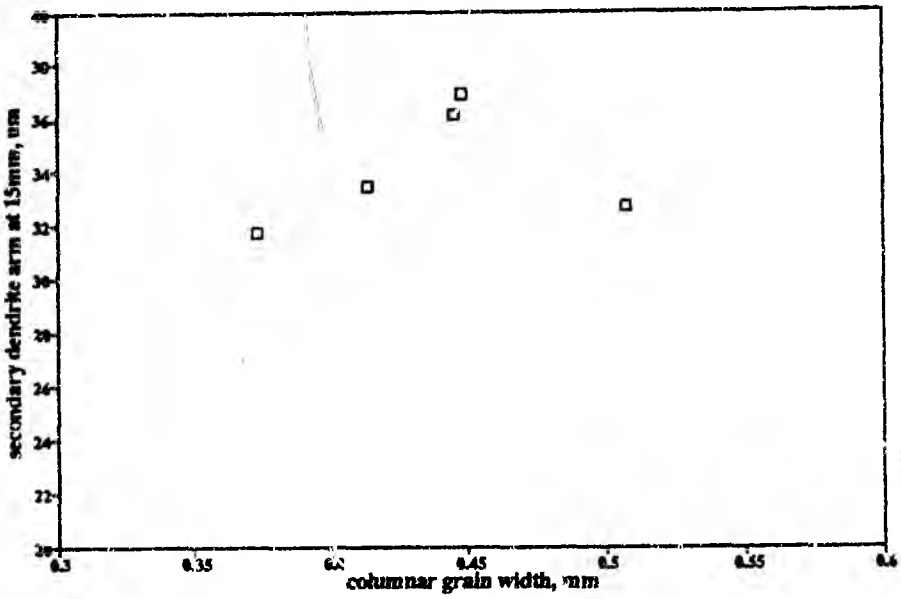

(b)

Figure 6.48 Change of (a) primary and (b) secondary arm spacings measured at 15 mm from the edge of ingots with FeSiZr additions as a function of columnar grain widths measured at 6 mm from the edge

This is similar to the trend observed with ingots containing misch metal although the secondary dendrite arm spacing showed a slight increase initially followed by a drop. It should be noted here that these points for the secondary arm spacings should be treated cautiously due to an error range of 2 μm in measurements. This statement will be discussed further in the next chapter.

Changes in secondary arm spacings with primary arm spacings were also analyzed separately for each sample. The results were plotted against various parameters to establish possible correlations. The change in secondary arm spacing per 100μm change in primary arm spacing is plotted against the amount of added Zr in Figure 6.49. This suggests a relationship which confirms the earlier observation that as the amount of Zr increased the secondary dendrite arm spacing tended to get smaller whereas the primary arm spacing increased. This in effect means that if the secondary arm spacing is kept constant the primary arm spacing increases.

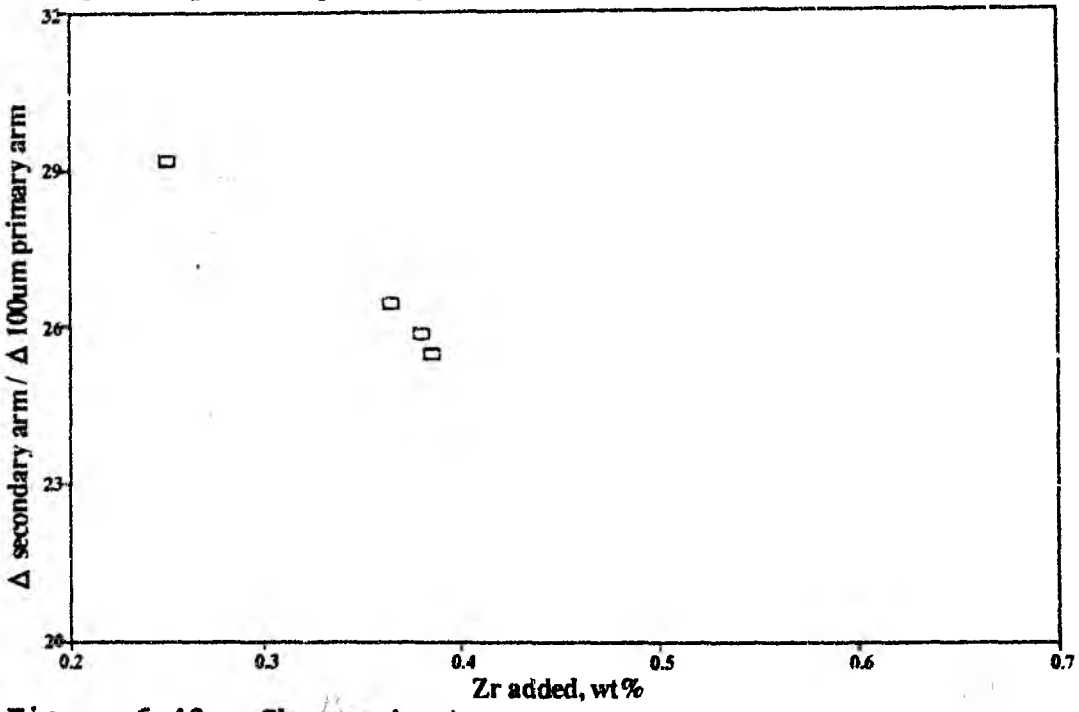

Figure 6.49 **Change in Δ secondary arm spacing/Δ100μm primary arm spacing of ingots as a function of Zr addition**

6.4 Mechanical Properties of the As-Cast AISI310S with or without Additions

6.4.1 Tensile and Impact Test Properties

The results of the tensile and impact tests carried out on specimens from selected base metal ingots and ingots cast with misch metal, and FeSiZr additions are summarized in Table **6.14**. The values in parentheses are those obtained from material in the as-cast condition. The rest of the results were obtained from material that had been homogenized at 1150°C for 2hr and water quenched.

Tensile test results are plotted as a function of columnar grain width to determine whether the additions had any effect on the strength of AISI310S other than that which might have resulted from a finer grain structure.

As can be seen from Figure **6.50(a)** the tensile strength of the homogenized base metal castings showed an initial drop in strength with increasing columnar grain width. However as the macrostructure changed to 70% equiaxed from a columnar one, the tensile strength showed an increase of about 12% from 452 MPa to 510 MPa.

The difference between the transversal and longitudinal tensile strengths also decreased as the grain width decreased. For a grain width of 0.666mm the difference was a mere 0.4 MPa and increased to about 23.4 MPa as the grain width increased to 0.975mm at 14mm from the edge. It should also be noted that the longitudinal samples had higher tensile strengths.

Table 6.14 Mechanical properties of the as-cast AISI310S ingots with or without additions

Ingot no	Columnar grain width (mm)		YS MPa	TS MPa	Elongation %	Reduction in Area %	Reduction in Diameter % (Transverse) Long axis Short axis	Reduction in Diameter % (Longitudinal) Long axis Short axis	Notch Impact Energy (J)
	6mm	14mm	Trans. Long.	Trans. Long.	Trans. Long.	Trans. Long.			
B6	0.711	0.975	269.1 233.3	466.3 492.7	46.5 53.0	72.0 70.0	58.0 38.1	53.0 38.0	260 262
B8	0.517	0.710	247.8 258.0	441.4 454.5	47.5 45.0	60.8 58.8	48.6 28.2	45.5 27.2	170 196
B13	0.434	0.666	240.5 249.3	452.4 452.0	50.0 54.0	69.6 66.7	49.0 41.4	46.8 38.6	242 253
B15	0.321	-	287.0 278.6	509.6 516.1	50.0 48.0	65.0 62.5	41.8 39.6	40.0 37.6	220 230
B17*	0.595	0.780	244.0 (208.8) 260.0 (204.0)	453.0 (433.0) 469.0 (458.0)	52.0 (48.2) 55.0 (47.1)	69.8 (66.5) 67.9 (62.2)	50.0 (57.6) 38.1 (38.0)	44.0 (43.4) 40.0 (34.0)	240 250
MM20	0.355	0.485	260.0 262.5	454.0 475.1	50.5 48.0	71.1 62.9	53.0 39.8	45.4 33.4	232 286
MM23	0.429	0.549	258.1 269.8	457.5 472.1	47.5 45.0	65.9 65.8	54.9 45.6	50.6 36.8	296 302
MM21	0.464	0.553	243.2 246.5	454.5 463.3	51.0 51.0	72.1 67.2	52.0 42.8	47.0 40.4	195 217
MM22	0.440	0.572	247.0 248.0	456.0 460.7	50.3 51.0	74.9 67.8	46.8 37.3	45.8 37.6	196 251
ZR18	0.354	0.493	- (203.7) 219	- (443.0) 458	- (52.0) 66.0	- (52.7) 65.1	- (39.5) - (23.0)	44 38	175 225
ZR19	0.373	0.471	215.0 (196.1) 231	438.0 (432.9) 458	54.4 (48.0) 52.0	69.8 (51.7) 66.0	34.7 (44.5) 35.4 (15.5)	37.5 36.5	180 210
ZR22	0.507	0.674	247.8 268.4	449.5 476.5	49.0 45.0	61.6 60.9	43.6 33.2	39.2 35.8	230 270

*AISI310S ingot test results taken from a parallel work

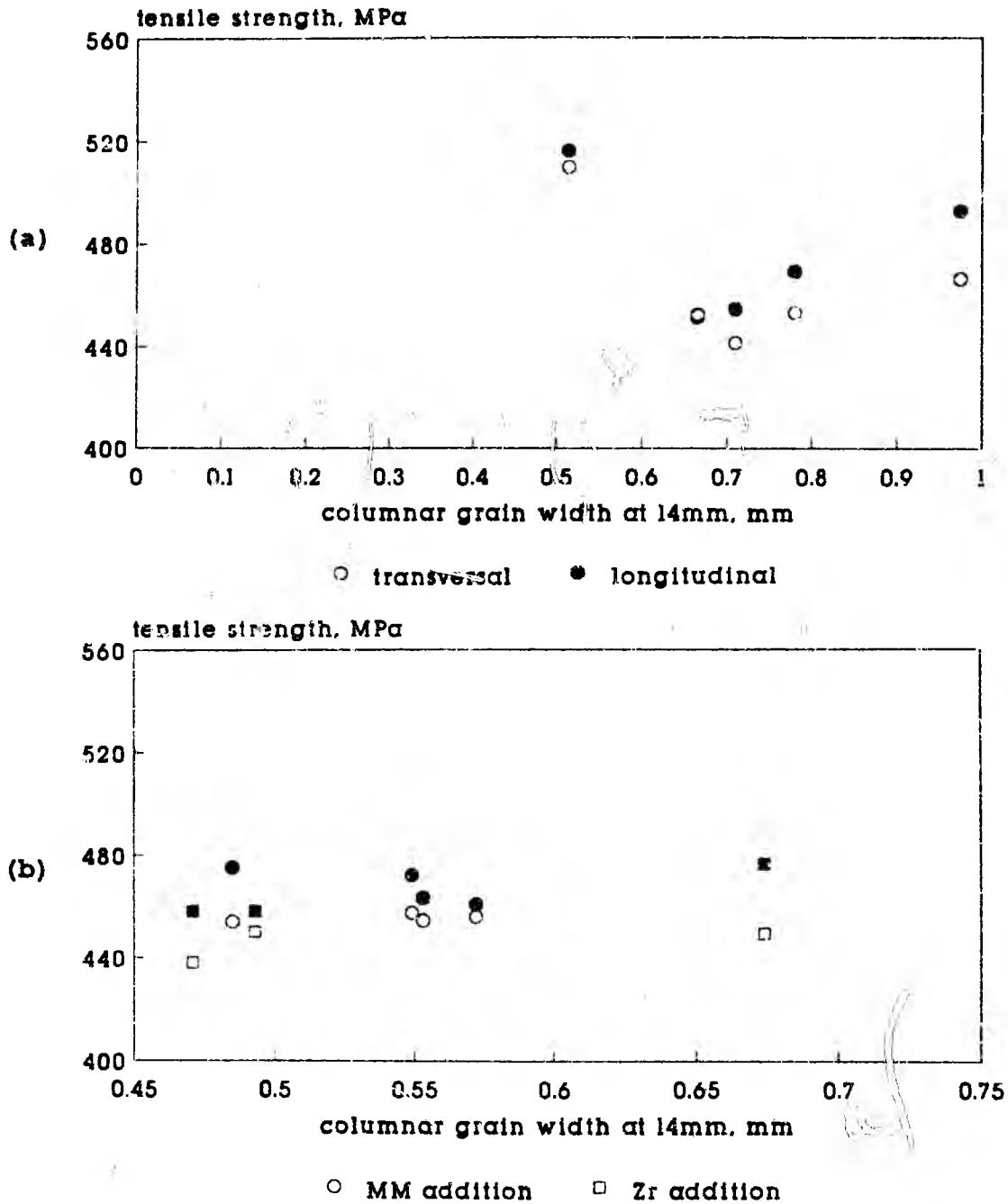

Figure 6.50 Change in tensile strength as a function of columnar grain width for as-cast AISI310S steel ingots with (a) no addition and (b) misch metal or FeSiZr additions

Figure **6.50(b)** gives the tensile strengths obtained for the castings with misch metal and FeSiZr additions. All these samples are taken from the columnar zone of the ingots which did not have a comparable equiaxed zone. As can be seen from these plots, the ingots with misch metal and FeSiZr additions, on average, followed the same trend as that of the base ingots.

All these values are well below the values obtained from equiaxed grained ingot. However, it should be borne in mind that these ingots (with MM and FeSiZr) were cast in the temperature range 1545 to 1550°C, whereas the base metal ingots were cast from temperatures between 1436 and 1537°C. The difference between transversal and longitudinal strengths is minimal especially in the lower grain width range for all the additions.

Figure **6.51** gives the yield strengths obtained with the base metal ingots and the ingots with additions. The yield strength of base metal ingots decreased from 293.3 MPa at 0.995mm grain width to 249.3 MPa at 0.666mm grain width. Transverse yield strengths for the same ingots decreased from 269.1 MPa to 250.5 MPa within the same range of grain width. Thus the yield strength of longitudinal samples decreased by about 15%, whereas that of transverse samples decreased by 10% for the same range of grain width. This suggests that in the longitudinal direction the material is more sensitive to changes in grain width.

When the decrease in tensile strengths for the same grain width range is considered (8.3 and 3.0% in the longitudinal and transverse directions respectively), it can be said that the yield strength is more sensitive to changes in columnar grain width than the ultimate tensile strength.

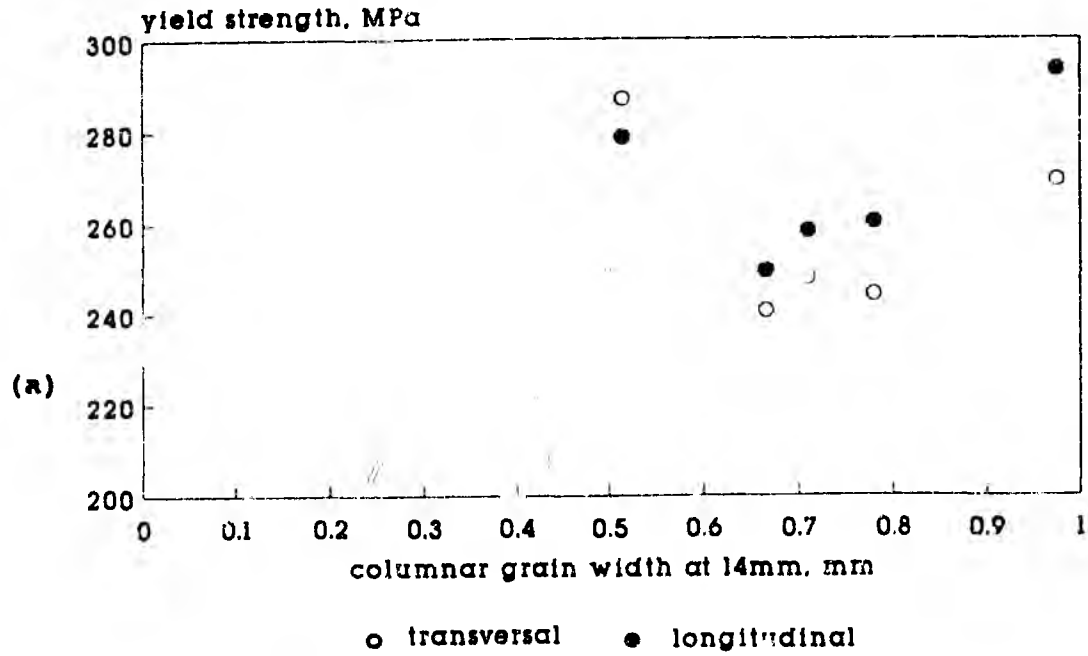

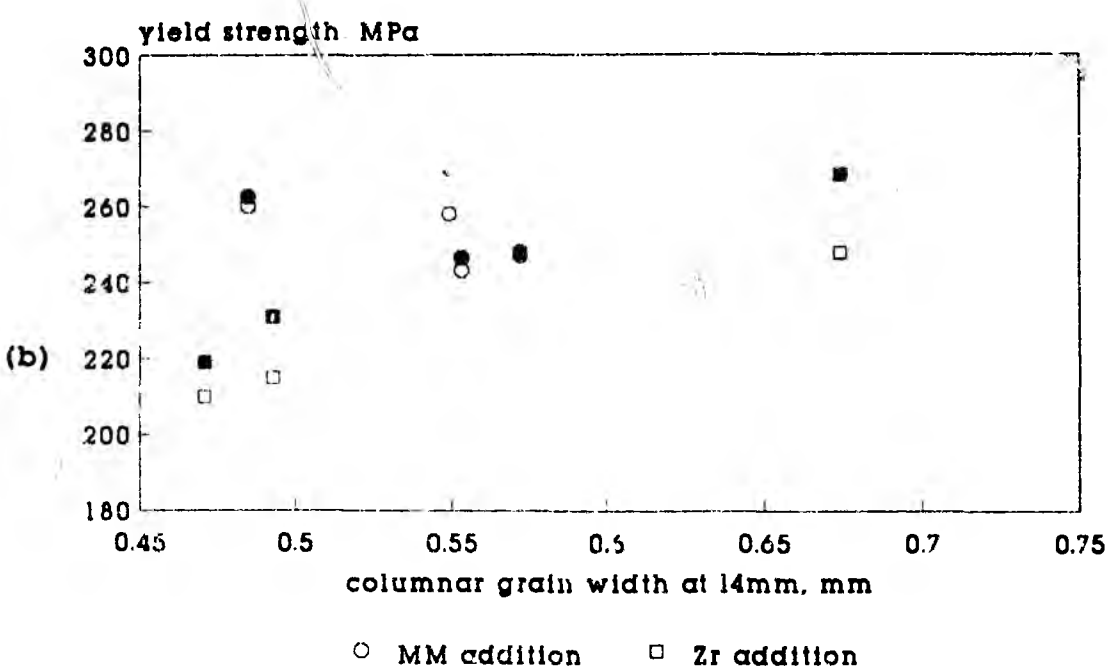

Figure 6.51 Yield strength as a function of columnar grain width for as-cast steel ingots with (a) no additions and (b) misch metal and FeSiZr additions

The difference between longitudinal and transverse yield strengths decreased from about 8.3% to about 3.5% as the grain width decreased from 0.995 to 0.666mm (Figure **6.51**). In the equiaxed grained ingot (the first set of two points in Figure **6.51**) the yield strength was significantly higher than that obtained with columnar ingots except for the ingot with the largest grain width. The mean value of yield stress for the equiaxed ingot and the ingot with the greatest grain width (Figure **6.51**) is practically the same. However the equiaxed ingot shows a greater degree of isotropy.

Figure **6.51**(b) shows a plot of yield strength against columnar grain width for ingots with additions. As can be seen, the ingots with misch metal additions showed a marginally higher yield strength at smaller grain widths. However the yield strength was still lower than that of base metal equiaxed ingots or ingots with large columnar structures. These ingots also showed a reduced variation in yield strength from one direction to the other. When FeSiZr was added to castings, there appeared to be a drop in yield strength unless the FeSiZr was added together with Al as was the case with ingot ZR22 (Table **6.14**). The difference in yield strength in the two directions is comparable to that observed with base metal castings.

Figure **6.52** gives the elongations obtained from ingots with or without additions as a function of columnar grain widths. Elongations for the base metal ingots showed a marginal deviation from the average value of about 50%. These deviations are of the order of 3 to 4%, and therefore no firm conclusions can be drawn from them.

The plot of elongation against grain width for ingots with additions was very similar to that for base metal ingots except for ingot ZR18 (Table **6.14**) whose elongation

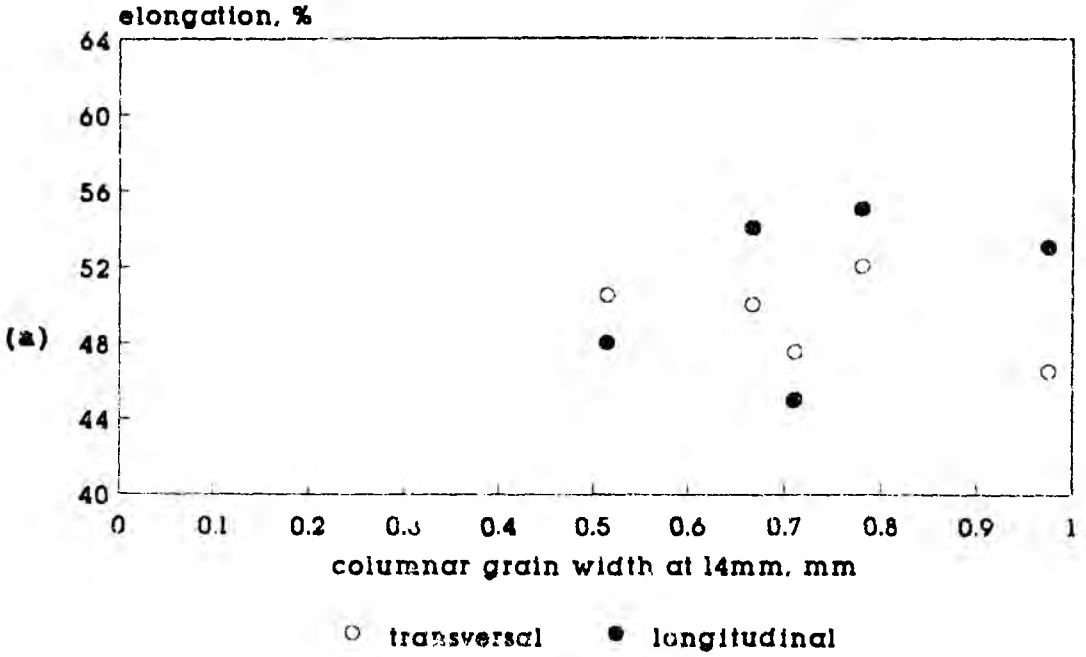

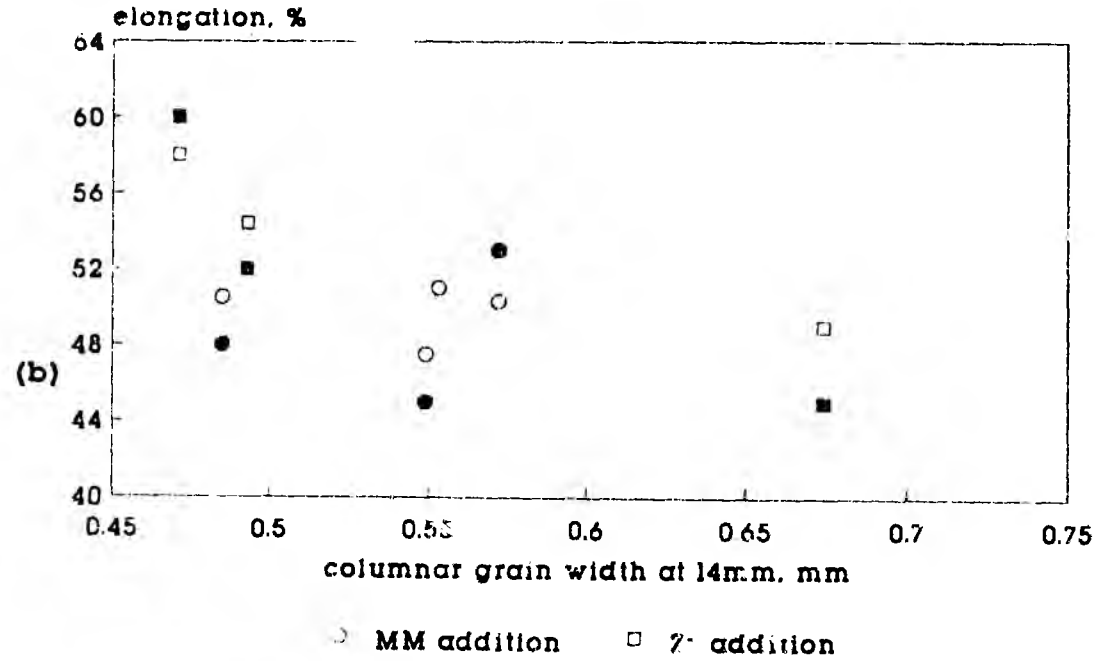

Figure 6.52 Change in % elongation as a function of columnar grain width for as-cast ingots with (a) no addition and (b) misch metal and FeSiZr additions

was 60%. It should be noted here that the majority of the samples from ingots with additions had elongations which did not vary much in the two directions. Elongation results do not show whether one of the directions was consistently superior to the other in ductility.

Figure **6.53** gives the change in reduction in area (RA) with columnar grain width for ingots with or without additions. Figure **6.53(a)** shows a slight decrease in RA as the grain width gets smaller. Ingot B15 which was 70% equiaxed had a RA of 64%, whereas B6 with a completely columnar structure and a grain width of 0.975mm had an RA of 71% (average of two directions). The RA's obtained from ingots with additions (Figure **6.53 (b)**) showed that with misch metal and FeSiZr, the reduction in area on average was as high as the highest obtained with the base castings (B6, 71%).

It can be seen that transverse RA's are higher than those obtained with longitudinal samples for almost all the ingots with or without additions.

The fracture surfaces of samples with columnar structures were elliptical in section due to anisotropic behaviour. In order to examine the influence of additions, grain width and grain structure on the uniformity of deformation, the long axis and short axis of the fracture surface of the tensile samples was measured and is given in Table **6.14**.

The differences in length between the long and short axes are plotted as bar graphs in Figure **6.54**. In bar graph **(a)**, which gives the differences for base ingots, it can be seen that the difference in length between the two axes of the fracture surface decreased as the grain width decreased.

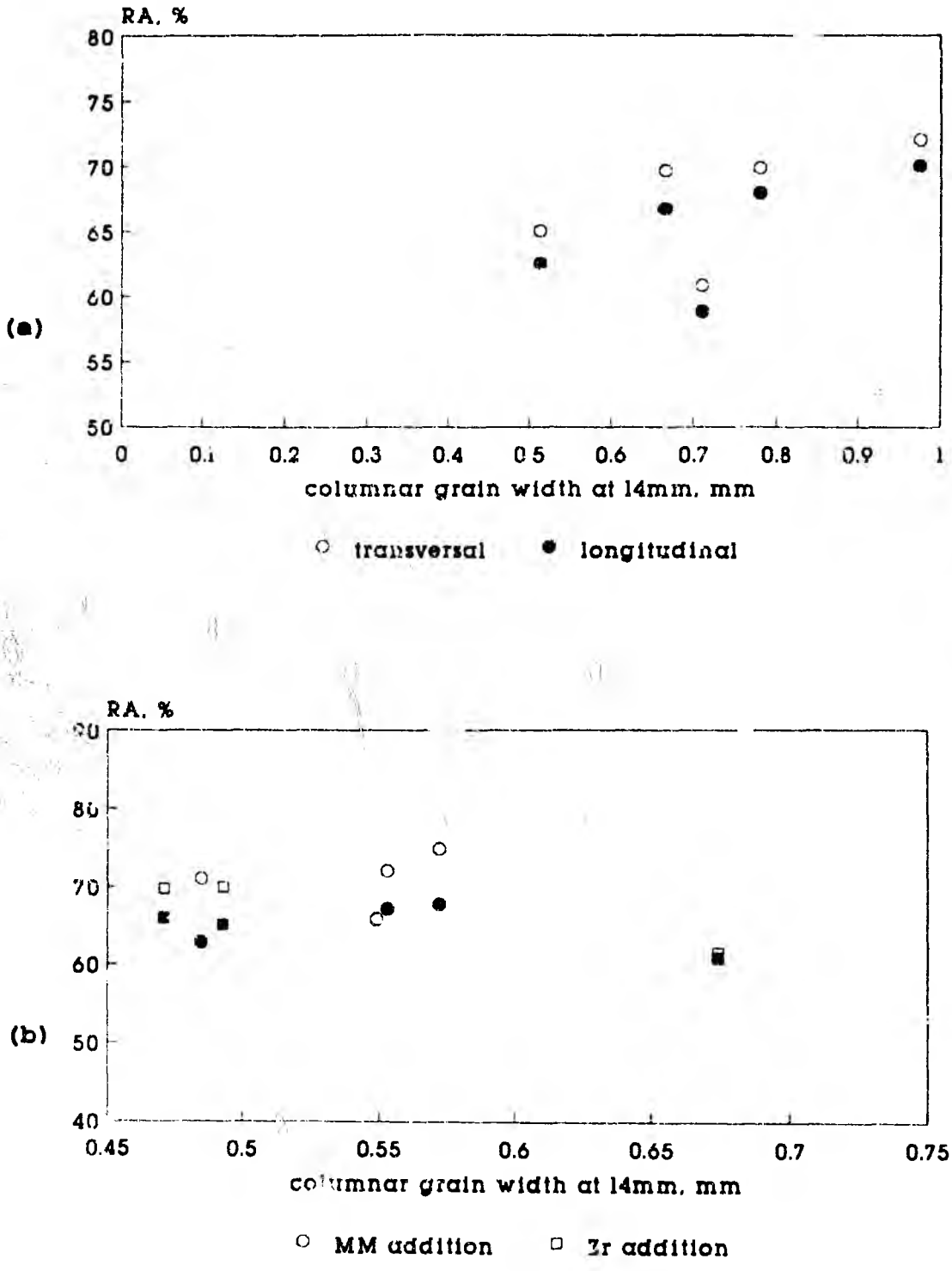

Figure 6.53 Change in % reduction in area as a function of columnar grain width for as-cast ingots with (a) no addition and (b) misch metal and FeSiZr additions

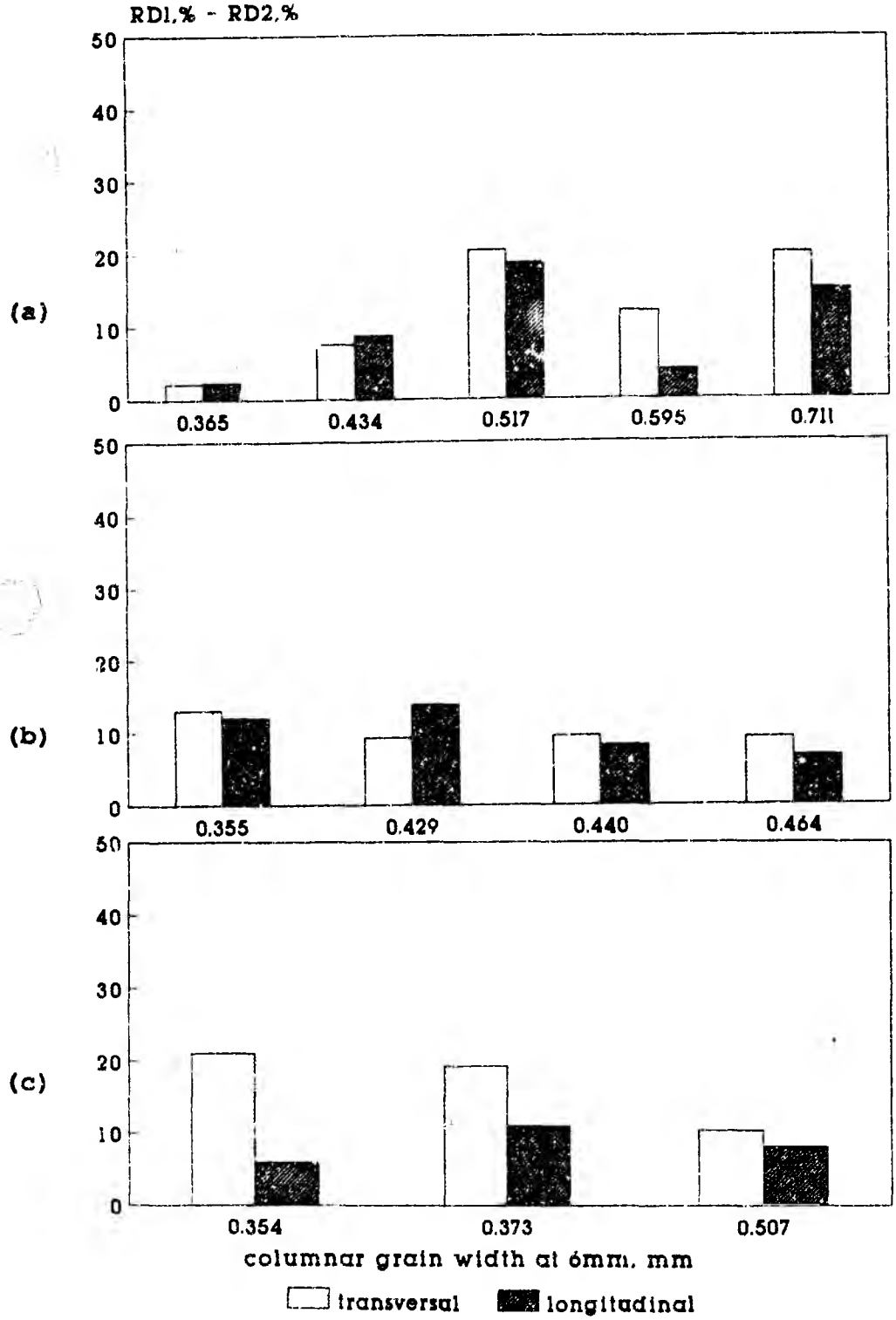

Figure 6.54 Histograms displaying the differences in percentage reduction in diameter along two perpendicular axes of the fracture surfaces for the longitudinal and transverse tensile test pieces of ingots with (a) no addition, (b) misch metal addition and (c) FeSiZr addition

The difference between the two axes of the ingot with 70% equiaxed zone was 2.2% whereas that in the ingot with a columnar structure of 0.975mm grain width was about 20%. Misch metal and FeSiZr containing ingots showed differences in the range of 6 to 15% in the lengths of their two axes. This indicates a more or less uniform deformation prior to failure of the test pieces. The bar graphs also indicate that, in most of the cases, longitudinal samples showed smaller differences between their long and short axes than did transverse samples. The differences in the shape of the fracture surfaces of some of these samples are shown in Figure **6.55**.

6.4.1.1 Tensile Properties in the As-Cast Condition

Selected samples were tested in tension in the as-cast condition (prior to homogenization) to study the effect of additions on tensile properties. The results are given in parentheses below the corresponding values obtained with homogenized specimens in Table **6.14**. From this limited number of results, the major effect of homogenization appears to be an increase in yield strength of up to 35% for a 2h treatment at 1150°C followed by a water quench (Figure **6.56**).

The improvement in tensile strength for the same ingots was not as impressive as that in yield strength, being only a few percentage points (Figure **6.57**). The bar graphs in Figures **6.58** and **6.59** give the changes in elongation and RA due to the homogenizing treatment. As can be seen for some of the ingots, homogenization does not have a significant effect on ductility. On average, the ductilities of the as-cast samples were similar to those of their homogenized counterparts.

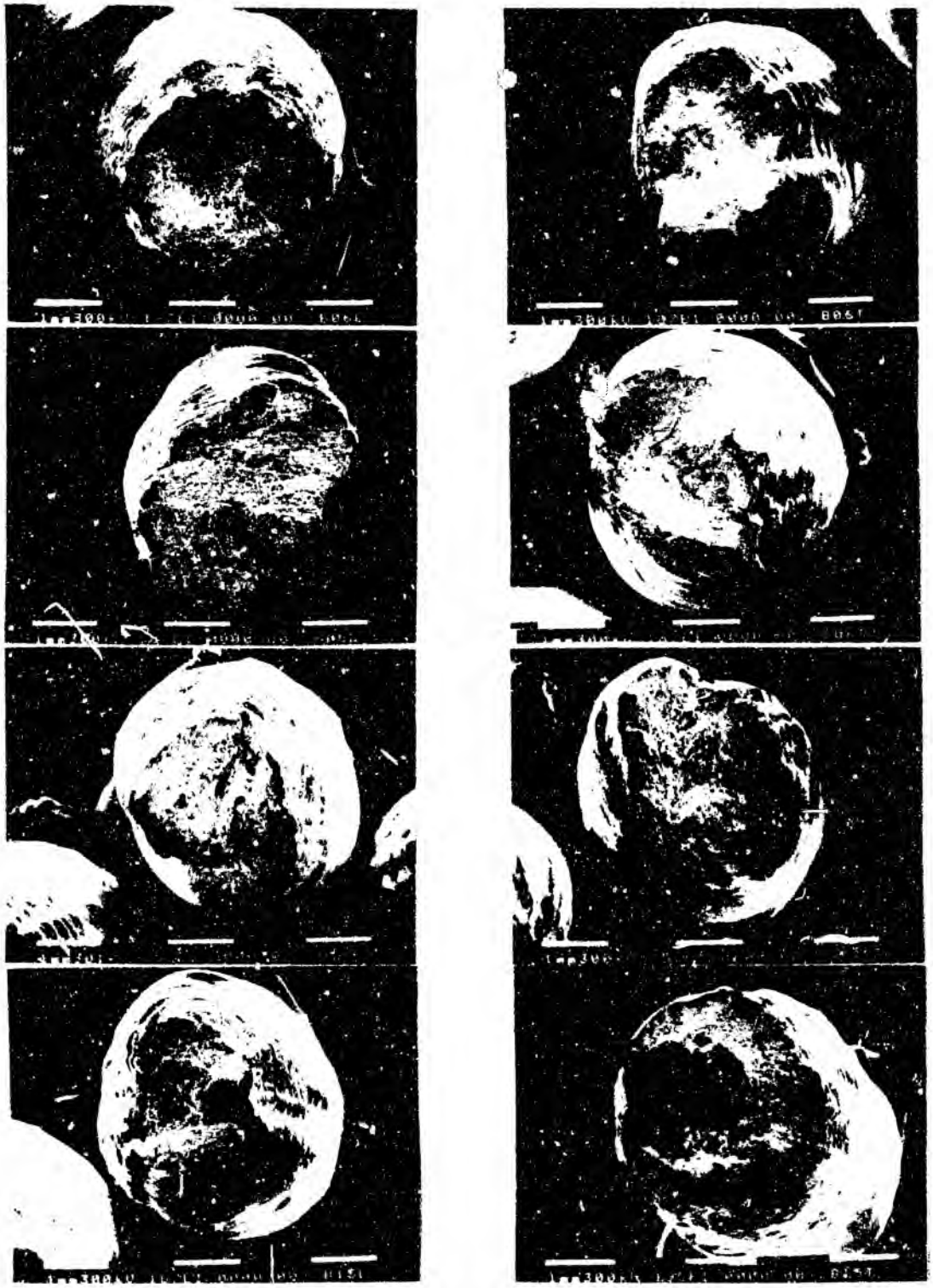

Figure 6.55 Fracture surfaces of selected tensile test pieces

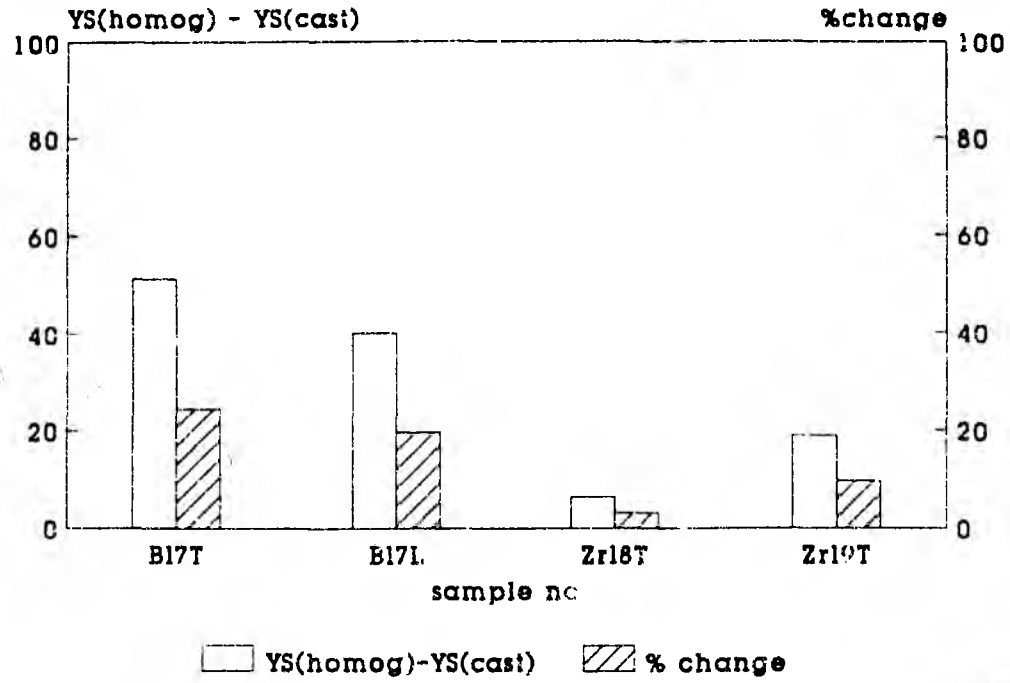

Figure 6.56 **Change in yield strength due to heat treatment of ingots with no addition and with FeSiZr addition**

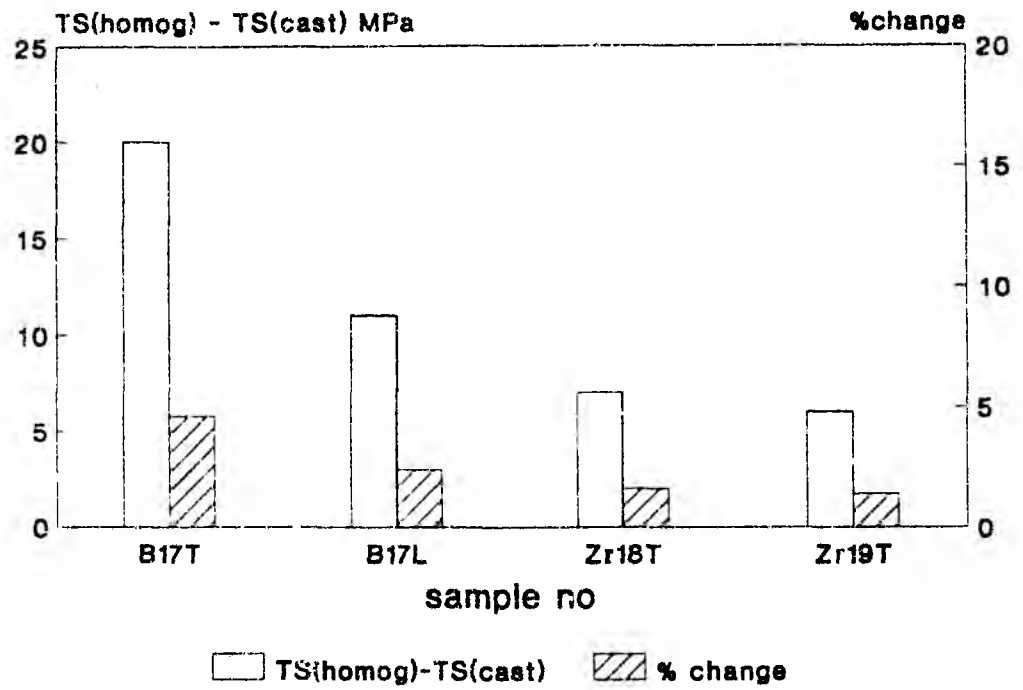

Figure 6.57 **Change in tensile strength dua to heat treatment of ingots with no addition and with FeSiZr addition**

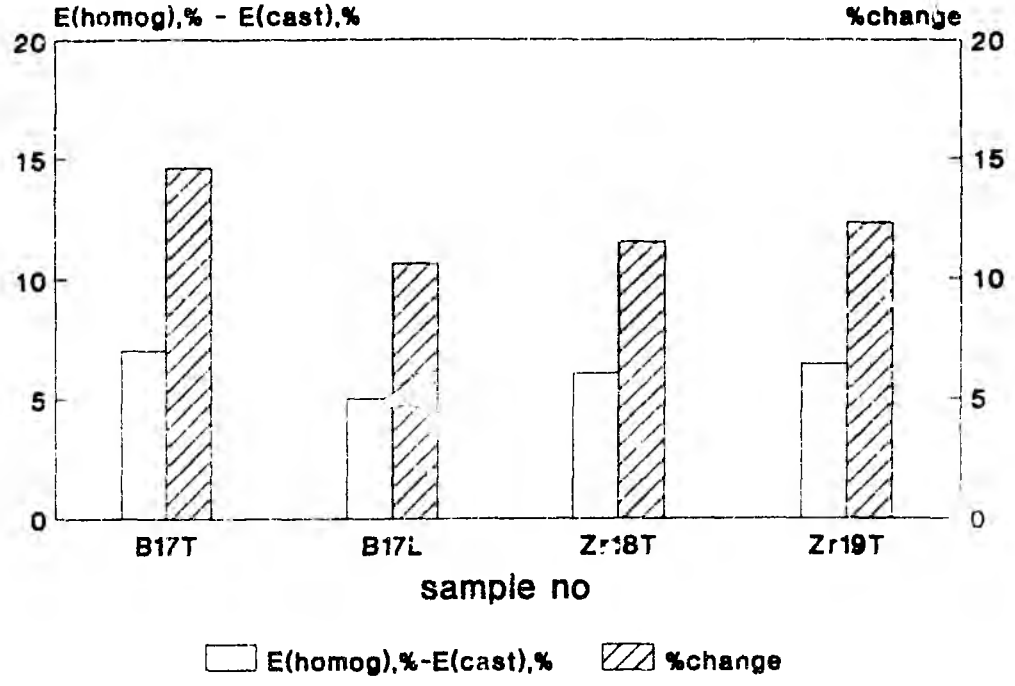

Figure 6.58 Change in % elongation by heat treatment of ingots with no addition and with FeSiZr addition

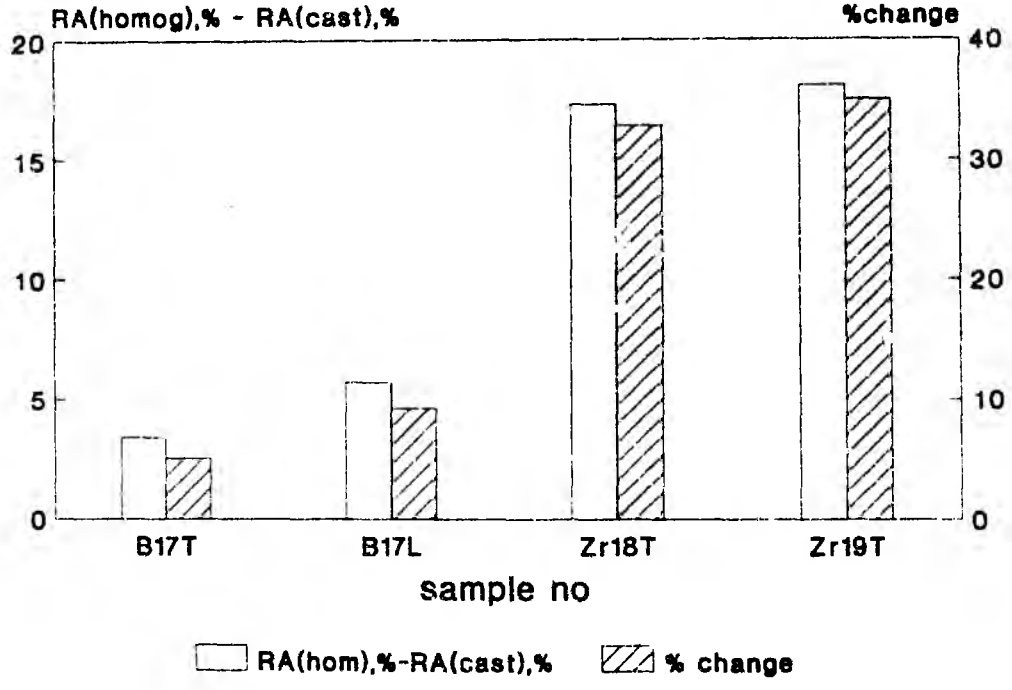

Figure 6.59 Change in % RA by heat treatment of ingots with no addition and with FeSiZr addition

6.4.2 Impact Test Results

Impact test results are given in Table **6.14**, and Figure **6.60**. From these results it can be said that the additions did not have a detrimental effect on the impact properties of AISI310. In fact in a few cases impact properties improved slightly with additions. It should again be noted here that longitudinal samples showed superior toughness values over transverse ones. The scatter in the results however made it difficult to relate results to any one parameter. The fracture surfaces produced were fully ductile and the values obtained were high compared to other austenitic stainless steels.

6.4.3 Hardness Test Results

Micro and macro-hardness values for selected ingots in the as-cast condition are presented in Tables **6.15** and **6.16**. They are given together with the corresponding grain widths measured at 6mm and 14mm from the edges. The hardness values were analyzed with respect to these grain widths. No correlation was found between the two. The hardness values were plotted (Figure **6.61**) against the corresponding primary arm spacings measured at 6mm from the edge of the relevant ingots (the values given in parentheses in Table **6.15**). It can be seen from Figure **6.61** that there appears to be a correlation between hardness and primary dendrite arm spacing. Smaller primary dendrite arm spacings appear to result in increased hardness for metal ingots as well as for ingots containing misch metal. The Zr-containing ingots did not show a very clear trend.

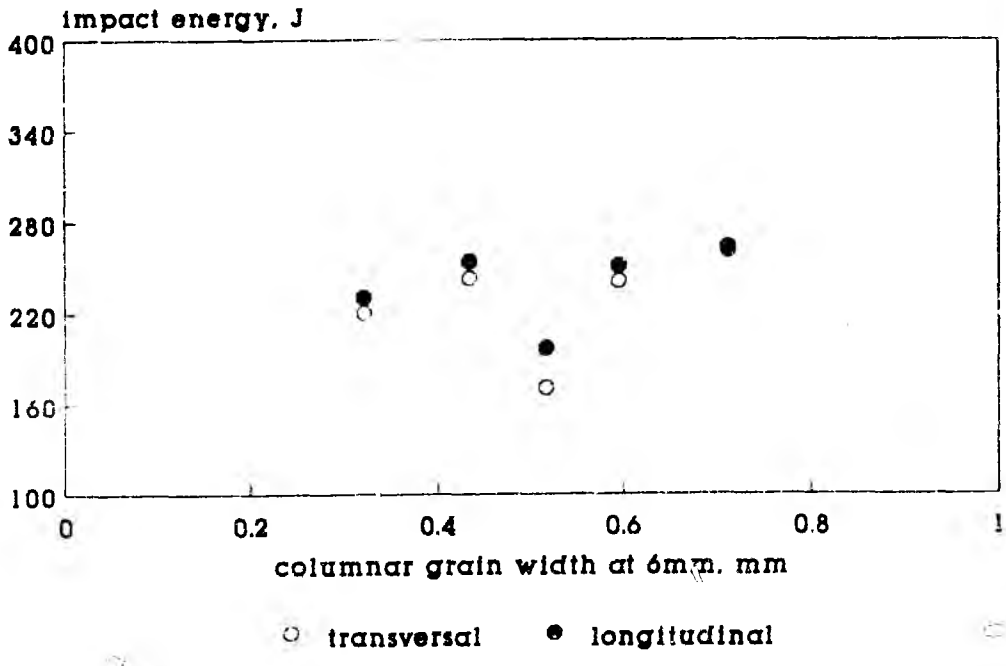

(a)

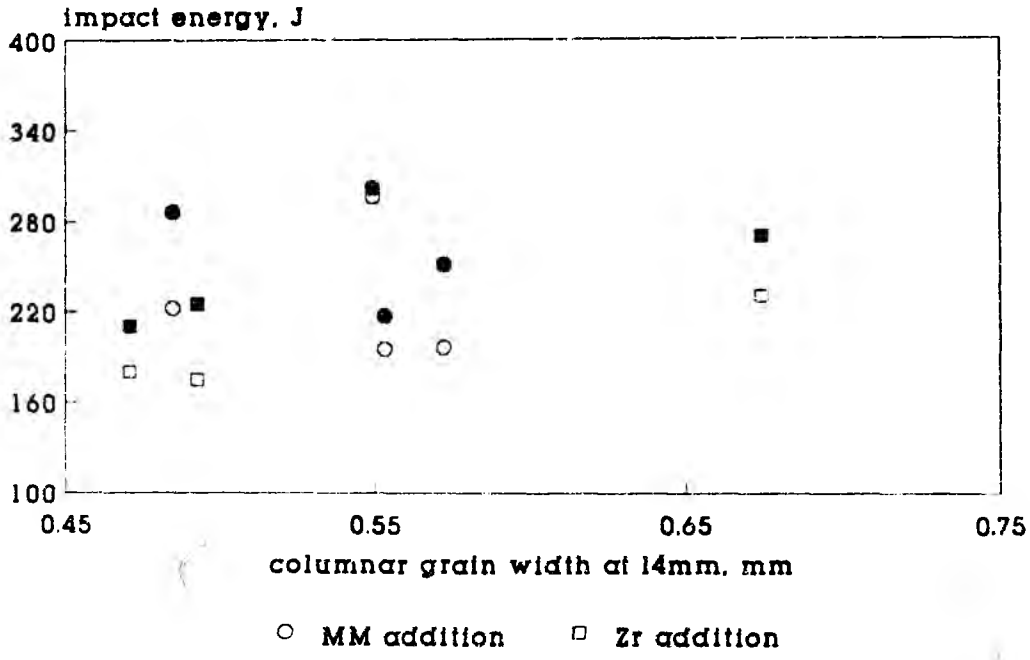

(b)

Figure 6.60 Change in notch impact energy with columnar grain width for ingots with (a) no addition and (b) misch metal and FeSiZr addition

Table 6.15 **Vickers hardness values for as-cast base metal ingots with their respective columnar grain widths and primary arm spacings (given in parenthesas)**

Sample no	Columnar Grain Width (mm)		Macro Hardness HV5
	6mm	14mm	
B2	1.055 (93)	1.134	138
B3	0.844 (80)	1.030	132
B4	1.047 (105)	1.204	140
B5	0.666 (86)	0.920	146
B6	0.711 (118)	0.975	139
B7	0.551 (85)	0.704	157
B8	0.517 (108)	0.710	112
B9	0.498 (125)	0.672	140
B10	0.456 (109)	0.647	140
B11	0.511 (137)	0.669	119
B12	0.749	0.920	137
B13	0.434 (139)	0.666	123
B14	0.482	-	142
B15	0.365	-	121

Table 6.16 **Vickers hardness values for selected as-cast ingots with additions and their respective columnar grain widths and primary arm spacings (given in parentheses)**

Sample No	Columnar Grain Width (mm)		Macro-Hardness HV5
	6mm	mm	
MM7	0.377	0.617	126
MM8	0.530	0.695	140
MM9	0.350	0.476	124
MM15	0.345 (92)	0.482	139
MM16	0.370 (126)	0.530	133
MM17	0.353 (91)	0.505	164
MM18	0.323 (126)	0.441	142
MM19	0.351	0.493	121
MM20	0.355	0.485	126
MM21	0.464	0.553	133
MM22	0.429 (130)	0.549	123
MM23	0.440 (106)	0.572	132
ZR9	0.413 (83)	0.507	119
ZR10	0.445 (108)	0.640	126
ZR11	0.450	0.592	136
ZR13	0.408	0.557	133
ZR14	0.479	0.658	126
ZR15	0.412	0.514	135
ZR16	0.409	0.547	146
ZR20	0.373	0.479	156
ZR21	0.448 (102)	0.578	123
ZR22	0.507	0.674	137

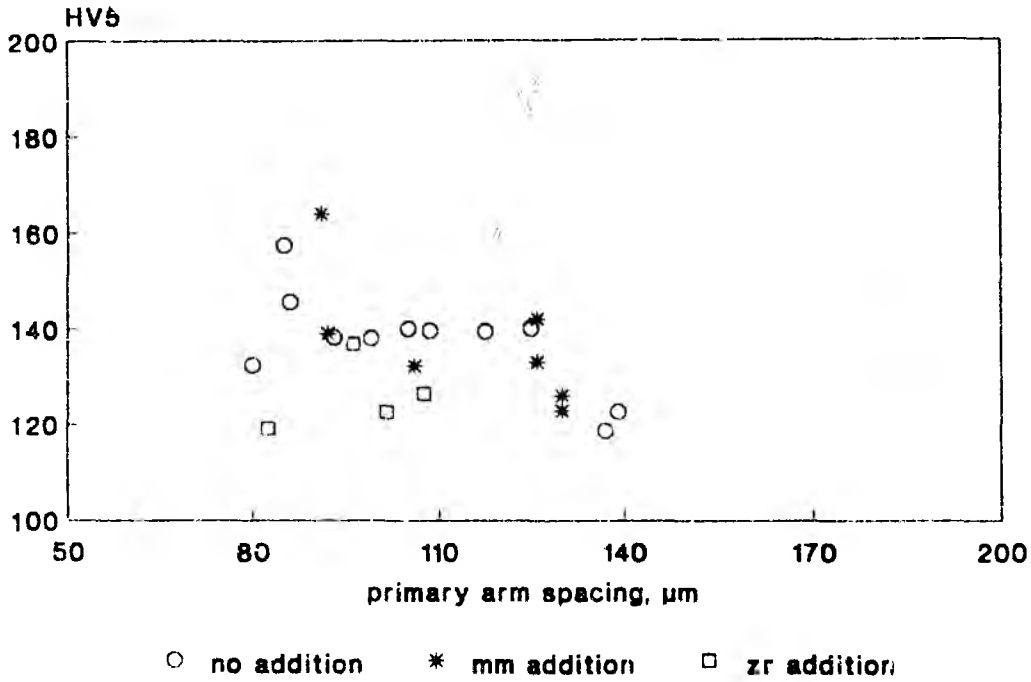

Figure 6.61 Changes in hardness as a function of primary arm spacing for ingots with and without addition

6.4.4 Summary of Mechanical Test Results for Material in the As-Cast Condition

The results of the mechanical tests (tensile, impact and hardness) carried out selected base metal ingots with no additions and on ingots with misch metal and FeSiZr can be summarized as follows:

(i) The tensile and yield strength in base metal ingots decreased as the columnar grain width decreased.

(ii) The base metal ingot with 70% equiaxed zone showed superior tensile and yield strengths over ingots which consisted mainly of a columnar zone. Only the ingot with the largest columnar grain width had a yield strength comparable to that of this ingot.

(iii) The elongation of specimens from the ingot with a 70% equiaxed structure was the same as that obtained from ingots with columnar structures. Two ingots with smaller columnar grain showed a slight positive deviation from the average.

(iv) The values of RA decreased as the grain width decreased and as the structure became mainly equiaxed.

(v) The ingots with misch metal and Zr additions had tensile and yield strengths which did not deviate significantly from the average strengths obtained with base metal ingots. If some of them did, then the deviation was positive.

(vi) Values of elongation obtained for ingots with misch metal additions were similar to those obtained with base metal castings, whereas the ingots with zirconium additions had larger than average elongation values in the smaller grain width range. This suggests an increase in elongation with these ingots as the grain width decreased.

(vii) Values of RA obtained with material containing misch metal and zirconium were similar to those obtained from base metal castings.

(viii) With only one or two exceptions, tensile and yield strengths obtained with longitudinal samples were superior to those obtained with transverse samples. On the other hand values of RA obtained with longitudinal samples were lower than those obtained with transverse samples. These observations hold for ingots both with and without additions.

(ix) The difference between the transverse and longitudinal values of yield and tensile strengths and elongation decreased as the columnar grain width decreased, becoming minimal for ingot B15 which comprised 70% equiaxed structure. This means that deformation becomes more uniform and isotropic as the grain width gets smaller and/or as the structure becomes equiaxed.

(x) For almost all the ingots cast with additions, the difference between the transverse and longitudinal values of yield

and tensile strengths was minimal. In most cases the difference was smaller than that observed with base metal castings, suggesting more uniform mechanical properties in all directions, most probably due to grain refinement of the cast structure.

(xi) The shape of the fracture surfaces of the tensile samples revealed that as the grain size decreased, the deformation became more uniform, and was almost completely isotropic for the ingot with equiaxed structure. Additions of misch metal and Zr resulted in more uniform deformation.

(xii) Testing of selected as-cast samples (unhomogenized) revealed that homogenization had its major impact on the yield strength, increasing it by up to 35% in some samples.

(xiii) No relationship was found between the tensile properties of the ingots with or without additions and the primary and/or secondary dendrite arm spacings measured at various distances from the edge for the same ingots.

(xiv) Impact test results suggested that misch metal additions could improve the toughness of the as-cast ingots. Longitudinal samples showed superior toughness over transverse ones.

(xv) Hardness tests suggested that there may be a correlation between hardness and primary dendrite arm spacing, with hardness increasing as the primary arm spacing

decreases. Grain width does not seem to influence the hardness of as-cast AISI310S steel.

As an overall evaluation of the mechanical test results summarised above, it can be said that small and/or equiaxed grained as-cast structures had more uniform and isotropic mechanical properties and deformation patterns. This was so especially when the structures were obtained by pouring with lower superheat during casting or by adding MM and Zr to castings poured with higher superheat.

6.5 Properties of Stainless Steel AISI310S in the As-Rolled Condition

Five ingots with no additions and 13 ingots with additions were hot rolled down to 15mm in thickness which corresponds to 80% reduction. Hot rolling was carried out at 1100°C. The finishing temperature was about 800°C. After hot rolling, these ingots were solution treated at 1200°C for two hours and quenched in water. Specimens were cut for macro- and micro-analyses and hardness tests. Two tensile and two Charpy impact test specimens were prepared from each slab. Tensile and impact test results together with results of their as-cast columnar grain width, primary and secondary dendrite arm spacing and hot rolled grain size measurements are given in Table **6.17**.

6.5.1 The Relationship Between As-Cast and As-Rolled Grain Sizes

A plot of grain sizes in the as-rolled and as-cast ingots (Figure **6.62**) shows no apparent correlation between the two. However when the secondary dendrite arm spacing in as-cast ingots is plotted against the as-rolled grain size (Figure **6.63**), it can be seen that as the secondary dendrite arm spacing increased, the grain size in the as-rolled condition tended to increase as well.

6.5.2 Tensile Properties

6.5.2.1 Yield Strength

Specimens taken from ingots with and without additions and deformed by 80% were tested under comparable conditions. It can be seen from Figure **6.64**, that smaller grain sizes resulted in higher yield strength.

Table 6.17 Tensile and impact test results for the hot rolled AISI310S ingots with or without additions and their corresponding grain sizes and dendrite arm spacings in the as-cast and as-rolled conditions

Ingot no	Columnar grain width (mm)		Dendrite arm spacing (μm)				Grain size (mm)	YS MPa	TS MPa	Elongation %	Reduction in Area %	Notch Impact Energy (J) Standard	Notch Impact Energy (J) Subsize
			Primary		Secondary		as-rolled	Trans. Long.	Trans. Long.	Trans. Long.	Trans. Long.	Trans. Long.	
	6mm	14mm	6mm	15mm	6mm	15mm							
B5	0.666	0.920	55.5 72.2	206.9 228.9	26.2 26.8	52.6 42.6	0.380	241.1 239.6	489.3 509.2	- 63.7	- 71.5	- 338	
B7	0.551	0.704	75.2 137.6	222 297.9	23.7 22.7	38.3 33.8	0.412	219.0 219.0	494.0 509.0	63.9 60.3	70.8 73.0	195 331	87
B9	0.498	0.672	112.9 140.5	284.0 335.8	22.6 26.6	39.5 42.8	0.460	221.0 228.7	514.5 514.4	- 54.0	- 73.0	297 330	100
B12	0.749	0.920	206.3 260.2	272.8 333.5	31.3 33.3	34.6 41.7	0.319	223.0	514.0	- 70.0	- 74	232 344	118
B14	0.482	-	-	-	-	-	0.113	300.0	555.0	- 60.0	- 77.7	276 352	102
B16A	-	-	-	-	-	-	0.500	- 267.2	- 519.5	- 50.0	- 68.0	-	110
B16B	-	-	-	-	-	-	0.840	233.0 226.5	468.4 473.7	41.0 74.0	55.0 78.0	-	110
B16C	-	-	-	-	-	-	1.350	217.5 194.5	402.3 443.1	38.8 38.8	66.4 76.0	-	119
MM14	0.391	0.685	128.7 189.5	193.7 322.7	23.8 26.7	41.2 43.5	0.092	287.7 282.1	604.1 589.1	58.4 59.0	76.7 74.9	318 214	63
MM15	0.345	0.482	65.9 55.7	267.0 253.5	22.6 23.2	45.3 50.0	0.354	222.0 232.2	484.0 504.2	- 58.8	- 73.7	300 356	106
MM16	0.370	0.530	113.3 196.6	259.3 280.0	28.8 32.9	50.3 42.8	0.400	234.6 241.0	509.2 513.0	- 59.0	- 68.0	204 274	90
MM17	0.353	0.505	80.2 128.7	186.7 253.1	27.4 33.9	40.4 35.0	0.676	259.6 229.7	514.2 489.3	49.4 54.0	65.6 72.5	159 330	85
MM18	0.323	0.441	95.7 117.0	108.6 153.2	32.7 33.7	31.2 39.5	0.186	217.7 226.1	494.3 514.2	53.3 60.6	65.9 71.0	153 316	90
MM19	0.351	0.493	76.9 142.5	93.0 -	30.9 42.4	42.6 52.6	0.541	- 219.0	- 509.0	- 63.9	- 73.0	223 358	114
ZR9	0.413	0.507	80.9 87.0	198.9 225.9	27.0 23.6	35.1 34.4	0.084	254.6 273.0	544.2 557.0	- 62.0	- 73.5	- 358	129
ZR10	0.445	0.640	92.0 108.0	217.3 201.7	23.1 23.4	52.0 35.9	0.223	241.0 249.0	555.3 555.0	- 65.0	- 75.0	272 357	114
ZR20	0.373	0.479	204.0 -	183.9 199.2	31.2 -	25.9 35.0	0.222	253.6 257.2	554.2 564.2	54.4 54.0	73.5 75.5	- 358	123
ZR21	0.448	0.578	-	133.6 166.1	28.9 35.4	45.9 52.8	0.670	219.0 219.0	483.8 504.1	65.1 63.5	73.0 75.0	313 342	-

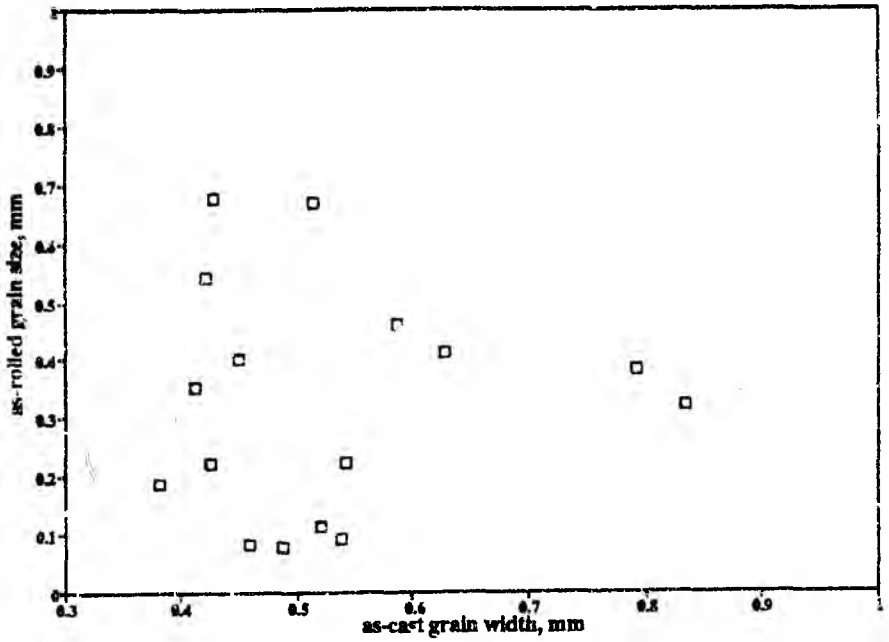

Figure 6.62 As-rolled grain size against as-cast columnar grain width for AISI310S steel with or without additions

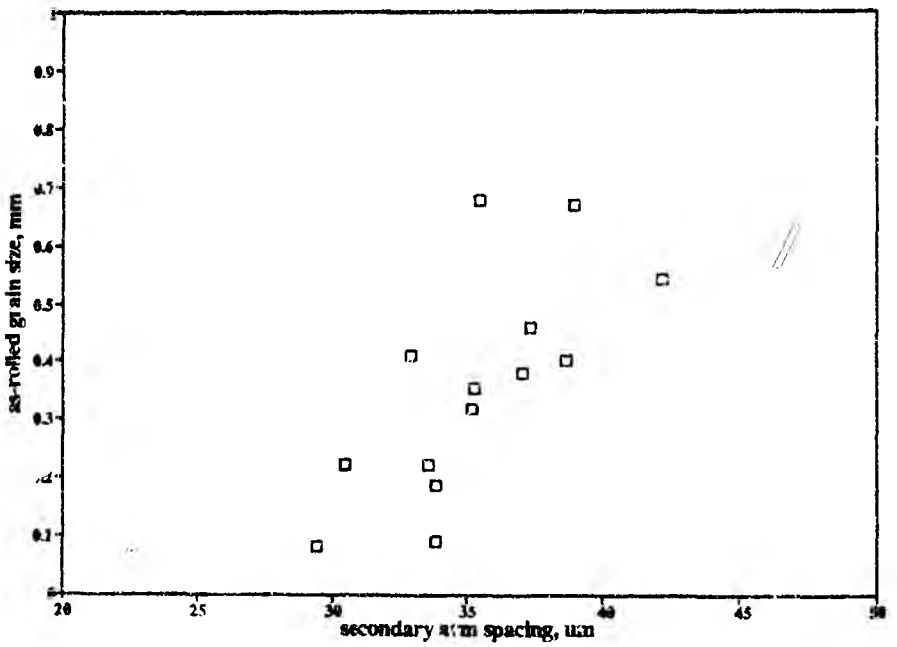

Figure 6.63 As-rolled grain size against secondary dendrite arm spacing for AISI310S steel with or without additions

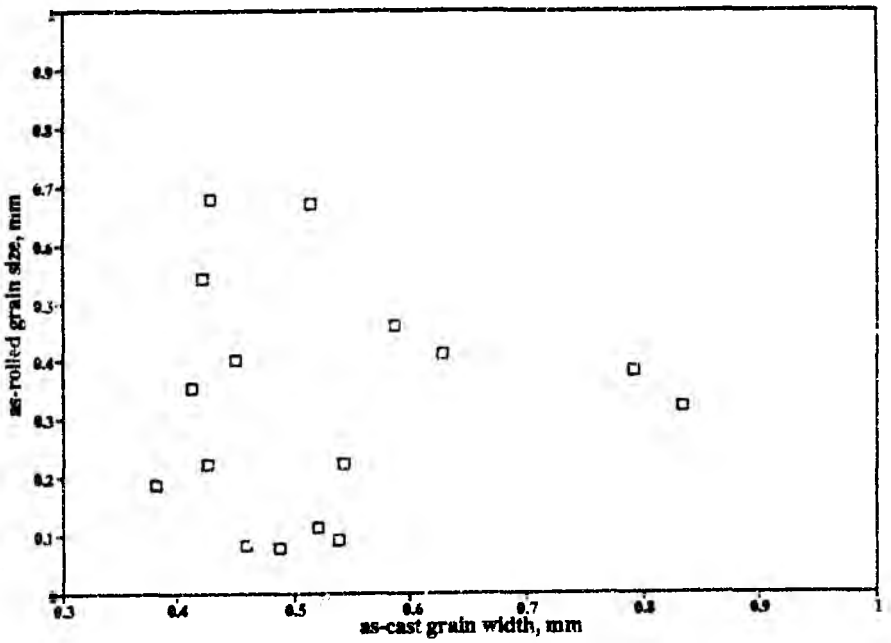

Figure 6.62 As-rolled grain size against as-cast columnar grain width for AISI310S steel with or without additions

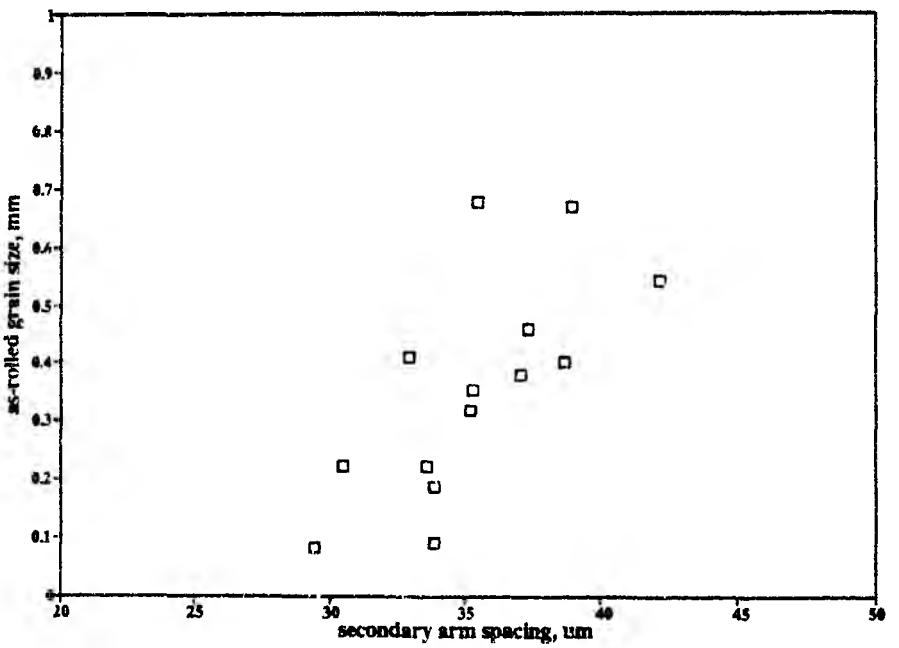

Figure 6.63 As-rolled grain size against secondary dendrite arm spacing for AISI310S steel with or without additions

A regression analysis gave the following Hall-Petch type relationship between the yield strength and the grain size of the base ingots:

$$\sigma_{y.s.} = 170 + 42.2\, d^{-1/2} \quad \ldots\ldots\ldots\ldots \quad 6.9$$

where $\sigma_{y.s.}$ is the yield strength in MPa, d is the grain size in mm.

The correlation coefficient of the equation is relatively low at 0.82, most probably due to the high yield strength obtained for the sample with a grain size of 0.5mm (Figure **6.64**). It should be noted here that the sample with the smallest grain size and highest yield strength (B14) had an appreciably large equiaxed zone of 50% in the as-cast condition. Figure **6.64**, indicates that the yield strength of ingots with misch metal or FeSiZr additions showed the same trend, but was slightly lower than that obtained with base metal of a similar grain size.

6.5.2.2 Tensile Strength

The plot of tensile strength against grain size (Figure **6.65**) shows a trend similar to that of the plot of yield strength against grain size. Regression analysis done for the data of the ingots without additions, showed that the best fitting curve is a fourth degree polynomial (Table **6.18**) with a correlation coefficient of 0.90 as opposed to the values of 0.874 and 0.943 respectively, obtained with a Hall-Petch type equation and second degree polynomial. However the regression line in Figure **6.65** was plotted using the second degree polynomial equation, which shows almost a linear relationship between tensile strength and grain size in this range of grain sizes.

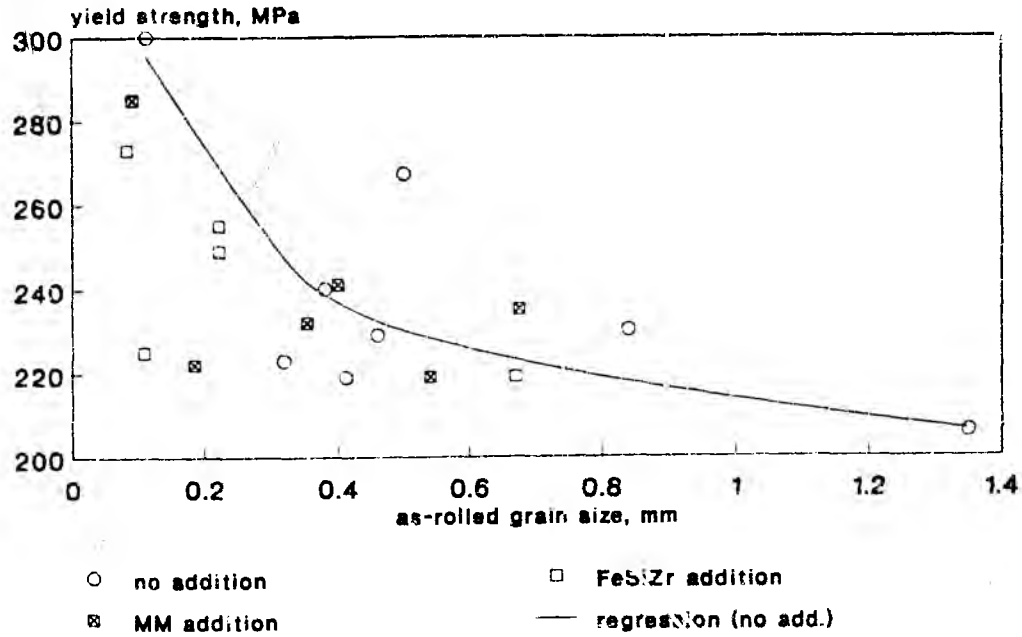

Figure 6.64 Change in yield strength with as-rolled grain size of AISI310S steel with or without additions

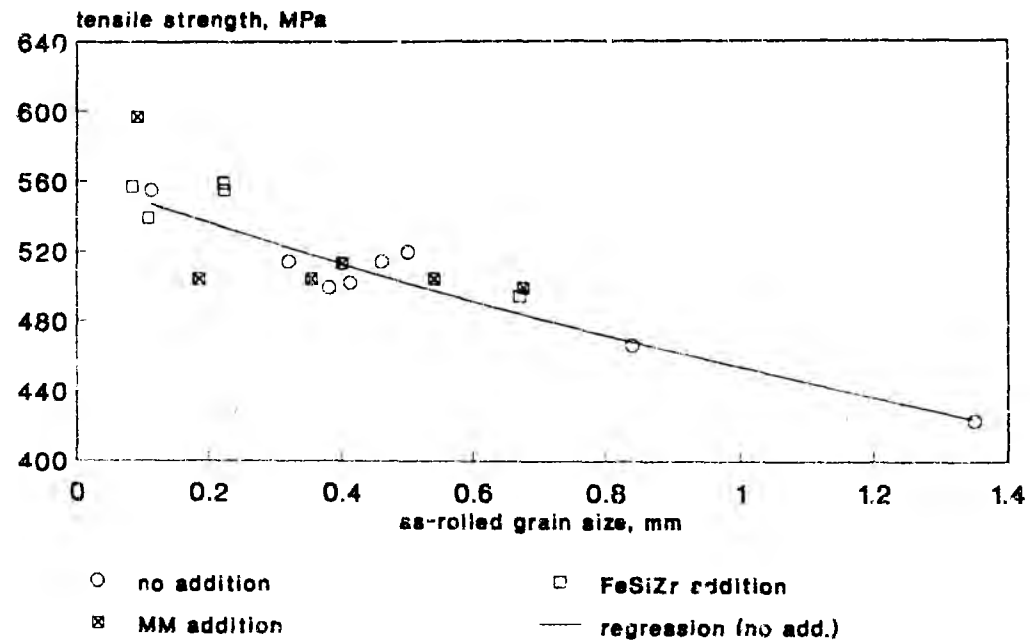

Figure 6.65 Change in tensile strength with as-rolled grain size of AISI310S with or without additions

Table 6.18 Regression Equations for Tensile Strength as a Function of Grain Size in Hot Rolled and Annealed Conditions for AISI310S steel

Hall-Petch Type : $\sigma_{TS} = 431.2 + 46.1d^{-1/2}$ 6.10
corr. coeff. : 0.874

where σ_{TS} is in MPa and d is in mm.

2nd Degree Polynomial : $\sigma_{TS} = 56.2 - 13.2d + 2d^2$ ..6.11
corr. coeff. : 0.94

4th Degree Polynomial :

$\sigma_{TS} = 66.5 - 135.3d + 392.8d^2 - 445.6d^3 + 162.3d^4$.....6.12

corr. coeff. : 0.98

where σ_{TS} is in $kPa*10^4$ and d is in mm.

The slight positive deviation in the slope of the curve in the grain size range of 0.400 to 0.500mm is neglected. A fourth degree polynomial would most probably produce a curve which would also show this change in slope. However considering the abnormal yield strength obtained with the sample of grain size 0.500mm, the slightly higher than average tensile strength obtained with the same sample can be ignored. This makes the use of the second degree polynomial to express the general trend in tensile strength in this grain size range, more justifiable.

As can be seen from Figure 6.65 the results obtained with hot-rolled ingots with Mm and FeSiZr additions did not show a positive or negative deviation from those obtained with base metal ingots of the same grain size range.

However it should be noted that these base metal ingots were cast from a temperature range of 1481 to 1454°C. Of the ingots with additions, 90% were cast within the temperature range 1540 to 1545°C. It can, therefore, be seen that with additions of MM and FeSiZr, the same tensile properties were obtained in material cast from a higher temperature range, owing to the grain refining effect of the additions on the steel in the as-cast condition and after rolling.

6.5.2.3 Elongation

Values of percentage elongation are plotted against as-rolled grain size in Figure **6.66**. A regression analysis for the ingots cast without additions gave a fourth degree polynomial as the best fitting curve. This was:

% Elongation =

$$6.35 + 706.35d - 2352.75d^2 + 2738.90d^3 - 1015.2d^4 \quad \ldots \quad 6.13$$

The correlation coefficient is 0.997.

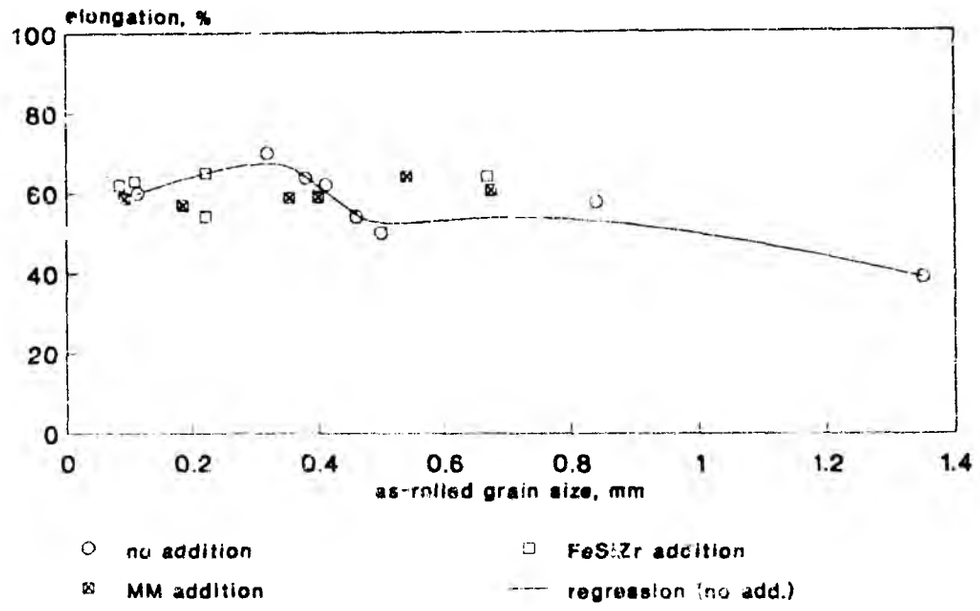

Figure 6.66 Change in % elongation with as-rolled grain size of AISI310S steel with or without additions

It can be seen from Figure **6.66**, where this regression line is plotted, for a wide range of grain sizes, that elongation did not change substantially as the grain size decreased from about 1.4mm to about 0.5mm. As the grain size decreased from 0.5 to about 0.3mm the elongation increased from about 50% to about 70%. Thus for a 40% decrease in grain size there was a 20% increase in elongation. The elongation decreased to 60% as the grain size decreased from 0.3mm to 0.1mm. This drop in elongation should be considered with the simultaneous increase in the yield and tensile strengths (Figures **6.64** and **6.65**) of 36 and 8% respectively.

Figure **6.66** also shows that the hot rolled ingots containing misch metal and FeSiZr had elongation comparable to that of the base metal. It may therefore be said that the grain refining additions had no detrimental effect on the ductility of the hot rolled material. The minimum elongation obtained with additions of grain refining agents was 50% which is highly satisfactory.

At this point, attention should be drawn to the tensile properties of certain ingots with misch metal and FeSiZr additions, namely MM14, ZR9, ZR10 and ZR20. Even though the casting temperature of these ingots was on average 1550°C, which is almost 100°C higher than that of B14, they had tensile properties comparable to those of this base metal ingot which comprised 50% equiaxed material in the as cast condition and showed the best tensile properties among the base ingots in the as-rolled condition. MM14 had an average yield strength of 285MPa, tensile strength of 600MPa, elongation 59% coupled with a reduction in area of 76%. The corresponding values obtained with B14 were 300MPa yield strength, 555MPa tensile strength, 60% elongation and 77.7% reduction in

area. MM14 had a yield strength about 5% lower, a tensile strength 8.1% higher and practically the same ductility as B14. If the results obtained with MM14 are compared with those obtained with B5 which was cast from 1545°C, a dramatic difference is witnessed : MM14 had 19% better yield strength, 20% better tensile strength, 8% less elongation, and 5% better reduction in area. This means that better strength was obtained with MM14 without significant loss in ductility.

When the results of ZR9, ZR1[illegible]nd ZR20 which are similar were averaged and compared with those obtained for B14, the yield strength was found to be 15% lower, the tensile strength almost the same, the elongation the same or slightly higher, and the reduction in area slightly lower.

When compared to B5, the yield strength was about 5% higher, the tensile strength 11% higher, the elongation almost the same, and the reduction in area slightly (4%) higher. The impact toughness of the ingots containing FeSiZr was consistently higher than that obtained with base metal ingots, whereas misch metal containing ingots showed significant scatter in results. This was particularly true of transversal samples. Longitudinal samples gave results similar to those obtained with base metal ingots.

For the majority of the samples, the yield strength, tensile strength, reduction in area and Charpy impact values obtained with longitudinal samples were consistently higher than those obtained with transversal samples.

6.5.2.4 Reduction in Area

Reduction in area (RA) for the hot rolled slabs is plotted against the as-rolled grain size in Figure **6.67**. Regression analysis gave a second degree polynomial as the best fitting curve in this grain size range. The relationship obtained was as follows.

$$\% RA = 81.9 - 33.0d + 18.5d^2 \quad \ldots\ldots\ldots\ldots \quad 6.14$$

(d is in mm)

with a correlation coefficient of 0.90.

As can be seen from Figure **6.67**, in the grain size range of 0.113 to 0.840mm, RA decreased as the grain size increased. For grain sizes above 0.840mm, it appears that RA remains fairly constant or increases slightly with increasing grain size. It is also apparent from the graph that additions of MM and Fe iZr did not have a detrimental effect on the ductility of the alloy measured as RA.

6.5.2.5 Charpy Impact Tests

Impact energy results obtained from longitudinal samples of AISI310S hot rolled ingots with or without additions are plotted against as-rolled grain size in Figure **6.68**. A regression analysis carried out for the base metal ingots gave the following expression for the change in impact energy with grain size:

$$\text{Impact Energy (J)} = 351.3 + 26.6d - 165.75d^2 \quad \ldots 6.15$$

(d is in mm)

with a correlation coefficient of 0.96.

This expression holds true only for the grain size range of 0.113mm to 0.460mm and for longitudinal samples of AISI310S only. The number of transversal samples that survived the impact test was not sufficient for a reliable regression analysis. Also the number of subsize charpy samples was not sufficient to deduce any trend. There appears to be a slight reduction in impact energy with misch metal additions, whereas an increase is observed with FeSiZr additions. As can be seen from Figure **6.68**, as the grain size of base material increased, a slight decrease in toughness was obtained. Results of samples from ingots with additions showed considerable scatter around the regression line. However, it can be said that misch metal and FeSiZr additions do not seem to impair the toughness of longitudinal samples of AISI310S, whereas in the transversal direction, results suggest that certain amounts of misch metal may lead to a deterioration of the impact toughness of this material. It should be noted that the energy absorbed remained very high under all conditions (in excess of 200J).

6.5.2.6 Hardness Tests

Results of micro- and macro-hardness tests done on the hot-rolled ingots of AISI310S with or without additions are given in Table **6.19**. Macro-hardness results are plotted against as-rolled grain size in Figure **6.69**. It can be seen that specimens from all ingots exhibited decreasing hardness with increasing grain size. The addition of misch metal or FeSiZr had no definite influence on the hardness of hot rolled material.

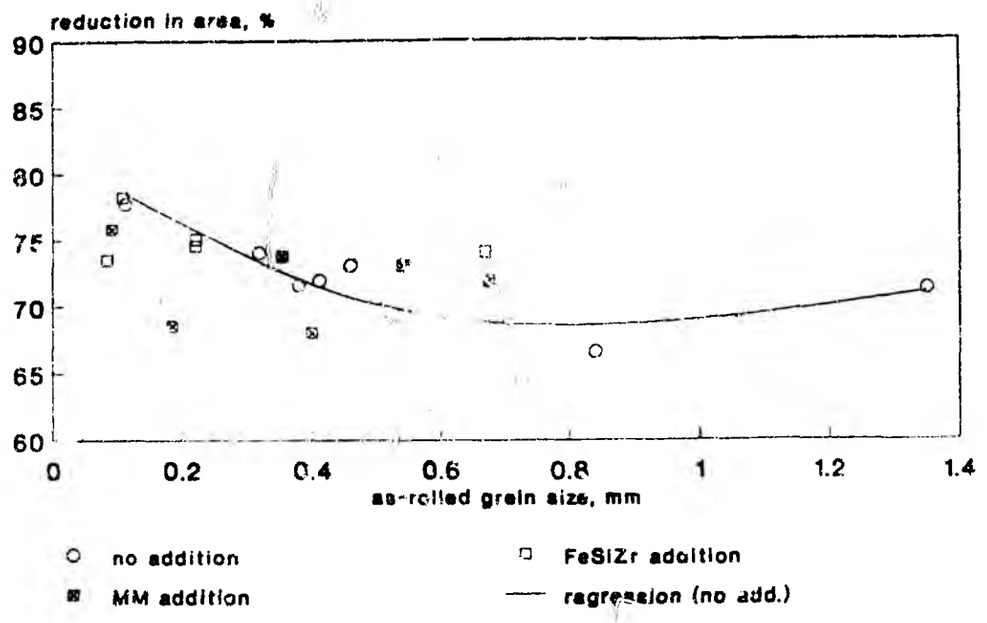

Figure 6.67 Change in % reduction in area with as-rolled grain size of AISI310S steel with or without additions

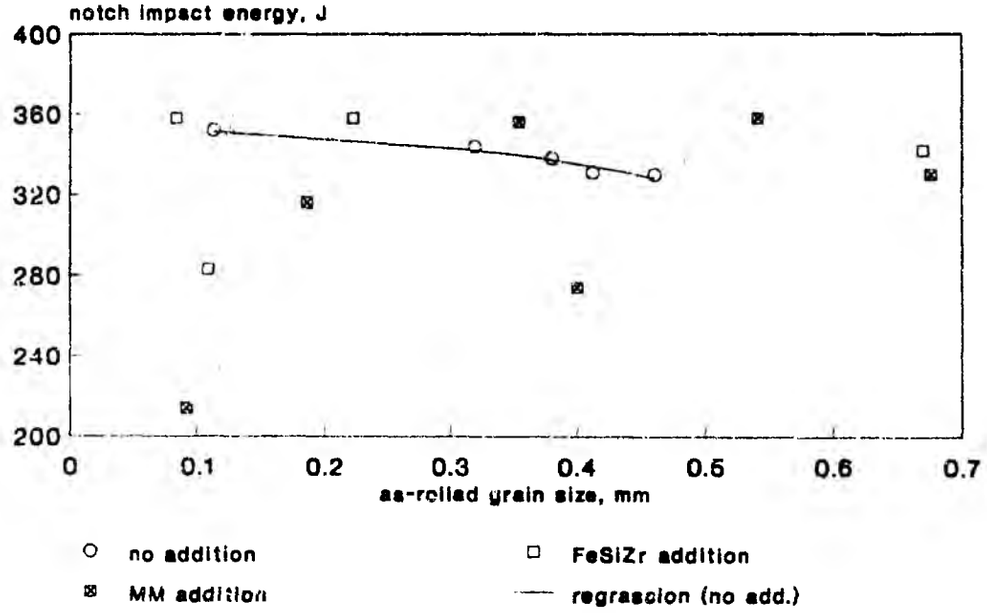

Figure 6.68 Change in notch-impact energy with as-rolled grain size of AISI310S steel with or without additions

Table 6.19 Micro- and macro-hardness values for the hot-rolled AISI310S ingots with or without additions

Ingot No.	Grain Size (mm) as-rolled	Macro Hardness VH_5	Micro Hardness $VH_{0.5}$
B5	0.380	149	174
B7	0.412	129	139
B9	0.460	136	143
B12	0.319	141	162
B14	0.113	138	149
MM14	0.092	150	170
MM15	0.354	138	164
MM16	0.400	150	167
MM17	0.676	144	164
MM18	0.186	141	157
MM19	0.541	136	134
ZR9	0.084	142	178
ZR10	0.223	160	-
ZR20	0.222	153	168
ZR21	0.670	130	150

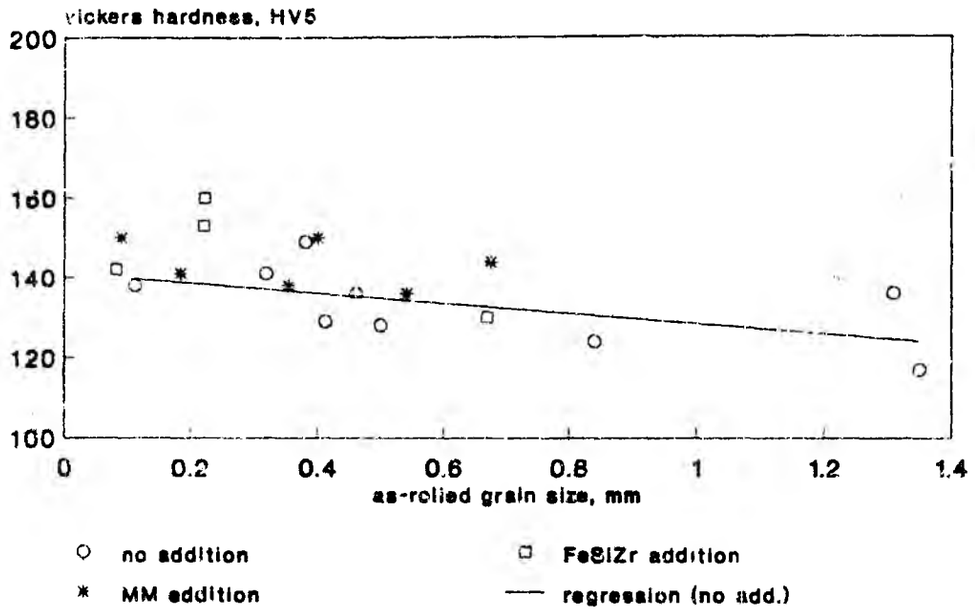

Figure 6.69 Change of hardness with as-rolled grain size of AISI310S steel with or without additions

6.6 Properties of Stainless steel AISI310S in the As-Cold Rolled Condition

One ingot with no addition (B5), three ingots with FeSiZr additions (ZR9, ZR10, ZR20) and two ingots with misch metal additions (MM14, MM15) were cold rolled to reductions of 25%, 50% and 75% without lubricant on a two-high mill. The photographs given in Figure **6.70** show the effects of cold rolling on the surface characteristics of billets rolled from different ingots. As can be seen from this figure, ingots with additions exhibited surfaces with a fine-texture in the cold rolled condition whereas B5 exhibited an extremely rough surface.

Table **6.20** gives the hardness results obtained on the cold rolled and the cold rolled/annealed materials after various annealing times. It can be seen from Figure **6.71**, that with all three types of material annealing caused an initial softening to a minimum hardness followed by a gradual increase in hardness with further increases in annealing time. This effect was not very pronounced, causing increases in hardness of about 10% or less from the minimum hardness values. The effect however appeared to be more pronounced in the materials cast with additions. It could be said, therefore, that misch metal and FeSiZr additions do not have a significant effect on the hardness of cold rolled and annealed material.

However, as can be seen from micrographs of selected billets with or without additions reduced 75% and annealed at 975°C for 20 minutes(Figure **6.72**), ingots with additions have a finer microstructure compared to ingots without additions. This is most probably due to a finer microstructure in the hot rolled condition. There seem to be no solid solution and/or precipitation hardening effects which take place solely because of the additions.

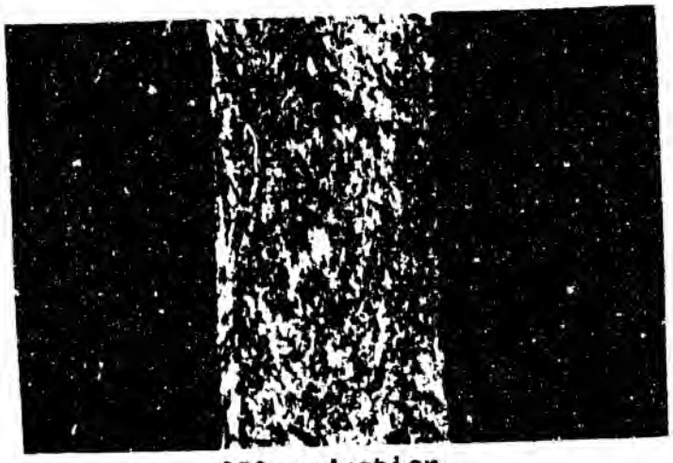

25% reduction



50% reduction



75% reduction

Figure 6.70 Surface characteristics of billets cold rolled from different ingots at various reductions (a) B5



25% reduction

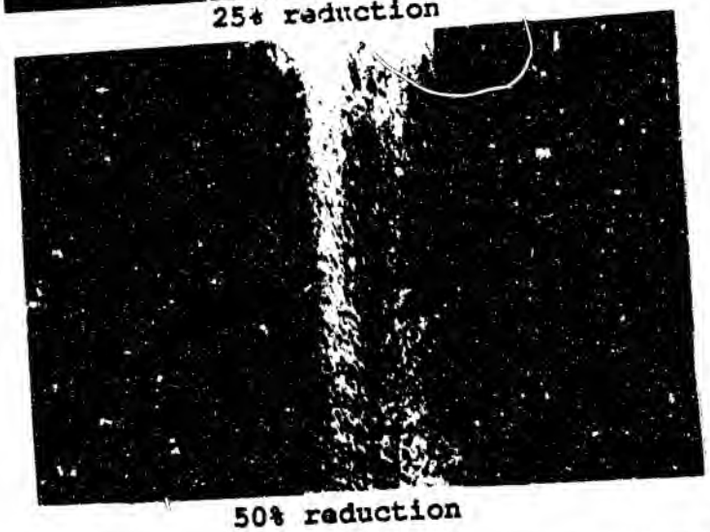

50% reduction



75% reduction

Figure 6.70 contin. (b) MM14

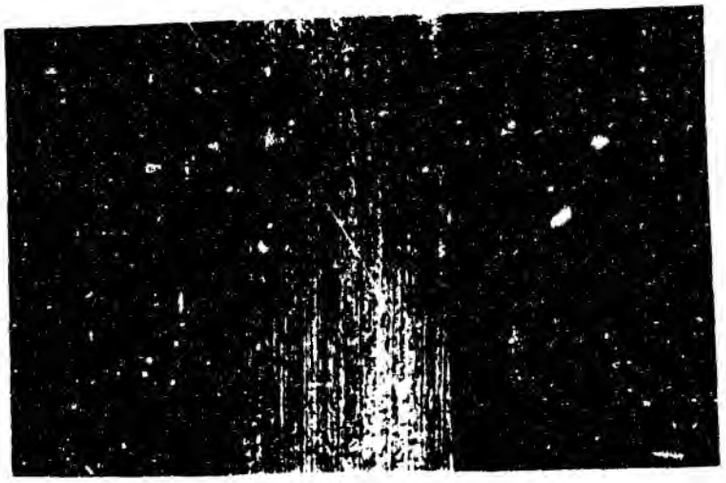

25% reduction

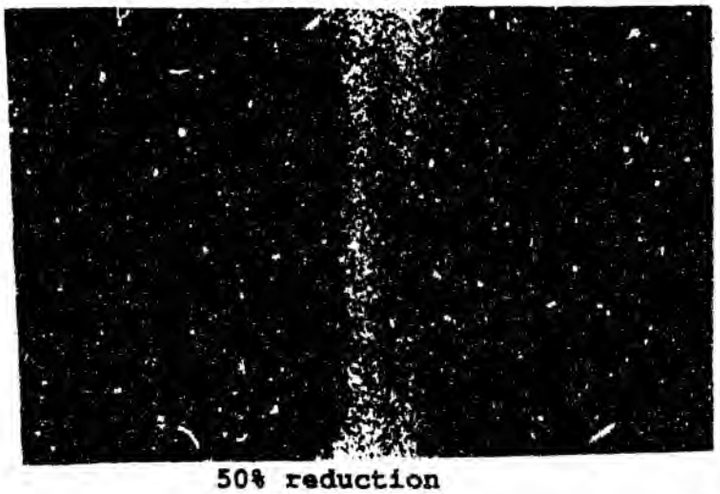

50% reduction



75% reduction

Figure 6.70 contin. (c) ZR9

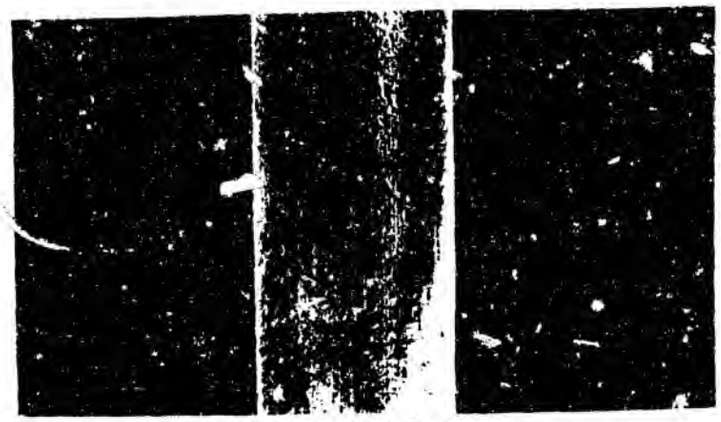

25% reduction

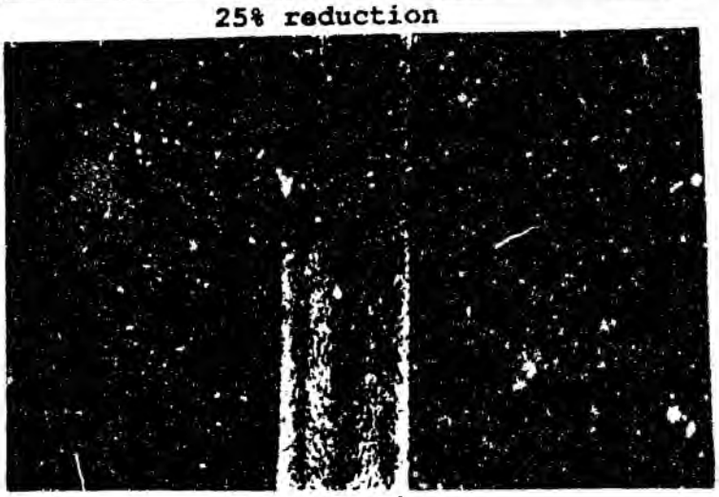

50% reduction

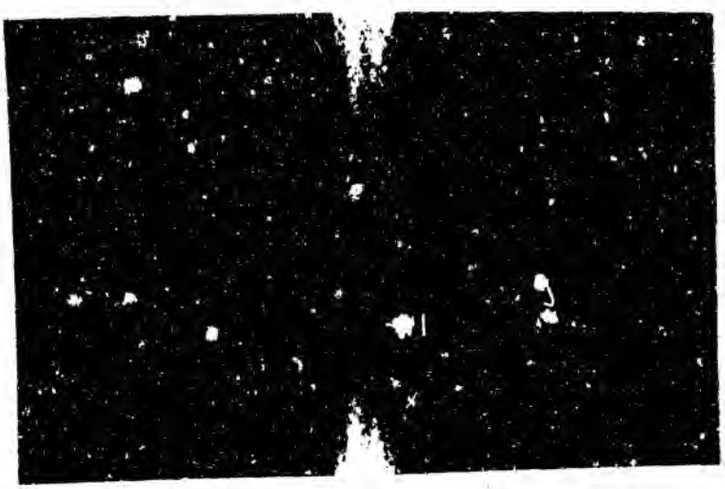

75% reduction

Figure 6.70 contin. (d) ZR10

7.1 Effect of Superheat on the Solidification Mode of AISI310S

Stainless steels can solidify by different modes. The modes, or solidification sequences, are known to be influenced by the relative concentrations of γ- and α-stabilizing solute elements in the steel. For instance small changes in C or N_2 content can cause a shift from one sequence to another, since they both favour the formation of γ. The section from the Fe-Cr-Ni equilibrium phase diagram shown in Figure 7.1 gives the ferrite/austenite ratio during solidification and the solidification interval as a function of the ratio Ni'/Cr' for austenitic stainless steels. As can be seen from this figure, AISI310S is the most stable of the four grades of austenitic stainless steels considered due to its high Ni'/Cr' ratio. This ratio for the AISI310S grade used for the present work was calculated to be 0.845, which falls into the $L \rightarrow L + \gamma \rightarrow \gamma$ transformation sequence under equilibrium conditions.

Although there are well established pseudo-binary diagrams for other austenitic stainless steels, like 304 and 316, non could be found for the 310 grade. So, within the framework of this research, it was also attempted to draw a pseudo-binary phase diagram for AISI310S using the ternary iron-chromium-nickel diagrams provided by Rivlin[306]. The pseudo-binary diagram produced for this alloy at 25% Cr is given in Figure 7.2. This pseudo-binary diagram together with the diagram shown in Figure 7.1 shows that under equilibrium conditions, AISI310S solidifies directly into γ on cooling from the liquid phase.

Table 6.20 Hardness measurement results obtained on the cold rolled and the cold rolled/annealed materials

	%	Macro Hardness HV0.5					Micro Hardness HV0.2				
		Annealing Times minutes at 975 +\- 15°C/water quenched									
	Reduction	0	10	15	20	60	0	10	15	20	60
B5	25	252	155	153	151	154	279	169	167	164	176
	50	294	163	161	150	156	347	178	185	163	190
	75	387	192	160	164	172	391	203	171	176	208
ZR9	25	277	191	174	217	188	275	234	199	189	281
	50	317	190	193	183	178	360	194	209	196	214
	75	392	209	197	177	198	430	218	206	192	265
ZR10	25	290	160	165	181	182	371	171	177	181	228
	50	327	161	180	193	191	366	173	195	192	180
	75	371	167	140	145	166	393	180	155	154	206
ZR20	25	305	205	224	218	189	279	221	236	214	168
	50	322	188	186	202	186	328	199	205	198	165
	75	329	225	206	214	203	335	220	209	224	211
MM14	25	308	172	179	194	201	315	195	203	221	272
	50	358	184	196	189	198	355	207	235	210	240
	75	425	204	204	198	187	393	214	225	215	209
MM15	25	270	169	169	169	159	283	176	179	188	172
	50	279	176	174	174	168	310	193	184	200	202
	75	356	179	179	180	180	360	203	190	192	244

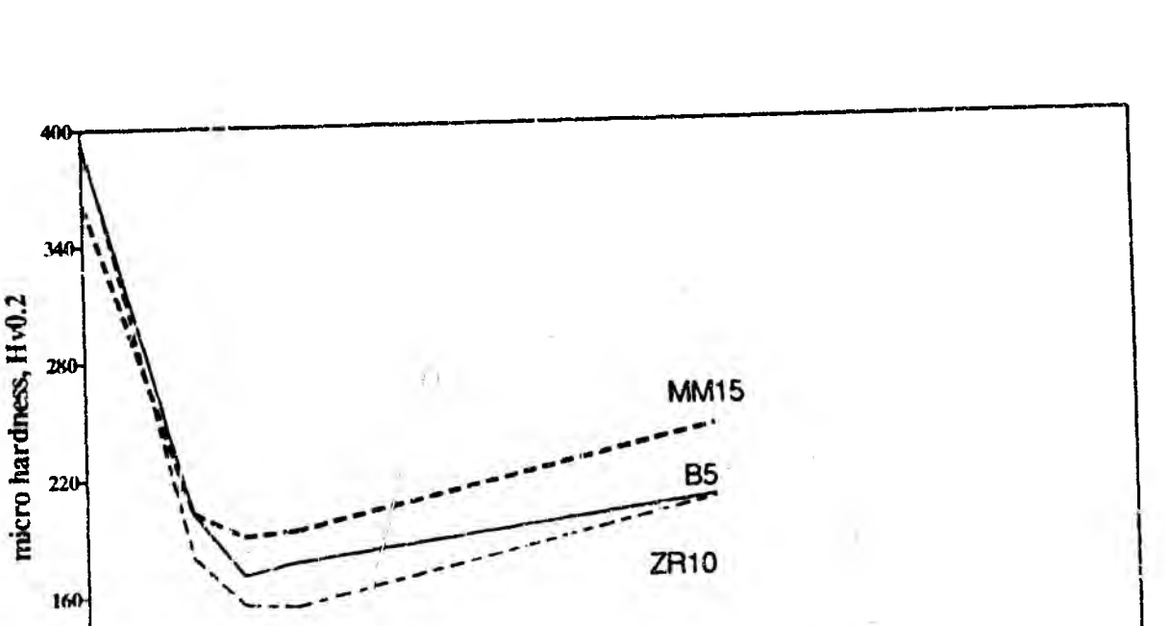

Figure 6.71 Change of hardness with annealing times of the cold rolled billets

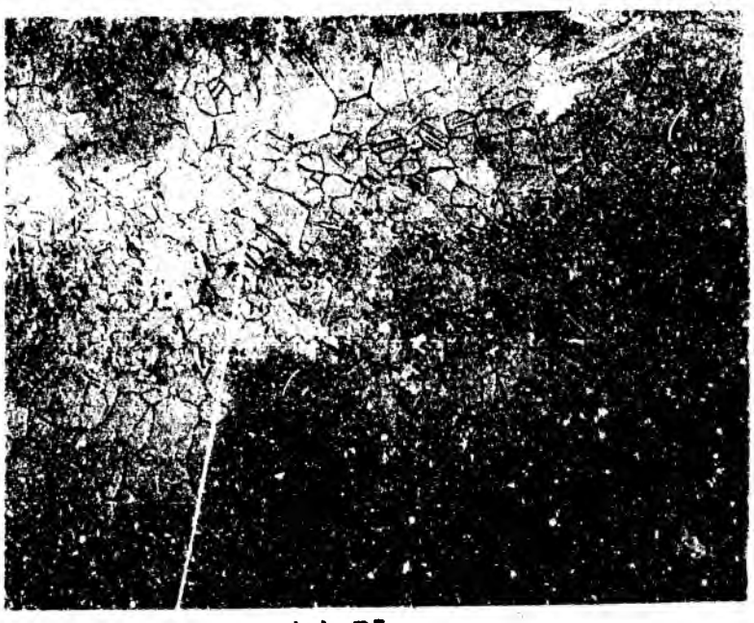

(a) B5

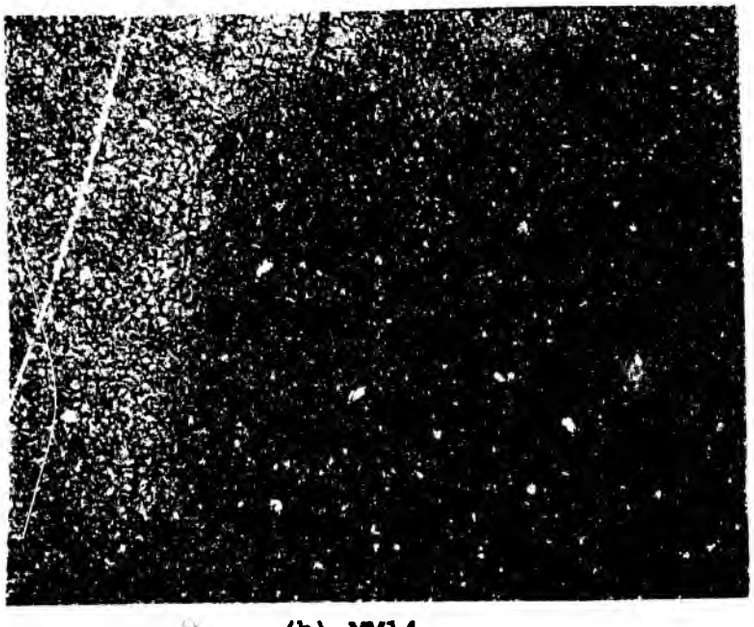

(b) MM14

Figure 6.72 Micrographs of cold rolled billets with or without additions reduced 75% and annealed at 975°C for 20 minutes



(c) ZR9

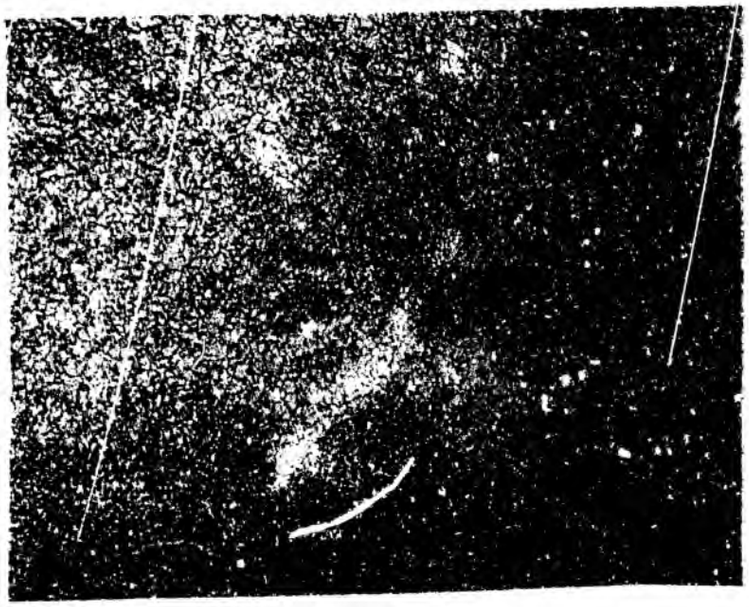

(d) ZR10

Figure 6.72 contin.

7. DISCUSSION AND THE PROPOSED QUASI-EMPIRICAL SOLIDIFICATION MODEL FOR AISI310S STAINLESS STEEL

The aim of this work was to refine the as-cast structure of the austenitic stainless steel AISI310S which contains about 25% Cr, 15% Ni, 1.6% Mn, 0.45% Si, and 0.05% C, by using additions of misch metal and FeSiZr. Al was also used in selected castings together with misch metal and FeSiZr additions.

The influence of the changes that took place in the cast structure, on the mechanical properties of as-cast, hot rolled and cold rolled material was investigated to establish whether structural modification had beneficial or detrimental effect. AISI310S was chosen as the subject material for this work because it is known to solidify as γ. It might be expected therefore that its structural modification would not be easy unlike other types of steel which either solidify to form δ-ferrite or form delta ferrite initially which later transforms to austenite. The difficulty of refining the γ phase when it happens to be the primary phase lies in the fact that no known nucleant exists that is potent enough and can survive the high casting temperatures used in industry. Limited work done on steels which solidify directly to γ at low cooling rates[186] or at low thermal gradients[205] gave promising results.

However, the effect of these additions was not studied at cooling rates and thermal gradients utilized in the continuous casting of these steels. The mechanisms contributing to the refinement of the as-cast structure due to these additions are not known.

In this work, the following areas of the structural modification of as-cast AISI310S were investigated to gain a fuller understanding of the processes involved in the solidification of austenitic stainless steels and the influence these processes have on the as-cast structure, and eventually on the mechanical properties at different stages of the processing of such materials.

1. Effect of superheat on the solidification mode of AISI310S.

2. Effect of superheat on the as-cast macrostructure (columnar grain size and shape, % equiaxed zone).

3. Effect of superheat on the as-cast microstructure (primary and secondary arm spacings).

4. Effect of additions on the as-cast macrostructure of AISI310S, and the influence of superheat on the effectiveness of these additions.

5. Effect of structural modification on the properties of as-cast (unhomogenised and homogenised), hot rolled and cold rolled material and on the recrystallization process during annealing of cold rolled material.

These aspects of the structural modification and properties of the steel are analysed in the same order in the following five sections.

However as mentioned in section **6.3.1.1** and observed in Figure **6.30**, primary δ-ferrite grain boundaries were present in some of the ingots and these grain boundaries were not in one to one correspondence with the austenite columnar grains. This phenomenon was considered to be evidence of a peritectic transformation that took place on cooling from the liquid phase. This has been observed in stainless steels such as 316 and 304 which go through a peritectic transformation on cooling.

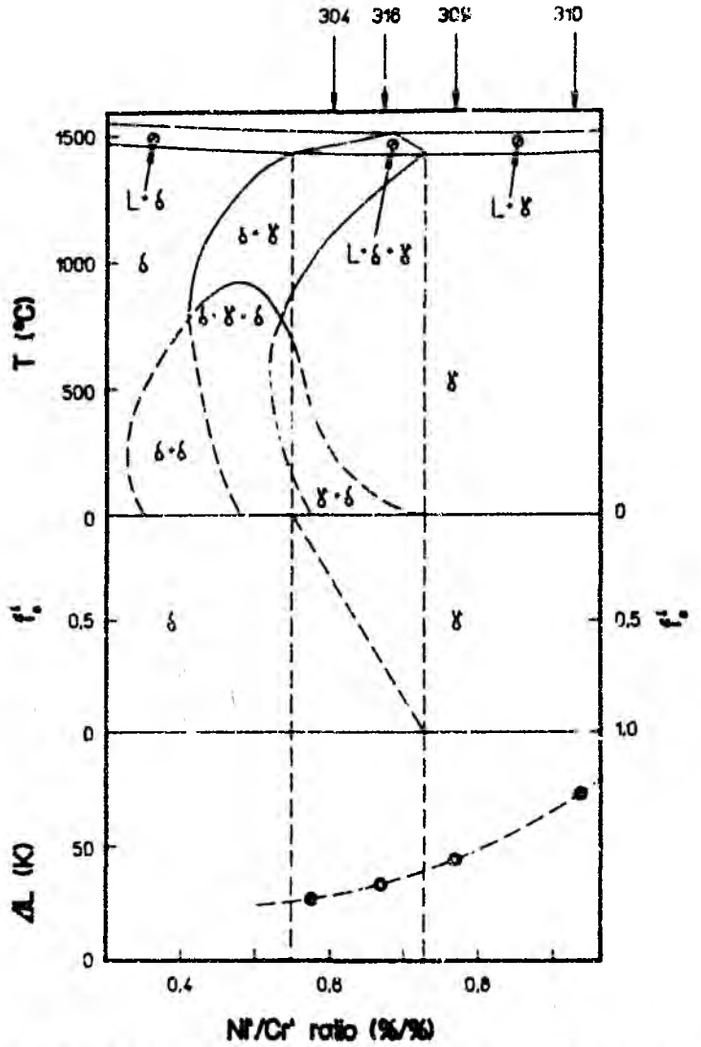

Figure 7.1 **Section from the Fe-Cr-Ni equilibrium phase diagram, the ferrite/austenite-ratio during solidification and solidification interval as a function of the ratio* Ni'/Cr' for austenitic stainless steels[307]**

*** Ni' = Ni + 0.3 Mn + 22 C + 14 N + 1 Cu**
Cr' = Cr + 1.5 Si + 1.4 Mo + 3 Ti + 2 Nb

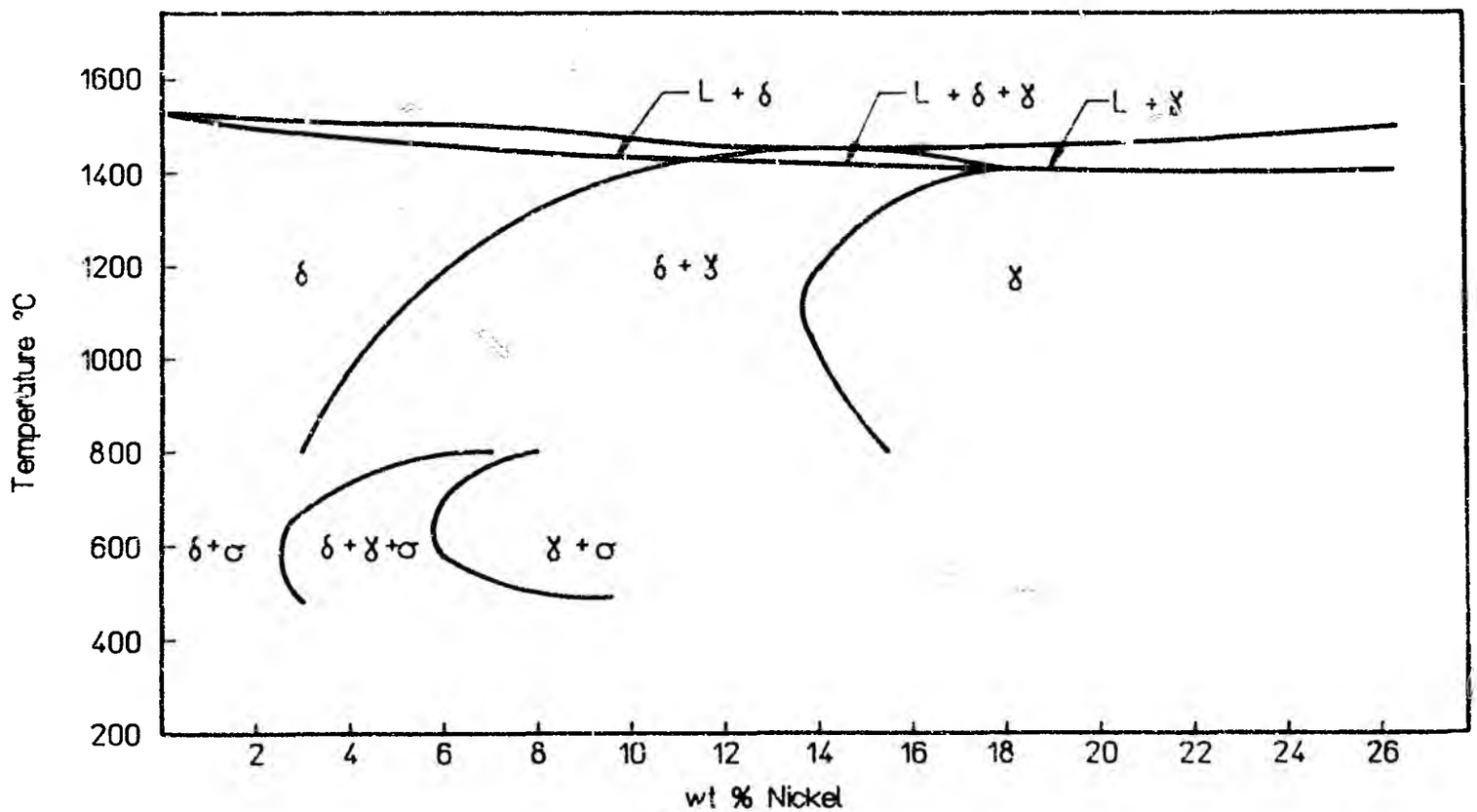

Figure 7.2 Fe-Ni-Cr pseudo-binary phase diagram at 25 wt% Cr

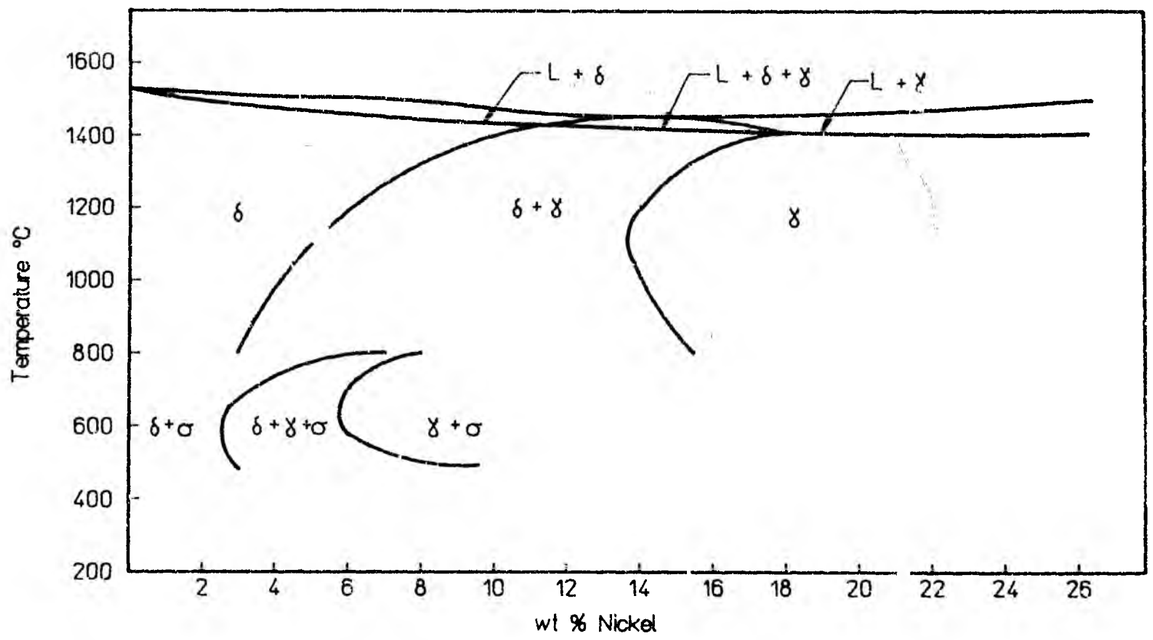

Figure 7.2 Fe-Ni-Cr pseudo-binary phase diagram at 25 wt% Cr

As can be seen from Figure 7.1 the Ni'/Cr' ratio in AISI310S differs significantly from those ratios which cause peritectic transformation during solidification. However, even 310S may go through a peritectic reaction due to high cooling rates which cause a shift in the transformation as shown below.

Low cooling rates : $L \rightarrow L + \gamma \rightarrow \gamma$ 7.1

High cooling rates :

either $L \rightarrow L + \delta + \gamma \rightarrow L + \gamma \rightarrow \gamma$ ...7.2

or $L \rightarrow L + \delta \rightarrow L + \gamma \rightarrow \gamma$ 7.3

or $L \rightarrow L + \delta \rightarrow \gamma$ 7.4

The cooling rate effect was also observed by other researchers, but was first discussed by Fredriksson[308] in his work on 18-8 stainless steel. He observed that some of his 18-8 steel, which was supposed to solidify to δ-ferrite on cooling, actually solidified to form a primary structure of austenite.

He performed a series of controlled-solidification experiments with various rates of solidification and various amounts of nitrogen. The results of these experiments are presented in Figure 7.3. This figure clearly demonstrates that the primary phase depends on solidification rate and nitrogen content. For a given nitrogen content the primary phase changes from austenite to ferrite when the solidification rate exceeds a certain value.

A similar shift in AISI310S is quite possible at high cooling rates, which is usually the case in continuous casting processes, where the cooling could be as high as $1440Ks^{-1}$ at 0.5 mm from the surface of the slab. It drops sharply to about $360Ks^{-1}$ at 1 mm and to about $75Ks^{-1}$ at 3 mm from the surface. These cooling rates for continuous

casting were derived during a study of the microstructural development of AISI304 on solidification by Wolf[309]. However in another work by Nari et al[239] with a low alloy steel, the cooling rates found were appreciably lower for the continuous casting process. This is entirely possible, since the cooling rate is determined by the process parameters such as section thickness, casting speed and so on, rather than the constitution of the steel, which does not change the heat transfer coefficient drastically. In the present work cooling rates were calculated using the relationship between secondary arm spacing and cooling rate, which was empirically found by Suzuki, et al[234] for AISI310S stainless steel (c.f. section **6.3.1.2**). The cooling rates found for these ingots showed that even though they were not as high as those found by Wolf[309], they were well within the range found in various types of continuous casting processes (see Table **7.1**).

High cooling rates were said to be responsible for the shift in the solidification sequence, i.e. they favoured peritectic transformation rather than solidification to γ, but this assumption on its own cannot explain the following two contradictory and interesting phenomena.

(a) The primary δ grain boundaries were not present in castings made with very high and very low superheat viz. above 150°C and below 50°C respectively.

(b) The γ dendrites were not in a one to one correspondence with the primary δ-grain boundaries. The austenite dendrites traversed these boundaries (as shown in Figure **6.30**) as if they were non-existent. EDS analyses showed that these boundaries were chromium

rich (Figure 6.31), which is contrary to expectations in the case of a δ-grain boundary.

The phenomenon in **(a)** does not appear to have been reported in the literature by other researchers and although **(b)** was observed initially by Hultgren[310], who recommended special etching techniques to reveal these primary δ grain boundaries in his very early work in 1929, and later by other recent researchers[308,243], no explanation was put forward as to why it was actually possible to observe them once the transformation was complete.

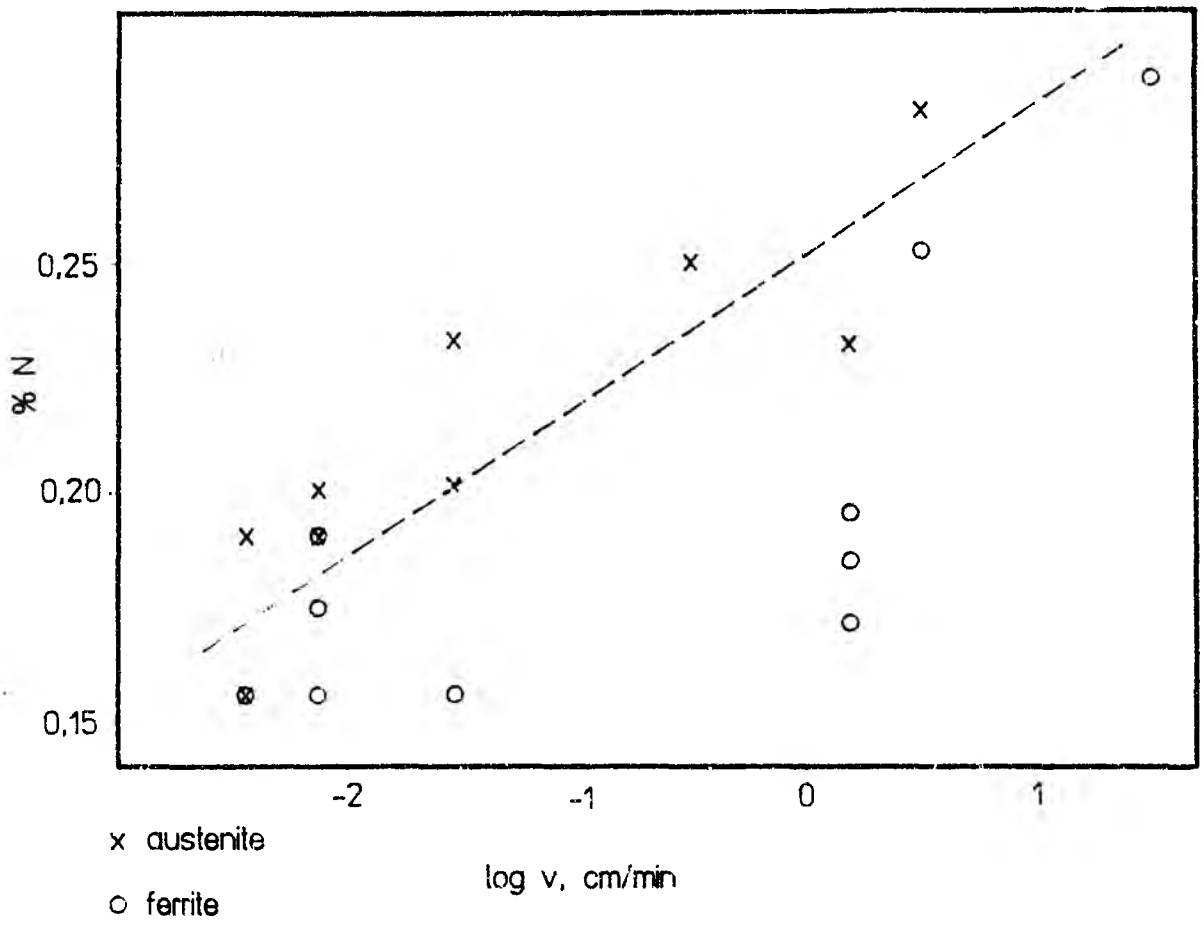

Figure 7.3 **The transition of primary δ-ferrite to austenite as a function of nitrogen content and cooling rate[308]**

Table 7.1 **Secondary arm spacing values measured for various types of continuous cast steels[311]**

Material	Casting Method	Section Thickness (mm)	Distance From Surface (mm)	Dendrite Arm Spacing (Micrometers)
Hi Si	Twin Roll	0.2	0	1
Hi Si	Twin Roll	0.2	0.1	7
304	Twin Roll	1.7	0.2	4
304	Twin Roll	1.7	0.8	8
304	Double Roll	2.4	0	9
Low Carbon	Twin Roll	2.5	1.3	40
Low Carbon	Horizontal KCC Belt	30	2	30
Low Carbon	Horizontal	30	15	70
Low Carbon	Hazelett Belt	40	1	50
Low Carbon	Hazelett Belt	40	10	100
Low Carbon	Hazelett Belt	40	20	150
304	Slab Caster	150	<10	40
Carbon	Slab Caster	250	<10	70
Carbon	Slab Caster	250	100	450

Possible explanations proposed for these phenomena in the order in which they are mentioned above are as follows.

(a) At very high casting temperatures, i.e. 1550°C and above, the chill grains of δ-ferrite that form on the surface of the mould remelt due to the high superheat of the liquid metal. Once these grains melt into the liquid, the temperature of the mould increases to such a degree that it reduces the thermal gradient and cooling rate, which suppress the formation of δ-ferrite a second time and allow for the direct transformation from liquid to γ. This is best illustrated by Figure **7.4**. This explanation is consistent with the relationship between the cooling rate and the transformation sequence proposed by other researchers.

With low superheat casting, the disappearance of δ-ferrite dendrites may be due to the fact that low thermal gradients reduce cooling rates to such a degree that liquid to γ transformation is favoured, rather than peritectic transformation.

As illustrated in Figure **7.4(b)**, in the temperature range 1450 to 1550°C, immediately after pouring, a high degree of undercooling caused by the cold mould walls provides the driving force (high cooling rate) for the liquid to nucleate and grow δ-ferrite grains on the mould wall. At the early stages, a mushy mixture of δ-ferrite and liquid forms. However, as the thermal gradient decreases, γ grains start to nucleate on the mould wall, and grow into this mixture as a result of peritectic reaction taking place between δ-ferrite and the liquid phase.

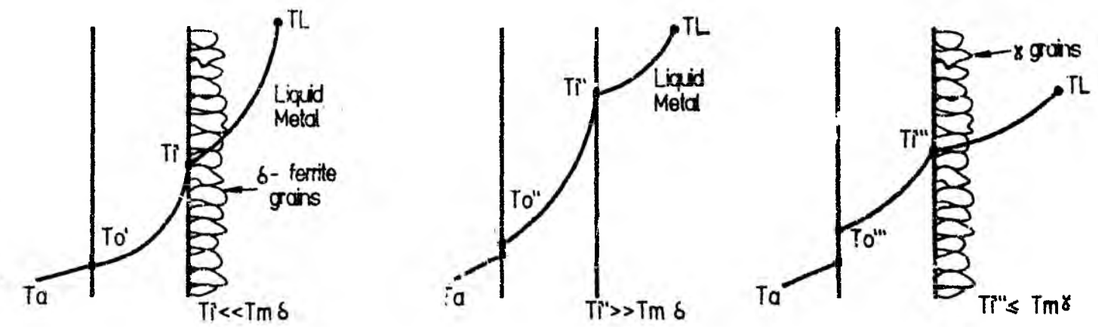

LEGEND
Ta = ambient temperature
To = mould wall outer surface temperature
Ti = mould wall inner surface temperature
TL = liquid metal temperature
Tm = metal melting temperature
Ts = solid metal temperature

Figure 7.4 Schematic description of solidification modes of AISI steel in separate casting temperature ranges (a) temperatures higher than 1550°C

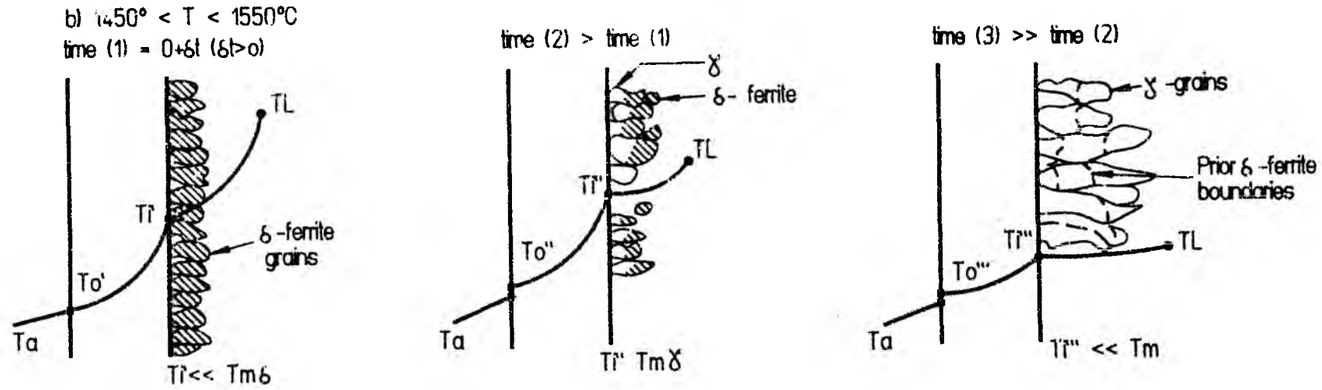

LEGEND
Ta = ambient temperature
To = mould wall outer surface temperature
Ti = mould wall inner surface temperature
TL = liquid metal temperature
Tm = metal melting temperature
Ts = solid metal temperature

Figure 7.4 contin. (b) temperatures between 1450 and 1550°C

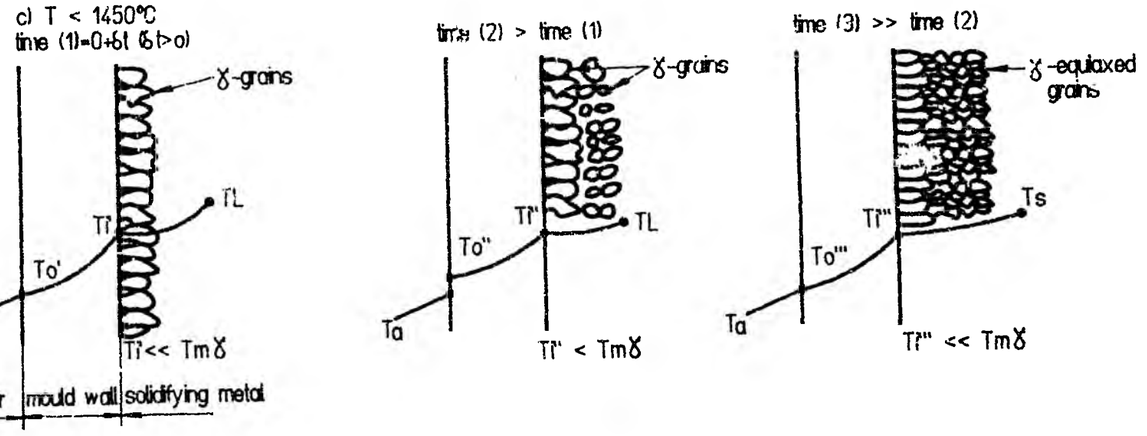

LEGEND
Ta = ambient temperature
To = mould wall outer surface temperature
Ti = mould wall inner surface temperature
TL = liquid metal temperature
Tm = metal melting temperature
Ts = solid metal temperature

Figure 7.4 contin. (c) temperatures lower than 1450°C

(b) Here, there seems to be a contradiction in the phenomena observed; i.e. the presence of the residual primary δ-ferrite grain boundaries in a matrix of γ grains. Grain boundaries of δ-ferrite are expected to be rich in γ-forming elements, rather than being rich in δ-ferrite forming elements, due to the rejection of γ-forming elements at the solid/liquid interface during growth of these δ-ferrite grains. The growing γ-grains may be expected to dissolve these solutes wherever they meet the "grain boundaries", and actually cause them to disappear completely. The observations were that:

(i) the initial δ-ferrite grain boundaries did not disappear,

(ii) the EDS analyses showed that these boundaries were chromium rich as expected with γ-grain boundaries.

The explanation put forward for these contradictory observations was possible by making use of Fredriksson's[308] results for the distribution coefficients of solutes in γ and δ-ferrite phases, and of Lippold, et al's[235] electron probe microanalyses results in austenitic stainless steel weldments. It should be noted here that although these two investigations involved austenitic stainless steels, which either solidify directly to γ or transform via peritectic reaction, their analysis was concentrated on the residual δ-ferrite preserved along the austenite grain and/or subgrain boundaries or the ferrite solidified as the last portion of the liquid which was rich in ferrite forming elements.

Here, the observed structure also contained the prior δ-ferrite grain boundaries, which were preserved in the austenite grains (Figure **7.5 (a)**), not only the δ-ferrite precipitation caused by the rejection of ferrite forming solutes into the dendrite arm boundaries. These were also observed in the same ingots, but they are not the subject of discussion at this time.

As can be seen from Figure **7.5 (b)**, the δ-ferrite grain formed initially rejected γ-forming elements like Ni, Mn, C, N, and Cu into the liquid just ahead of the solid/liquid interface. This created a thin layer of liquid rich in these solutes but relatively depleted in chromium. The thickness of this layer is estimated to be a few micrometers. Fredriksson estimated the distribution coefficients of Ni and Cr to be as follows:

$$K_{Ni}^{\delta/L} = 0.79 \quad and \quad K_{Cr}^{\delta/L} = 1.0$$

This indicates that it is the enrichment in Ni in this region which causes the depletion in Cr in relative terms.

The γ grains grow by advancing into the δ- ferrite grains which form initially at the mould surface. When a γ grain meets the boundary of a primary δ-ferrite grain Ni atoms which were rejected by the δ phase now begin to diffuse back into the γ (or transformed δ) owing to the high equilibrium distribution coefficient of Ni in γ

$$K_{Ni}^{\gamma/L} = 0.94$$ [308].

This increases the relative concentration of chromium at the grain boundary leading to a higher liquidus temperature of the material in a narrow band around the grain.

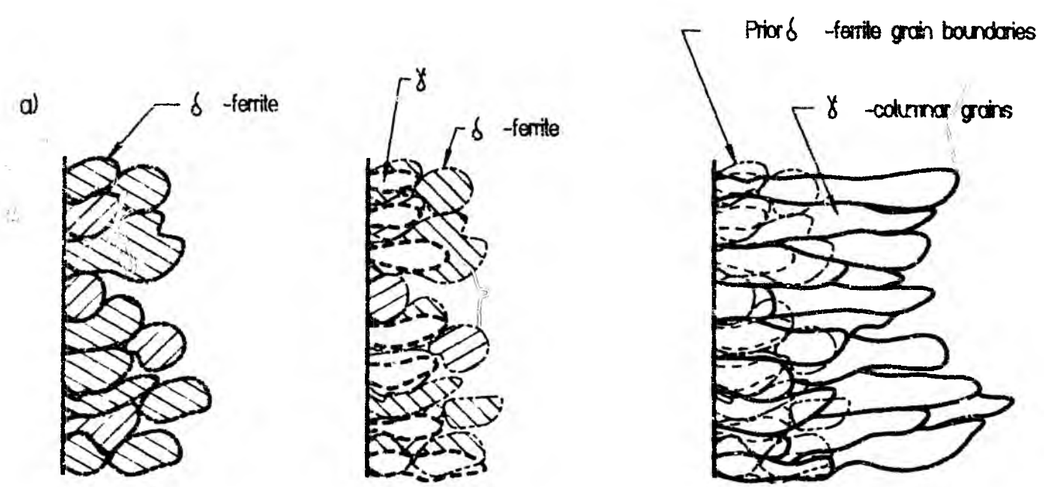

Figure 7.5 The schematic descriptic of how the prior δ-ferrite grain boundaries are preserved in γ-grains of AISI310S steel (a) nucleation and growth on the mould wall

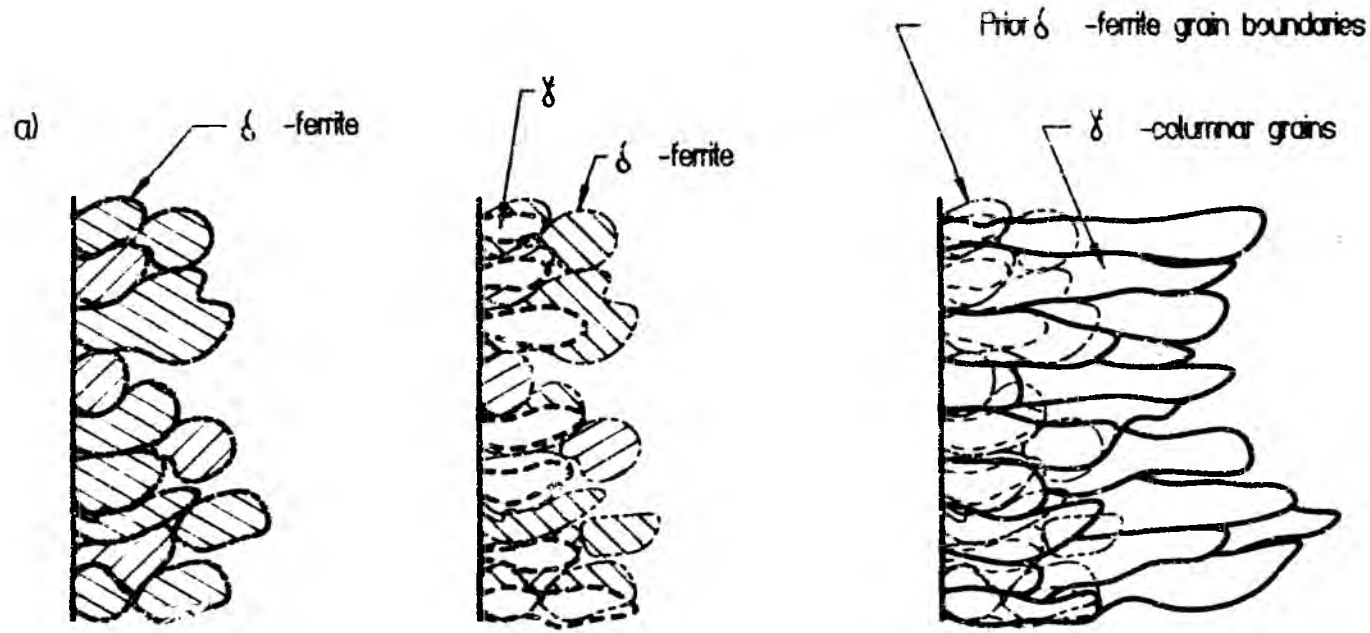

Figure 7.5 The schematic description of how the prior δ-ferrite grain boundaries are preserved in γ-grains of AISI310S steel (a) nucleation and growth on the mould wall

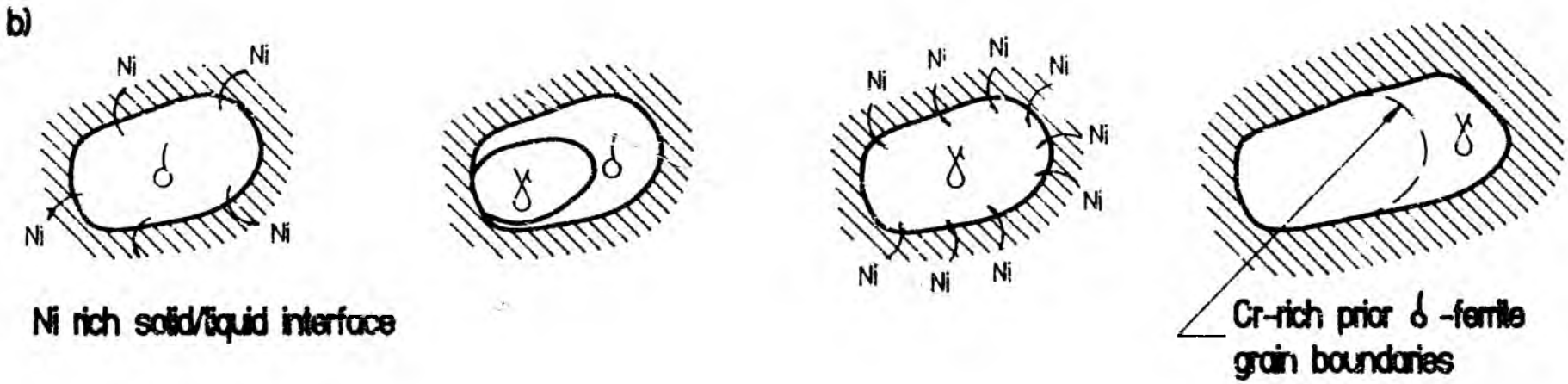

Figure 7.5 cont. (b) nucleation and growth of a single austenite grain

b)

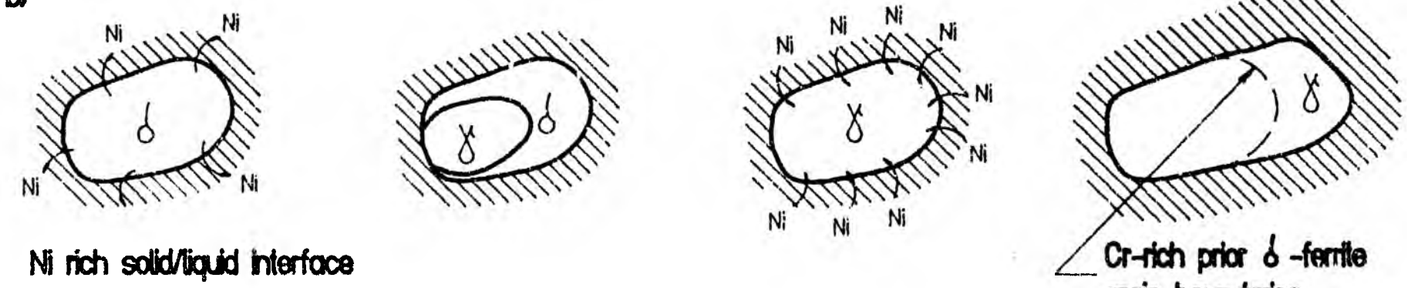

Figure 7.5 cont. (b) nucleation and growth of a single austenite grain

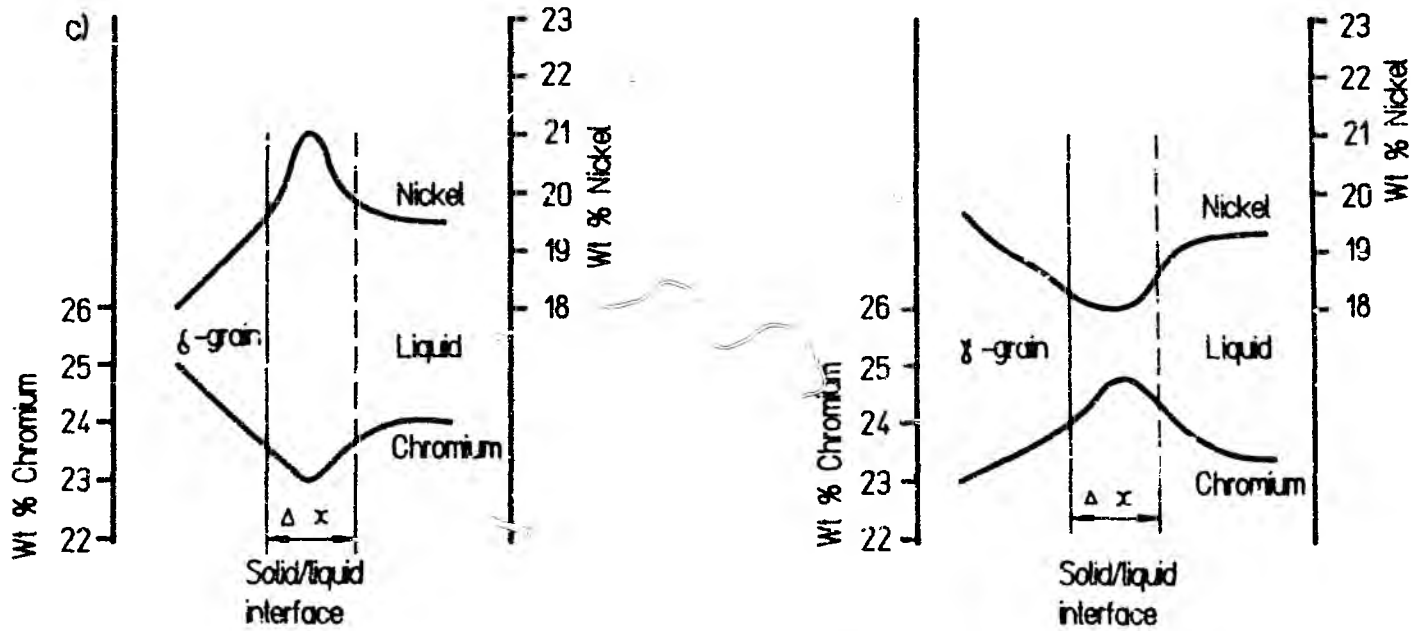

Figure 7.5 cont. (c) Concentration profiles of Ni and Cr at the solid/liquid interface

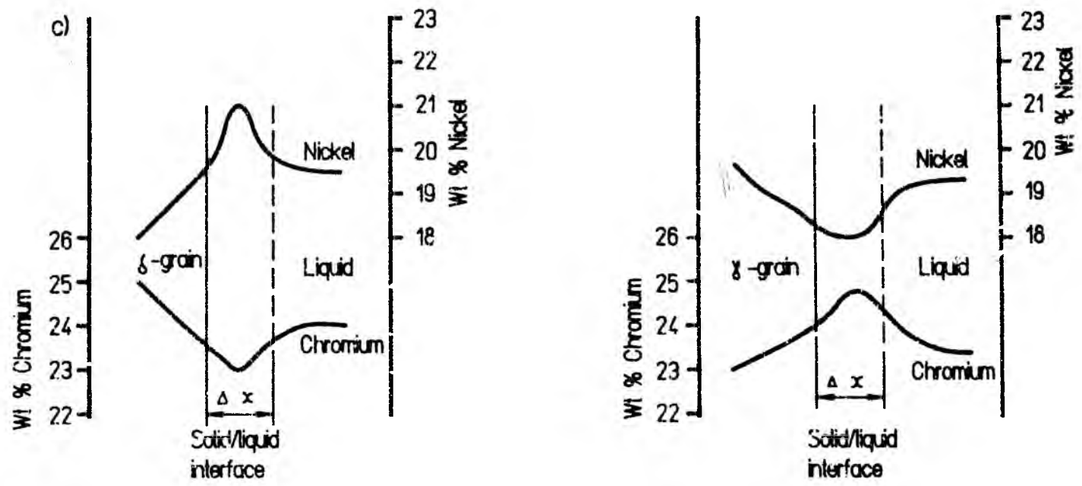

Figure 7.5 cont. (c) Concentration profiles of Ni and Cr at the solid/liquid interface

This in turn causes the material in this band to solidify instantly preserving a thin chromium-rich film inside the grain.

The resultant structure is composed of γ columnar grains with residual prior δ-ferrite grain boundaries in the grains. Prior δ-ferrite grain boundaries and freshly formed γ-grain boundaries do not have a one-to-one correspondence. There seems to be a critical cooling rate, where the transformation sequence shifts from direct solidification to γ, to peritectic transformation of $L \rightarrow L + \delta \rightarrow \gamma$. This cooling rate was estimated at between 1400 and 1500Ks^{-1} from an analysis of the secondary dendrite arm spacings.

Obviously the cooling rate drops exponentially as a function of the distance into the liquid from the mould surface. This drop is as much as 10-fold in the first mm distance as estimated by comparison between the measured dendrite arm spacings and those of Wolf's[309]. This fact indicates that the cooling rate on the inner surface of the mould is the factor that determines whether solidification is directly to the γ-phase or by peritectic reaction.

The important feature here is that γ-grains do not stop growing and start a new grain at these boundaries. This is most probably due to very high growth rates, which do not allow for the redistribution of solute atoms. Besides, an increase in the melting point of this boundary would not allow the "pushing" of this zone by the advancing γ/liquid interface. Moreover, it is already known that δ-ferrite is not a potent nucleant for γ. The lattice mismatch between the two is 7.9%. Thus, the driving force for grain growth exceeds that for γ-nucleation and growth becomes more favourable resulting

in the structure observed. This is valid only in the temperature range in which this phenomenon was observed.

This prior δ-ferrite grain boundary, preserved at room temperature, may be the cause for the low hot workability of AISI310S steel. As is already known for AISI310 type steel, ingot cracking may occur during the initial rolling operation which cannot be ascribed to hot shortness, and often slabs must be rolled to an intermediate size and conditioned to remove severe cracks prior to finishing. Also, hot band (~ 3-5 mm thick) may edge crack badly at normal finishing temperatures.
These problems indicate that there might be planes of weakness close to the edge of ingots or slabs. So, there is a possibility that apart from other factors such the type of steel, resistance to plastic flow and the columnar grain structure, these retained prior δ-ferrite grain boundaries may be one of the causes of inferior hot workability.

High cooling rates obtained during continuous casting processes make AISI310S vulnerable to peritectic transformation, and to the formation of this subgrain structure. So, it is of utmost importance to suppress this transformation sequence in favour of direct transformation to γ from the liquid phase, if it is wished to minimize the factors involved in reducing the workability of the steel. This could probably be achieved through constitutional adjustments such as the addition of austenite stabilizing elements such as C, N and so on. However, elimination of the long columnar crystals is also expected to improve the workability and the internal quality of the steel, as well as its mechanical properties. A refined macro and/or microstructure may well be a cure for the workability problems of AISI310S discussed above.

7.2 Effect of Superheat on the As-Cast Macrostructure of AISI310S Stainless Steel Without Additions

As expected, the results in Section **6.2.1** showed that a decrease in the superheat of the alloy brought about a decrease in columnar grain width and in the proportion of the columnar zone, with a concomitant increase in the proportion of the equiaxed zone.

Even though second or fourth degree polynomials were found to give slightly higher correlation coefficients for the relationship between grain width and superheat, logarithmic expressions were chosen because they fitted the data well and in order to facilitate the discussion and modelling processes. The interesting phenomenon observed here was that the grain widths measured at 6 and 14 mm from the edge changed at different rates as the degree of superheat was varied. This observation suggested the introduction of the parameter "**grain width ratio**" which is the ratio of grain width at 14 mm to grain width at 6 mm from the edge of the ingot. This ratio proved to be quite useful in describing the nucleation and growth characteristics of columnar structures, as will be seen from the present discussion.

As can be seen from Figure **6.12** in section **6.2.1**, the grain width ratio increased as the casting temperature was decreased. This phenomenon can best be explained by considering the changes that take place in the nucleation and growth rates of γ grains in this temperature range, as illustrated in Figure **7.6**.

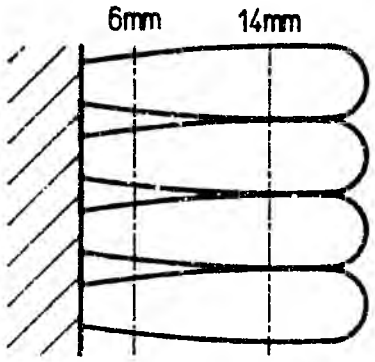

a) Nucleation Rate $\dot{N}$ is low
Growth Rate $\dot{G}$ is high
Grain width ratio is low

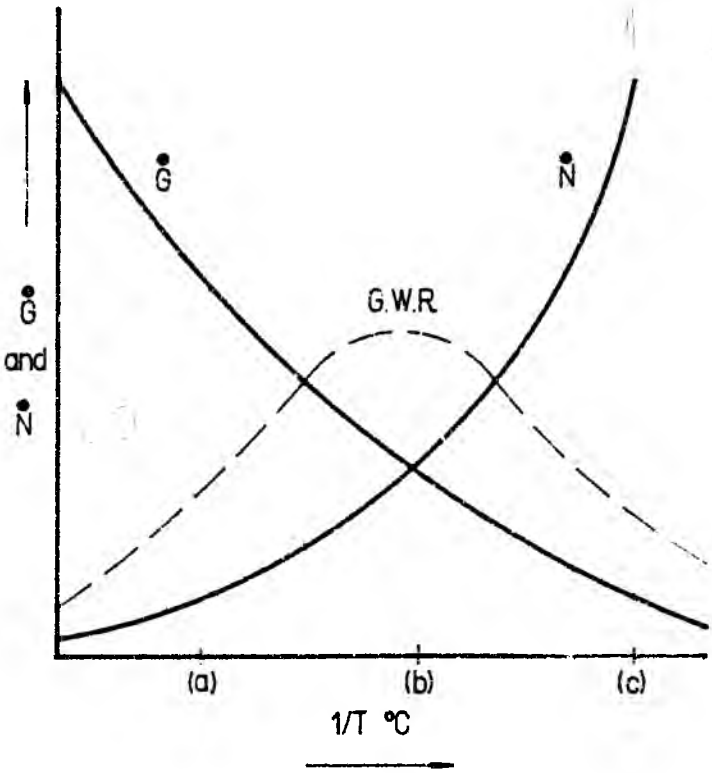

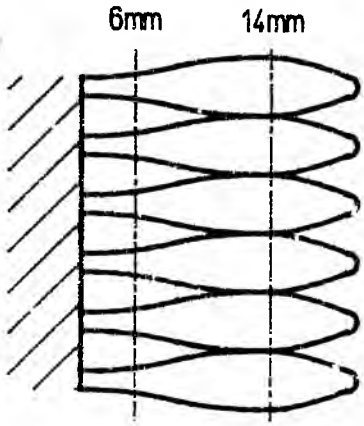

b) Nucleation Rate $\dot{N}$ is high
Growth Rate $\dot{G}$ is high
Grain width ratio is high

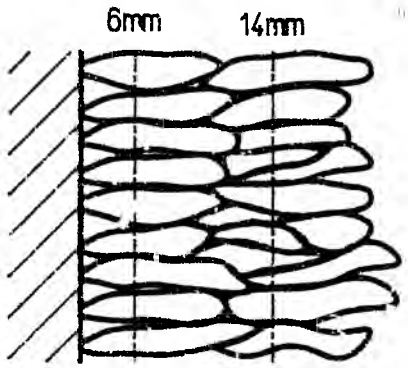

c) Nucleation Rate $\dot{N}$ is low
Growth Rate $\dot{G}$ is low
Grain width ratio is low

Figure 7.6 Illustrations showing the relationship between grain width ratio and various combinations of nucleation and growth rate conditions and corresponding grain size and shapes

In the high temperature casting range (1565 to 1610°C), ingots showed coarse columnar grains. In this range, the superheat was so high that the crystals that were nucleated initially were remelted by the heat remaining in the liquid after its surface had been chilled. The part of the mould near the region of contact with the liquid was heated to a temperature above the liquidus. As cooling continued, nucleation occurred when the liquid near the mould wall again cooled down to its nucleation temperature. Because cooling was slow, compared with the drastic chilling effect which produced primary nucleation, few nuclei formed. It should be born in mind that the initial chill zone grains were of δ-ferrite while the subsequent ones were γ-grains (Section 7.1). Since the nucleation rate was quite low, a few γ grains nucleated on the mould wall, grew towards the center of the mould, while thickening at the same time. In this temperature range, the growth rate was much higher than the nucleation rate. These conditions favoured growth rather than nucleation, resulting in the structure shown in Figure 7.6 (a). Since these grains compete with the same number of grains from the start of nucleation till they reach the center, their widths do not change much as they grow, thus the grain width ratio usually remains close to unity.

In the temperature range 1476 to 1545°C, the structure of the ingots had elongated columnar grains, again extending towards the center. The nucleation rate on the surface of the mould was higher than in castings poured in the high temperature region. The growth rate was lower, but still high enough to keep the grains, which nucleated on the surface of the mould, growing till they reached the center of the ingot. These grains outgrew the grains which had unfavourable growth directions forming a more or less strongly anisotropic macrostructure. That is why, although quite a few grains nucleated on the surface

of the mould, only a few of them grew inwards to any important extent. It is well known that, under these conditions, the grains that survive have a strongly preferred orientation; in face-centered cubic and body-centred cubic structures, for example, all the crystals have a <100> axis perpendicular to the mould wall. It is believed that the crystals with other orientations are suppressed because they do not grow away from the mould as fast as those that are more favourably oriented. This results in the structure where these favourably oriented grains get thicker as they grow into the liquid, since there are now fewer grains to compete with, thus increasing the grain width ratio.

As can be seen from Table **6.8**, with the two ingots cast from temperatures 1455 and 1436°C, the extent of the equiaxed zone did not allow for grain width measurement at 14mm from the edge of the ingot. Thus there were no grain width ratio data points for these two ingots in Figure **6.12**. However it can be seen from the macrostructures (Figure **6.5**) that the columnar zone of these ingots can be schematically illustrated as in **7.6 (c)**. Since the nucleation rate was high and the growth rate low due to low superheat, the growth of grains stopped a brief period after their nucleation. Repeated nucleation of new grains occurred ahead of the solid/liquid interface continuously. However the grains still showed a slight orientation effect due to the relatively high thermal gradients present close to the mould wall. This type of columnar zone is actually a transition from the coarse, strongly oriented columnar structure to an isotropic equiaxed structure and has been referred to as a columnar-equiaxed structure. Due to highly competitive nucleation and growth conditions, grains do not show much thickening laterally and the resultant grain width ratio is close to unity again, as

it was illustrated in Figure **7.6 (a)**.

The significance of grain width ratio is that it serves as a useful tool in depicting the shape of the grains, and thus the nucleation and growth conditions prevailing during the formation of a specific zone in the as-cast structure. However it is useful only when the structure is columnar or columnar-equiaxed, considering the fact that equiaxed structures are almost always isotropic i.e. their grain width ratio is supposed to be unity under ideal conditions. But, bearing in mind that in continuous casting processes the as-cast structures are almost always columnar or columnar equiaxed due to the very high thermal gradients present during solidification, the concept of grain width ratio could be applied to compare the as-cast structures obtained under different conditions. These could include changes in steel composition, slab thickness, casting speed and so on. In sections **6.2.2** and **6.2.3** where the influence of additions on the as-cast structure of AISI310S was analyzed, grain width ratio was one of the parameters which indicated some correlation with the refinement of the structure. This effect will be discussed in the section that follows.

7.2.1 Effect of Superheat on the Formation of Equiaxed Zone

As can be seen from Figure **6.10**, the extent of the equiaxed zone increased gradually to about 10% with a decrease of 100°C in superheat. It then increased to 77% for a further 60°C decrease in superheat. This change in the slope below 1490°C can be explained by considering the constitutional supercooling effect as illustrated in Figure **7.7**.

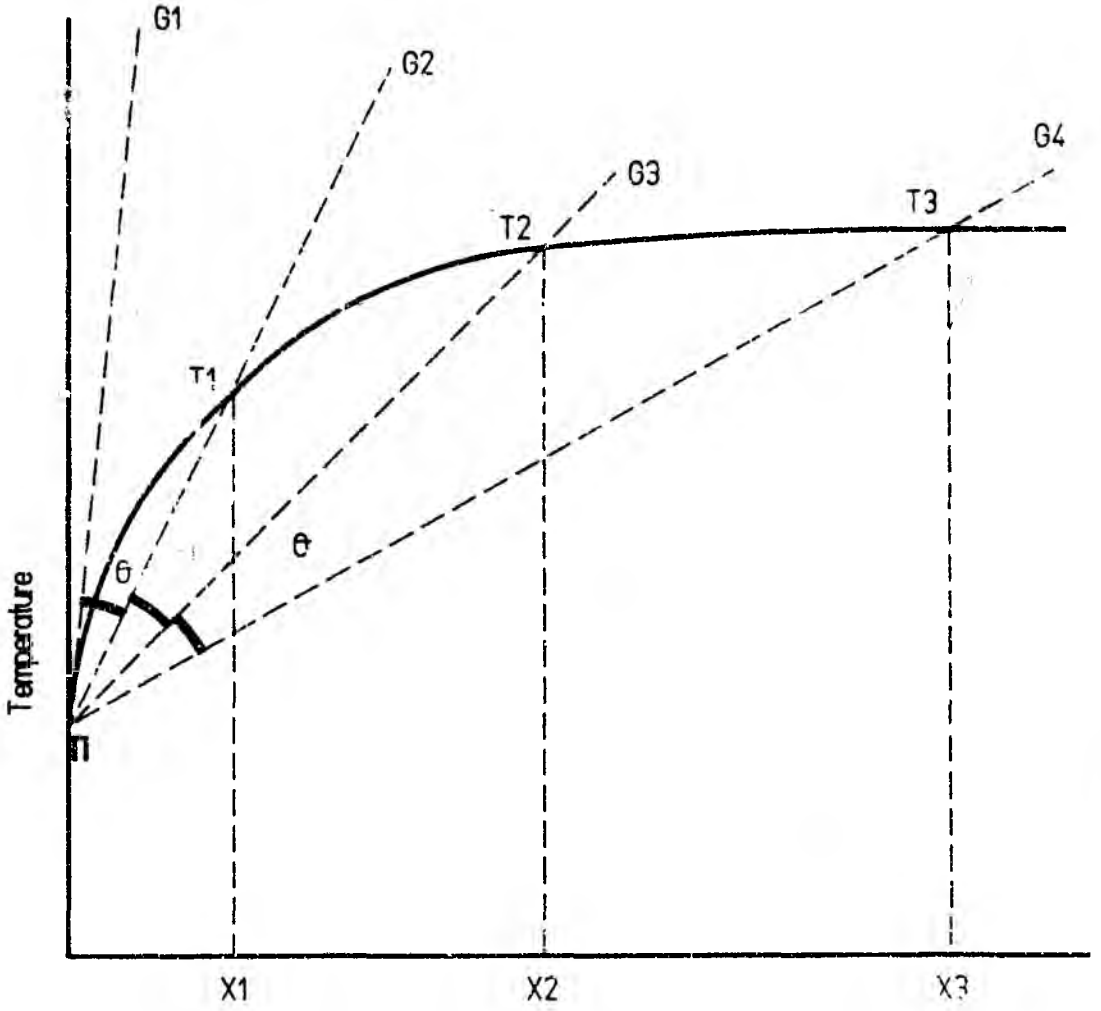

Figure 7.7 Changes in the amount of constitutional supercooling and the width of the supercooled region with change in the slope of the thermal gradient ahead of the solid/liquid interface[312]

As can be seen, the width of the supercooled region (x) changes much faster than the thermal gradient ahead of the solid\liquid interface.

Although the slope of the thermal gradients changes by equal amounts (equal to tanθ), the width of the supercooled zone increases exponentially.

This is in accordance with the relationship between x, the distance where maximum undercooling occurs, and the growth and system parameters given as[286]:

$$X = \frac{D}{R} \ln \left[\frac{mC_o(1-K_o)R}{GDK_o}\right] \quad \ldots\ldots\ldots\ldots\ldots\ldots\ldots\ldots 2.15$$

Where D is the diffusivity of solute in the liquid and can be taken as $5 \times 10^{-5} cm^2 s^{-1}$, which is more or less valid for all metallic liquids. The constitutional term $mC_o(1-K_o)/K_o$ was calculated by using data from the literature for Cr in Fe. The value of K_o for Cr in Fe has been given as

$$K_o(Fe\text{-}Cr) = 0.95 \quad \ldots\ldots\ldots\ldots\ldots\ldots\ldots\ldots 7.5^{295}$$

The slope of the liquidus in the Fe-Cr system has been given as

$$m^L = \left|\frac{\Delta^\circ C}{\Delta\ wt.\%X}\right| = 1.3 \quad \ldots\ldots\ldots\ldots\ldots\ldots\ldots\ldots 7.6^{295}$$

Thus replacing 0.95 and 1.3 for K_o and m^L respectively, it can be calculated that

$$\frac{m(1-K_o)}{K_o} = 0.068 \quad \ldots\ldots\ldots\ldots\ldots\ldots\ldots\ldots 7.7$$

and for AISI310S which has Cr concentration of 25%,

$$\frac{mC_o(1-K_o)}{K_o} = 1.7 = P \quad \text{.....7.8}$$

where P represents the alloy variables component of equation **4.1.**

Assuming that all the process parameters and growth rate (R) are constant, equation **2.15** can be written as :

$$X = A \ln\frac{B}{AG} \quad \text{.....7.9}$$

where

$$A = \frac{D}{R} \quad \text{.....7.10}$$

and

$$B = \frac{mC_o(1-K_o)}{K_o} \quad \text{.....7.11}$$

When the proportion of equiaxed zone was replotted against the inverse of superheat on a semi-log scale (ln(1/T)) as shown in Figure **7.8**, a strong correlation was found between the two (correlation coefficient = 0.95) in the temperature range 1436 to 1564°C, which can be expressed by the equation:

$$\%\ equiaxed\ zone = 244.5 + 49.4 \ln\frac{1}{\Delta T} \quad \text{.....7.12}$$

where ΔT = superheat in °C.

This equation has the same form as equation **2.15** and provides strong evidence to support the premise that the formation of the equiaxed zone is related to

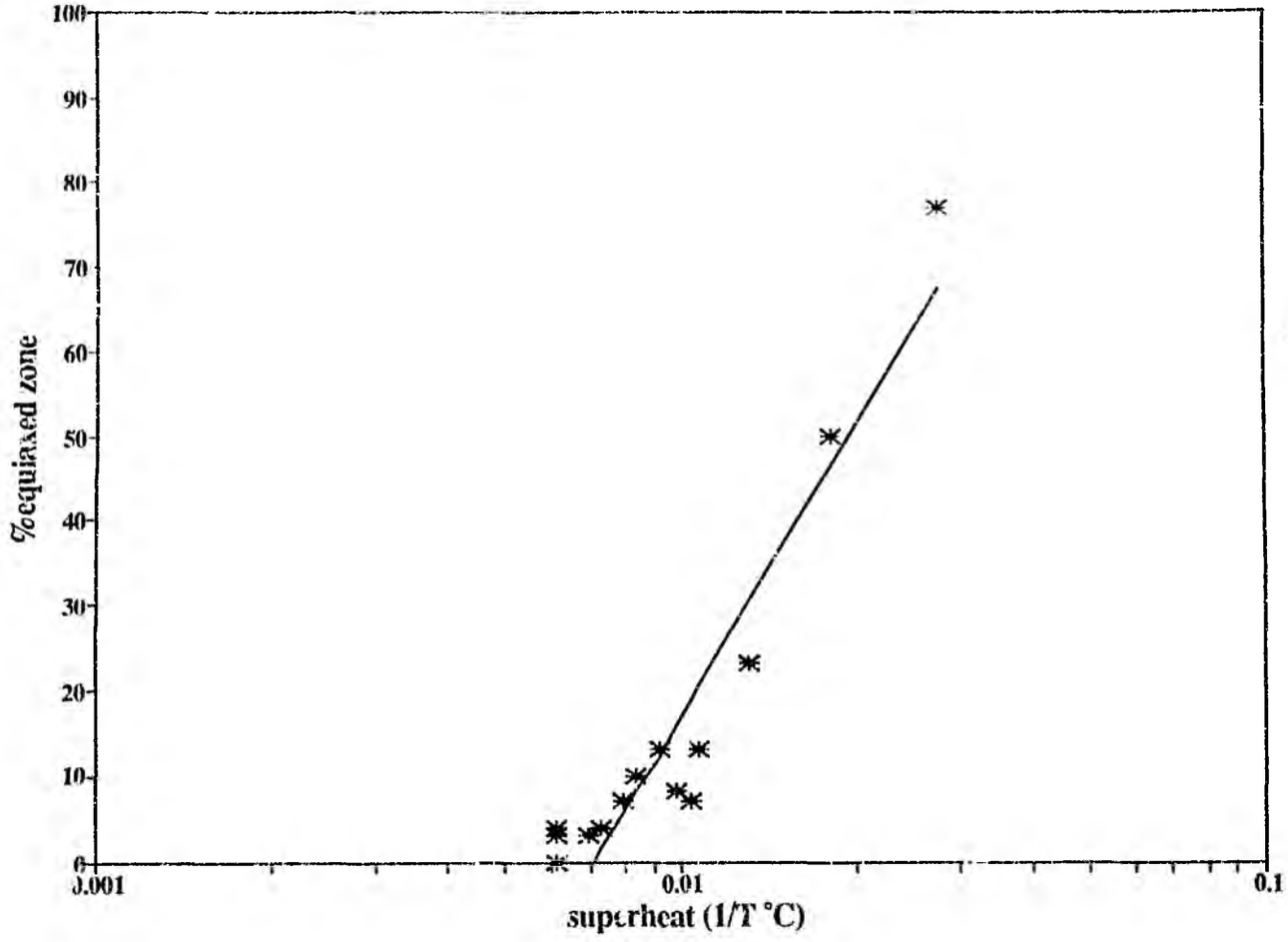

Figure 7.8 The change of the proportion of equiaxed zone with superheat

constitutional supercooling. However, although both equations have the same form, the units are different. A relationship between equations **2.15** and **7.12** was established by the following analysis.

Equation **2.15** may be expressed in the same form as equation **7.12** as follows.

$$\%\ equiaxed\ zone = \frac{1}{\alpha}\cdot\frac{D}{R}\ln\left[\left(\frac{mC_o(1-K_o)}{K_o}\right)'\frac{\alpha R}{GD}\right] \quad \ldots\ldots\ldots 7.13$$

where α is a coefficient.
Equation **7.13** may be written as :

$$\%\ equiaxed\ zone = \frac{1}{\alpha}\cdot\frac{D}{R}\left[\ln\left[\frac{mC_o(1-K_o)}{K_o}\right]'+\ln\frac{\alpha R}{GD}\right] \quad \ldots\ldots 7.14$$

or

$$\frac{1}{\alpha}\cdot\frac{D}{R}\ln\left[\frac{mC_o(1-K_o)}{K_o}\right]' + \frac{1}{\alpha}\cdot\frac{D}{R}\ln\frac{\alpha R}{GD} \quad \ldots\ldots\ldots\ldots\ldots 7.15$$

or

$$\frac{1}{\alpha}\cdot\frac{D}{R}\ln\left[\frac{mC_o(1-K_o)}{K_o}\right]' + \frac{1}{\alpha}\cdot\frac{D}{R}\ln\frac{\alpha R}{D} + \frac{1}{\alpha}\cdot\frac{D}{R}\ln\frac{1}{G} \quad \ldots\ldots 7.16$$

or

$$\frac{1}{\alpha}\cdot\frac{D}{R}\left[\ln\left(\frac{mC_o(1-K_o)}{K_o}\right)' + \ln\frac{\alpha R}{D}\right] + \frac{D}{\alpha R}\ln\frac{1}{G} \quad \ldots\ldots\ldots 7.17$$

Term G in equation **2.15** is analogous to ΔT in equation **7.12**. Replacing G in equation **2.15** by ΔT in equation **7.12** we obtain

% equiaxed zone =

$$= \frac{D}{\alpha R}\left[\ln\left(\frac{mC_o(1-K_o)}{K_o}\right)' + \ln\frac{\alpha R}{D}\right] + \frac{D}{\alpha R}\ln\frac{1}{\Delta T} \quad \ldots\ldots 7.18$$

The first term on the right hand side of equation **7.13** corresponds to the value of 244.5 in equation **7.12**. We may therefore write

$$244.5 = \frac{D}{\alpha R}\ln\left[\frac{mC_o(1-K_o)}{K_o}\right]' + \frac{D}{\alpha R}\ln\frac{\alpha R}{D} \quad \ldots\ldots\ldots 7.19$$

Furthermore, from equation **7.12**:

$$49.4 = \frac{D}{\alpha R} \quad \ldots\ldots\ldots 7.20$$

Equation **7.19** was solved for $\left[\frac{mC_o(1-K_o)}{K_o}\right]'$ by substituting 49.4 for $\frac{D}{\alpha R}$. This gave a value of 6970 which is 4100 times bigger than the value of P (=1.7) found in equation **7.8**. Thus the coefficient α was calculated as:

$$\alpha = 2.44 \times 10^{-4} \quad \ldots\ldots\ldots 7.21$$

or

$$\frac{1}{\alpha} = 4100 \quad \ldots\ldots\ldots 7.22$$

The theoretical growth rate R may then be calculated as:

$$R = 0.249 \text{ cm min}^{-1} \quad \ldots\ldots\ldots 7.23$$

This value is well within the range found by A. Suzuki et al[304] for the dendritic growth with tertiary arms in AISI310S. Dendritic structure with tertiary arms was the structure in the equiaxed zone observed in the sections of the ingots examined in the present work.

Substituting $[\frac{mC_o(1-K_o)}{K_o}]'$ by $P(-\frac{mC_o(1-K_o)}{K_o}) \times 4100$

and α by $2.44\ 10^{-4}$ equation **7.19** can be written as:

$$244.5 = \frac{D}{\alpha R}\ln[\frac{mC_o(1-K_o)}{K_o}\cdot\frac{R}{D}] \quad \ldots\ldots\ldots\ldots\ldots\ldots\ldots 7.24$$

by eliminating the coefficient α in the logarithmic term.

Equation **7.13** can be rewritten as:

$$\%\ Equiaxed\ Zone = \frac{D}{\alpha R}[\ln\frac{mC_o(1-K_o)R}{\Delta T\ D\ K_o}] \quad \ldots\ldots\ldots\ldots\ldots 7.25$$

where

$D = 3 \times 10^{-3}\ cm^2.min^{-1}$

$\alpha = 2.44 \times 10^{-4}$ (in the temperature range 1436-1564°C for AISI310S, from equation **7.21**)

$R = 0.249\ cm.min^{-1}$ (under the present conditions, from equation **7.23**)

For 25% Cr in Fe

$$\frac{mC_o(1-K_o)}{K_o} = 1.7 \quad \ldots\ldots\ldots\ldots\ldots\ldots\ldots 7.8$$

ΔT = Superheat in K.

Equation **7.25** expresses mathematicaly what was observed in the castings poured from the temperature range 1436-1564°C and the strong link between the kinetics of formation of the equiaxed zone and constitutional supercooling.

It should be borne in mind that coefficient α was calculated to show the strong relationship between the formation of the equiaxed zone and constitutional supercooling ahead of the interface. Otherwise Equation **2.15** contains qualitatively different terms to those found in Equation **7.25**. The proportion of equiaxed zone and ΔT in Equation **7.12** are not the same parameters as distance and thermal gradient ahead of the solid/liquid interface as in Equation **2.15**. The calculated value of R appears to be realistic. It nevertheless introduces an error since the growth rate at a specific spot in the ingot changes as the degree of superheat is increased or decreased. But this term can still be taken as constant, as this variation is not considerable, especially within the boundaries of the equiaxed zone. However the form of Equation **7.25** and the calculation of growth rate by use of the coefficient α showed that it may be possible to relate qualitatively as well as quantitatively the parameters % equiaxed zone and superheat (ΔT) to X and the thermal gradient respectively.

7.3 Effect of Superheat on the As-Cast Microstructure

While the grain size in as-cast ingots is an important structural parameter influencing properties, the structure within the grain (dendritic structure) is generally of as great, or greater, engineering importance. This is because regions within the grain and between 'dendrite arms' often **(a)** are rich in solute from microsegregation, **(b)** contain non-equilibrium second phases, **(c)** contain equilibrium second phases such as impurity compounds and non-metallic inclusions, **(d)** contain microporosity from gas, shrinkage, or both. These inhomogeneities are believed to influence the mechanical properties of cast or wrought material. There is sufficient evidence that **(a)** the degree of homogeneity which can be obtained in a cast alloy with commercially practical homogenization treatments depends on dendrite arm spacing, and **(b)** the mechanical properties of the heat-treated casting depend on the homogeneity obtained. In wrought alloys, microsegregation from the original ingot is carried to some extent into the final wrought product, and affects mechanical properties in a similar fashion. There has, therefore, been considerable interest in determining the effects of solidification variables on dendrite arm spac and establishing the mechanism of formation of dendrite arm spacing.

Experimental evidence available for a variety of cast alloys indicates that primary dendrite arm spacing depends on the product of thermal gradient and growth rate, GR, and results have been reported that correlate well with this parameter[304].

Although a considerable effort has been made to understand the dendritic type growth in as-cast

microstructures, there are still several aspects of dendrite growth which are not well understood. Most of the understanding of these structures comes from the study of the dendrite tip region, which includes the first few branches. However most theoretical models so far have only considered single dendrite tips. For most metallic alloys, it has been shown that the tip growth is indeed primarily controlled by solute diffusion[313], whereas the thermal undercooling plays a minor role on this microscopic scale. However, when considering the columnar and equiaxed growth morphologies frequently encountered in castings, diffusion and solute transport control the rate at which the whole dendritic grain solidifies. Empirical models have been developed, based on the experimental findings of various types of metal alloys. But an appropriate model for primary dendrite arm spacing in columnar growth is still missing. For example, Okamoto and Kishitake[314] formulated the following equation, by assuming that the liquid steel, surrounded by the secondary arms growing from the primary ones, solidifies as the secondary arms grow larger, and that the distance is determined by the moving distance of the solute:

$$\lambda = 2\varepsilon \, [mD_L \, C_o \, (1-K_o)/V]^{1/2} \quad \ldots\ldots\ldots\ldots\ldots\ldots\ldots \quad 7.26$$

where

λ : primary arm spacing

m : slope of liquidus line

D_L : diffusion coefficient of alloying element in the molten steel

C : solute content

K : equilibrium distribution coefficient

V : cooling rate

ε : constant related to the growth pattern of the thickening secondary arm

Furthermore, Okamoto and Kishitake[314] proposed the following modified equation, derived from the measurement of the columnar dendrite primary arm spacings resulting from the unidirectional solidification of Fe-Ni, Fe-Si, Fe-P and Fe-C alloys:

$$\lambda \propto [mC(K-1)]^{1/6}/V^{1/2} \quad \ldots\ldots 7.27$$

These two equations are similar to the previously proposed empirical relationships of the type:

$$\lambda \propto 1/G^{\alpha} R^{\beta} \quad \ldots\ldots 7.28$$

but with the constitutional term included. R in equation 7.28 is the growth rate, and α and β are statistically calculated constants.

Although Flemings noted that the product GR has the units of cooling rate, and expressed his experimental results against cooling rate[291], there is experimental evidence that the effect of these parameters could be analyzed separately. Suzuki et al's[304] work with AISI310S steel showed that primary dendrite arm spacing is proportional to $1/G^{0.4}R^{0.2}$ while both secondary and tertiary arm spacings depend on the cooling rate.

Moreover, their results indicated that for the same growth rate (R), the primary dendrite arm spacing is controlled by the thermal gradient and vice versa. However, the calculated exponent for growth rate (= 0.2) suggests that this parameter has a significant effect only at very high and very low rates. Moderate levels of growth do not influence the structure significantly, since $R^{0.2}$ tends to converge to unity.

At this stage it must be noted that, although various models have been developed to explain the dendritic growth in as-cast structures, like the dendrite tip model[315] and the solvability approach[315], these theoretical models have had limited success in explaining experimental results. Whereas the empirical models could find difficulties in their application to different alloy systems. However, in summary, the components of the empirical equations are:

1.Constitutional parameter : $mC_o(1-K_o)$
2.Diffusion coefficient of the solute : D
3.Growth rate : R
4.Thermal gradient : ΔG

The contribution of each of the above components differs from one alloy to another or from one researcher to another.

Thus a correlation between primary spacing and cooling rate is not completely adequate, since the temperature gradient at the dendrite tip should be taken into consideration in calculating the local cooling rate. The thermal gradients into the mould material, in the solid metal or in the liquid are not the factors determining growth rate. However a correlation may exist between the thermal gradient at the dendrite tip and gradients elsewhere in the ingot.

Figure **6.36** shows that as the columnar grain width was refined, the primary arm spacings got larger, i.e. the microstructure was coarsened. This suggests that the nucleation and growth mechanisms for macro-grains and primary arms may be different. However, since one comprises the other, or in other words, one is made up of the other one, they should somehow be related. The

micrographs in Figure **6.30** show that a coarse grain contained more primary arms than a finer one. As the grains got smaller, primary arms did not respond to this refining by getting smaller, instead their number per grain dropped. This can be explained by again considering the role of competition between the nucleation and growth parameters, especially during the early stages of solidification. As it was discussed before, at high superheat the nucleation rate on the mould is very low, due to an insufficient degree of thermal driving force, however growth rate is relatively high (since once the surface is created, it is thermally more feasible to grow rather than creating a new surface which requires a bigger undercooling). Thus, once a grain is nucleated at one point on the surface of the mould, it initially grows laterally to reduce the undercooling within a very narrow region ahead of the mould surface to a very low value. Growth continues until it meets the next grain growing in the opposite direction. As the thermal gradient at the solid/ liquid interface decreases, dendritic growth towards the center of the mould, starts. This growth in two perpendicular directions most probably takes place concurrently. This is illustrated in Figure **7.9**. Since the nucleation rate is higher with lower superheats (low thermal gradients), the number of grains is greater, but the number of primary arms is lower than that obtained with higher superheats within a unit area of mould surface. Low thermal gradients influence the nucleation rate, and disturb the strong anisotropy which is present under steep thermal gradients, thus causing a further increase in the average spacing between the arms. Low thermal gradients also lead to the coarsening of dendrite arms that are favourably oriented with respect to the direction of heat flow. This takes place at the expense of arms which are mis-oriented in this regard.

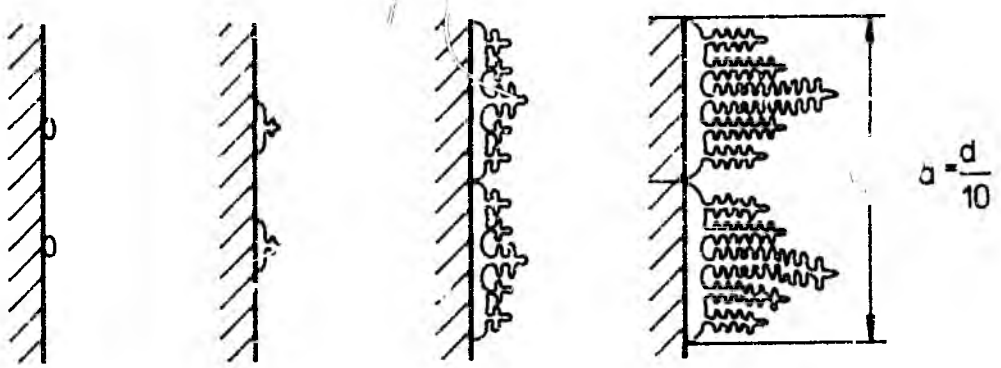

a) High superheat

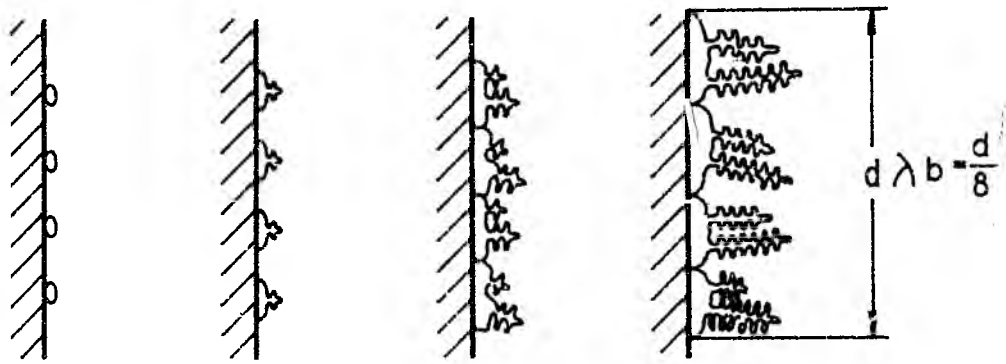

b) Low superheat

Figure 7.9 **Illustrations showing the influence of superheat on primary arm spacing**

It, therefore, appears quite possible that thermal gradients are the factor determining the primary arm spacing or the number of arms per unit volume of the solid. This conclusion is consistent with the effect of superheat on grain width ratios.

In his work on the effects of nucleation and constitutional supercooling on the properties of cast steel Church[316] showed that higher casting temperatures resulted in smaller primary and secondary arm spacings. He found that the difference in cooling rate between two ingots cast with about 100°C difference in superheat was small which is in good agreement with the results of this work. However, he also found that the local solidification time for higher casting temperatures was shorter than for lower temperatures resulting in a shorter mushy zone due to steeper thermal gradients in the mushy region. The relationship between thermal gradient, growth rate and local solidification time is given[291] by the equation:

$$t_f = \frac{\Delta Ts}{GR} \qquad \text{.....7.29}$$

where ΔTs is the non-equilibrium temperature range of solidification, and t_f is the local solidification time. The relationship between dendrite arm spacing and the local solidification time could be expressed as[291]:

$$\lambda_1 = a t_f^n \qquad \text{.....7.30}$$

This relationship, being exponential, explains the higher rate of increase of primary arm spacing with further decrease in superheat.

7.3.1 Proposed Primary Arm Spacing Model

Inspired by the analyses of the dendritic arm spacings observed at different superheats during the course of this work, which suggested a logarithmic relationship between the two, an empirical model which takes its form from the constitutional supercooling theory is proposed, to relate the primary arm spacings to the growth and constitutional parameters on a more universal basis. This model also has the potential to link the microstructural development to that of macrostructure, as will be discussed in the subsequent sections.

The proposed model is based on the fact that the coarsening behaviour of the dendrites is closely related to the extent of the supercooled region ahead of the solid/liquid interface. The larger the supercooled region, the coarser the dendrites become. When X (the distance ahead of the solid/liquid interface where supercooling is at maximum) is large enough to allow independent nucleation ahead of the solid/liquid interface, the equiaxed zone starts to form and dominates the as-cast structure. Tiller, et al[290] have shown that

$$X = \frac{D}{R} \ln \left[\frac{mC_o(1-K_o)R}{\Delta G D K_o}\right] \quad \ldots\ldots 2.15$$

where X is the distance ahead of the solid/liquid interface at which maximum undercooling occurs, D is the diffusivity of solute, R is the growth rate, m is the slope of the liquidus, C_o is the concentration of the solute in the melt, K_o is the distribution coefficient of the solute, and ΔG is the thermal gradient.

Since the growth rate and thermal gradient were not

measured during the course of this work, Suzuki et al's[304] experimental results for AISI310S and Cr-Mo steel were used as a basis to fit the model.

A statistical calculation based on the above proposed model and Suzuki et al's results, gave the form of the relationship as:

$$\lambda_2\ (cm) = \frac{2D}{R^{0.7}} \ln\left[\frac{mC_o(1-K_o)R^{0.08}}{K_o D\ (\frac{\Delta G}{10})^{\alpha}}\right] \quad \ldots\ldots\ldots\ldots\ldots 7.31$$

where the exponent α was found to be 1.95 for AISI310S and 2.5 for Cr-Mo steel. This variation is believed to be due to the difference in the liquidus temperatures of these two steels, ~1400°C for AISI310S and ~1500°C for Cr-Mo steel, since their solidification ranges and local solidification times are more or less the same.

This model is based on the following assumptions:

1. solute redistribution takes place by diffusion only

2. the diffusion coefficient is constant (3×10^{-3} $cm^2 min^{-1}$)

3. statistical calculation was carried out taking only Cr in AISI310S and C in Cr-Mo steel as the solutes contributing to the constitutional parameter.

The fit of this proposed equation (equation **7.31**) to Suzuki et al's experimental data is given in Figure **7.10** for AISI310S and Cr-Mo steel.

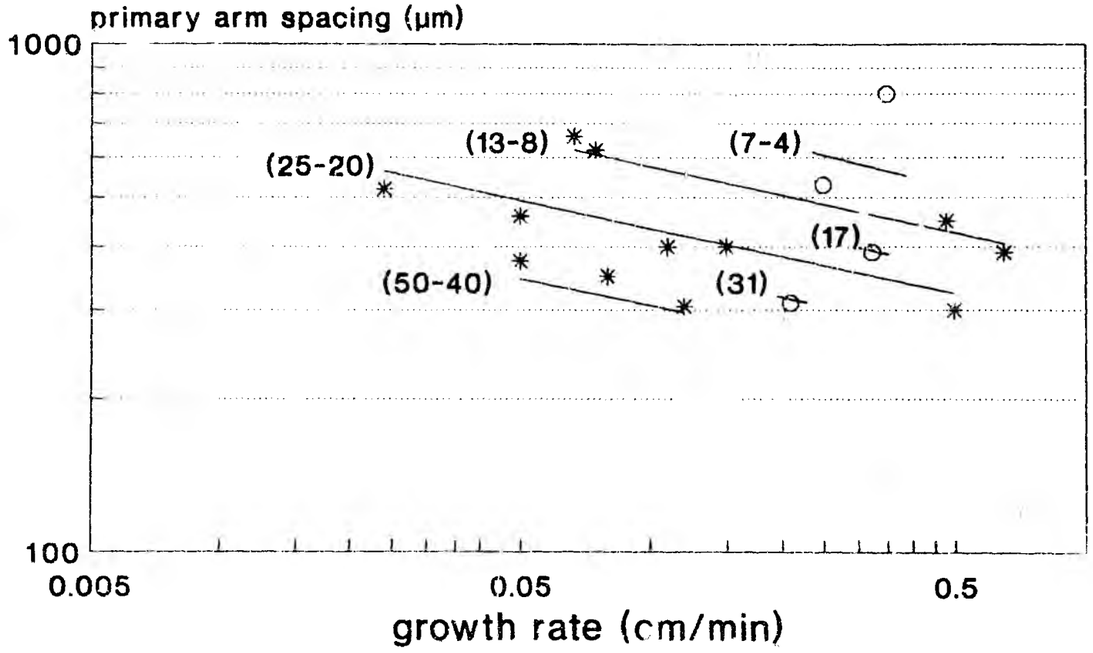

Figure 7.10 Primary arm spacings calculated by the proposed model and measured by Suzuki et al. at different growth rates of (a) AISI310S steinless steel and

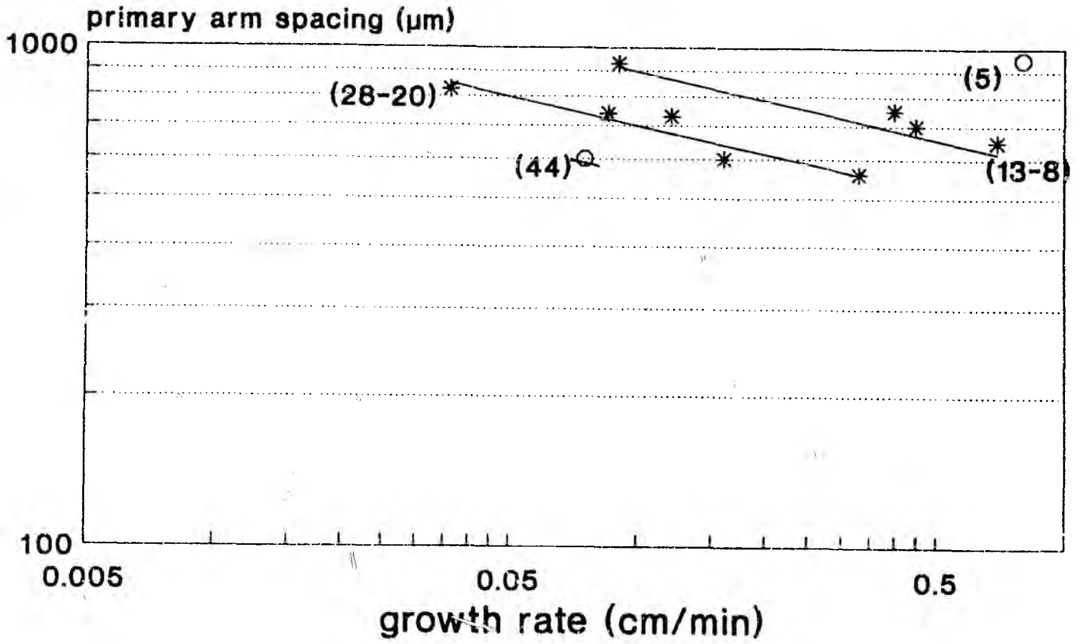

Figure 7.10 contin. (b) Cr-Mo steel

that these have a random pattern and could be considered to be errors due to measurement and experimental procedure. It should be noted that the model fits the experimental data much better for runs involving more than two experimental data points. Suzuki et al also had a few points obtained from one off experiments. It can be seen that the model fitted these points as well as it did the runs involving numerous experiments. The average value of the residual was 5% while the highest value obtained was 9%. Considering the thermal gradient ranges given by Suzuki et al (values in parentheses), the residuals are 95% within the upper and lower boundaries calculated in each range. There were also reading difficulties, which arose from the fact that they used a log-log scale, which may add another possible source of error. It is generally held that the reproducibility of measurements of primary dendrite arm spacing is of the order of 15%.

However, the second assumption, which takes the solute diffusion coefficient as constant for all the alloys and solute elements, is believed to contribute to the variation of the thermal gradient exponent. Equation **7.31** needs to be modified, by including a term which could compensate for the changes in liquidus temperatures and solidification times, in order to enable the use of a constant value for the exponent of the thermal gradient ΔG.

Table 7.2 **Comparison of the λ_1 values calculated using the quasi-empirical equation with Suzuki et al's[304] experimental data for AISI310S.**

$$\lambda_{310} = \frac{2D}{R^{0.2}} * \ln\left[\frac{mC_o * (1-K_o) * R^{0.08}}{K_o * D * (\frac{\Delta G}{10})^{1.95}}\right]$$

ΔG °C/cm	R °C/min	λ_s μm	λ_c μm	$\frac{\lambda_c - \lambda_s}{\lambda_s} \times 100$ %
8-13	0.067	660	621	-5.9
	0.075	620	608	-1.9
	0.480	450	424	-5.8
	0.650	390	403	+3.3
17	0.325	390	392	+0.5
20-25	0.024	520	564	+8.5
	0.050	460	494	+7.4
	0.110	400	427	+6.8
	0.150	400	404	+1.0
	0.500	300	324	+8.0
31	0.210	310	329	+6.1
40-50	0.050	375	346	-7.7
	0.080	350	319	-8.9
	0.120	305	297	-2.6

λ_s= experimental results of Suzuki et al
λ_c= calculated dendrite arm spacing values

Table 7.3 **Comparison of the λ_1 values calculated using the quasi-empirical equation with Suzuki et al's[304] experimental data for Cr-Mo steel.**

$$\lambda_{Cr\text{-}Mo} = \frac{2D}{R^{0.2}} * \ln\left[\frac{m * C_o * (1-K_o) * R^{0.08}}{K_o * D * \left(\frac{\Delta G}{10}\right)^{2.5}}\right]$$

ΔG °C/cm	R °C/min	λ_s μm	λ_c μm	$\frac{\lambda_c-\lambda_s}{\lambda_s} \times 100$ %
8-13	0.090	930	914	-1.7
	0.400	750	687	-8.4
	0.450	700	671	-4.1
	0.700	650	617	-5.1
20-28	0.036	825	848	+2.8
	0.085	740	721	-2.6
	0.120	730	675	-7.5
	0.160	600	640	+6.7
	0.330	560	558	-0.4
44	0.075	600	585	-2.5

The third assumption may also introduce an error, because in multicomponent alloy systems, solute interactions become too complicated to be expressed analytically. They involve tedious calculations of the changes which might take place in the activity coefficients of each solute element due to the addition of another solute element. Addition of a certain solute element may increase the activity coefficient of one solute and decrease that of another. Also the thermodynamic data available on the interaction coefficients between elements in iron alloys are not sufficient to estimate every single effect. It is a good approximation to choose one major solute element which may be the main contributor to the constitutional supercooling parameter, and try to estimate the effect of other solutes on its magnitude, considering the interaction coefficients which are available from the literature. But there will still be an element of error introduced into the calculations by these approximations. For example, although the value of P_c given as $P_c = \frac{mC_o(1-K_o)}{K_o}$ was calculated to be 124 for carbon in Cr-Mo steel of 0.41% C, a value of 50 was used in the model because it was found to fit the model more closely. The use of this value is believed to be justified in view of the fact that the alloy involved has a very complex composition. Thus the effects of Cr and Mo on the values of m, C_o and K_o are not precisely known.

The equation **7.31** proposed for the primary arm spacing appears to fit the hypothesis of constitutional supercooling well. It is directly proportional to the distance, X, ahead of the solid/liquid interface where maximum supercooling occurs constitutionally (equation **2.15**). It can easily be seen that as X gets larger (which is the case at lower thermal gradients and/or

steep liquidus lines), dendrites tend to advance further into the liquid in order to minimize the supercooling ahead of the interface. There is a borderline beyond which the degree of supercooling becomes big enough to allow independent nucleation ahead of the solid/liquid interface, i.e. the equi[illegible]d zone starts to appear. As it was proposed in the previous section, **7.2**, the extent of the equiaxed zone could also be shown to be directly proportional to ***X***.

Basically, the equation for primary arm spacing suggests that solute elements with steeper liquidus curves and higher concentration levels in liquid steel may cause coarsening of the microstructure, whereas the same solute elements may refine the macrostructure by increasing the nucleation rate ahead of the solid/liquid interface.